Soft microfabricated neural implants:
a path towards translational implementation

Thèse N° 9181

Présentée le 8 mars 2019

à la Faculté des sciences et techniques de l'ingénieur
Chaire Fondation Bertarelli de technologie neuroprosthétique
Programme doctoral en microsystèmes et microélectronique

pour l'obtention du grade de Docteur ès Sciences

par

Nicolas VACHICOURAS

Acceptée sur proposition du jury

Prof. H. Shea, président du jury
Prof. S. Lacour, directrice de thèse
Prof. K. Stankovic, rapporteuse
Prof. T. Stieglitz, rapporteur
Prof. Ph. Renaud, rapporteur

2019

EPFL

ÉCOLE POLYTECHNIQUE
FÉDÉRALE DE LAUSANNE

Ideas are easy.
Implementation is hard.
- *Guy Kawasaki*

To my parents…

Acknowledgements

My journey towards this PhD thesis would not have been possible without the help of many people, who provided me with great support and advice.

First of all, I would like to thank Prof. Stéphanie Lacour for giving me the opportunity to work in the Laboratory for Soft Bioelectronic Interfaces (LSBI) and providing me access to excellent facilities and infrastructure. I also would like to acknowledge her invaluable support and guidance throughout my thesis.

I would also like to thank Profs. Konstantina Stankovic, Thomas Stieglitz, Philippe Renaud and Herbert Shea for accepting to be the members of my thesis jury and reviewing my work.

I am also grateful to Profs. Jocelyne Bloch, Grégoire Courtine, M. Christian Brown and Daniel J. Lee for their scientific input, advice and for providing access to their facilities and teams.

Next, I would like to acknowledge the help of my colleagues at the LSBI, who provided scientific and intellectual support during these four years. In particular, my colleagues on the "e-dura team": Dr. Ivan Minev, Dr. Giuseppe Schiavonne, Dr. Xiaoyang Kang and Florian Fallegger, who I cannot thank enough for everything they have helped me with during these past years. I also want to thank Laurent Dejace and Aaron Gerratt for helping out debugging technical issues throughout my project. I am also grateful to Dr. Jennifer Macron, our COSEC and chemistry expert who helped me solve many issues and with whom I had the pleasure to ensure safety in our laboratory at Campus Biotech. I would also like to thank Dr. Amélie Guex for her help and whose previous work on the ABI project facilitated greatly my work with the project. I would also like to acknowledge the help of all semester and master students who helped on various parts of my work: Philippe Campiche, Valerio Tettamanti, Yohann Thenaisie, Lucie Petetin, Vivian Yu, Margaux Roulet, James Bourely and Laurine Kolly.

Finally, and most importantly, I would like to thank a very important person to whom I will be forever grateful, Christina Tringides, with whom I co-developped the technologies presented in my thesis. I cannot thank her enough for her amazing intellectual and scientific contributions to this work as well as her support all these years.

Acknowledgements

iv

Abstract

Neuroprosthetics are a class of medical devices that aim to restore lost or impaired functions of the nervous system by electrical stimulation or recording of neural tissue. State of the art neural implants suffer today from a mechanical mismatch compared with the soft and curved host tissue, as they constrain mechanically the physiological motion dynamics of the central nervous system. This mismatch causes poor electrode-tissue contact, leading to unspecific stimulation or recording, as well as chronic scarring. This fundamental limitation of conventional systems can be overcome by developing soft neural interfaces, using more compliant materials, which can achieve chronic bio-integration and conform to the static and dynamic mechanics of neural tissue. The development of such soft neural interfaces requires the use of electrical conductors that can elastically deform while maintaining their electrical conductivity.

The main objective of this thesis it to develop a new strategy to engineer elasticity in otherwise rigid materials by structuring them with specific patterns. This happens spontaneously at the microscale on stretchable gold films on silicone that display dense distributions of Y-shaped cracks to favor out-of-plane deformation. This work draws inspiration from these cracks by patterning Y-shaped cuts to engineer reversible elasticity in a multi-layer of metallic and plastic thin films. The geometry of these Y-shaped patterns was first optimized using finite element analysis and macroscopic models. Then, a fabrication process was developed enabling the micro-patterning of polyimide/platinum/polyimide interconnects with microscaled Y-shaped cuts (branches of dimensions ~ 15 μm), which were then encapsulated in silicone. These encapsulated micro-patterned interconnects exhibit a sheet resistance of $\sim$15-20 Ω/sq., and remained conductive when elongated by up to 70%, with a resistance increase less than 2.5 times. They were also shown to reversibly stretch at 10% tensile strain for 1 million cycles. This technology allowed patterning of tracks down to 20 μm in width on a wafer-level scale.

These patterned elastic films were then integrated as interconnects in neural implants, coupled with a previously described stretchable coating on the electrode sites. The main application addressed by this thesis is the auditory brainstem implant (ABI), a neuroprosthesis to stimulate the cochlear nucleus (CN) in deaf patients. Existing ABIs produce highly variable speech perception results and it is hypothesized that current ABIs are too stiff to conform to the curvature of the CN, which might lead to poor electrode contact with the neural structures.

Abstract

A soft human scale ABI was tested in a human cadaveric model to demonstrate that this novel electrode is robust to surgical manipulation and can easily be inserted in the brainstem using a dissolvable hydrosoluble guide. In addition, a scaled-down ABI array was tested in vivo in a mouse model and it was shown that it could reliably recruit the auditory system and remain durable for up to 4 weeks.

In addition to ABIs, this technology was also validated for neural recordings at the surface of the minipig cortex, in an acute setting, as well as for chronic spinal cord stimulation in non-human primates.

In the future, this technology could thus be used to develop personalized soft neural implants that can interface with various anatomical locations of the nervous system and could potentially provide a better chronic biointegration and a more robust interface throughout the implantation period.

Keywords: neuroprostheses, neural implants, auditory brainstem implant, soft bioelectronics, spinal cord stimulation, electrocorticography, stretchable electronics, kirigami

Résumé

Les neuroprothèses sont des implants médicaux destinés au rétablissement des fonctions neurologiques partiellement ou totalement endommagées, via une stimulation électrique des tissus nerveux ou grâce à l'enregistrement de l'activité neuronale. Les implants neuronaux actuellement implanté chez les patients ne sont pas parfaitement adaptés, leurs propriétés mécaniques étant trop différentes de celles des tissus nerveux. En effet, la surface du cerveau et de la moelle épinière présentent une courbure complexe et les tissus nerveux sont très souples. A contrario, les implants cliniques sont constitués de matériaux épais et rigides, incapables de se conformer de manière optimale à la dynamique du corps humain. Ces différences en termes de propriétés mécaniques entraînent une incompatibilité à l'interface entre les électrodes et les tissus, empêchant d'une part la spécificité de la stimulation ou des enregistrements et pouvant provoquer d'autre part une cicatrisation chronique. Pour résoudre ces problèmes, une nouvelle génération d'implants à base de matériaux souples et élastiques a été proposée : l'objectif de leur utilisation est de réussir une meilleure intégration biologique de l'implant en conciliant ses propriétés mécaniques à celles des tissus nerveux. Cependant, le développement de neuroprothèses souples nécessite l'utilisation de conducteurs électriques susceptibles de se déformer de manière élastique tout en maintenant leur conductivité électrique.

Dans ce contexte, l'objectif principal de cette thèse est de développer une nouvelle stratégie pour introduire des propriétés élastiques dans des matériaux intrinsèquement rigides, comme les métaux, en les structurant avec des motifs spécifiques. A l'échelle microscopique, ce principe est illustré par l'apparition spontanée d'une distribution dense de micro-fissures en forme de Y dans des films fins d'or étirable évaporé sur du silicone. Cette distribution favorise notamment les déformations hors du plan du film d'or, lui permettant ainsi d'être étirable. Le travail décrit ici s'inspire de ce phénomène et propose la micro-structuration par le biais d'entailles en forme de Y dans des multi-couches fines composées de métaux et plastiques, pour leurs conférer des propriétés élastiques. Dans un premier temps, la forme géométrique de ces motifs en Y a été optimisée en utilisant des simulations à éléments finis, ainsi que des modèles macroscopiques. Un procédé de fabrication a dans un second temps été développé afin de micro-structurer des pistes électriques composées d'un assemblage de polyimide/platine/polyimide. La structuration de l'assemblage est effectuée à l'aide de motifs en Y à l'échelle microscopique (segments des Y de taille ~15 μm), avant que les pistes soient encapsulées dans du silicone. La résistance de couche de ces pistes micro-structurées a été mesurée à ~15-20 Ω/carré. Ces dernières peuvent par ailleurs supporter une élongation

Abstract

jusqu'à 70 %, tout en maintenant leur conductivité électrique, avec une augmentation de résistance inférieure à 2.5 fois par rapport à la valeur initiale. Il a aussi été démontré que ces pistes peuvent être étirées de manière réversible à 10% d'élongation pendant un million de cycles et qu'il était possible de fabriquer des pistes électriques jusqu'à 20 μm de largeur à l'échelle d'un wafer. Ces pistes électriques étirables ont finalement été intégrées dans des implants neuronaux, couplées à un composite élastique, utilisé comme revêtement à la surface des électrodes et décrit dans de précédentes études.

L'application principale mise en lumière dans cette thèse est l'implant du tronc cérébral auditif (ABI), une neuroprothèse qui stimule le noyau cochléaire (CN) chez des personnes sourdes. Actuellement les résultats cliniques des patients avec un ABI sont très variables en termes de reconnaissance vocale : les ABI actuels sont supposés trop rigides pour se conformer à la courbure du CN, provoquant un mauvais contact physique entre l'électrode et le tissu nerveux. Dans le cadre de ce travail, un ABI souple de taille humaine a été fabriqué et testé dans un spécimen cadavérique afin de mettre en évidence la robustesse de cette nouvelle génération d'ABI souple à la manipulation chirurgicale et la facilité de son insertion dans le tronc cérébral auditif à l'aide d'un guide hydrosoluble greffé à l'implant. De plus, une version miniaturisée de l'ABI a été testé dans un modèle de souris, démontrant que cet implant pouvait stimuler le système auditif et rester fonctionnel pour une durée de 4 semaines.

En plus des ABIs, cette technologie a aussi été évaluée dans le cadre d'enregistrement corticaux intra-opératifs dans un cochon nain, ainsi que pour la stimulation chronique de la moelle épinière dans des primates.

Dans le futur, cette technologie pourrait être utilisée pour développer des neuroprothèses souples personnalisées, capables de cibler différentes localisations anatomiques du système nerveux, en vue de fournir une meilleure intégration biologique chronique et une interface plus robuste durant la période d'implantation.

Contents

Contents

List of Figures

List of Tables

1 Introduction

A specific state of the art will given at the beginning of each subsequent chapter of the thesis. The aim of this introduction is to briefly present implantable neural systems and to motivate the use of soft bioelectronic technologies.

1.1 Implantable neural systems

Neural implants are a class of implantable medical devices which interface with the nervous system to address diseases and traumas that affect the central nervous system (CNS) and peripheral nervous systems (PNS). Standard devices consist of an array of electrodes, which are either used to **record** neural activity or to electrically **stimulate** neural tissue. Typical clinical applications for neural stimulation include cochlear implants [1] or Auditory Brainstem Implants (ABI) [2] to restore hearing in deaf patients, Deep Brain Stimulation (DBS) to alleviate symptoms in Parkinson's disease [3], spinal cord stimulation to reduce chronic pain [4], or stimulation of the retina to partially restore vision in blind patients [5]. Neural implants for recording are most often used in electrocorticography (ECoG) for detection of epileptic foci [6], and more recently Utah arrays penetrating intracortical electrodes have been used to record brain signals from tetraplegic patients in order to allow them to control robotic arms [7]. More recent devices combine both modalities, typically in a closed-loop system, performing both recording and stimulation, such as the NeuroPace device that triggers electrical stimulation of the brain upon detection of an epileptic seizure onset in order to silence it [8]. A combined brain recording and spinal cord stimulation device has also been proposed in non-human primates to restore locomotion after spinal cord injury [9].

Classifications   Neural implants can be classified based on their anatomical location: (1) electrodes for the CNS (brain and spinal cord) or (2) electrodes for the PNS (ex. vagus nerve stimulation for epilepsy [10]). Another classification can be made based on how these implants interface with the nervous tissue: (1) penetrating electrode arrays pierce neural tissues to access deeper neuronal layers (e.g. deep brain stimulation for Parkinson's [3] or Utah arrays for recording motor intentions in tetraplegic patients [7, 11]), whereas (2) surface electrodes are

1

less invasive arrays that are positioned onto the surface of the neural tissue, usually underneath the dura mater (e.g. subdural arrays for electrocortiography to locate the foci in epileptic patients [6]). This thesis focuses exclusively on applications relating to surface electrodes for the CNS (Fig. 1.1**A**), even though the technology presented here could be used in the PNS or potentially be modified to allow for neural tissue penetration.

Neural implant system components   A neural implant system is made of three main components: (1) the electrode array that interfaces with the neural tissue, (2) a cable that links the array to a recording/stimulation device and (3) the recording/stimulation device itself. Recording/stimulation devices can either be internal or external. For example in spinal cord stimulation, the stimulation device is an implantable pulse generator (IPG) located subcutaneously at the thoracic level. In epileptic patients, the electrocorticography (ECoG) array is connected to an external recording system through cables that come out directly from the patient's skull. These patients are thus hospitalized during the recording sessions until the array is explanted at the moment of the neurosurgery. Cochlear implants (CI) users wear the stimulating and processing units around their ear and the energy and information is wirelessly transmitted through the skull to a receiver connected physically to the CI. Researchers have been trying in recent years to replace the cable with a completely wireless system [12, 13], but for now only a recent pacemaker for the heart developed by Medtronic uses such an interface in clinical practice [14].

This thesis focuses on the neural interface itself, but it is important to keep in mind that it is part of a larger and more complex system, as all components come with technical interdependent challenges which cannot be overlooked.

Electrode array components   Conventional electrodes arrays in neural interfaces can be subdivided into three electrical sub-components (Fig. 1.1B): (1) The **connector** links the neural implant with the rest of the system (stimulator or recording unit). (2) The **interconnects** (or wires) carry the electrical signal from the connector to the electrodes (or vice versa in recording mode). (3) The **electrodes** interface with the neural tissue and are the points from which the current enters or exits neural tissue.

Each of these components are the subject of intense academic research and represent major challenges in the field of neural electronics. Indeed as electrode arrays become smaller and denser, the voltage at the interface of the electrode becomes larger and generates undesired chemical side-reactions. To address this issue, many groups have been working on the development of electrode coatings to diminish the electrode-tissue interface impedance [15, 16]. Likewise, the development of denser electrode arrays has sparked challenges in developing connectors for large number of electrodes, while maintaining long-term hermeticity. Finally, new technologies have to be developed to manufacture interconnects that can allow high density of electrodes. This thesis mainly focuses on the development of novel interconnects technologies and their interface with existing electrode coatings and connectors.
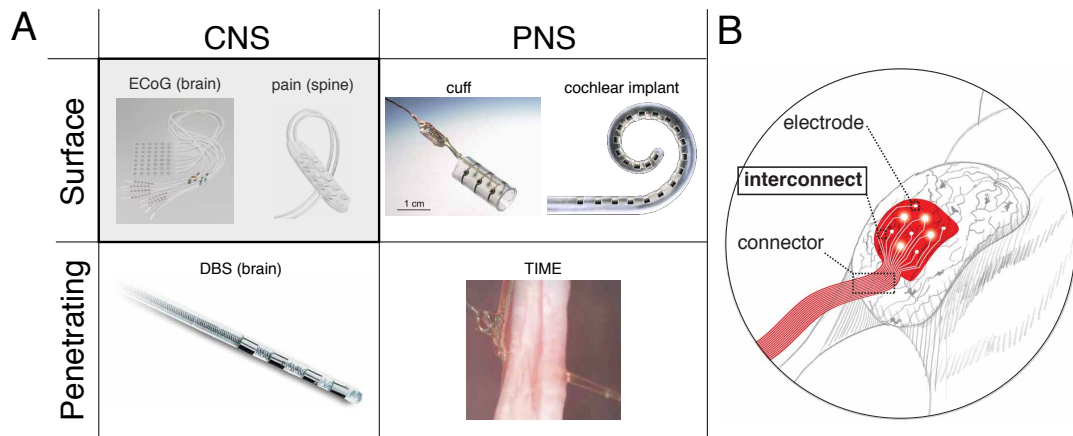
Figure 1.1 – **Focus of thesis.** (**A**) Examples of neural implants classified based on the invasiveness (penetrating or surface) and anatomical location (central or peripheral nervous system, CNS and PNS): a stimulation array for chronic pain relief (www.medtronic.com), a surface array for brain recording and stimulation (www.diximedical.com), a deep brain stimulation probe for Parkinson's disease (www.medtronic.com), a cuff electrode [17], a cochlear implant [18], and Transversal Intrafascicular Multichannel Electrode (TIME) [19] to interface with the PNS. (**B**) Illustration of the three main components of a conventional neural interface. The subject of this thesis is highlighted in bold: surface electrodes for the CNS, with a technological focus on interconnects.

1.2 State of the art in the clinic

The first neural implant was developed in 1953 to stimulate the cochlea of deaf individuals to partially restore their audition. Since then, many more applications have been well established in the clinic, with the largest markets currently being cochlear implants, DBS for Parkinson's disease and spinal cord electrical stimulation for relieving chronic pain [20]. Interestingly, in the past 70 years, independently of the application or the manufacturer, neural implants in the clinic are mostly made the same way: large electrode paddles fabricated with thick platinum–iridium (PtIr 90/10) electrode disks are welded to metallic wires (typically MP35N, a nickel-cobalt-chromium-molybdenum alloy) embedded in a millimeter-thick silicone matrix [21]. Moreover, a large part of the manufacturing process is made manually. Table 1.1 summarizes the geometrical properties of some of these clinical devices and Figure 1.2 shows pictures of various conventional clinical devices.

Table 1.1 – **Geometrical properties of clinical neural implants.** Spinal Cord Stimulation (SCS) from Medtronic (Specify 5-6-5 [22]), electrocorticography (ECoG) array from AD-TECH (AD-TECH FG08A-SP10X-000 [23]) and Auditory Brainstem Implant (ABI) from Cochlear Ltd (ABI541 [24]).

Device	Electrode area	Electrode thickness	Paddle thickness	# of channels
SCS	$6 \, mm^2$	~ 1 mm	2.0 mm	16
ECoG	$4.15 \, mm^2$	~ 200 µm	1 mm	8
ABI	$0.385 \, mm^2$	250 µm	0.7 mm	21
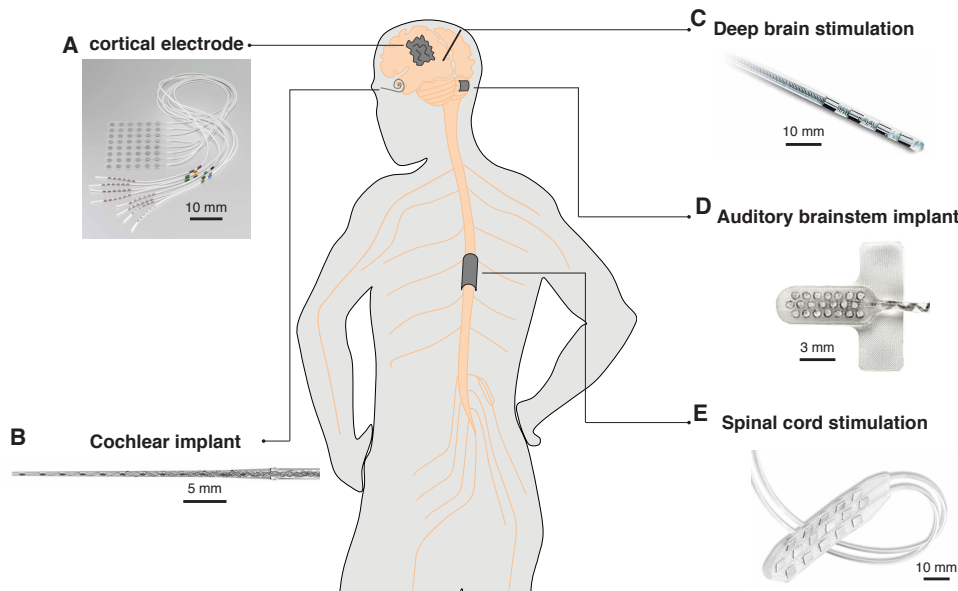
Figure 1.2 – **Examples of clinical devices.** (**A**) Subdural electrode grid from DIXI Medical, (**B**) cochlear implant from MED-EL Corporation, (**C**) deep brain stimulation probe from Medtronic, (**D**)auditory brainstem implant from Cochlear Ltd (**E**) and spinal cord implant from Medtronic.

Thanks to their simplified manufacturing process, these clinical electrodes are quite robust. Indeed, their stiffness guarantees minimal strains on the electrical interconnects when manipulated by surgeons. Moreover, the electrodes are thick enough, such that metal loss due to corrosion is negligible over the lifetime of the device. Finally, in the context of neurostimulation, the use of metallic wires as interconnects and large electrode sizes guarantees low electrode resistance, which allows the use of neural stimulators with relatively low voltage compliances (usually around 10 - 12 V) in order to obtain the target current outputs. More generally, for medical devices, the simpler the manufacturing process the easier it is to control it and thus to ensure proper functionality of the device once implanted.

However, because of these manufacturing processes and geometrical characteristics, the technologies used in current clinical devices lack various important features that will shape future neural interfaces:

- **Personalization**: Because of the manual processing of these devices, it is difficult to rapidly develop devices with varying electrode layout. Indeed, in the age of personalized healthcare and despite regulatory roadblocks, it is desirable to use radiological images from patients brains to optimally position electrodes at specific locations. For example Cortec-Neuro GmbH., a manufacturer of neural implants, used MRI (Magnetic Resonance Imaging) scans to fabricate a custom neural implant to detect epileptic foci in a young girl [25]. This was made possible by their novel manufacturing technique using laser-cut platinum sheets embedded in silicone.

- **Electrode density**: The use of thick platinum disks is not compatible with the manufacturing of micro-electrodes (surface area < 1 mm^2). Dense arrays of micro-electrodes hold the promise to potentially increase selectivity of neural stimulation and recording. For example, an ECoG array using micro-electrodes was shown to resolve cortical somatosensory response patterns on the pig at a much finer resolution (< 1 cm) compared to conventionally sized electrodes [26].

- **Implant stiffness**: Because of the millimeter-thickness of the paddles and the hard materials used for the metalic PtIr electrodes disks, curent clinical devices are inherently rigid and don't conform well to complex curved surfaces such as the brain or spinal cord. As this will be explained in the next section, these technologies present overall a large biomechanical mismatch with the soft neural tissues, thus limiting optimal biointegration and long-term functionality [27].

These limitations motivated the start of soft bioelectronics, a new field that consists in the development of mechanically compliant electronics designed to interact with biological tissues [28, 29]. These new technologies are usually compatible with the manufacturing of micro-sized electrode arrays in a more automated way.

1.3 Towards soft neural implants

1.3.1 Mechanical characteristics of neural tissue

The previous section described how clinical implants are made of stiff and thick metals and thick silicone materials. Their design not only creates a mechanical mismatch with the soft neural tissues and the curved complex surfaces they interface with, but they also constrain mechanically the physiological motion dynamics of the CNS [28]. It is therefore critical to understand what are the important mechanical characteristics of neural tissues in order to design better neural interfaces.

Elastic modulus   Tissues comprising the CNS are inherently soft and during the past six decades multiple groups have attempted to quantify their mechanical properties[30, 31]. One relevant metric useful in the context of neural implants fabrication is the elastic modulus. Studies on that subjected have reported elastic moduli ranging from 100 Pa to 100 kPa for the brain [32, 33] and spinal cord [34]. That large range can be attributed to several factors. First, measurement techniques can vary across these studies and the scale at which these measurements are performed can greatly affect results. Typical measurements are performed with oscillatory shear rheology or with AFM (Atomic Force Microscopy), and various parameters can also affect these results, from the applied strain to the shear rates, or simply the size of the probes. Moreover, studies have shown differences between different regions of the CNS that are constituted by different cell types; typically grey matter (mainly made of cell bodies) has been reported to be stiffer than white matter (mainly made of axons) [35, 36], even though another study showed the opposite [37]. Other factors such as age, species, or the way the tissues are preserved after explantation could also explain these differences.

Complex surface   In addition to being soft, the CNS has an extremely structured surface. Even though the brain of rodents is quite smooth, the brain of primates is circumvoluted, as the tissues at the surface of the cortex form gyri and sulci thus hiding a large part of the brain surface. These sulci can reach millimeter-sized bending radii [38, 39]. The spinal cord also has a cross-sectional bending radius around 10 mm in humans and depending on the posture of the spine, it can have a second bending radius [40].

Dynamic system   The CNS is also a very dynamic mechanical system. The spinal cord is the best example, as it can experience large tensile and compressive strains up to 10-20% during back movements, thus causing elongation of the soft spinal cord [34]. It is also hypothetized that these deformations can even be larger in smaller animal models such as non-human primates or rodents [27]. The brain also experiences constant micro-motion due to blood flow, respiration and cerebrospinal fluid (CSF) pulsation, resulting in volumetric strains around 0.01-0.03% [41].

The relevant mechanical and geometrical properties of the human CNS described above are summarized in Table 1.2.

Table 1.2 – **Mechanical and geometrical properties of the human CNS relevant to surface implants.** Values are indicative, as these vary in the literature.

Neural Structure		Dynamic Strain	Bending Radius (mm)	Modulus (kPa)
Spinal Cord		10-20 % [34]	~ 10 [40]	~ 100 [34]
Brain	Cortex		~ 9 [39]	
	Central Sulcus	0.01-0.03 % [42]	~ 0.5 [38]	~ 1-10 [32, 43]
	Cochlear Nucleus		~ 1.5 [44]	

1.3.2 Biomechanical mismatch

In light of these observations, it comes as little surprise that the use of stiff materials in devices leads to a large biomechanical mismatch with soft neural tissues. As described in the previous section, most clinical implants are made out of thick stiff materials and even more recent clinical devices such as the Utah array are made of silicon (Si), which has an elastic modulus of 170 GPa, six orders of magnitude larger than neural tissues [45] (Fig. 1.3A).

Foreign body reaction One of the most important effects of this stiffness contrast is the inflammation caused by implants on the CNS. Inflammation plays a key role in the longevity of neural interfaces: once implanted into the body, the devices trigger a foreign body reaction (FBR) process whereby microglia, the immune cells of the CNS, as well as general adverse immune responses of the CNS, encapsulate the implant to isolate it from the neural tissue [46, 47]. This biomechanical mismatch as well as electrode size and footprint have been shown to cause an increased tissue damage and electrode failure [48–51]. Typically for recording electrodes, neural signals fade away relatively quickly upon implantation (typically around 4-6 weeks) [52].

Soft bioelectronics These results have lead researchers to integrate softer materials into devices aimed at interfacing with the nervous system and thus reduce this mechanical mismatch [53–55]. For example, it was shown that penetrating probes made of compliant materials caused less gliosis and neurodegeneration as compared to probes made of stiff materials, by reducing the strain fields around the vicinity of the implant [56] (Fig. 1.3B). Using softer materials was also shown to improve biointegration in the context of surface arrays for spinal cord stimulation. 3D reconstructions and histological analysis of explanted spinal cords showed that after 6 months of implantation, a subdural surface implant made of PDMS (polydimethylsiloxane), an elastic silicone which has an elastic modulus close to the one of the dura mater (E

≈ 1 MPa), generated a reduced inflamatory response and less tissue damage than an implant made of polyimide, a much stiffer material with an elastic modulus of E ≈ 2 GPa [57] (Fig. 1.3C). Similar results were reported in another study, where rigid and soft materials were integrated into surface implants for the spinal cord and were compared [58]. There is now a trend trying to use even softer materials, such as gels, which have typical elastic moduli in the range of 10 kPa - 100 kPa, to reduce this mismatch even more [59, 60]. However it is still unclear if reducing the elastic modulus of these implants further would have any benefits in chronically implanted devices [61].

Reversible elasticity   The mechanical dynamics of the implant environment described above also need to be taken into account in the design of these devices. Indeed, neural implants need to accommodate the movements of the neural tissue, and thus their ability to reversibly stretch, called the tensile stiffness, is another important parameter [27]. Based on the values described above (Table 1.2), the strains these implants need to survive over their lifetime once inside the human body are in the range < 10%, even though a little margin of error is necessary [62]. For smaller animal models, such as non-human primates or rodents, these numbers might even be larger. The rodent spinal cord surface arrays used in Minev et al. were for example made in elastic materials that were shown to be able to electro-mechanically survive strains of 20% up to one million stretching cycles [57].

Conformability   In addition to the elastic properties described above, in the context of surface implants, it is also important to take into considerations the complex curvilinear topography of the CNS described above. One way to conform to surfaces with such small radii of curvature is to thin down these films, thus reducing their flexural stiffness. The flexural stiffness D of a film, defined in Equ. 1.1, scales cubically with the film's thickness [63].

$$D = \frac{Eh^3}{12(1 - v^2)} \tag{1.1}$$

, where E is the elastic modulus of the film material, h its thickness and v its Poisson's ratio.

For example, in the simplistic model of a cylindrical surface (principal curvatures: $\kappa_1 > 0$ and $\kappa_2 = 0$) with radius r, a film will conform to it by capillarity if $L_{EC}/\sqrt{2} < R$, where L_{EC} is the elastocapillary length of the film and corresponds to the radius of curvature that is generated by capillary forces on a film with a set flexural stiffness, and is defined in equation 1.2 [64].

$$L_{EC} = \sqrt{\frac{Eh^3}{12(1 - v^2)\gamma}} \tag{1.2}$$

, where E is the elastic modulus of the film, h is its thickness, v its Poisson coefficient and γ is the surface tension of the liquid.

Nevertheless, strictly cylindrical surfaces in the CNS don't exist and most of the time these surfaces form non-developable surfaces with non-zero Gaussian curvature (i.e. they cannot be flattened into a two dimensions flat sheet, Fig. 1.3D). Gaussian curvature K is defined as the product of the two principal curvatures of a space κ_1 and κ_2:

$$K = \kappa_1 \kappa_2 \tag{1.3}$$

This means that a thin film cannot conform to a curvilinear topography without undergoing mechanical strain such as buckling [65]. In that case a stretchable material would be necessary to conform to such a surface [66]. This is illustrated in Fig. 1.3E, where a phantom monkey brain was fabricated to match the mechanical and geometrical properties of a brain (2% agarose in water) . When implanted into the central sulcus, a 150 μm thick film of PDMS (a stretchable elastomer with elastic modulus ~1 MPa) conforms better than a 8 μm thick film of polyimide (a flexible polymer with elastic modulus ~7 GPa) that creases, even though both films have the same flexural stiffness.

These calculations hold true for uniform thin films, but it is also important to consider the impact of the electrodes on the overall device conformability. Indeed, thick electrodes with large diameters and made of bulk metal will have poor conformability. It is thus also important to find strategies that combine thinner and smaller diameter electrodes, and to consider the use of softer conductive materials.

Handling and surgical implantation The importance of the mechanical environment of the neural interface once implanted was extensively described above, but it is also important to consider the surgical insertion itself. This is especially true for penetrating soft probes: these probes will usually buckle when trying to perforate the outer brain tissue thus preventing penetration of the tissue. Some solutions involve using mechanical guides and shuttles [67,68] or dissolvable polymer coatings to temporarily stiffen the probes during insertion [69].

Similar issues arise with surface implants made of flexible polymers, typically like polyimide or parylene, which are often engineered to be extremely thin (~ 10 μm) to conform to the CNS (to compensate for their elastic modulus which lies in the range of the GPa). These devices are extremely hard to handle during surgery and tend to fold onto themselves due to electrostatic forces. To facilitate their handling, similar methods are used, mostly with temporary rigid biodegradable backing which dissolves when in contact with aqueous solutions [70] or by freezing the implant before insertion [71]. However, these tricks still remain a problem for clinical translation. An advantage of using inherently softer materials (with low elastic moduli) is that they can be manufactured to be thicker and still compliant enough. Generally, it is hard to quantify how practical and easy to handle a device is. Thus the development of such new tools requires close discussion with surgeons. However, even soft surface implants that are thick enough for handling can be difficult to surgically insert between two layers of tissues such as the central sulcus [72]. There is therefore a general need to develop strategies to allow for soft surface implants to be easily manipulated during implantation.
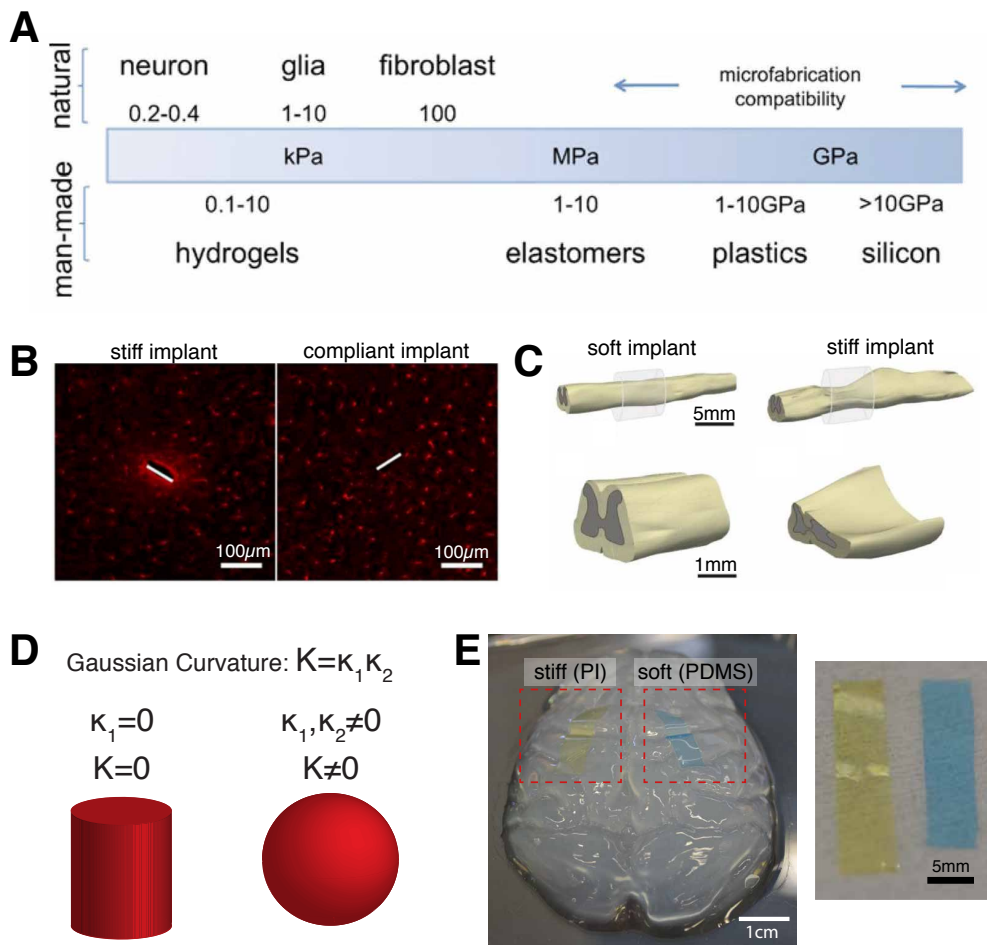
Figure 1.3 – **Biomechanical mismatch between implants and soft tissue.** (**A**) Logarithmic scale of the elastic moduli of natural and made-made materials relevant in the context of neural interfaces [55]. (**B**) Fluorescence microscopy of microglia and macrophages populations in a stiff (left) and a compliant material (right) after 16 weeks implantation in rats cortex [56]. (**C**) 3D reconstructions of explanted rat spinal cords after a 6 weeks implantation of a surface array made of a soft (left) and a stiff (right) material [57]. (**D**) Illustration of 3D objects with zero (left) and non-zero Gaussian curvature (right). (**E**) Phantom brain in agarose with films made of a flexible but non-stretchable material (polyimide in yellow) and a stretchable material (PDMS colored in blue) inserted into the sulcus (left). The picture on the right shows the films after testing and put in evidence creases in the non stretchable material.

1.3.3   Summary of challenges

The main challenges linked to the dynamic and static mechanical environment of the neural implant can be summarized in four points:

- Elastic modulus mismatch between the neural tissue and the implant and device footprint

- Complex curvature of the brain and spinal cord surface

- Micro and macro motion of the brain and spinal cord

- Handling of the device during surgical implantation

Each of these challenges can be related to requirements in the geometrical and mechanical properties for the neural implant:

- Low **bending stiffness** for conformability

- Reversible **stretchability** to sustain micro and macro motion of neural tissue

- **Elastic modulus** of the implant matching the neural tissue mechanical properties and smaller electrode footprint

- Strategies to allow easy manipulation of soft implants during implantation

These challenges and their impact on neural implants properties are illustrated in Figure 1.4.
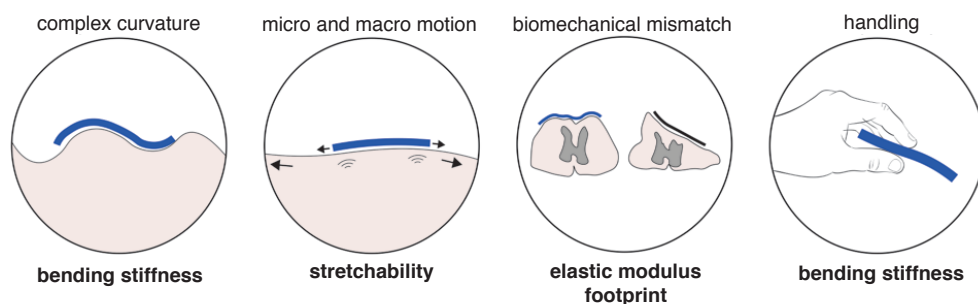
Figure 1.4 – **Summary of mechanical challenges.** These challenges are linked to the static and dynamic mechanical properties of the implantation environment, and their impact on mechanical properties of the implant.

1.4 Regulatory requirements

General A major challenge for bringing neural interfaces to the clinic are the regulatory roadblocks associated with the development of medical devices. Regulatory bodies have put in place strict directives to control the commercialisation of medical devices, such as the Medical Device Regulation (MDR, EU 2017/745) which came in force on April 5th 2017 in Europe. These regulations require that development activities for medical devices take place within the framework of a Quality Management System (QMS), which is often challenging to reconcile with academic activities. Nevertheless, it is still worth to keep in mind basic regulatory requirements during the development of neural implants technologies that would be eventually intended for human use, as it could facilitate future translation of these technologies to the clinic. A recent review breaks down some of the main steps to bring a neural implant to the clinic by highlighting some of the main challenges [73] (Fig. 1.5). Below, some of these aspects are briefly examined.
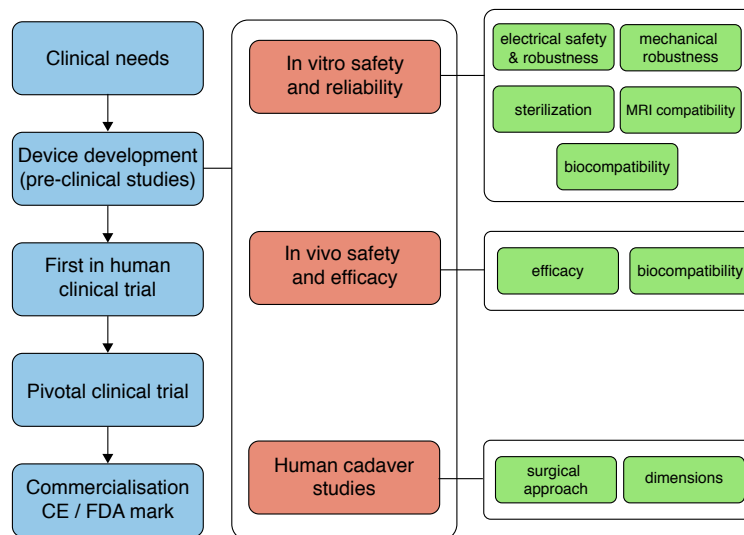
Figure 1.5 – **Roadmap of a clinical device.** Steps in red and green can typically be undertaken in an academic environment. Adapted from [73].

Biocompatibility Demonstrating the biocompatibility of the neural implant is probably one of the most important aspects to take into account when developing new technologies that are intended for humans. A well recognized standard that deals with biocompatibility is the "ISO 10993-1:2018 Biological evaluation of medical devices". Typical tests for chronically implanted (> 30 days) neural interfaces include cytotoxicity, sensitization and irritation [74]. It is also good to keep in mind that even if one uses materials with certificates for chronic use within their device, the final assembled device still needs to be fully tested. Indeed, the post-processing of "biocompatible" materials can generate chemical or physical changes that might alter their long-term effects in the body. Nevertheless, using materials that are already approved for clinical use can simplify the validation process compared to using new exotic

materials.

Electrical safety and robustness   Demonstrating electrical safety and robustness of neural implants can sometimes be very challenging, especially for stimulating devices. The reference norm in the EU for electrical safety is the "IEC 60601-1:2015 Medical electrical equipment – Part 1: General requirements for basic safety and essential performance". This standard is mainly intended for implantable active electronics, such as implantable pulse generators (IPG), but some of these requirements impact also the neural interface itself, such as guaranteeing electrical insolation of the device from the external environment, as well as between independent channels. Hermeticity is indeed a critical aspect of soft neural implants to avoid any diffusion of liquids that could short-circuit or corrode the embedded electronics. Addressing these aspects can be particularly challenging, especially in the context of silicones which are known to be permeable to water vapour and might breakdown or decompose [75].

Another issue with micro-electrode arrays is corrosion of the electrodes. Indeed as the latter become smaller, the voltage drop at the interface upon stimulation increases and can reach values high enough to generate corrosion of the electrodes, even in materials considered as inert, such as platinum [76, 77]. Unfortunately, as the development of micro-electrodes is recent, there are no clear guidelines into how to deal with these issues, and only a few devices using micro-electrodes are currently approved for human use, such as the Argus II retinal prosthesis from Second Sight [78].

As most neural interfaces are intended to be permanently implanted, it is required to demonstrate functionality and safety for periods of time that usually span 5 to 10 years, and up to 80 years, as an increasing number of younger patients receive such implants. A predictive method to demonstrate such long term functionality is the use of accelerated ageing protocols. For diffusion limited degradation processes in polymers, the most commonly used method to do so is the "10 degrees rule", which states that "for every 10° C rise in temperature the rate R of a chemical reaction will be increased by a given factor Q_{10}" (Eq. 1.4) [79]:

$$R = Q_{10}^{\frac{T_A - T_{ref}}{10}} \tag{1.4}$$

, where T_A is the temperature at which the polymer should be aged, T_{ref} the reference temperature (37° C in vivo), and Q_{10} the accelerated aging factor, which should be equal to 2 or less [80]. These accelerated tests are usually performed in Phosphaste Buffered Saline (PBS) to mimic the pH environment of the nervous system, and recent studies have also suggested the use of reactive oxygen species to better mimic the harsh in vivo environment [81].

Mechanical robustness   Mechanical testing of these devices is also very important, especially with respect to surgical handling and manipulation. There are no general guidelines on how these tests should be conducted, but these can be inspired from the standard "EN

45502-2-3:2010 Active implantable medical devices. Particular requirements for cochlear and auditory brainstem implant systems", which describes precise forces and elongations cochlear implants and auditory brainstem implants need to mechanically survive, as well as fatigue tests to mimic bending movements during the implant lifetime.

Sterilization   A very critical aspect to take into account when developing implantable neural implants is the ability to sterilize them. Manufacturers of implants must be able to find at least one sterilization method that the device can go through and still remain functional as intended. Typical sterilization methods include the use of steam, ethylene oxide (EtO) or ultraviolet germicidal irradiation. In all cases, it is important to demonstrate that the sterilized device does not have any residual micro-organisms. One recognized standard to perform such tests is the "ISO 11737-1:2018 Sterilization of health care products".

MRI compatibility   MRI (Magnetic Resonance Imaging) compatibility is increasingly required for medical devices, especially in the context of neural implants which interface with the brain, as MRI images can help confirm proper placement of the implant or detect adverse events such as subdural hematomas in the context of subdural surface arrays. More and more researchers are thus now testing MRI safety and compatibility of new technologies for neural implants [82–85].

It is important to make the distinction between an MRI compatible and MRI safe device:

- **MRI-Safe** Device that does not present additional risk to patients or other individual but may affect diagnostic information of the MR images.

- **MRI-Compatible** Device that is MR-safe and the diagnostic information of MR images and the operation of the device are not affected.

Table 1.3 lists five norms published by the American Society for Testing and Materials (ASTM) which are good references for guidelines on how to comply with MRI safety and compatibility. These describe mostly methods to assess safety with regards to magnetically induced heating, displacement and torque on the medical device, as well as artefacts generation that could impend diagnostic information.

Table 1.3 – **Lis of MRI safety and compatibility ASTM norms.**

Description	Norm
Magnetically induced displacement force	ASTM-F2052 [86]
RF induced heating on/near passive implants	ASTM-F2182 [87]
Magnetically induced torque	ASTM-F2213 [88]
MR image artifacts from passive implants	ASTM-F2119 [89]
Marking and labeling of medical devices for MR	ASTM-F2503 [90]

1.5 Aims

General objective   The overall objective of this thesis is to propose a technology for the clinically compatible fabrication of stretchable interconnects embedded into a soft neural implant. The proposed technological solution addresses the challenges presented in this chapter in relation to the mechanical dynamic and static properties of the neural implant environment, while putting an emphasis on the compatibility of such a technology for translation towards the clinic, and keeping in mind regulatory requirements.

Aims   This work is subdivided into three aims:

- Development, optimization and electromechanical characterization of micro-structured stretchable interconnects

- Integration of the interconnect technology into a fully embedded implantable neural interface

- Demonstration of the neural interface for neural stimulation and recording applications

Outline   The thesis is divided into five chapters:

1. Introduction of neural interfaces and the current state of clinical implants and associated challenges

2. State of the art in the field of soft bioelectronic interfaces and extensive description of the technological novelty proposed in this thesis to develop stretchable electronics for implantable devices

3. Application of the technology for neural stimulation in the context of an auditory brainstem implant (ABI). The chapter first presents the work to develop a soft human-sized ABI and then shows functionality of a scaled down ABI in a chronic mouse model.

4. Application of the technology for electrical neural recordings in the context of electro-corticography in an acute pig model.

15

5. Application of the technology for electrical stimulation of the spinal cord in non-human primates (NHP).

Figure 1.6 graphically summarizes the outline of this thesis and highlights how each chapter and section contributed to the main patent and scientific publications related to this thesis.
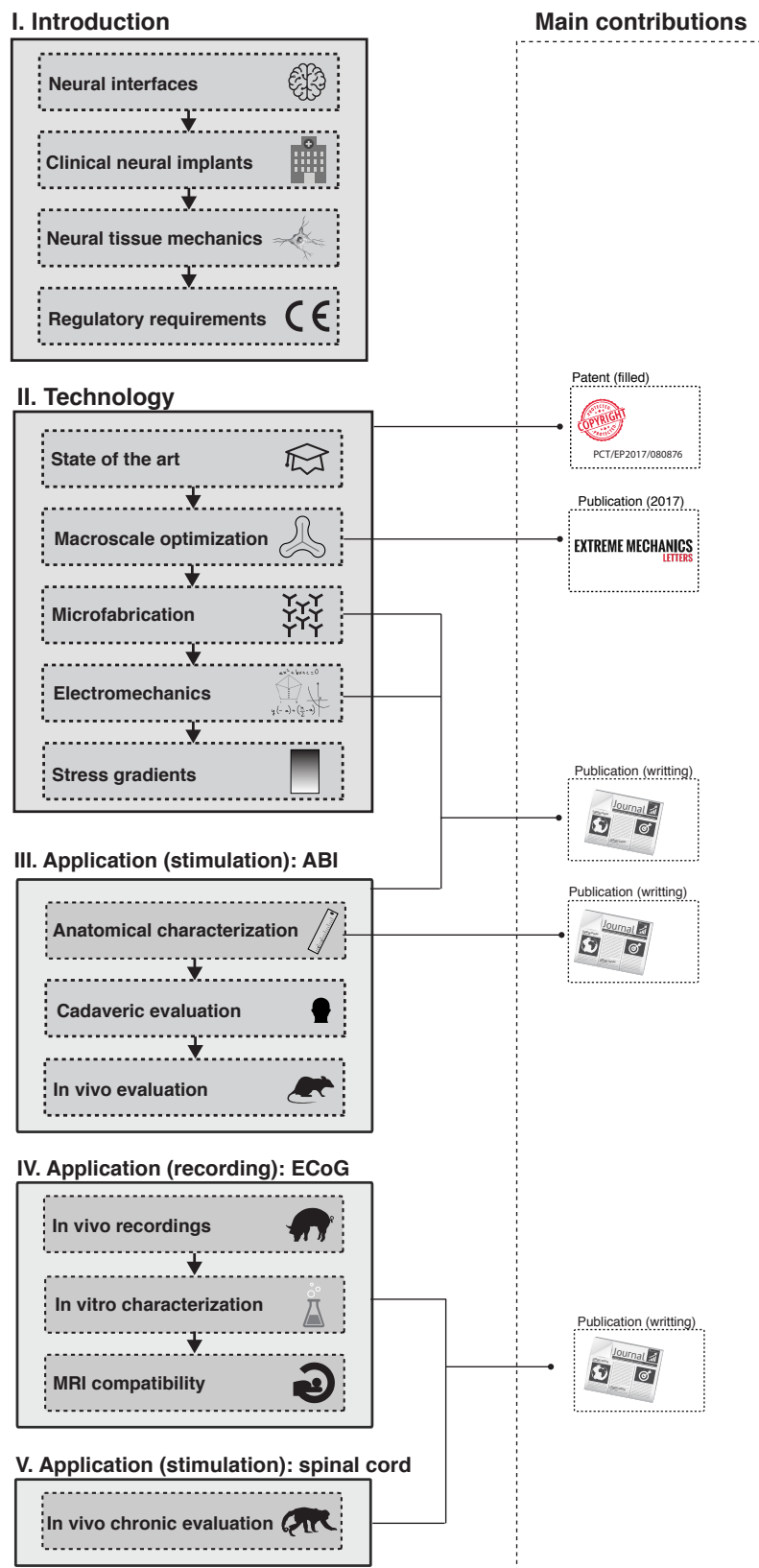
Figure 1.6 – **Thesis outline.** Outline of the thesis highlighting the main contributions.

2 Technology for stretchable electronics

Outline   This chapter presents a new technology to engineer stretchability in electrically conductive materials by patterning arrays of Y-shaped cuts. It is organized in six sections:

1. **State of the art** on stretchable electronics

2. **Macroscopic study** of kirigami patterned thin films with Y-shaped cuts

3. **Optimization study** of smoothed Y-Shaped cuts

4. **Microfabrication** of thin-film electronics with micro-patterned Y-shaped cuts

5. **Electromechanical characterization** of micro-patterned thin-film electronics

6. **Strain gradients** using Y-shaped cuts (macroscopic proof of concept)

Scientific Contributions   The contents of this chapter were published in a manuscript, and a second manuscript is in preparation. A PCT patent was also submitted [91]:

- **Nicolas Vachicouras**, Christina M. Tringides, Philippe B. Campiche, and Stephanie P. Lacour, "Engineering reversible elasticity in ductile and brittle thin films supported by a plastic foil.", Extreme Mechanics Letters 15 (2017): 63-69.

- **Nicolas Vachicouras**, Osama Tarabichi, Vivek V. Kanumuri, Christina M. Tringides, Yohann Thenaisie, Lorenz Epprecht, Jennifer Macron, Florian Fallegger, Valentina Paggi, Stephen McInturff, Ahad Qureshi, M. Christian Brown, Daniel J. Lee, Stéphanie P. Lacour, "Micro-patterned elastic film technology enables proof of concept of a soft auditory brainstem implant" (in preparation)

2.1 State of the art

Requirements The fabrication of soft electrical neural implants, and more particularly stretchable neural implants, requires the development of electrical interconnects that can be reversibly stretched, while maintaining stable electro-mechanical characteristic. The main requirements for such stretchable electrically conductive materials are listed below.

- **Reversible elasticity** for repeated **small strains** around ~10% (due to bodily movements once implanted)

- Accommodation of larger one-time **tensile strains** in the range of 20-40% (due to surgical manipulations during implantation)

- **Electrical conductivity** high enough to allow conventional implantable neurostimulators (typically with a voltage compliance around 10-15 V) to functionally stimulate neural tissues

- Compatibility with processes allowing for **patterning of dense arrays of microelectrodes**: typically 8-256 electrodes of diameters <1 mm with narrow tracks (< 100 μm)

- Use of **conventional materials** to facilitate translation to the clinic

Strategies Conventional electrically conductive materials are mostly made of metals (e.g. platinum or gold) or conductive oxides (e.g. Indium Tin Oxide; ITO). However metals are ductile and will deform plastically at strains around 1-5%, while oxides present a brittle behaviour and will usually fracture at these low strains. Moreover, these materials have relatively large elastic moduli, typically in the range of 10-1000 GPa. These materials are therefore not suitable for stretchable electronics in their simple form [92]. New strategies to develop stretchable neural implants are thus necessary to build soft neural implants. It is possible to classify methodologies to develop such materials in two categories: with the use of (1) **intrinsically stretchable materials**, or (2) **conventional rigid materials in unconventional designs** [28, 66, 93]. These approaches are reviewed below.

2.1.1 Intrinsically stretchable conductors

Definition Intrinsically stretchable materials refer to a class of materials whose micro- and nano-scale structure allow for percolating pathways to conduct electricity while experiencing elongation. Usually the formation of these structures, such as meshes and composites, depend on stochastic processes and initiate spontaneously under certain environmental conditions.

Composites and percolating circuits Percolating composites are made of nanostructures (such as graphene, or single-walled carbon nanotubes) mixed in a rubber matrix to form a stretchable conductive composite. These nano-structures can slide upon stretching, while

maintaining a percolating pathway [94,95]. For example, graphene sheets on PDMS have been reported to stretch up to 6% [96], while gold nanomeshes on PDMS can stretch up to 200% [97] (Fig. 2.1A).

Other approaches consist in mixing filler particles, such as micro or nanospheres, in an elastomeric matrix, that can also accomodate strain thanks to their relative motion, while maintaining a percolating pathway [98]. Such composites can be synthetized by mixing metallic particules with an uncured elastomer before polymerization [57] (Fig. 2.1B), or can be formed by low-energy ionic implantation of metals into a polymerized elastomer [99]. High aspect ratio nanostructures such as nanowires can be used to improve the stretchability and conductivity of such composites [100, 101] (Fig. 2.1C).

Mixtures of conductive polymers (CPs) with elastomers have also been shown to allow stretchability up to 100% with conductivities of 120 Scm^{-1} [102] . Another strategy using CPs was proposed using PEDOT:PSS (poly(3,4-ethylenedioxythiophene) : polystyrene sulfonate) enhanced with ionic additives that allows the creation of soft and hard domains in the semi-crystalline structure of PEDOT:PSS (Fig. 2.1D). High conductivities (3000-4000 Scm^{-1}) and large fracture strains (800%) have been reported using that strategy [26].

A different approach to form nano-meshed circuits consists in thin films of gold (25-60 nm) evaporated on PDMS that spontaneously forms a microcracked structure (of size 1-10 μm) that allows the metal to stretch by out-of-plane deformation of these microcracks (Fig. 2.1E), while allowing the microcracks to maintain a percolating pathway for electrical conductivity. Strains up to 40% have been reported with this method [103–106].

Liquid conductors Because of their inherent weak intra-molecular bonds, conductive liquids can also be used in conjonction with microfluidic channels to form stretchable conductors [107]. Typically ionic liquids have been used [108], even though they are quite resistive and can undergo electrochemical reactions that might damage them [109]. A common alternative is the use of liquid metals at low temperatures, such as eutectic gallium-indium (EGaIn) [110,111].

These strategies, although interesting, can be difficult to interface with conventional electrical circuits. A promising alternative approach was recently proposed by forming a biphasic film of $AuGa_2$ that can stretch up to 400% with a low sheet resistance (0.5 Ω/sq) and that is compatible with conventional photolithographical patterning techniques [112] (Fig. 2.1F).

Advantages and downsides The main advantage of intrinsically stretchable materials is that they can be directly patterned into their desired shaped (e.g. through coating or printing), thus facilitating the design of complex electrical circuits. Typically nanocomposites can be coated or printed onto their substrate [113], while micro-cracked gold films and biphasic $AuGa_2$ films can be patterned through a shadow mask. Moreover, such conductive structures

can accommodate isotropic stretchability. However, these strategies usually rely on exotic materials, which have limited data demonstrating biocompatibility for long-term implantation into the body. Moreover, some of these techniques rely on stochastic physical and chemical processes that are not always perfectly understood and/or are difficult to model, and thus their electro-mechanical properties are not always easily controlled.
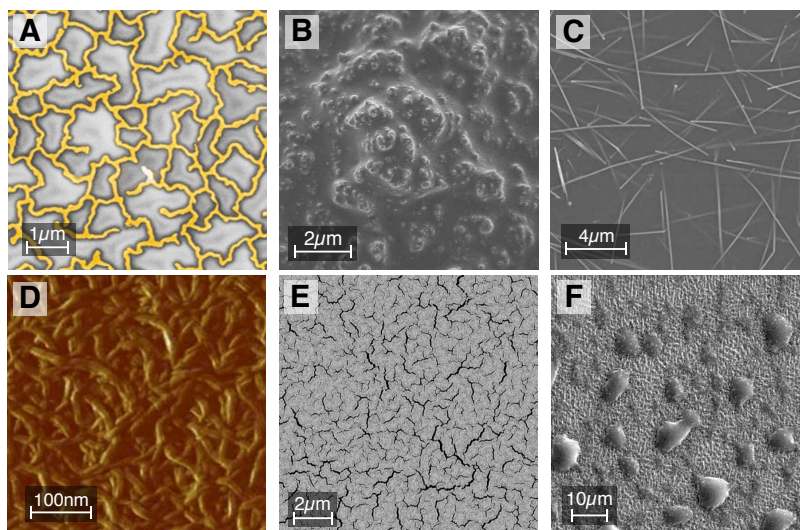
Figure 2.1 – **Review of intrinsically stretchable conductors.** (**A**) Colorized SEM image of a gold nanomesh on PDMS [97]. (**B**) SEM image of platinum microparticules embedded in a matrix of PDMS [57]. (**C**) SEM image of a silver nanowire film transferred on a PDMS substrate [101]. (**D**) AFM image of a PEDOT:PSS film incorporated with an ionic additive [26]. (**E**) SEM image of a micro-cracked gold film thermally evaporated on PDMS [105].(**F**) Liquid-solid biphasic $AuGa_2$ film deposited on PDMS [112].

2.1.2 Stretchability by design

Definition   The other category of stretchable conductors involves the use of conventional materials patterned into unconventional geometries [114]. These strategies mostly rely on structures than can deform in 3D space with out-of-plane deformation to relieve local strain, as well as the use of pre-strained structures.

Pre-strain   Methods relying on pre-strained substrates usually consist in the transfer of conductor films (such as metals or semi-conductors) onto a pre-stretched elastomeric substrate which form wrinkles once relaxed (Fig. 2.2A). These conductive films can then be stretched through out-of-plane wrinkling and can thus accommodate some strain during elongation. Peak strains in such designed materials can then be much smaller than the intrinsic failure limits of the material. Typically Si nanomembranes can be pre-stretched up to 37% before fracture (i.e. 20 times larger than their fracture strain) [115].

Metal interconnects can typically be directly thermally evaporated onto pre-strained PDMS

[116, 117] or first deposited onto a plastic support which is then laminated onto the PDMS. Such structures were shown to mechanically survive tensile strains up to 275% [118]. Similar approaches make use of even more brittle materials such as silicon (Si) nanomembranes bonded onto pre-strained silicones [119, 120]. These Si ribbons can also be bonded on preferential sites [121, 122] (Fig. 2.2B).

Meanders   It is also possible to avoid using pre-strained substrates, by designing tortuous spring-like conductive tracks that can unfold themselves upon tensile loading. These structures are usually composed of a metalic layer deposited onto a plastic support. The iconic tortuous path is of a serpentine configuration and has been reported to accomodate strains up to 50% [123] (Fig. 2.2C). Others have compared multiple geometries by Finite Element Analysis (FEA) as well as experimentally and found that horse-shoe structures performed better and could mechanically elongate up to 100% before mechanical failure [124–126] (Fig. 2.2D). Others have proposed more sophisticated geometries using fractal patterns [127] (Fig. 2.2E). For example structures with three orders of fractal horseshoes were theoretically predicted to accomodate elongations up to 1200% [128].

Kirigami approaches   The methods described above rely on the optimization of the track pattern. An equivalent approach is to look at the problem from a different perspective, by considering the pattern that is cut out of the conductive material. These methods are usually described as a kirigami approach, from the Japanese art of cutting paper [129, 130]. For example elasticity was engineered into a sheet of CNT (carbon nanotubes) nanocomposite by photolithographically patterning an array of slits that can deflect out of plane, thus increasing the maximum elongation of the film from 4% to 370% [131] (Fig. 2.2F).

Effect of encapsulation and substrate   Some of the described structure rely on out-of-plane as well as in-plane deformations. However, FEA revealed that even for the latter these tortuous interconnects have a tendency to slightly deform out-of-plane [114]. This raises the question of the effect of a substrate and encapsulation that would hinder these out-of-plane motions.

Studies have shown that the stretchability of interconnects decreases with the elastic modulus and thickness of the encapsulation and substrate [132]. One way of limiting this effects is therefore to use thinner and softer encapsulation. For example a substrate made of ecoflex (a silicone with elastic modulus E = 60 kPa) increased the stretchability of serpentines from 30% to 115% compared to using a substrate made of PDMS (E = 1 MPa) [133]. A more extreme solution is to use a non-polymerized silicone matrix (i.e. in its liquid form) injected between the substrate and the encapsulation thus not hindering out of plane motion of serpentine interconnects and alowing elastic behavior of the interconnects up to 46% [134].

Interestingly, it was also observed that these spring-like metallic interconnects highly benefit of being deposited onto an underlying more rigid flexible material, such as polyimide (PI, elastic modulus E≈ 2 GPa). Indeed serpentines made of copper laminated on PDMS could stretch twice as much if they were initalliy deposited onto a PI support. In that case, the stiff PI

layer acts as a stress buffer between the metal track and the PDMS substrate [135].

Advantages and downsides   These approaches are interesting for biomedical implants as the design principles are usually independent of the materials used, thus allowing the use of medically approved materials to facilitate their clinical translation. Moreover, these designs have the advantage of being deterministic and their electromechanical behaviour can be more easily predicted and controlled. The stretchability of such approaches, although lower than intrinsically stretchable materials, is also sufficient for applications in neural implants. In general, the use of pre-strained substrates increases the stretchability, typically up to a factor of 3, depending on the geometry and the amount of pre-strain [136]. However, in the context of neural implants, wavy structures might not allow optimal contact of the electrode to the underlying tissue when relaxed. Another downside is that most of these designs have one or sometimes two preferential directions of stretching, which is not ideal when trying to conform to non-zero Gaussian curvatures that require isotropic stretchability. That limitation however, can be overcome with new geometries, such as fractal designs [137]. These approaches also require careful design of the electrical circuits taking into account the shape of the meander, as the scale of the patterns are usually in the same range as the interconnects themselves.
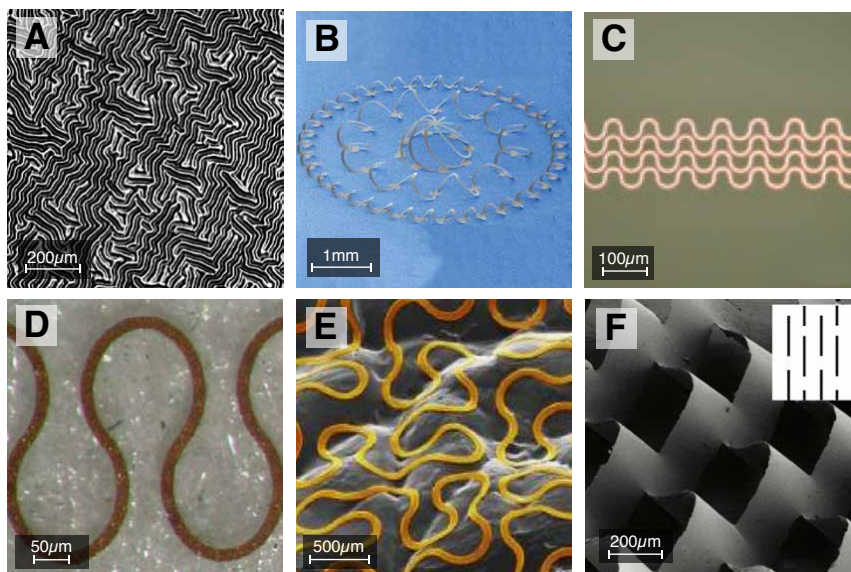
Figure 2.2 – **Review of stretchable conductors by design.** (**A**) SEM image of wave patterns formed by metals evaporated onto a PDMS substrate [116]. (**B**) SEM image of silicon nanomembranes selectively bonded onto various locations of an elastomeric substrate [121]. (**C**) Optical micrograph of gold serpentine tracks encapsulated into a PDMS substrate [123]. (**D**) Optical micrograph of a horshoe metal interconnect [124]. (**E**) Colorized SEM image of a metallic interconnect shaped into a fractal configuration [127].(**F**) SEM image of a GO-PVA (graphene oxide - Poly(vinyl alcohol)) nanocomposite after photolithography patterning of slits (shown in the inset) [131].

2.1.3 Stretchable neural implants

Soft bioelectronics have been used for the development of microelectrode arrays to interface with the nervous system. Most of these devices are only flexible and rely on extremely thin devices ($< 10\,\mu m$) such that they can closely wrap around the brain or spinal cord [138–141]. Only a few notable neural interfaces have been reported using stretchable electronics.

The manufacturing of such stretchable neural implants require strategies as the ones described above to engineer elasticity in the conductive interconnects. These are then interfaced with arrays of electrodes on one end, and with a connector on the other end to communicate with an external device. Figure 2.3 shows the main stretchable neural implants reported in the literature and table 2.1 reports, for each device, which strategy was used to implement stretchability, as well as various relevant electro-mechanical and geometrical characteristics.
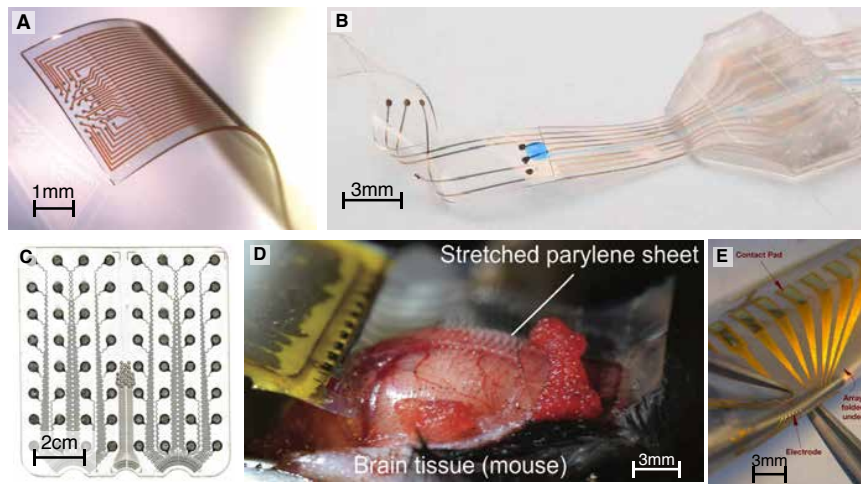
Figure 2.3 – **Images of stretchable surface electrodes.** (**A**) Au-TiO2NW-PDMS composite encapsulated in PDMS [142]. (**B**) Micro-cracked gold film embedded in PDMS [143]. (**C**) Platinum foil laser cut in serpentines embedded in silicone [144]. (**D**) Parylene sheet cut with an array of kirigami slits [145]. (**E**) Gold serpentine interconnects embedded in PDMS [146].

Table 2.1 – **Characteristics of stretchable surface electrodes.** Definitions: Impedance at 1kHz in vitro (Z), diameter ($\oslash$), total implant thickness (t) and maximum elongation (σ_{max}). *composite of TiO2NW coated Au nanowires and PDMS

Substrate	Stretch. strategy	t (μm)	Electrode $\oslash$(μm)	Z ($k\Omega$)	σ_{max}	Ref.
PDMS	nanocomposite*	80	50	9	100%	[142]
PDMS	μ-cracked Au	120	300	5	30%	[143]
PDMS	Pt foil meanders	60	1'000	1	50%	[144, 147, 148]
Parylene	kirigami slits in Pt	10	50	300	650%	[146]
PDMS	Au meanders	80	60	20	8%	[145]

2.2 Elastic interconnects: a macroscopic study

2.2.1 Introduction

The Y-shaped motifs observed on micro-cracked gold films described in the previous section inspired the use of Y-shaped cuts patterned into non- or minimally-elastic materials to engineer reversible elasticity into electrically conductive multilayered films (Fig. 2.4). These hexagonal patterns of Y-shaped motifs had been previously suggested by Lacour *et al.* to model the electro-mechanical behaviour of the micro-cracked gold films [149].

This study focuses on a macroscopic (mm-scale) design of these patterns to better understand the electro-mechanical behaviour of plastic films patterned with Y-shaped motifs. This study demonstrates that this approach is compatible with plastic foils and also allows for the design of stretchable multi-layers composed of ductile or brittle thin films supported by a plastic foil.
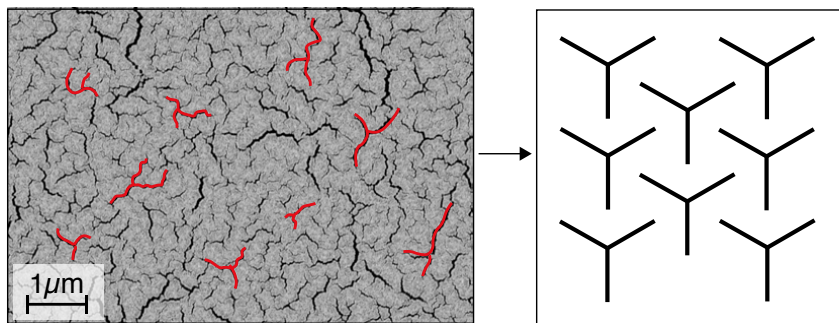
Figure 2.4 – **Inspiration for the Y-Shaped kirigami pattern.** SEM images of microcracked gold films inspired the use of Y-shaped motifs patterned into non or minimally elastic materials in order to engineer reversible elasticity.

Disclaimer: This section (2.2) is adapted from the following article with permissions of all co-authors and journal:

Nicolas Vachicouras, Christina M. Tringides, Philippe B. Campiche, and Stephanie P. Lacour, "Engineering reversible elasticity in ductile and brittle thin films supported by a plastic foil.", Extreme Mechanics Letters 15 (2017): 63-69.

My contribution: Conceptualization, experiments, figures and writing

2.2.2 Methods

Sample preparation   Plastic carrier substrates, polyimide (Kapton Ⓡ HN – Standard Rolls
- 610 mm wide) and PET (polyethylene terephthalate, Mylar Ⓡ) foils (75 µm thick), were
purchased from Lohmann Technologies. Y-shaped patterns were cut into the foils with a
Plotter Cutter (RoboPro CE5000- 40-CRP) using a DXF file generated from a MATLAB
(R2015b) script. The contour of a dogbone shape (norm DIN 53504 [150], Appendix Figure
A.1) was overlayed on the cut film. The wider ends of the dogbone were left without cuts to
allow for firm clamping of the sample in the tensile equipment, while the thinner central part
was covered with the Y-shaped cuts that could stretch.

Thin titanium / platinum (Ti / Pt, 25 / 100 nm thick) films were evaporated by e-beam
(Alliance-Concept EVA 760) on polyimide foils that were first activated using an oxygen
plasma, in order to improve the metal films adhesion to the plastic. Indium tin oxide (ITO)
films (100 nm in thickness) were sputtered (Pfeiffer SPIDER 600) on the PET foil.

PDMS membranes (poly(dimethylsiloxane), Sylgard 184, Dow Corning, mixed at 10:1 (w:w)
with a pre-polymer crosslinker) were prepared by spin-coating on silicon (Si) wafer. First, the
Si wafer was coated with a self-assembled layer of trichloro (1H,1H,2H,2H-perfluorooctyl)
silane (Sigma Aldrich) in a desiccator. Next, PDMS was spin-coated on the Si wafer (750
RPM for 35 s) and cured at 80°C for at least 3 h in a convection oven. The PDMS membrane
was then cut out using the same technique as for the plastic foils and released manually from
the wafer.

Electromechanical characterization   All samples (except bulk PI and PET) were stretched
in a tensile tester (MTS Criterion Model 42, with a load cell of 100 N maximum capacity)
using a strain rate of 1 mm/s. The samples were clamped and secured to the plates of the
stretcher with double-sided tape. The electrical resistance of the conductive films was recorded
during stretching using a Keithley 2400 sourcemeter.

The bulk PI and PET were characterized in a 100 kN MTS 809 axial–torsional servohydraulic
testing machine with a load cell of 10 kN. The force-displacement data was measured at a
sampling frequency of 100 Hz using the MTS TestSuite TW software and analyzed using
MATLAB (R2015b). For longer-term cycling, the samples were mounted to a home-made
uniaxial stretcher and stretched at 10% of their initial length at 1 Hz (1 stretching cycle per
second). The electrical resistance was measured using a 4-probe system and a Keithley 2400
sourcemeter. The stretcher and sourcemeter were both controlled using custom made software
based on LabView 2015. The resistance was recorded (sampling rate of 5 Hz) and saved only
every 10 cycles per decade of cycles.

Radial stretching   A circular piece of PI, 11 cm in diameter, was covered in the Y-shape cuts.
Then, a band of Ti/Pt was evaporated, which was 8 cm long and slightly wider than one motif.
Four pads, two at each end, were included to facilitate a 4 point resistance measurement of
the sample. The circle was mounted in a home-made radial stretcher following the designs

from [151]. The diameter of the stretcher was manually increased in 1 mm steps. Once each stretch step was completed, the track resistance was measured and recorded. The sample was able to increase its area by 40% before failure of the first ligament.

Scanning Electron Microscopy (SEM)   SEM images were acquired with a Zeiss Merlin microscope using an annular detector at a beam energy of 1 keV.

Finite element analysis (FEA): Mechanical   Mechanical simulations were performed using ABAQUS (6.14) in order to evaluate the effect of the different geometries parameters. The standard static procedure was used with a damping factor of 1e-7. The S4R element was used with a global mesh size of 0.15 mm and no dependence on the mesh size was observed. Two steps were created with a first step of perturbations applied on three random points and in the direction perpendicular to the film's surface and clamped extremities. The influence of perturbations magnitude was analyzed and no influence on the force–displacement behavior was observed. The second step consisted of a clamped boundary condition on one end and a displacement in the stretching direction on the other end while deactivating the perturbations. The two steps of the simulation are shown in Figure 2.5
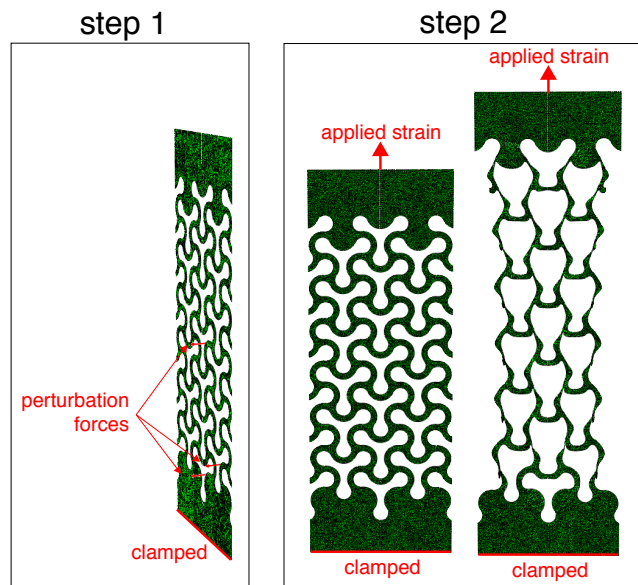
Figure 2.5 – **Methodology of ABAQUS mechanical simulations.** Steps used for the mechanical simulation in ABAQUS. The boundary conditions and applied forces are shown in red.

Finite element analysis (FEA): Electrical   Electrical simulations were performed with COM-SOL (2015) in order to estimate the resistance of a 100 nm thick conductive sheet of Pt, which was cut out with various geometries of the Y-shaped pattern. The ground boundary condition was applied on one end of the sheet and a terminal with 1 A was applied to the other hand (Fig. 2.6). The resulting maximum voltage field was finally used to calculate the total sheet resistance.
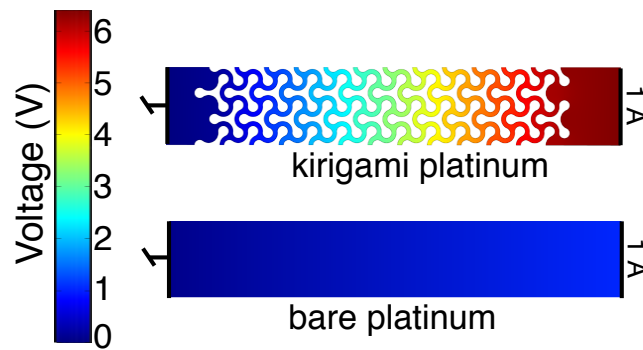
Figure 2.6 – **Methodology of COMSOL electricals simulations.** The electrical resistance of kirigami patterned films was calculated relative to the resistance of a bare film.

2.2.3 Results

The proposed Y-shaped pattern was designed using three branches of the Y motif of equal length (parameter a) and width (w). The Y shapes are spaced such to form a hexagon: the distance between two motif's centers, on the x-axis, is L. After the motifs were cut in the PI film, the film was cut into the shape of a dogbone with a Plotter Cutter. Both ends of the dogbone were clamped in the plates of a uniaxial stretcher, in order to apply a strain of 10% to the sample at a rate of 1 mm/s. At 10% applied strain, the PI ligaments deflect out-of-plane and locally relieve strain. The Y-Shaped design, dogbone test sample and the stretched sample are shown in Figure 2.7.
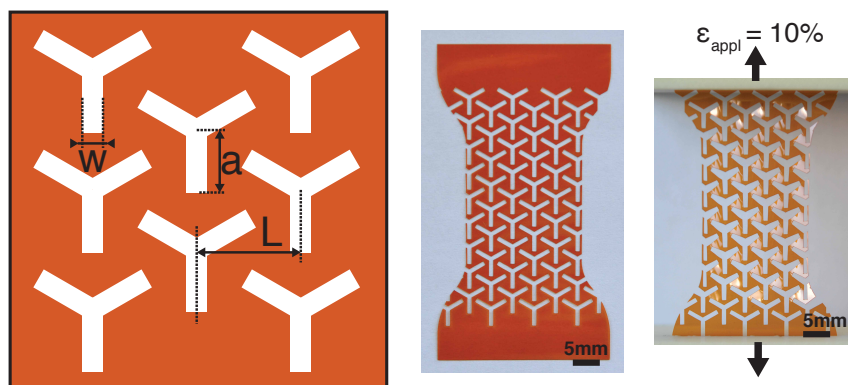
Figure 2.7 – **Mechanical behavior of engineered polyimide foil.** The Y-Shaped motif geometrical parameters (a, w and L) are defined in the left. The center picture shows a typical dogboned-shaped PI sheet that was cut with the Y-Shaped motif and that was used for the macrosopic electromechanical study. The picture on the right shows the sample stretched with an applied strain of 10%.

Mechanical behavior This mechanical behavior of the sample under strain was correctly predicted by a FEA, which supplements the experimental results by offering an estimation of the local strain of various points along the branches. When side-by-side image comparisons of

the results from experiment and simulation are done, they show a good correspondence in the regions that undergo maximum levels of strain, as well as the deformations seen during deflection. These results are shown in Figure 2.8.
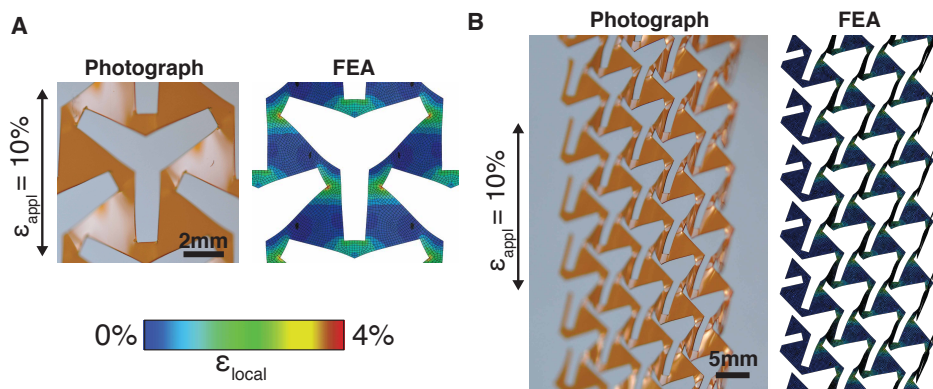
Figure 2.8 – **Comparison of mechanical behavior of the Y-Shaped motif with FEA.** (**A**) Front view of a single Y-shaped motif held at ϵ_{appl} = 10%: photograph(left) and finite element model (right) of the stretched motif. (**B**) Tilted view of the sample held at ϵ_{appl} = 10% (photograph and FEA model views) showing the out-of-plane deflection of the Y motif patterns. The color bar represents the computed local strain from ABAQUS simulations.

Mechanical characterization   First, the Y-shape motif parameters were optimized. Twelve different combinations of a, w, and L were cut and then stretched until failure, which was defined as the time at which the first motif broke. There were 4 different ratios of a/L (0.5, 0.6, 0.7, 0.8) and 3 different values of w (0.7 mm, 1.1 mm, 1.5 mm). Each combination was tested three times, to provide error bars to both the displacement and force at break. Films of bulk (uncut) Kapton and a film of uncut PDMS were also stretched until failure. Each film was 75 µm thick. All 14 force-displacement curves are plotted in Figure 2.9, with an inset showing a comparison of just the two bulk films.

It was found that as w and as the ratio of a/L increases the maximum displacement reached by the film increases. The effective spring constant, calculated as the slope of the linear region of the force-displacement curve, diminishes, as shown on Figure 2.10A. This is because the spring constant of the film decreases as the struts between motifs become less wide. For larger values of w, there is a more noticeable change to the spring constant while varying a/L. It is worth mentioning that the spring constant of the bulk PDMS is similar to that of an a/L ratio of 0.8. When comparing the elongation at break, as a function of these variables, it is again seen that the largest w has a more prominent influence on the amount the sample was able to stretch (Fig. 2.10B).

From these three experiments graphs, it was determined that the optimal geometry for the Y-shapes was that of maximum a/L, 0.8, and second largest value of w, 1.1 mm. To understand the effect of film thickness on the spring constant, films of PI of the above given Y-shape parameters were cut on a varying thickness of PI films (25, 50, 75 µm). When plotted logarithmically, it was observed that the spring constant scaled as a function of the film thickness cubed (Figure 2.10C). For comparison, bulk PI of these same thickness was
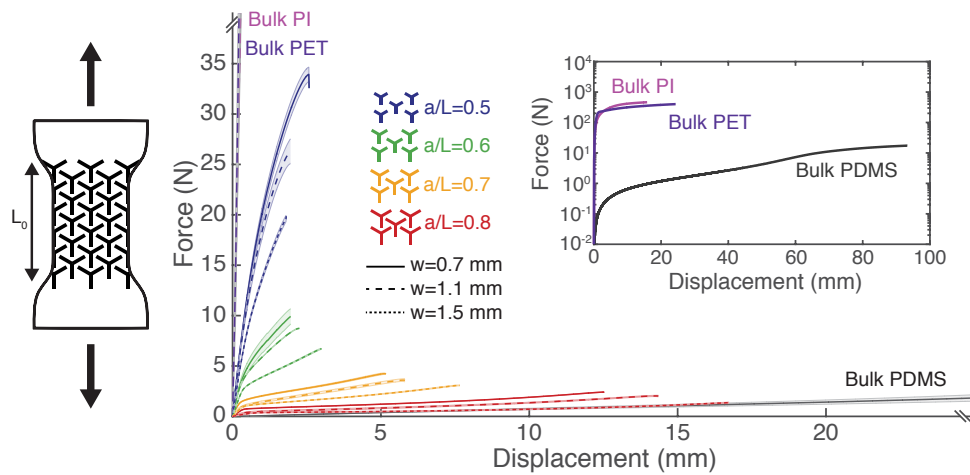
Figure 2.9 – **Mechanical characterization of engineered polyimide foil.** Force–displacement curves of engineered polyimide (PI) foils, until the point of failure, for various design parameters (n = 3 per design). Bulk (unaltered) PI and PDMS, each 75 µm thick, are shown in purple and black respectively (shown in full in the inset). Shaded areas denote standard error of the mean. All samples have the same external dogbone shape and dimensions.

also stretched. Here, the spring constant scaled as a function of the film thickness, only. When the Y-shapes were simulated on PI of different thicknesses (5, 10, 25, 50, 75, 125 µm), the observed scaling law on spring constant matched that observed in the experiment. The difference between bulk and engineered PI is thought to come from the buckling and deflection mechanisms seen by the branches, where the force scales in function of the cube of the thickness. The analytical equations of this behavior were not investigated, but the experiments match the simulation predictions and we expect a cubic relationship between the spring constant and the thickness, as the bending stiffness scales cubically with thickness.
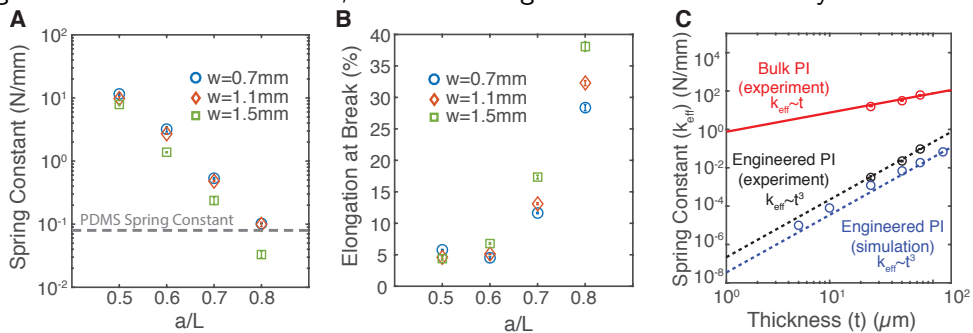
Figure 2.10 – **Spring constant and elongation at break analysis.** Effective spring constant k_{eff} (**A**) and elongation at break (**B**) of engineered PI foils as a function of design parameters. The effective spring constant of PDMS is shown in dotted gray for comparison. Error bars denote standard deviation. (**C**) Logarithmic plot showing the scaling laws of effective spring constant as a function of film thickness for bulk PI (in red, experimental and fitted, R = 0.926) and engineered PI with parameters a/L = 0.8 and w = 1.1 mm (in black, experimental and fitted, R = 0.993, and in blue simulation and fitted, R = 0.993).

Corner shape optimization   Since the Y-shapes have sharp corners at the end of each branch, this causes high local strains at these angles. It was hypothesized that rounding the ends would decrease this strain and thus increase the displacement of the film; further, if circles with a diameter larger than w were added to the ends of the branches, the elongation at break of the film should increase even more. Four branch end geometries were compared: squared, rounded, circles with radius 1.2 mm, and circles with radius 1.3 mm. For the rounded ends, the corners of the squared ends were simply rounded to avoid sharp bends. The circles were added such that the total length of each branch was unchanged, as indicated in the schematic in Figure 2.11. Because the branch length was the same for all samples, the spring constant of the four samples was relatively unchanged. However, the maximum displacement of the film increases quite substantially for the circles of largest diameter as shown in Figure 2.11. This increase in displacement is thought to be because of a decrease in local strain at the branch ends. The FEA model confirmed that the maximum local strain decreases as circles of larger diameter are added (bottom of 2.11). Additionally, with the addition of circles, the strain is better distributed throughout the entire Y-shape, and this uniformity probably helps to prevent early failure or delamination that occur from sharp changes in strain. Since the circles of 1.3 mm demonstrated much better mechanical properties, this end branch geometry was used for the majority of the remaining characterization experiments performed.
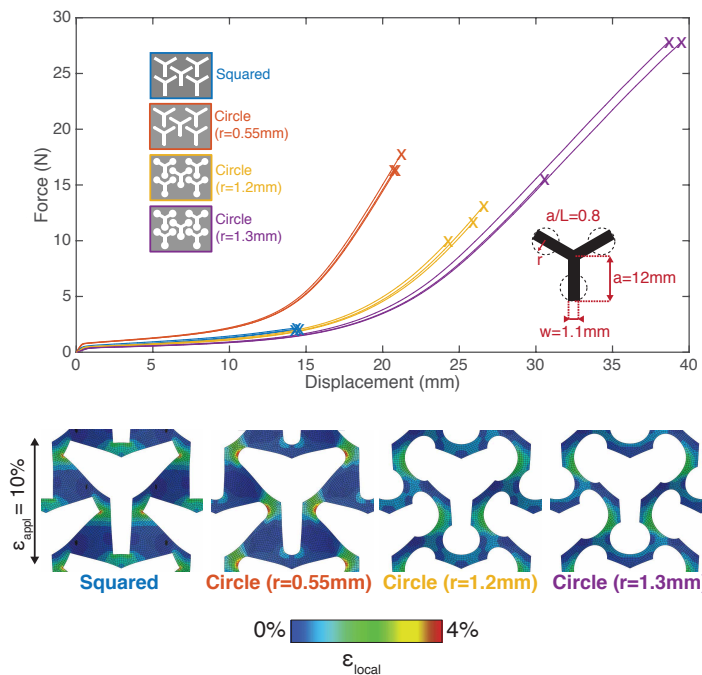
Figure 2.11 – **Effect of the corner shape on mechanical characteristics.** Force–displacement curves for dogbones with Y motif patterns with four different types of corner shapes (square or circle with radius r = 0.5 mm, 1.2 mm and 1.3 mm) are compared (top). The crosses indicate the point of mechanical failure. n = 3 for each different corner shape. The bottom images are representative local strain map simulated for each corner shape (ϵ_{appl} = 10%). The color code bar is the same for all four images.

Electro-mechanical trade-off   Once a mechanical characterization of the PI films was completed, the effects of the Y-shapes on electrical conductivity was explored. First, a ductile metal, platinum (Pt) was evaporated on one side of the Kapton film, after the cracks had been cut, as illustrated on the left of Figure 2.12. Since a larger surface area of Y-shapes corresponds to smaller amount of material between struts, there is a trade-off geometries of the Y-shapes and the resistance of the film, as shown in Figure 2.12. For the largest w, with an a/L of 0.8, the resistance is almost 3 times larger than for an a/L of 0.5. This is a further justification of why the w of 1.1 mm was chosen, rather than 1.6 mm.
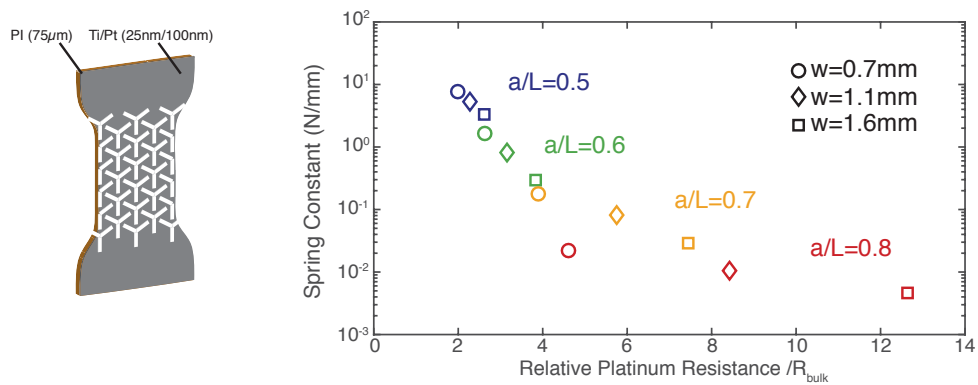
Figure 2.12 – **Electromechanical trade-off of engineered PI coated with a conductive film.** Engineered Polyimide coated with a bilayer of titanium and platinum (Ti/Pt, 25/100 nm). The effective spring constant of the structure (computed from simulations) is shown for various geometries using squared corners (w = 0.7, 1.1, 1.5 mm, and a/L = 0.5, 0.6, 0.7 and 0.8) as a function of the electrical resistance (computed by COMSOL simulation).

Electromechanical behavior of Pt on PI   After evaporation of the Ti/Pt, the dogbone films were still able to stretch and deflect in the same way as with the Kapton. The films, which had motifs with circular ends of radius 1.3 mm, were stretched on the uniaxial stretcher, and were able to stretch up to 70% before experiencing failure, while still remaining conductive. All samples failed first mechanically before electrically. These results are shown in Figure 2.13.

To investigate the robustness of the films, they were stretched for 100,000 cycles at an applied strain of 10%. The circular end (r =1.3 mm) samples were plotted and compared to the rounded end samples. In the solid line is the resistance at 10% applied strain, and in the dashed line is the resistance at 0% applied strain, for each cycle. In both the rounded and circular ends, there is a difference between solid and dashed line, yet this gap is proportionally larger for the rounded samples. While the rounded undergo an increase in resistance of about 50% from start to finish, the circular samples see an increase of about 10%. From the simulations, shown in Figure 2.11, the Y-shape regions of maximum strain can be identified. These areas were imaged under the SEM, and indeed regions of delamination and cracks can be seen, where as the rest of the sample looked unaffected. The rounded sample had significantly more delamination and in a greater amount of the film. The sample with circular ends had a few
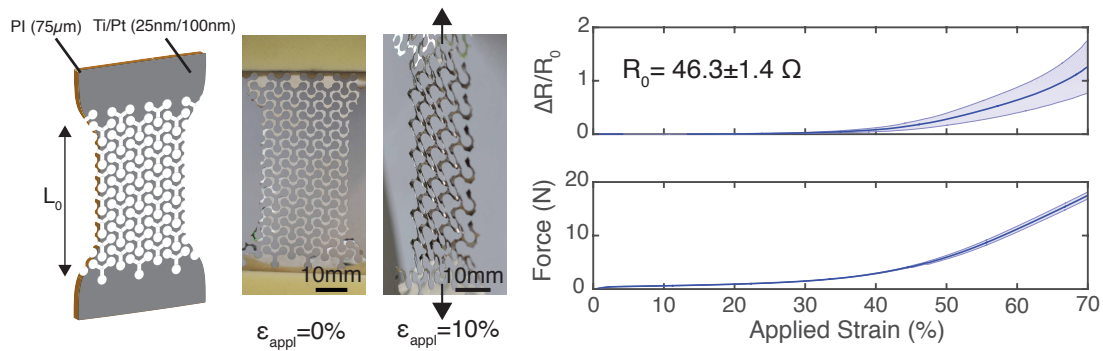
Figure 2.13 – **Electromechanical behavior of Pt on PI under elongation until failure.** Top pictures show the Pt/PI construct patterned with Y motifs with circular endings (r = 1.3 mm) at 0% and 10% applied strain. The bottom plots show the mean change in electrical resistance (top) and displacement (bottom) during uniaxial stretching, for n = 3 samples (shaded area denotes standard error of the mean).

cracks in the film, but little delamination. These results are shown in Figure 2.14.
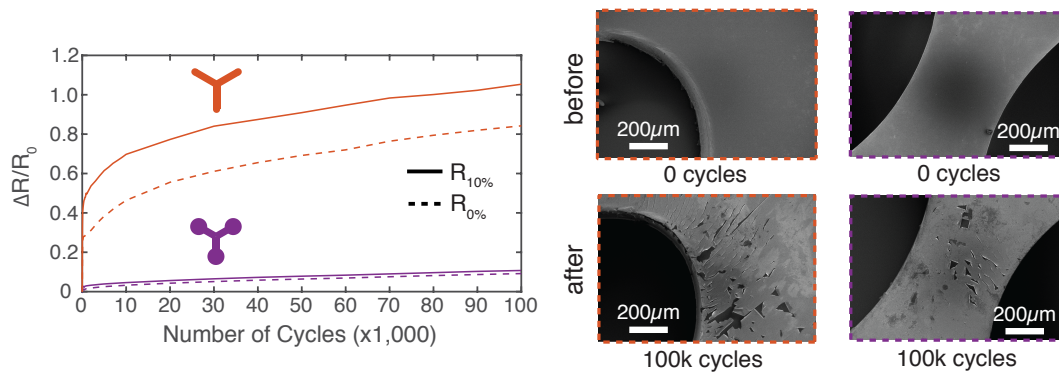
Figure 2.14 – **Electromechanical behavior of Pt on PI under cyclic elongation at 10%.** Change in resistance as a function of stretching cycles to 10% applied strain for two corners geometries (circles with r = 0.55 mm in orange and r = 1.3 mm in purple). SEM images on the right show the regions that experience the highest local strain (as calculated in Figure 2.11) before and after 100,000 cycles, for both corner geometries (left column: circles with r = 0.55 mm, right column: circles with r = 1.3 mm).

Radial stretchability   One advantage of the Y-shapes is that they stretch, non-preferentially, in all directions, rather than just the direction of the cuts. A circular piece of PI was covered in the Y-shape motifs, and then a band of Ti/Pt was evaporated. The metallization band width was as tall as a motif. After the sample was mounted in a radial biaxial stretcher, the stretcher diameter was increased until there was failure in a motif. The sample was able to increase its area by 40% while remaining conductive. These results are shown in Figure 2.15.
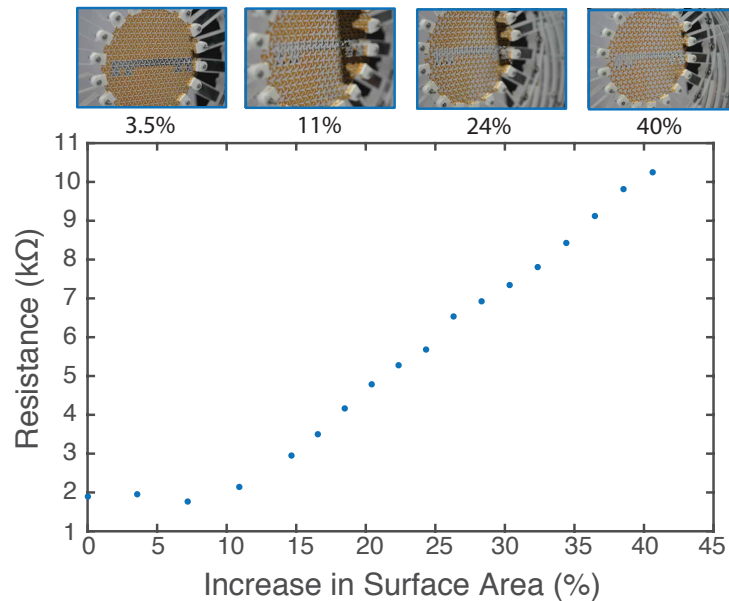
Figure 2.15 – **Radial stretching of macroscopic Y-shaped motifs.** Increase in electrical resistance of a conductive line of platinum evaporated on a PI sheet cut with Y-shaped motifs while it is been radially stretched. The insets at the top show the mechanical deflection of the Y-shaped motifs at various strains.

Electromechanical behavior of ITO on PET   To demonstrate the effectiveness of this approach to engineer elasticity in brittle films, which typically fail after an applied strain of 5%, indium tin oxide (ITO) was sputtered on the top layer of a PET film, after the Y-shapes had been cut into the polymer. After the deposition of the conductive material, the sample was mounted to the uniaxial stretcher, as with the previous samples, and stretched to an applied strain of 10%. As the sample was stretched, it underwent the same mechanical deformations as described before. The resistance of the film was measured as it was stretched up to 70%. Here, while the sample still remained electrically conductive, an increase of ~10 times was observed in the resistance. This was hypothesized to be from the brittle nature of the film, and the formation of very small cracks that delaminated during the elongation. Unlike with the Pt, the ITO exhibits electrical failure before it shows signs of mechanical failure. At an applied strain of 40%, the resistance in the film is almost 5 times greater while the mechanical force at this strain level barely increased. These results are shown in Figure 2.16.

The ITO-PET film was also cycled 100,000 times at 10% applied strain. Within the first
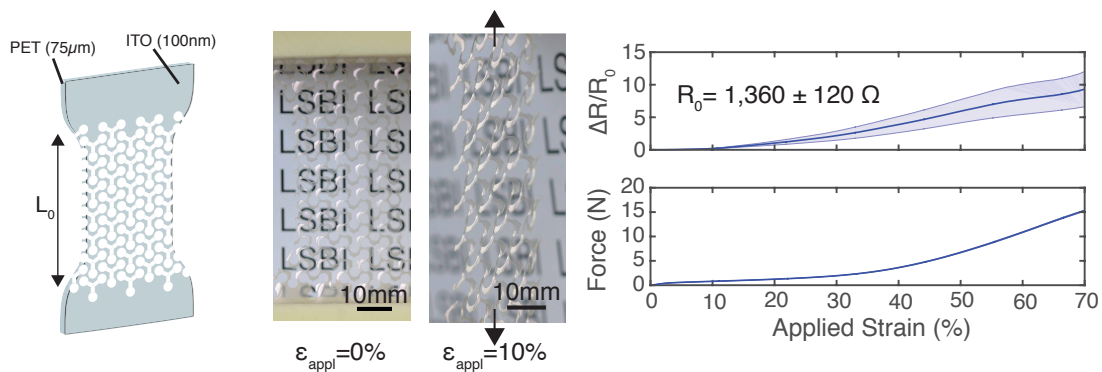
Figure 2.16 – Electromechanical behaviour of engineered PET coated with ITO under elongation until failure. The top picture show the engineered PET foil coated with a layer of Indium Tin Oxide (ITO, 100 nm). The pictures show the PET/ITO structure with circular endings (r = 1.3 mm) at 0% and 10% applied strain. The bottom plots show the mean change in electrical resistance (top) and displacement (bottom) during stretching, for n = 3 samples (shaded area denotes standard error of the mean).

few cycles, the resistance increased by a factor of 6, possibly due to the formation of small cracks in the ITO. However, after this jump, the resistance remained much more stable and, by the end of the 100,000 cycles, had increased less than a factor of 2. With the ITO, the gap between resistance at 0% and 10% applied strain is much smaller than that observed in the Pt. When the film was imaged under the SEM, no obvious regions of large cracks, delamination or failure were identified. There were some portions that looked "scratched" or a bit darker, which could correspond to a thinner and thus less conductive amount of ITO. These results are shown in Figure 2.17
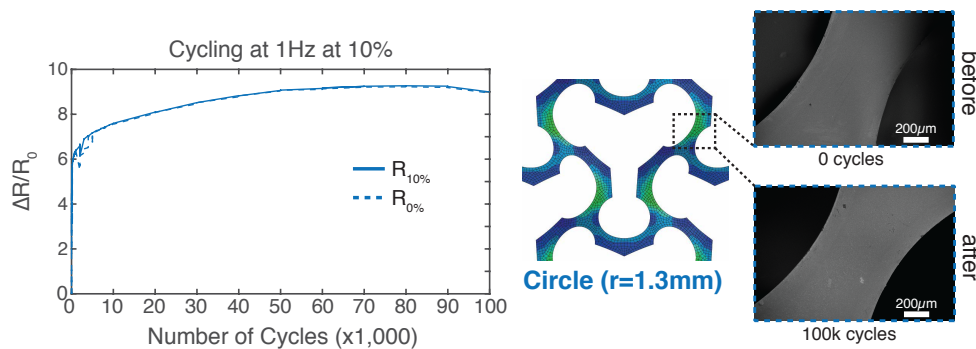
Figure 2.17 – Electromechanical behavior of engineered PET coated with ITO under cyclinc elongation at 10% applied strain. Change in electrical resistance as a function of stretching cycles to 10% applied strain. SEM images on the right show the region of the patterns that experiences the highest local strain (as calculated in Figure 2.11) before and after 100,000 cycles.

2.2.4 Summary and discussion

Summary In summary, this study demonstrates an efficient approach to engineer elasticity in films supported by a plastic carrier. The symmetry of the Y motifs allows for multi-axial stretchability, which few alternative techniques enable. Strain relief relies on out-of-plane bending of the substrate ligaments and re-organization of the Y motif openings. By optimizing the Y motifs endings with disks, the strain within the plastic films ligament can be further minimized and offer larger elasticity. Other motifs could be explored as kirigami patterns. However, we showed here that the Y motifs are sufficient to allow for conductors with combined multi-axial stretchability and low electrical resistance. Once coated with thin conducting film(s), the multi-layered construct can stretch reversibly while maintaining reliable electrical conductivity.

Discussion This study focused mainly on understanding the effect of the geometrical parameters of the Y shaped cuts on the electromechanical characteristics of conductive films supported by a plastic foil. For the purpose of this study the dimensions were in the mm-scale, but the goal is to scale the kirigami-inspired approach to the micro-scale, as explained in the following sections. The concept shown here is indeed compatible with thin-film electronics processing.

However, before scaling down these shaped to the micro-scale, further shape optimization was performed in order to minimize local strains that would generate local cracks into the metallic layer, thus increasing the resistance. Indeed, the optimized Y shape proposed here still contains sharp angles.

2.3   Shape optimization study

2.3.1   Introduction

The Y-shaped motifs presented in the previous section (Section 2.2) were further optimized by rounding all remaining 90° angles thus achieving a completely "smooth" Y-shaped motif. The three design iterations are summarized in Figure 2.18A. The new smooth design is defined with three independent parameters: a, r and L (Fig. 2.18B). Here, the new "smooth" Y-shape parameters are optimized using only computer simulations in order to maximize the electromechanical properties (maximum stretchability and minimum electrical resistance).
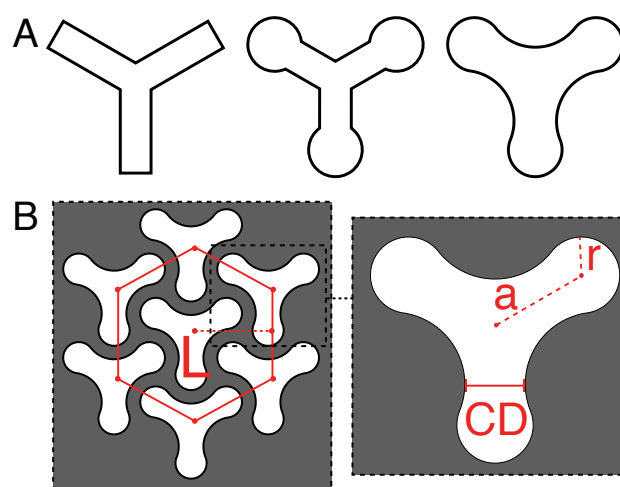
Figure 2.18 – **Smooth Y-shape motif.** (**A**) Iterations of the three Y-shape design optimization. (**B**) Description of the three independent parameters defining the new smooth motif: a, r and L. CD refers to the Critical Dimension of the structure.

2.3.2   Methods

Smooth Y-Shaped motif   The smooth Y-Shaped motif is defined by three new independent parameters: a, r and L, and is constructed by the intersections of three circles of radius r and three circles of radius r (dependent parameter), aligned on an hexagonal matrix of three-branched structure, where a is the length of the branches, and L is the horizontal distance between two motifs. (Fig. 2.19 and Table 2.2).
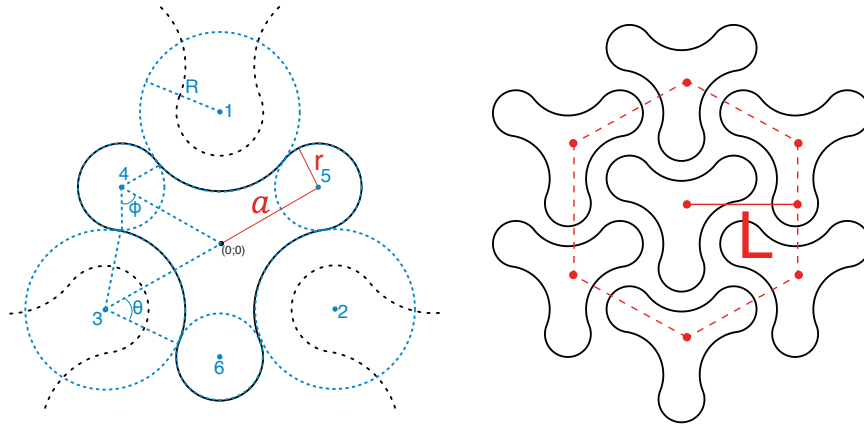
Figure 2.19 – **Geometrical construction of the smooth Y-Shaped pattern.** The three independent parameters a, r and L are indicated in red. The other definitions and construction lines are shown in blue. The coordinates of the circles center points are indicated in Table 2.2.

Table 2.2 – **2D coordinates of the center points of the circles forming the smooth Y-shaped motif.**

Pt #	X coordinate	Y coordinate
1	0	$L\frac{2}{\sqrt{3}} - a$
2	$L - a\frac{\sqrt{3}}{2}$	$\frac{a}{2} - \frac{L}{\sqrt{3}}$
3	$a\frac{\sqrt{3}}{2} - L$	$\frac{a}{2} - \frac{L}{\sqrt{3}}$
4	$-a\frac{\sqrt{3}}{2}$	$\frac{a}{2}$
5	$a\frac{\sqrt{3}}{2}$	$\frac{a}{2}$
6	0	$-a$

The three dependent parameters r, θ and ϕ are given by:

$$R = \sqrt{\left(\frac{4}{3}L^2 - \frac{6aL}{\sqrt{3}} + 3a^2\right)} - r \quad \theta = \arctan\left(\frac{a\sqrt{3}}{\frac{4L}{\sqrt{3}} - 3a}\right) \quad \phi = \arctan\left(\frac{2L - a\sqrt{3}}{3a - \frac{2L}{\sqrt{3}}}\right)$$

Critical dimension   The Critical Dimension (CD) of the kirigami shape is important to consider during photolithography patterning of the multi-layer. CD is given by Equation 2.1 (referencing Fig. 2.20):

$$CD = 2\left[\left(L - a\frac{\sqrt{3}}{2}\right) - R\right] \tag{2.1}$$

Finite Element Analysis (FEA)   See methods in Section 2.2.
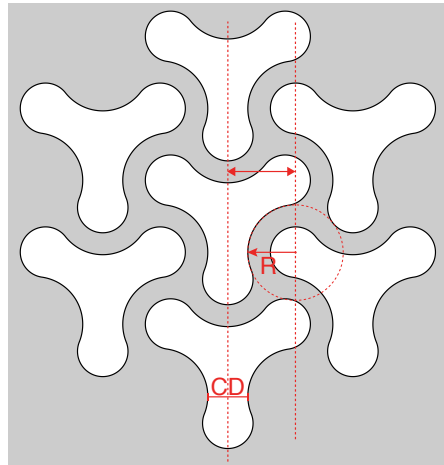
Figure 2.20 – **Critical dimension of the kirigami pattern.** The red arrow indicates the distance from the center of the motif given by the coordinates of point #2 from Fig. 2.19.

Samples and electromechanical testing   The validation of the optimization study was performed using microfabricated devices. The fabrication of such devices is presented in Section 2.4 and the electromechanical testing methodology is presented in Section 2.5. The dimensions of the Y-Shapes was decreased by a factor of 1'000 from the macroscopic FEA study to the microscopic tested samples.

2.3.3   Results

Simulation   The optimization of the smooth Y-shape was performed on macroscopically scaled FEA simulations: 2D dimensions of the patterns were in mm, and the thickness of the film was 75 μm. To facilitate the comparison of different designs, the parameter L was fixed at 26 mm. The parameters being optimized were a and r (Fig. 2.19). Moreover, only designs where the critical dimensions (CD) was larger than CD>5 were tested, because the microfabrication process of these structures is easier if an aspect-ratio of 1:1 is respected between the minimum feature size and the photoresist (PR) thickness (a PR of 5 μm was used, as described in the next Section 2.4). The two electromechanical criteria to be optimized were **resistance** and **stretchability**.

Resistance criteria   Resistance was defined as the geometrical increase in resistance of a metallic sheet compared to a uniform film as computed by FEA (adimensional).

Stretchability criteria   Stretchability depends on the maximum local strain in the film during elongations. Thus the mechanical criteria was defined as the maximum local strain around a Y motif at 20% applied strain. That was computed by FEA on a macroscopic model of patterned PI film, because it was easy to simulate and convergence was fast (<2 hours). The hypothesis here was that if a geometry has a lower local strain than another geometry on the macro-scale, then that would also be the case in the micro-scale.

Mechanical simulation   An example result from the mechanical simulation of a smoothed Y-shaped (a = 16 μm, r = 5.5 μm and L = 26 μm) is shown in Figure 2.21A, highlighting the maximum local strain upon an applied strain of ϵ_{app} = 20% over the whole structure. The strain map on a non-deformed mesh shows the location of the maximum strain peaks.
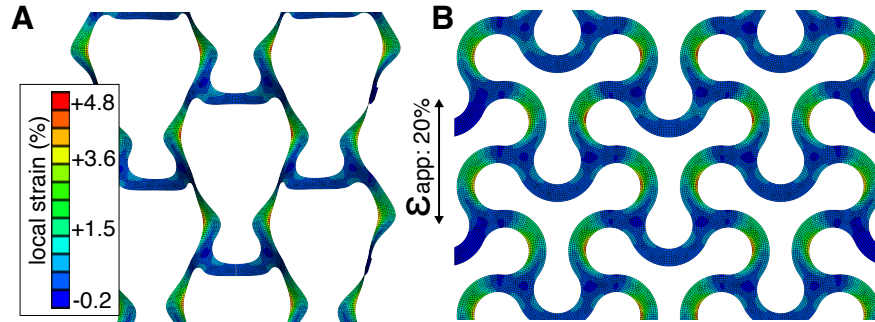
Figure 2.21 – **Mechanical FEA of the smooth Y-Shape.** Maximum local strain map in the kirigami-cut PI sheet upon an applied strain of ϵ_{app} = 20%. The local strain map is shown on a deformed (**A**) and non-deformed (**B**) mesh of the structure. The geometry shown here corresponds to a = 16 μm, r = 5.5 μm and L = 26 μm.

Geometries comparison   Overall, 30 different combinations of a and r were simulated, and the maximum local strain and relative resistance were plotted on a 2D plane (results in Fig. 2.22, detailed values can be found in Appendix A.3). Trying to avoid an increase of relative resistance above 10, three geometries were selected to be tested: design 1 (a = 13.75 and r = 5.25), design 2 (a = 16 and r = 5) and design 3 (a = 16 and r = 5.5), as shown on the right of Figure 2.22. The 2D plane suggests that design 3 should perform the best mechanically, whereas design 1 should be the worst.
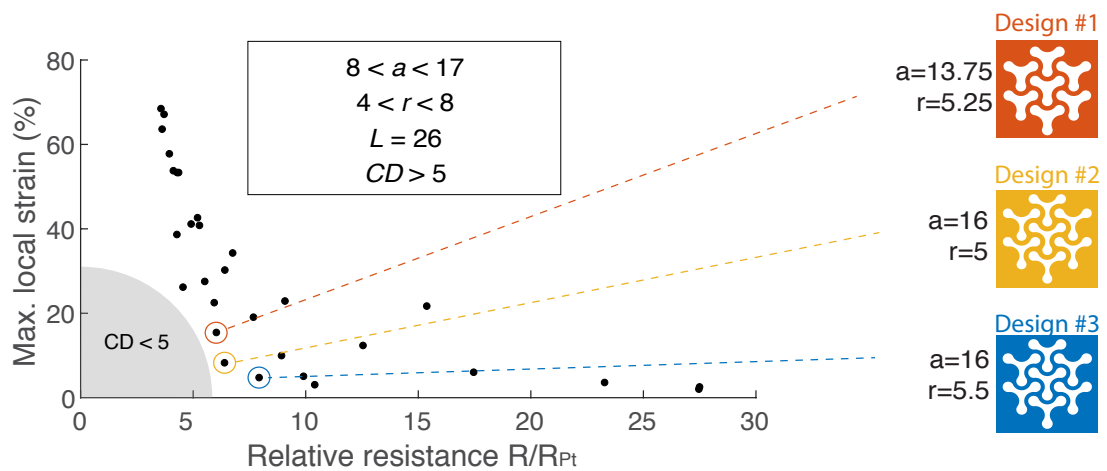
Figure 2.22 – **Graphical representation of the optimization study.** Each dot represents a kirigami pattern with a different combination of parameters a and r. Three selected designs are highlighted on the right.

Experimental validation   To test this assumption, it was hypothesized that if a design has a lower maximum local strain under stretch, this would mean that under repeated cyclic tensile strains, the increase in resistance should be lower, as the metallic layer would experience less local degradation. The hypothesis was tested using microfabricated samples made of 8 micro-patterned tracks of PI/Pt/PI (1/0.1/1 µm) encapsulated between two layers of 100 µm and 20 µm PDMS (details in Sections 2.4 and 2.5). Each sample was stretched 1000 cycles at 10% elongation and the resistance was monitored at uniform intervals on a logarithmic scale. The results show that indeed the change in electrical resistance after 1,000 cycles was the lowest for design 3, and the largest for design 1.
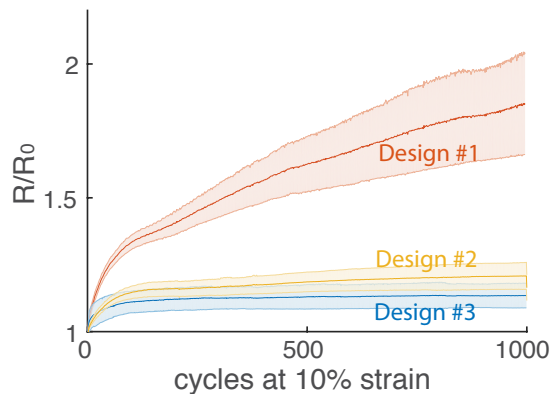
Figure 2.23 – **Electromechanical validation of the optimization study.** Plot showing the relative increase in resistance during cyclic stretching (10%) of electrical tracks using three different designs of smooth Y-Shapes.

2.3.4   Summary and discussion

Summary   In this study, mechanical and electrical FEA was used to define a smooth Y motif to be used as a kirigami pattern to engineer reversible elasticity into multi-layers of plastic and metallic thin films. This analysis revealed a similar electro-mechanical trade-off that was shown in the previous macroscopic study. Even though important hypotheses and simplifications were made, the study narrowed down the space of possible geometries to a design with parameters: a = 16 µm, r = 5.5 µm and L = 26 µm. That design will therefore be used in all subsequent devices presented in this thesis. In addition, this study shows that the electro-mechanical behaviour can be partially predicted using simplistic FEA models, which facilitates rapid optimization. Moreover a large range of electrical and mechanical properties can be obtained using the proposed geometry, thus allowing to tune the parameters depending on the requirements of the application.

Comparison with other geometries   Interestingly, continuous optimization of the Y-Shaped motif shows convergence of the negative unit cell into known shapes, namely the horse-shoe design, that was found to be the optimal geometry for spring-like interconnects [124]. A

fundamental difference here is that the proposed smooth Y-shaped motif can be seen as an extension to a multi-axial horse-shoe. It is thus interesting to draw some insights from previous studies from horse-shoe designs. In particular, it was previously shown that increasing the angle θ in the horse-shoe (Fig. 2.24) increased both the stretchability [137] and the resistivity of the track [126]. Carta et al. reported an increase of the resistivity by a factor of 2 and an increase of the stretchability from 57% to 78%, with an angle $\theta = 0°$ and $\theta = 45°$ respectively. In the case of the Y-shaped motif, decreasing the critical dimension (CD) is equivalent to increasing the angle θ in the horse-shoe design. Moreover, a similar electro-mechanical trade-off was shown in this optimization study.

Another interesting observation is that the location of the maximum local strains for arrays of Y-Shaped motifs is similar to serpentine-like designs as reported in previous FEA studies [152].
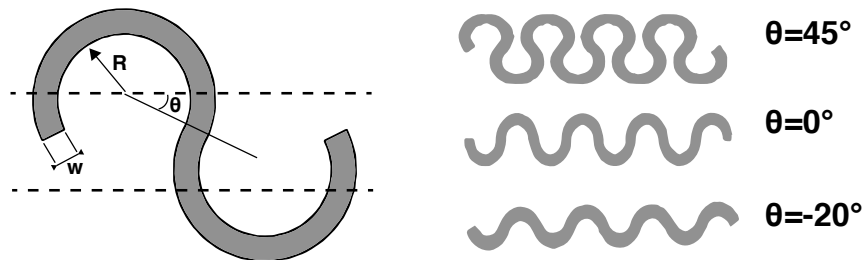
Figure 2.24 – **Horse-shoe design parameters.** Figure adapted from [124, 126]

Microfabrication limitations   The study indicates that to achieve structures with lower local strain maxima and lower resistance would necessitate geometries where the CD is $<$ 5 µm (shaded semi-circle in Fig. 2.22). This could be possible through optimization of the microfabrication process (which currently is limited to 5 µm by the PR thickness as explained in the next section) or by simply reducing the PI thickness. Indeed, here that limit was reached with the selected design (design 3 with parameters a = 16 µm, r = 5.5 µm and L = 26 µm), whose critical dimension was CD = 5 µm.

Limitations and outlook   The main limitations of this study is that the stretchability of the patterned interconnects was approximated in the FEA model using macroscopically free-standing sheets of plastic. This poses two problems. (1) The free-standing kirigami patterned film can deflect out-of-plane, whereas encapsulated structure will be partially or completely constrained to in-plane deformation (depending on the elastic modulus and thickness of the encapsulation). (2) The FEA used macroscopic models of the Y shapes (mm-sized Y-Shapes with thickness of 75 µm), whereas the target scale for these patterns will be µm-sized (1000x smaller) with films of thicknesses ~ 35x smaller (2 µm). Nevertheless, experimental validation using micro-patterned structures encapsulated in silicone, showed that the general trends observed with the simplified FEA were consistent. Still, future optimization work could benefit from a more realistic FEA model.

2.4 Microfabrication

2.4.1 Introduction

The concept of the proposed technology is to pattern the Y-shaped motifs onto a multilayer of PI/Pt/PI (1/0.1/1 µm) on the micro-scale, which would be encapsulated in between two layers of stretchable silicone (Fig. 2.25). The Y shapes presented in the previous section are thus reduced in size by a factor of ~1,000 in the 2D plane. The PI layers serve as support layers [135] as well as electrical insulators, while the Pt serves as an electrical conductor. Here, the manufacturing process of the silicone encapsulated micro-patterned PI/Pt/PI construct is described.

Two types of devices were manufactured using this technique: conductive tracks with pin-connectors for electro-mechanical testing, and implantable electrode arrays to interface with the nervous system. In the latter case, a Pt/PDMS composite coated, previously developed in the laboratory, was applied on the electrode contacts [57].
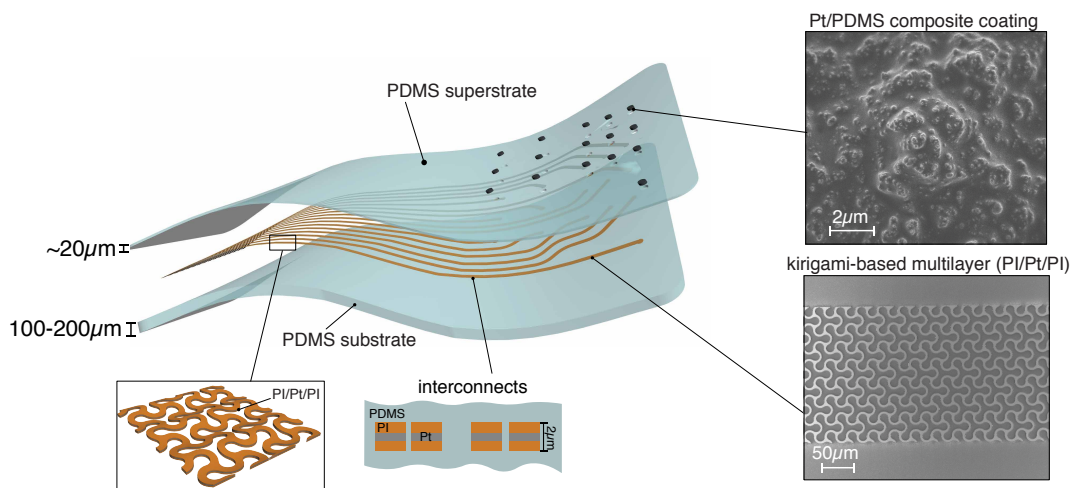
Figure 2.25 – **Technology concept using a kirigami patterned multi-layer of PI/Pt/PI encapsulated in a silicone matrix.** Illustration of the technology concept: a micro-patterned multi-layer of thin film PI/Pt/PI (1/0.1/1 µm) is encapsulated in a silicone matrix. Electrodes are coated with Pt/PDMS composite.

2.4.2 Methods

Design First the electrical layout is designed independently of the Y-shaped motifs. The hexagonal matrix of Y-shaped motifs is overlaid on top of the electrical layout only at the end of the design process. To avoid software issues, it is easier to first invert the layout and overlay an array of the Y-shaped motifs, thus allowing the software to instance only one motif (Fig. 2.26).

This design file is then used to pattern a Cr (chromium) quartz mask using direct laser photolithography (VPG200, Heidelberg). The mask can then be used for repeated UV photolithography on multiple wafers.
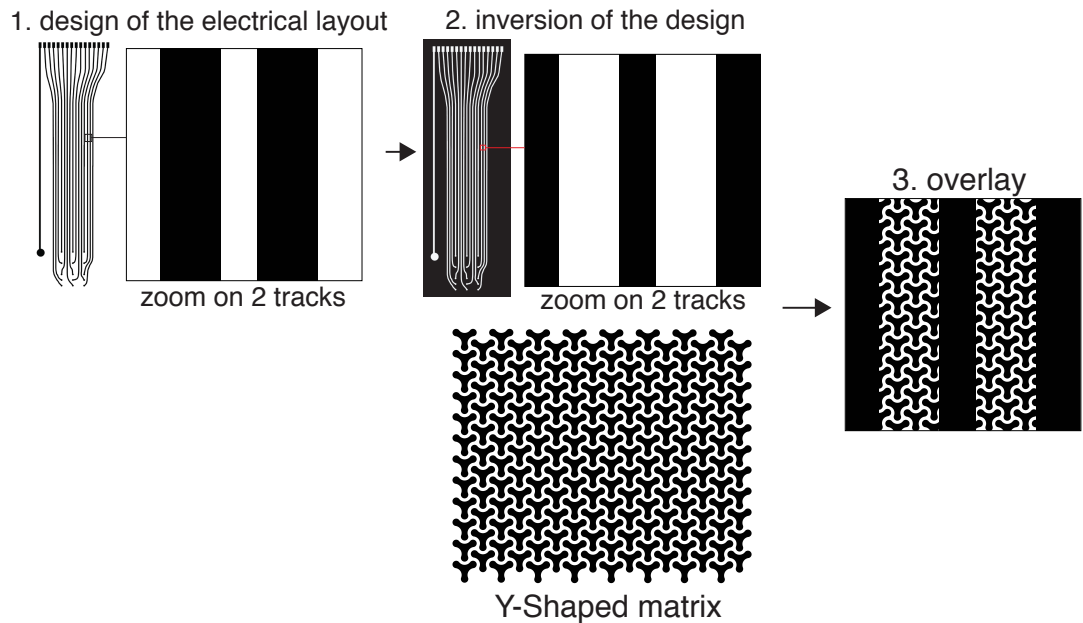
Figure 2.26 – **Design methodology for implementing Y-shaped motif to electrical layout.** Illustration of the methodology for designing an electrical layout patterned with Y-shaped motifs

Layers deposition   A sacrificial layer of Ti/Al layer (25/100 nm) is first deposited on a 4'' Si wafer by e-beam evaporation (Alliance-Concept EVA 760). Then an adhesion layer of SiO_2/Ti (25/5 nm) is sputtered (Pfeiffer SPIDER 600). This SiO_2 layer will be used to plasma bond the polyimide (PI) onto the PDMS in a later step [153]. An adhesion promoter(VM652, HD Microsystems) is then spin-coated (Sawatec LSM200) at the surface of the Ti and a 1 µm layer of PI (PI2610, HD Microsystems) is spin-coated and baked at 300°C for 4 hours under N_2 atmosphere. Subsequently, a multi-layer of Ti/Pt/Ti (25/100/25 nm) is sputtered on top of the PI after a 1 min O_2 plasma (Pfeiffer SPIDER 600). The Ti serves as an adhesion layer between the PI and Pt. The VM652 adhesion promoter is spin-coated again followed by a second layer of 1 µm PI. Finally, another layer of Ti/SiO_2 (5/25 nm) is sputtered at the surface of the PI, after a 1 min O_2 plasma. Figure 2.27 summarizes these steps.

Micro-patterning   Next, the multi-layer stack is patterned with the Y-shaped motifs and electrical layout. These patterns are etched through the entire multi-layered stack simultaneously. First, a HMDS (Bis(trimethylsilyl)amine) monolayer is deposited on top of the SiO_2 to promote adhesion of the photoresist (PR). A 5 µm thick PR (AZ ECI 3000, MicroChemicals)

45

1 Aluminum deposition
Ti/Al evaporation (25/100nm)

2 SiO2 deposition
SiO2/Ti sputtering (25/5nm)

3 Polyimide coating
PI spin-coating (1μm)

4 Platinum deposition
Ti/Pt/Ti sputtering (25/100/25nm)

5 Polyimide coating
PI spin-coating (1μm)

6 SiO2 deposition
Ti/SiO2 sputtering (5/25nm)
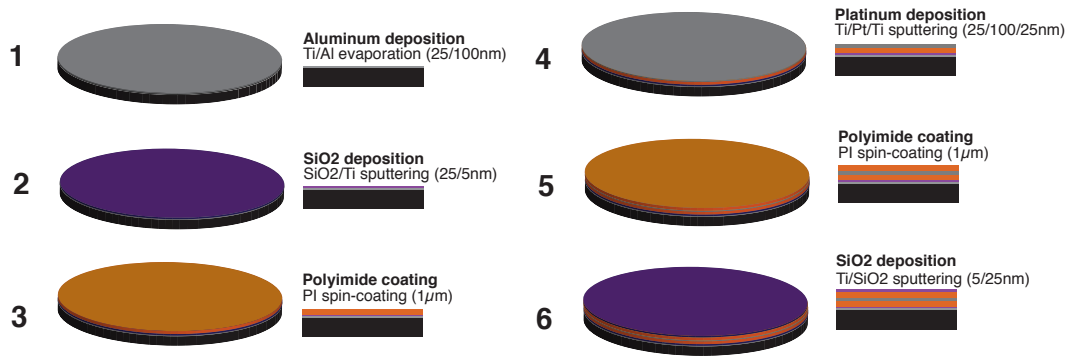
Figure 2.27 – **Process flow of multi-layer deposition.** Deposition steps for constructing the PI/Pt/PI multi-layer stack with intermediate adhesion layers.

is photolithographically patterned and serves as an etching mask. The SiO_2 and PI layers are etched by reactive ion etching (RIE) using a He/CHF3 chemistry for the SiO2 and in an O_2 plasma for the PI (SPTS Advanced Plasma Systems). The Ti/Pt/Ti metal layers are etched by ion beam etching (Nexus IBE350, Veeco). The bottom PI and SiO_2 are etched similarly. The remaining PR is stripped away in a sonicating bath of remover (Microposit Remover 1165, MicroChem) at 70°C.

The second photolithography consists in exposing the Pt layer at the location of contact pads and electrodes. A 4 μm thick PR is photolithographically patterned. The top Ti/SiO_2 and PI layers are etched by RIE and the top Ti layer is etched by ion beam etching. The remaining PR is stripped away. The photolithography and etching steps are summarized in Figure 2.28.

1 Photoresist spin-coating

2 Photoresist exposition and development

3 Etching (RIE+ IBE)

4 Photoresist spin-coating

5 Photoresist exposition and development

6 Etching (RIE)
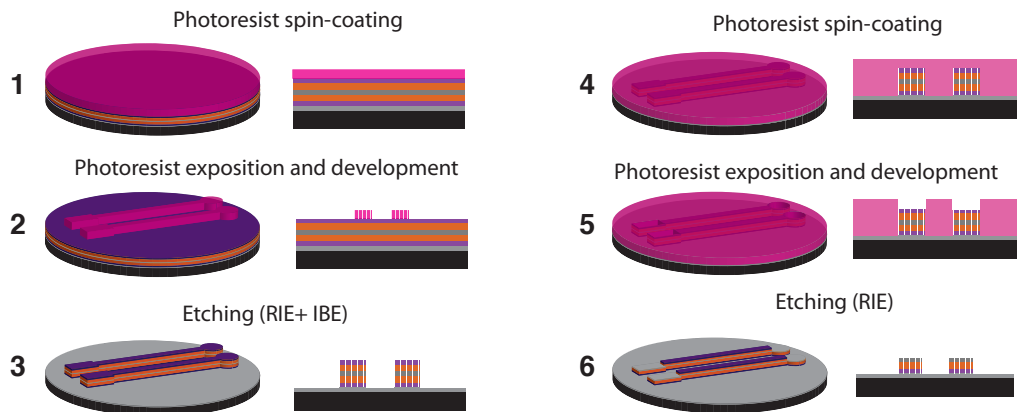
Figure 2.28 – **Process flow of multi-layer patterning.** Summary of the patterning steps to transfer the Y-shaped motifs and electrical layout onto the PI/Pt/PI multi-layer stack.

Top layer substrate fabrication   The following steps consist in transferring the multi-layer PI/Pt/PI film between two layers of PDMS. First, the multi-layer is transferred onto the top layer substrate that contains openings on the contacts and electrode sites. To manufacture the top layer substrate, a 20 μm support layer of PDMS (1:10 of cross-linker ratio, Sylgard 184, Dow Corning) is first spin coated onto a Si wafer and cured at 75°C in a convection oven for at least 3 hours (Fig. 2.29(1)). Then, a 23 μm PET sheet (DuPont Mylar 23A, Lohmann) is laminated at the surface of the PDMS (Fig. 2.29(2)). This PET sheet will be used as a screen-printing mask in the final steps of the manufacturing process. A second layer of PDMS is subsequently spin-coated and cured on top of the PET sheet (thickness around 20 μm, Fig. 2.29(3)). That PDMS layer will act as the top layer substrate for the final device. Finally, a protective 23 μm PET sheet is laminated on top (Fig. 2.29(4)). The PET-PDMS-PET stack is manually peeled off the wafer (Fig. 2.29(5)). The openings are etched through the entire PET-PDMS-PET stack using a femto-second laser source ($\lambda = 1030$ nm, OPTEC WS TURRET-200, Fig. 2.29(6)).

1   **PDMS coating**
Spin-coat PDMS at 3200rpm
Cure at 75°C for 3 hours

4   **PET protection**
Laminate 23μm PET on PDMS

2   **PET screen-print mask**
Laminate 23μm PET on PDMS

5   **PET-PDMS-PET peel-off**

3   **PDMS top layer substrate**
Spin-coat PDMS at 3200rpm
Cure at 75°C for 3 hours

6   **Laser etching**
Laser etch openings through all layers
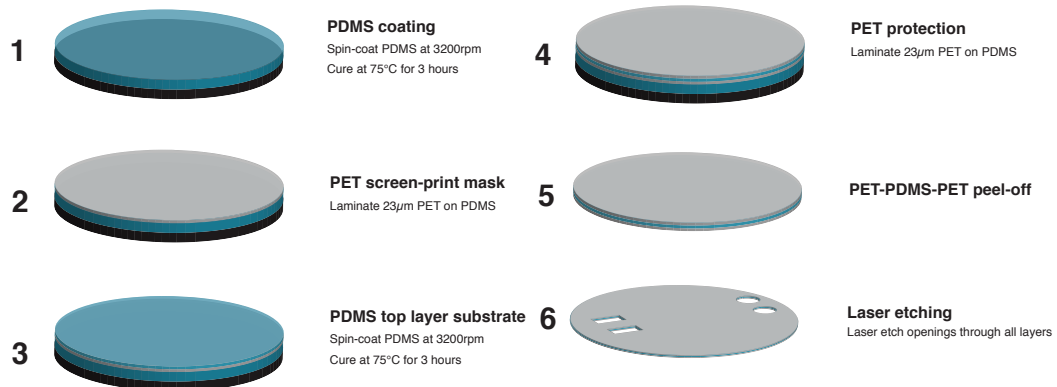
Figure 2.29 – **Process flow of the top layer substrate manufacturing.** Manufacturing steps of the PET-PDMS-PET stack used as a top layer substrate.

Transfer to PDMS   After removing the protective PET layer, the PDMS-PET stack is aligned and plasma bonded onto the PI/Pt/PI multi-layer on the Si wafer (Fig. 2.30(1)). After bonding, the PDMS-PET layers are laser-cut on top of the wafer to separate individual devices and the multi-layer of PI/Pt/PI/PDMS/PET is released from the wafer by anodically dissolving the Al sacrificial layer in a NaCl bath (1.5 V are applied between the Al layer and a Pt counter electrode for about 8 hours (Fig. 2.30(2)). The released samples are then washed with DI (de-ionized) water. Finally, the individual devices are plasma-bonded to the PDMS bottom layer substrate (100-200 μm thick) previously spin-coated and cured onto a Si wafer with a sacrificial layer of cured PSS (Poly(sodium 4-styrenesulfonate), Sigma Aldrich, Fig. 2.30(3)).

Connections and coating   Connectors were surface mounted on top of the pads, using screen-printed silver paste (EPOXY Technology Inc.,H27D Part A) and were encapsulated

1. Top layer substrate encapsulation
(plasma bonding)

PET-PDMS

2. Laser cut & anodic release

3. Bottom layer substrate encapsulation
(plasma bonding)

PDMS
PSS sacrificial layer
Si wafer

Pt counter electrode (-)

wafer with
Pt/Pt/Pl multi-layer (+)

NaCl bath with stirrer
at room temperature

PI/Pt/PI on PDMS-PET

1cm
released devices
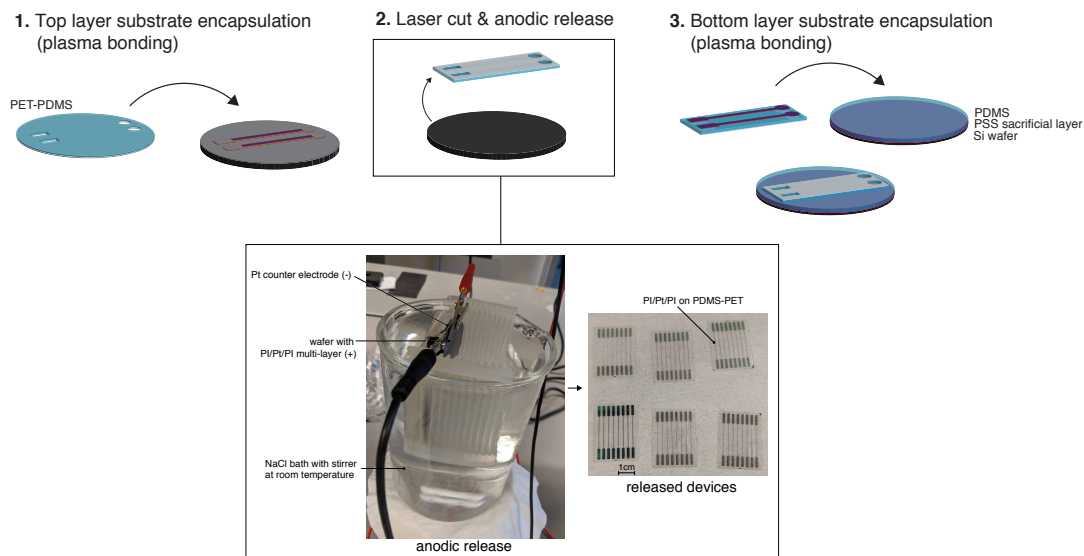
anodic release

Figure 2.30 – **Transfer of multi-layer to PDMS.** (**1-3**) Processing steps to transfer the PI/Pt/PI multilayer between two layers of PDMS by plasma bonding. The devices are released from the wafer by anodic dissolution of the Al layer, as shown in the picture at the bottom.

with a silicone adhesive (Dow Corning, DC 734 RTV clear). The PET sheet served as a screen printing mask (Fig. 2.31(1)). Similarly, the electrodes were coated by screen-printing a custom-made Pt/PDMS composite. The outer-dimension of the device was laser cut through the PDMS (Fig. 2.31(2)) and the device was released from the wafer by dissolving the PSS sacrificial layer in DI water (Fig. 2.31(3)).

1. Screen printing & connection

silver paste

Pt/PDMS composite

PET screen-printing mask

silicone adhesive

2. Contours laser cut

3. Release in DI water
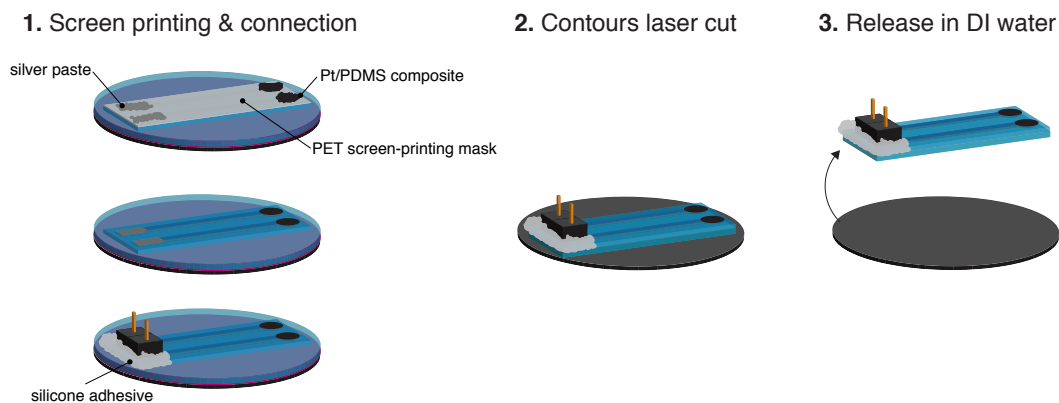
Figure 2.31 – **Connection and electrode coating.** Processing steps to surface mount connectors using screen-printed silver paste and coating the electrodes with a Pt/PDMS composite (1). The contours of the device are laser cut through the PDMS (2) and the device is released from the wafer by dissolving the PSS sacrificial layer in DI water (3).

Pt/PDMS composite fabrication   The Pt/PDMS composite used as a coating was described previously in [57]. Briefly, Pt micro-particles (avg. size 0.27-0.47 µm, 99.9% purity, STREM Chemicals, ref:93-7833) are mixed with PDMS (Dow Corning, Sylgard 184) at a w/w 30%. Hexane is used in the mixture to temporarily liquefy the composite and facilitate screen-printing. The coating was previously demonstrated to be reversibly stretchable up to 45 % applied strain [57].

Full encapsulation   To avoid issues of exposed Pt on the multi-layer, some devices were fabricated such that the Pt was completely encapsulated in PI (Fig 2.32A). The fabrication process is similar, except that the Ti/Pt/Ti layer is initially patterned with a scaled down version of the Y-shape before the deposition of the top PI layer. Then the PI/Ti/SiO$_2$ layers are deposited as before and the normal-sized Y-Shape with the electrical layout are etched through the SiO$_2$/PI/PI/SiO$_2$ layers. This step requires a precise alignment to avoid intersection of the small Y patterns in the Pt layer with the larger Y patterns etched through the PI. To make it easier, the smaller Y-shaped motifs in the Pt were scaled down such as to allow a 1 µm alignment error without running into issues (Fig. 2.32B).
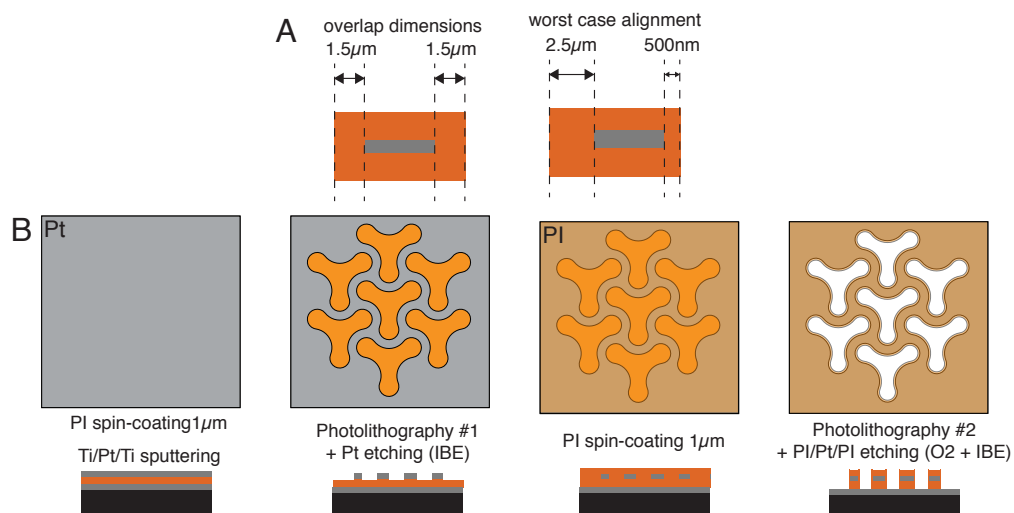
Figure 2.32 – **Full encapsulation of the Pt layer into the PI.** (**A**) Cross-sectional view of the critical alignment for the Pt to be completely embedded in PI. (**B**) Process flow (top view and cross-sectional view) showing the two photolithographical steps to achieve complete encapsulation of the Pt in the PI.

2.4.3   Results

Microfabrication   A finished wafer is shown on Figure 2.33A, where 6 devices for electromechanical testing were fabricated. SEM images show that the Y-Shaped motifs were properly etched throughout the PI/Pt/PI multi-layer (Fig. 2.33(B-C)). The 60° tilted view of the Y-Shaped motif shows that the top PI layer is slightly over-etched laterally (Fig. 2.33D), but this is not expected to alter the mechanical behaviour too much. However, this means that some parts of the Pt are exposed. The transition between a contact pad and a track shows clearly that the top PI layer was etched to expose the metallic contacts (Fig. 2.33(E-F)).
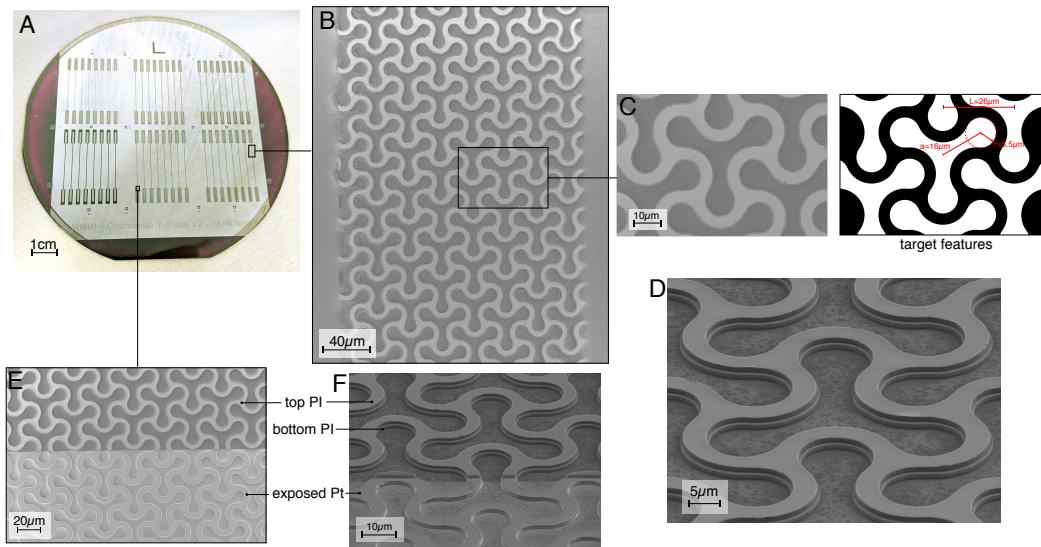
Figure 2.33 – **SEM imaging of PI/Pt/PI microstructuring with Y-shapes.** (**A**) Finished wafer with microstructured PI/Pt/PI layers for 6 devices with 8 tracks each. (**B-D**) SEM pictures of the Y-Shaped patterns etched throughout the multilayer (top view (**B-C**) and tilted at 60° (**D**)). (**E-F**) Transition to pad openings where the top PI has been removed to expose the Pt.

Full encapsulation SEM imaging revealed that some Pt was exposed between the two PI layers. For long-term implantation, the presence of voids and defects in the silicone layers might allow water vapor condensation that could cause bubbles and eventually delamination between the silicone layers and the PI tracks. This could potentially lead to corrosion of the exposed Pt by ingress of ionic body fluids. [75]. To avoid this issue for long-term implants, a slightly modified process was developed to fully encapsulate the Pt layer in the PI (Fig. 2.34A). This method requires a precise (~1 μm) alignment, but results show that it is feasible (Fig. 2.34B). The downside is that the Pt tracks are slightly narrower, resulting in a larger electrical track resistance.
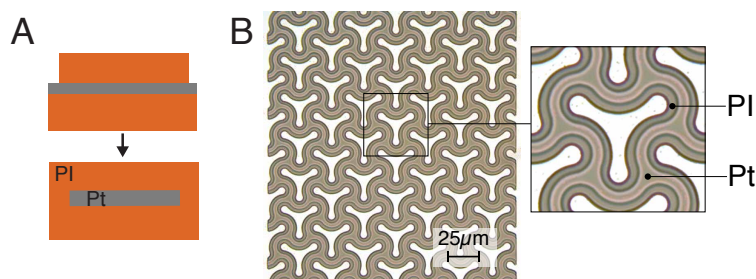
Figure 2.34 – **Full encapsulation of the Pt layer into the PI.** (**A**) To avoid exposed Pt between the two PI layers, the Pt is completely encapsulated in PI. (**B**) Optical micrography of a electrical track, where the Pt track can be seen completely encapsulated by PI.

Final Devices Optical images of finalized devices show that the micro-patterned tracks survive the transfer process. An example of a 16-electrodes array shows how the composite is screen-printed over the electrode sites (Fig. 2.35(B)). An example of a 3-electrodes array (Fig. 2.35(D)) shows how precise the PDMS contour can be laser cut close to the tracks (<100 μm distance from the edge, Fig. 2.35(E)).
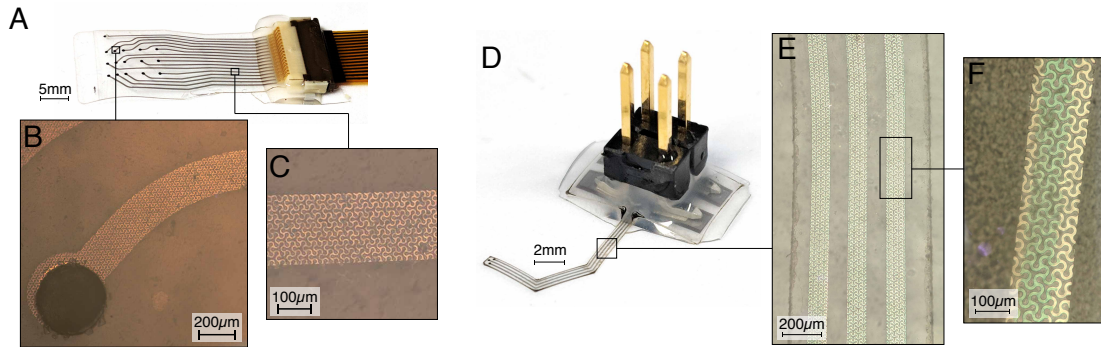
Figure 2.35 – **Example of finalized devices using micro-patterned tracks.** (**A**) Electrode array device with 16 electrode contacts connected to a flexible cable. (**B**) Optical photography of a track and the composite coating on the electrode site. (**C**) Optical photography of a patterned track embedded in PDMS. (**D**) Electrode array with 3 electrodes connected to pin headers. (**E-F**) Optical photography of patterned tracks.

2.4.4 Summary and discussion

Summary Here was demonstrated the possibility of patterning electrical tracks with arrays of micro-sized Y-shaped motifs through a ~2 μm thick multi-layer of PI/Pt/PI, and encapsulating those tracks in a silicone matrix to form a final device that can be hand manipulated, connected to external connectors and coated on electrode sites. The simplicity of designing tracks independently of the Y-Shaped motif was also highlighted. This means it is for example possible to draw straight lines on the electrical layout.

Hermetic encapsulation It was also shown that it is possible to avoid exposed Pt between the two PI layers, by fully encapsulating the Pt with the PI. That required an extra photolithography step and a precise (1 μm) alignment. Even though PI is more appropriate as an hermetic barrier compared to PDMS due to its higher stability [154], it is known that even PI will eventually breakdown when subject to repeated electrical field (typical of stimulating neural implant) and in a wet ionic environment (such as in the body). One promising solution is to use silicon carbide (SiC) as an additional long-term encapsulation [155, 156] (Fig. 2.36). The implementation of SiC is a priori possible in the proposed process flow but would require further optimizations. In the context of this thesis, this was not deemed necessary as devices were not aimed to be used in vivo for more than a few months. SiC could have the added benefits that it has also previously been used an adhesion layer between PDMS and PI [157]. It could thus also replace the external SiO_2 layer currently used.
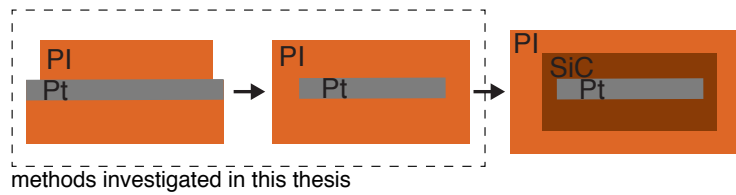
Figure 2.36 – **Future work using SiC as an hermetic encapsulation.** Envisioned improvement of the multi-layered film to increase hermeticity by using silicon carbide (SiC).

Materials In the technology proposed in this section, the materials used are so far not medically approved. Nevertheless, the technology proposed here is technically transferable to other materials, including medically approved ones.

In that regard, switching from the current PDMS (Sylgard 184) to a medically approved silicone (such as a NuSil MED-6215) should be relatively straightforward, as it has a similar viscosity (5500 cP vs 3100 cP for Sylgard 184) suitable for spin-coating at similar thicknesses, similar elastic modulus (E≈2.2 MPa vs E≈1.5 MPa for Sylgard 184) and can also be plasma-bonded (Appendix A.2).

As of now, PI is not a very common material for clinical devices. It is currently used in by Retina Implant (Reuligen, Germany) in the IMS-alpha and AMS-alpha devices, which both hold a CE mark [158]. However, a much more common material is parylene-C, which could be used as an alternative to PI. Its processing would require some optimization, but parylene-C has similar properties (mechanically and chemically) and could be suitable as a more conventional medically approved replacement [159]. Still replacement of the PI is not as critical as the silicone, as it is technically not exposed to neural tissue in the configuration presented here.

Outlook Future work to transfer this technology to a neural implant that can be implanted into humans for long-term would mainly require the transfer of the materials to medically approved materials with known and demonstrated long-term biocompatibility as well as the incorporation of a SiC encapsulation to improve long-term (> 10 years) hermeticity of the tracks, as described above. Nevertheless the technological achievements presented here are more of a proof of concept and are a priori suitable for short-term (< 6 months) neural implants in animal models. In the next section, these micro-patterned tracks will be electro-mechanically characterized.

2.5 Electromechanical characterization

Here, the electro-mechanical properties of kirigami micro-patterned multi-layered tracks of PI/Pt/PI embedded in silicone are evaluated.

2.5.1 Methods

Samples preparation Using the manufacturing process presented in Section 2.4, samples were prepared with 8 tracks (17 mm x 0.2 mm) each. The PDMS substrate was 140 µm thick, and the PDMS superstrate was 20 µm thick. Pin headers were used to record the electrical resistance of each track (Fig 2.37).
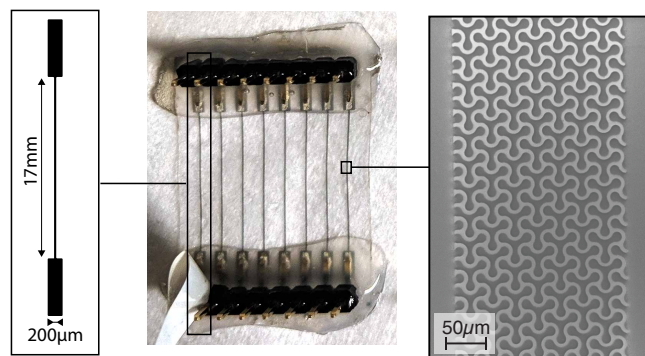
Figure 2.37 – **Sample preparation for electromechanical testing.** Samples for electromechanical testing were made of 8 tracks micro-patterned with arrays of Y-shaped motifs.

Electromechanical characterization Samples were stretched in a tensile tester (MTS Criterion Model 42, with a load cell of 10 N maximum capacity) using a strain rate of 1 mm/s. The samples were clamped and secured to the plates of the stretcher. The electrical resistance of the conductive films was recorded during stretching using a custom-made circuit made of voltage dividers and a 8-channels multiplexer, controlled by an Arduino Uno board. For longer-term cycling, the samples were mounted to a home-made uniaxial stretcher and stretched at 10% of their initial length at 1 Hz (1 stretching cycle per second). The electrical resistance was measured the same way. The resistance was recorded (sampling rate of 5 Hz) and saved only every 10 cycles per decade of cycles. Both stretchers and electrical resistance recording systems were synchronized and controlled using custom made software with LabView 2015.

Conformability testing Cylindrical agarose structures were fabricated to conduct an experimental conformability study. The agarose gel was obtained by dissolving agar powder (3% w/v, Agar Agar Patissier) in DI water; the solution was then shaped in custom-made molds with varying radii (R = 2 mm, 3 mm, 4 mm). Rectangular shaped films (4 mm x 6 mm) were prepared and tested on agarose. Samples were fabricated both in the form of standalone

PDMS and as a multilayer of PDMS and kirigami PI/Pt/PI. For each material type, multiple thicknesses were tested on all cylindrical structures and conformability or lack thereof was visually observed. Experimental observations were compared to theoretical calculations.

2.5.2 Results

Track width If the kirigami pattern is randomly overlaid on an interconnect, the minimum allowable track width must be such that at least one conductive ligament is always present within the track. That minimum track width is shown with the red arrow in Fig. 2.38 and is given by width$_{min}$=2R+$\sqrt{3}$a. For the selected geometry (a = 16 µm, r = 5.5 µm and L = 26 µm) width$_{min}$ = 47 µm.
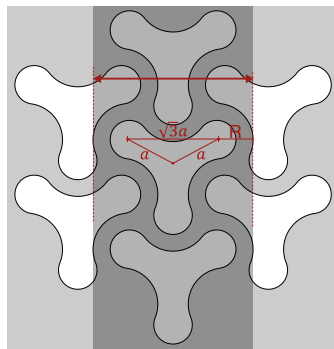
Figure 2.38 – **Smallest track width using a kirigami pattern.** The smallest track width is shown in the shaded area, if the kirigami patterns are randomly aligned on the track. The red arrow indicates the smallest track width.

If the kirigami pattern is properly aligned on top of the track, the theoretical ultimate narrowest track (shown with the double-arrowed line on Fig. 2.39) is given by w$_{min}$=L-CD=R+a$\frac{\sqrt{3}}{2}$. For the selected geometry (a = 16 µm, r = 5.5 µm and L = 26 µm), w$_{min}$ = 21 µm, as shown on the SEM picture in Fig. 2.39.
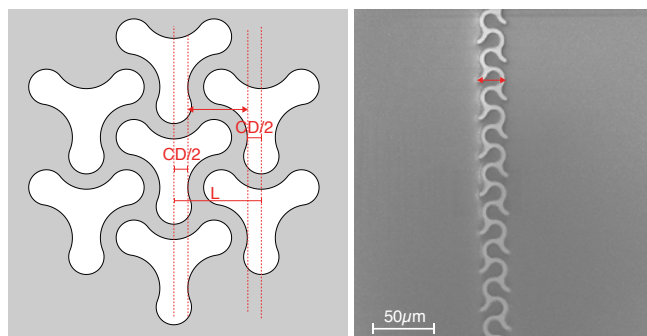
Figure 2.39 – **Theoretical smallest track width using a kirigami pattern.** The theoretical smallest track width is given by the red double arrow (left). An SEM image shows an example of such a track (right)

Electrical model   The equivalent electrical circuit of an array of Y patterns shows that the electrical resistance depends only on the vertical ligament, as the voltage at each node is the same, thus there is no current flowing through the horizontal segments (Fig. 2.40).
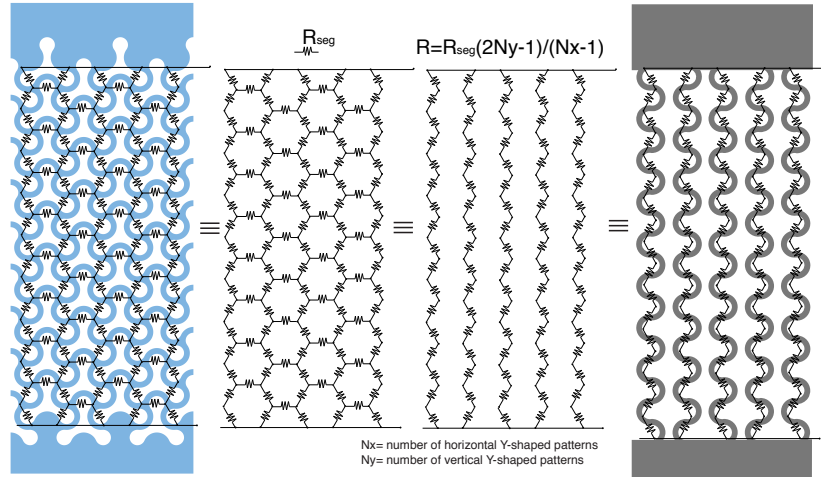
Figure 2.40 – **Equivalent electrical circuit.** Equivalent electrical circuit for a track patterned with the Y-shaped motifs, with the hypothesis that all segments have equal resistance R_{seg}.

One can therefore decompose each track in unitary resistances for each segment (R_{seg}). The total resistance R of a track is then given by Equation 2.2.

$$R = R_{seg}\frac{2N_y - 1}{N_x - 1} \tag{2.2}$$

, where N_x and N_y are the number of Y-shaped patterns on the horizontal and vertical axes, respectively. For a given track of width w and length l, Nx=floor($\frac{w}{L}$) and Ny=floor($\frac{l}{L\frac{2}{\sqrt{3}}}$).

The value of R_{seg} is best calculated using FEA, using the same methodology described in Section 2.2. For the parameters used here (a = 16 µm, r = 5.5 µm and L = 26 µm), the FEA gives R_{seg} = 10.1 Ω, using an experimental sheet resistance measured with micro-fabricated tracks without any patterning. To validate the model, a micro-patterned track of length l = 17 mm and width w = 200 µm was fabricated. Theoretically, its total track resistance should be given by Equation 2.3 (using Equation 2.2 above, with N_x = 8 and N_y = 567):

$$R = R_{seg}\frac{2N_y - 1}{N_x - 1} = 10.1\frac{2 \cdot 567 - 1}{8 - 1} = 1'634\Omega \tag{2.3}$$

In comparison, the experimentally measured track resistance (n = 72 samples) was in average 1'400 Ω (Fig 2.41A).
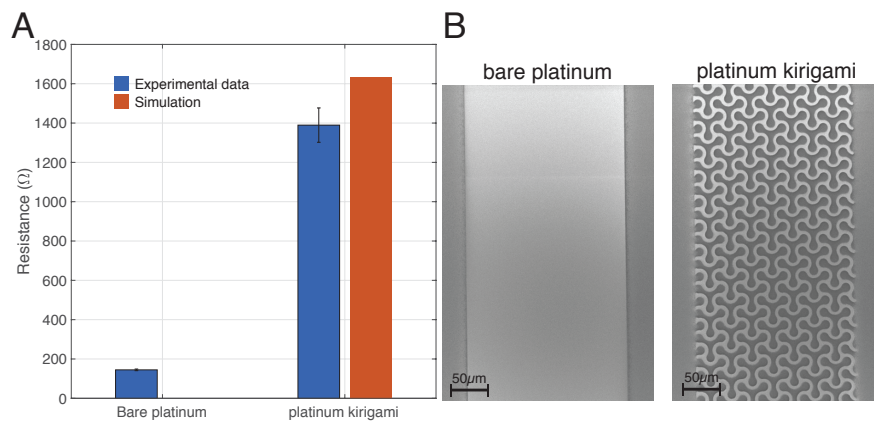
Figure 2.41 – **Electrical resistance of kirigami patterned platinum.** (**A**) Electrical resistance measured on 17×0.2 mm^2 tracks without patterning (n = 24) and patterned with the kirigami motif (n = 72) in blue. The resistance predicted by FEA is in red. Bars denote standard deviation. (**B**) SEM pictures showing a bare track without (left) and with (right) micro-patterning.

Electrical redundancy   Even though the equivalent electrical model of the micro-patterned tracks is equivalent to parallel meanders (Fig 2.40), this is not the case if one takes into account defects that may arise typically during micro-fabrication. Indeed, if a ligament presents a defect, or is in the worst case electrically ruptured, then the proposed patterning allows for electrically redundancy (Fig. 2.42). This can be quantified by comparing the probability of complete electrical failure. As an example, statistical modelling using parameters of $N_x = 6$ and $N_y = 10$ show that the probability of complete electrical failure for 10% cuts density is <1% for the kirigami approach, compared to 35% for the parallel meanders (Fig. 2.42).
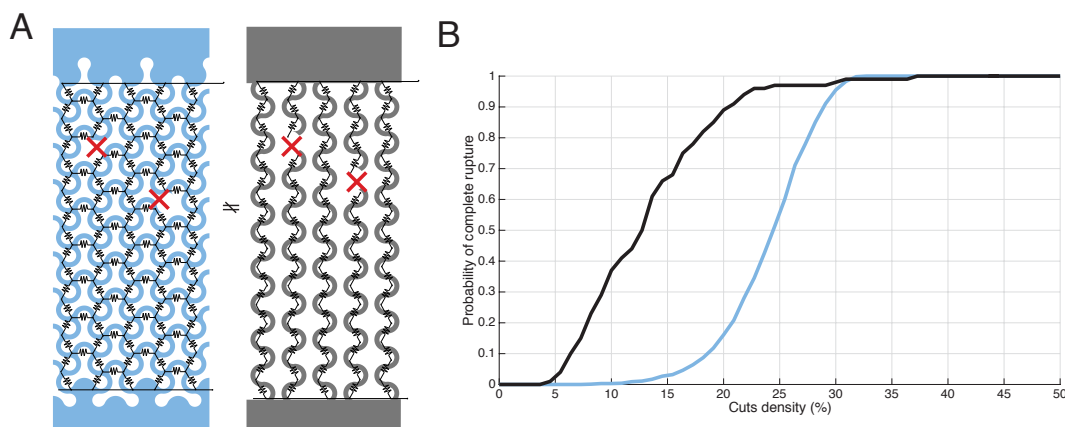
Figure 2.42 – **Electrical redundancy of tracks with Y-shaped kirigami patterns.** (**A**) If some segments are electrically broken, the two designs don't have the same equivalent electrical circuit. (**B**) Probability of a track to be completely ruptured as a function of the number of cuts for the kirigami-patterned track (blue) than for simple meanders in parallel (black). Values computed for $N_x = 6$ and $N_y = 10$ by computational modelling.

Tensile testing Samples containing 8 micro-patterned tracks (200 µin width) embedded in PDMS were stretched uni-axially up to failure. During elongation, the total force and the electrical resistance of each track was monitored. The force-strain curve has a similar behaviour for both the standalone PDMS sample and the PDMS with micro-patterned tracks (Fig. 2.43A). The micro-patterned tracks remained conductive up to 80% elongation, and by then the electrical resistance of the tracks had increased in average by less than a factor of 3 (Fig. 2.43B). The tracks failed electrically only when the sample broke mechanically. Moreover, one can observe two regimes during the change in electrical resistance as a function of applied strain ϵ_{app}. For $\epsilon_{app} < 10\%$ the resistance changes less than 2% and for $\epsilon_{app} > 10\%$ the resistance increases non-linearly. In comparison, a sample of PDMS with non-patterned tracks failed both mechanically and electrically very early during stretching at $\epsilon_{app} = 2.5$-3% (Fig. 2.43B), as the non-patterned PI/Pt/PI multi-layer and PDMS ripped apart (Fig. 2.43D). The apparent elastic modulus of the 140 µm thick PDMS with the embedded micro-patterned tracks increased by 40% compared to a standalone PDMS sample without any tracks (from 2.3 MPa to 3.2 MPa respectively), whereas the apparent elastic modulus of the PDMS with non-micropatterned tracks increased by 540%, to 14.7 MPa (Fig. 2.43C).
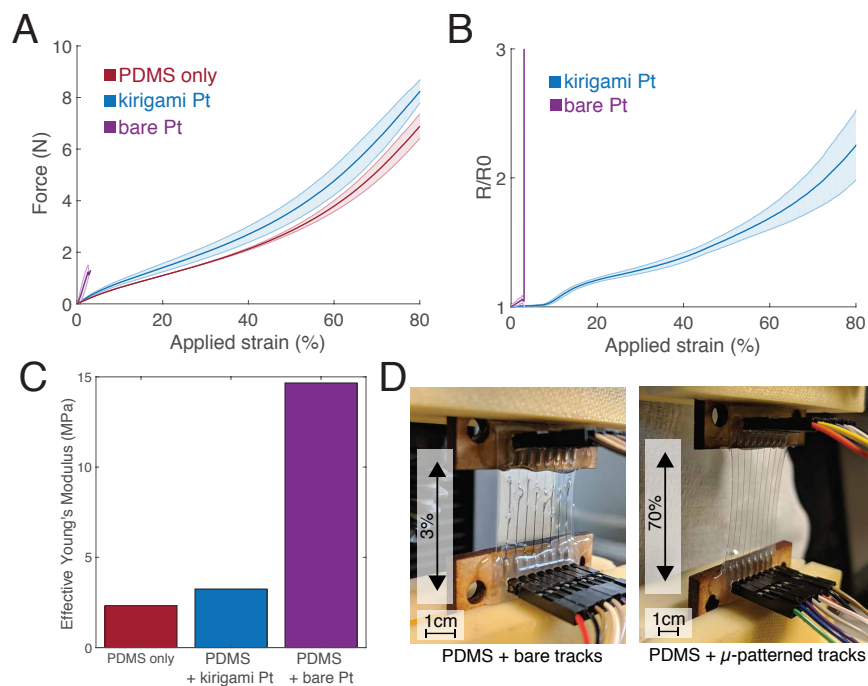
Figure 2.43 – **Micro-patterned tracks under uni-axial tensile strain.** (**A**) Measured force under applied strain for 3 types of samples (same dimensions): standalone PDMS (red), PDMS with 8 micro-patterned tracks (blue) and PDMS with 8 non-patterned tracks (purple). n = 2 samples for each type. (**B**) Relative change in resistance during applied strain for patterned (blue) and non-patterned (purple) tracks. n = 16 tracks tested for each type (2 samples with 8 tracks each). (**C**) Apparent elastic modulus for each sample type. (**D**) Pictures of a sample with non-patterned tracks breaking at an applied strain of 3% (left) and a sample with patterned tracks stretching at an applied strain of 70%. Shaded areas denote standard deviation.

Effect of track width   A sample made of 8 tracks of various widths (200, 150, 120, 100, 80, 60, 40 and 20 μm) embedded in PDMS was stretched up to failure (Fig. 2.44A). The change in resistance of each track as a function of applied strain was similar for all track widths (Fig. 2.44B). However, the elongation at break was smaller for narrower tracks: the 20 μm wide track failed at $\epsilon_{app} = 65\%$ whereas the 200 μm wide track failed at $\epsilon_{app} = 94\%$ (Fig. 2.44C). As expected, the nominal resistance at rest was larger for narrower tracks (Fig. 2.44D).
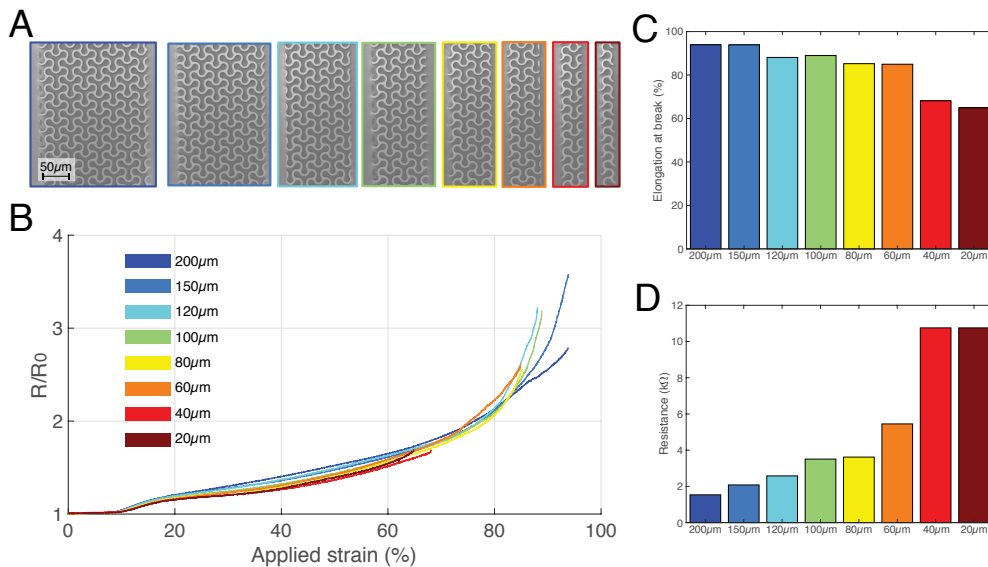
Figure 2.44 – **Effect of track width on the electro-mechanical properties of micro-patterned kirigami tracks.**   (**A**) SEM pictures of the 8 different track widths that were electro-mechanically tested. (**B**) Relative change in resistance as a function of applied strain for all 8 track widths (n=1 sample with 8 tracks, each of a different width). (**C**) Elongation at electrical break for each track width. (**D**) Nominal resistance at rest for each track.

Mechanical cycling   A sample with eight 200 μm wide tracks embedded in PDMS was cycled for 1 million cycles at $\epsilon_{app} = 10\%$. The resistance after 1 million cycles had increased by a factor of 8 to 45% (Fig. 2.45). Interestingly, tracks on the edges of the sample experienced a higher change in resistance than the tracks in the center portion of the sample, resulting in a wide range of resistance change. This is due to poor sample design (squared sample instead of a dogbone shape), resulting in a non uniform strain field across the sample that is larger on the edges of the samples.
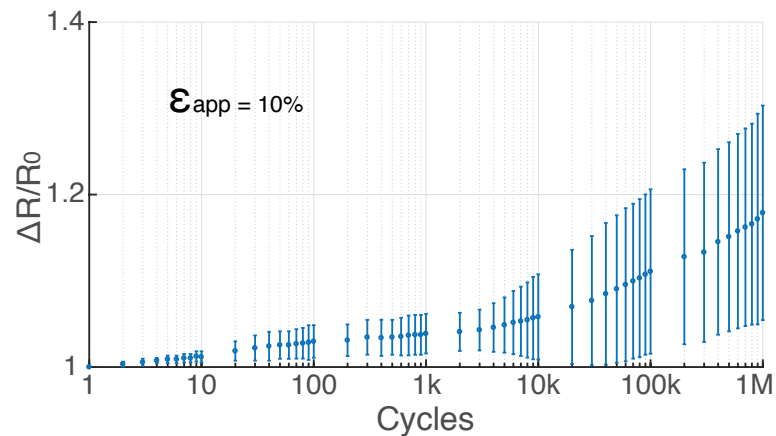
Figure 2.45 – **Cyclic stretching of micro-patterned kirigami tracks.** Relative change in resistance as a function of stretching cycles at an applied strain of 10%. n=8 tracks (1 sample). Bars denote standard deviation.

Uniaxial stretching SEM   To better understand the mechanical mechanisms of the micro-patterned PI/Pt/PI film, a sample made of a single conductive track was manufactured on a PDMS substrate without any top encapsulation. The sample was uni-axially stretched under SEM and pictures were taken at various strains (Fig. 2.46). SEM images might to indicate that in that configuration, ligaments slightly deflect out of plane for the first 0-20%. Microcracks can then be observed in the PI layer at around 20-25% applied strain. Eventually one of the ligaments breaks at an applied strain of 60-65%. Unfortunately, imaging at a tilted position was not possible with the stretching setup.
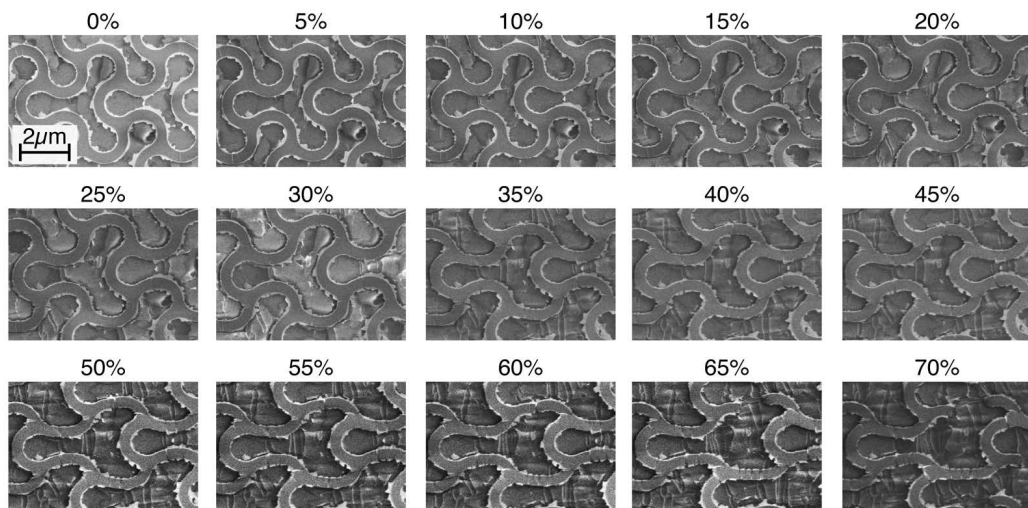
Figure 2.46 – **Stretching of micro-patterned PI/Pt/PI under SEM.** SEM images of the micro-patterned PI/Pt/PI film at various applied strains.

Conformability Here, the impact of the micro-patterned film on the conformability of the overal structure was assessed. The critical condition for a film of thickness t to conform to a wet cylinder of radius R is set when the surface energy $E_{surface}=\gamma L$ per unit width overcomes the bending energy $E_{bend}=\frac{Eh^3L}{12(1-v^2)2R^2}$ per unit width. The critical thickness for which the film conforms to the cylinder (Fig. 2.47A) is therefore given by Equation 2.4 when $E_{surface}=E_{bend}$:

$$t_{critic} = \sqrt[3]{\frac{R^2 \cdot 24\left(1-v^2\right)\gamma}{E}} \tag{2.4}$$

, where v and E are the Poisson coefficient and Young's modulus of the film and γ is the surface tension of the liquid on the cylinder. This equation was derived from [64]. The critical thickness as a function of R was calculated for a PDMS membrane (E = 1 MPa, v = 0.5) on a cylinder wet with water ($\gamma = 61.55\ \frac{mJ}{m^2}$), as shown in Fig. 2.47B.

Theoretical conformability of PDMS on cylindrical agarose structures was confirmed experimentally for a range of thicknesses, as shown on Fig. 2.47B, where red dots indicate samples that didn't conform and green dots indicate samples that did. The influence of the micro-patterned multi-layered PI/Pt/PI film embedded in PDMS was then evaluated. No significant detrimental effect to the compliance was observed with the micro-patterned multi-layer (Fig. 2.47C).
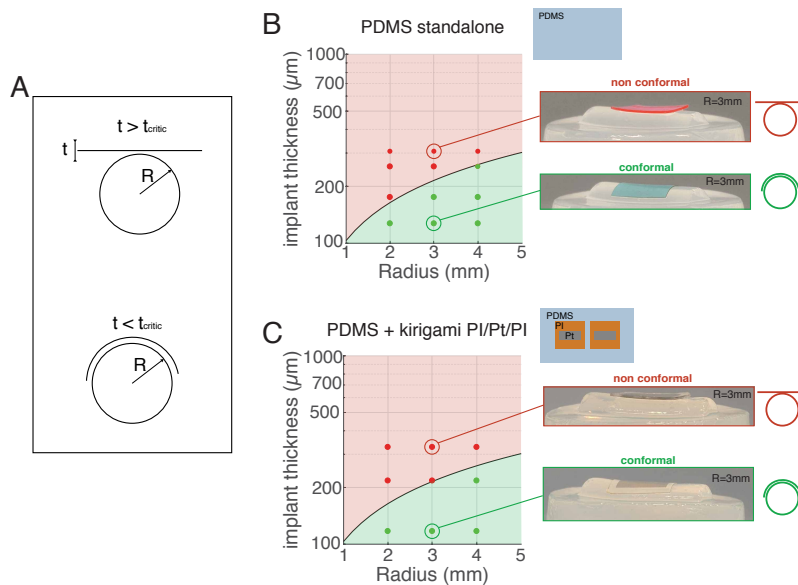
Figure 2.47 – **Impact of micropatterned films on the conformability of PDMS membranes.** (**A**) The conformability by capilarity of a membrane on a wet cylinder depends on its thickness compared to a critical thickness t_{critic}. (**B**) Theoretical critical thickness for a PDMS membrane as a function of cylinder radius. The dots indicate sample that experimentally did conform (in green) or didn't conform (in red). The insets shows colorized PDMS membranes that were used to assess conformability experimentally. (**C**) The same experiment was performed using PDMS membranes with an encapsulated film of micro-patterned PI/Pt/PI.

2.5.3 Summary and discussion

Summary   Electrical modelling of the micro-structured tracks with Y-shaped motifs show that their resistance can easily be estimated using FEA. In particular it was found that for the selected geometrical parameters (a = 16 µm, r = 5.5 µm, L = 26 µm) a micro-patterned track has an increase in resistance by a factor of 9 compared to a non-patterned track of same width. Moreover, statistical models demonstrate the benefit of such patterning compared to simply replacing a track with parallel meanders, as the kirigami pattern allows for redundancy in case of defects that could appear during manufacturing and thus decreases the probability of having a complete track failure.

Tensile tests showed that micro-patterned tracks can stretch up to 80% before mechanical and electrical failure, whereas non patterned tracks failed at strains around 2-3%. Moreover, it was noticed that there is very slow change in resistance for $\epsilon_{app}<10\%$ ($\Delta R/R_0<5\%$). However, at larger applied strains, the resistance starts increasing rapidly, as the PI/Pt/PI probably starts to plastically deform and creating cracks in the Pt layer, thus increasing its resistance. SEM imaging of non-encapsulated PI/Pt/PI interconnects bonded on PDMS substrates showed that micro-cracks in the PI layer could be visible at around $\epsilon_{app} = 20\text{-}25\%$. It is hypothesized that for completely encapsulated tracks this failure happens earlier, as ligaments are probably constrained to in-plane deformation. This electro-mechanical behaviour was consistent for various track widths ranging from 200 µm down to 20 µm. Moreover, cyclic tensile testing at $\epsilon_{app} = 10\%$ for track widths of 200 µm showed that the elasticity is reversible, as the tracks resistance increased by less than 50% after 1 million cycles, indicating limited fatigue. Moreover, it was shown that the micro-patterned PI/Pt/PI stack has mechanically little impact on the apparent elastic modulus of the complete structure as well as its conformability to cylindrical structures (compared to free-standing PDMS films).

Mechanism of stretchability   FEA and experimental results in previous sections showed that free-standing patterned films with Y-shaped cuts deformed by out-of-plane buckling of the ligaments during elongation. However, patterning interconnects with these Y-shaped motifs on the microscale and encapsulating these interconnects between two layers of PDMS (E=1 MPa, t=~150 µm), it is unclear what is the mechanism of stretchability. An analytical mechanical model and more complex FEA could offer more insights onto the deformation modes. SEM imaging of partially encapsulated micro-patterned films (only bottom encapsulation) shows some slight out-of-plane deformation for strains around 10-15%, and cracks can be seen in the top PI layer at strains around 20-20%. This seems to indicate that after unfolding, these structures start to deform in plane plastically and irreversibly. Even if SEM imaging during uniaxial tensile testing of partially encapsulated tracks is informative, the behaviour is still different from completely encapsulated tracks. Other studies performed for metal interconnects supported by polyimide and shaped into serpentines can offer some insights into these mechanisms.

It was previously proposed that there are three possible deformation modes for serpentines

bonded to a substrate: wrinkling, buckling, and in-plane scissoring. These were shown to depend on the ratio of the metal width and thickness t_m/w_m [160]. It could therefore be interesting to know what modes of deformation are in action for the geometries and materials presented in this section. Some understanding can be found from studies which have analyzed the effect of the substrate and encapsulation on the stretchability of serpentine interconnects.

Effect of substrate   Pan et al. for example studied the effect of the substrate on serpentine interconnects. Their analysis was centred around a critical length l_{cr} [133]. They showed that if the length of the straight part of the serpentine interconnects l, was smaller that this critical length ($l<l_{cr}$), then the interconnects would wrinkle (local buckling), whereas if it was larger ($l>l_{cr}$) the interconnects would globally buckle with a much larger amplitude. In the latter mode, the out-of-plane deflection thus allowed to increase stretchability by reducing the local strain at a given elongation.

The critical length l_{cr} depends on the effective thickness and elastic moduli of the interconnects and substrate. These can be calculated using the bending stiffness of a multi-layered film given by Equation 2.5.

$$\overline{EI_{tot}} = \sum_{i=1}^{n} \overline{E_i} h_i \left(b - \sum_{j=1}^{i} h_j - \frac{h_i}{2} \right) + \sum_{i=1}^{n} \frac{\overline{E_i} h_i^3}{12} \tag{2.5}$$

, where h is the thickness of the material, the plane strain modulus for a given material i is defined as $\overline{E_i} = \frac{E_i}{1-v_i^2}$ and depends on its elastic modulus E_i and Poisson ratio v_i. Parameter b is the location of the neutral plan (Equ. 2.6).

$$b = \sum_{i=1}^{n} \left\{ \overline{E_i} h_i \times \left[\sum_{j=1}^{i} h_j - (h_i/2) \right] \right\} / \sum_{i=1}^{n} \overline{E_i} h_i \tag{2.6}$$

The effective thickness of the multi-layered interconnect h_f and its effective plane-strain elastic modulus $\overline{E_f}$ can then be calculated using Equations 2.7 and 2.8.

$$h_f = \sqrt{\frac{12EI}{\sum_{i=1}^{n} \overline{E_i} h_i}} \tag{2.7}$$

$$\overline{E_f} = \frac{\sum_{i=1}^{n} \overline{E_i} h_i}{h_f} \tag{2.8}$$

For the thicknesses and properties of the materials used in this work (Appendix A.4): $h_f \simeq 1.6$ µm and $\overline{E_f} \simeq 22.5$ GPa. These values are quite close to the interconnects used in Pan et al.

They showed that interconnects on a PDMS substrate made of Sylgard 184 thicker than 100 µm would exhibit wrinkling. It could thus be hypothetized that this is also the case for the work presented here. Moreover, in-plane deformation is probably more plosible as studies have shown that adding a top encapsulation hinders even more out-of-plane deflection [132, 133].

These studies show that these deformation behaviours are very sensitive to the elastic modulus and thickness of the substrate and encapsulation. Pan et al for example showed that the stretchability could be increased from 30% to 130% by using Ecoflex (E $\simeq$ 50 kPa) compared to Sylgard 184 [133]. Thus, the use of softer encapsulation materials is a promising route towards increasing the overall stretchability of these structures, if it was deemed necessary.

Outlook   Overall the studies presented here demonstrate a proof-of-concept of using Y-shaped kirigami patterns to engineer sufficient elasticity in metal conductors in the context of neural implants. However, the discussion above motivates the use of FEA and mechanical analytical models for future work to provide insights onto how the various parameters of the materials (mainly their thickness and elastic modulus) could be tuned to eventually increase the global stretchability of the devices. These mathematical and numerical analyses could also be supplemented with experiments where various thicknesses of materials and encapsulations of varying elastic moduli are tested.

2.6 Strain gradients

2.6.1 Introduction

One challenge associated with stretchable electronic circuits, is the integration of rigid components, such as active electronics (e.g. multiplexers, or on-board pre-amplifiers) or simply connectors (typically made of rigid materials such as silicon, E ≈ 150 GPa), onto the soft substrate (E ≈ 1 MPa). The rigid to soft interface between the stretchable tracks and the connector is a weak point of the system under elongation. Indeed, this mechanical mismatch causes a local increase of the local strain and typically leads to the delamination of the rigid components from the soft substrate .

Various approaches have been suggested to overcome this challenge. The general idea is to create a smooth gradual change in the materials softness to avoid any strain peaks at the interface. This can be done for example by using combination of materials with varying elastic moduli [161], or modifying the local structure of the same silicone to change locally its elastic modulus [162]. Another idea is to create a non-strain zone around the component using embedded rigid islands in the soft substrate. By tuning the geometrical parameters of these islands, it is possible to smooth the strain field around the rigid component [163]. In the end, all these methods rely in a strain gradient to minimize the peak strain and eventually increase the long-term reliability of these systems under cyclic elongation.

Mechanical analyses from Section 2.2 showed that changing the geometrical parameters of the Y-shaped motifs modified the spring constant of the overall structure. It was therefore thought that modifying locally the shape of these motifs along the track could mimic a strain gradient. In this section, this idea is briefly explored on a macroscopic scale to demonstrate the proof of principle of using these Y-shaped motifs to engineer strain gradients.

2.6.2 Methods

Samples preparation PET sheets (100 µm thick, Avery Zweckform) were laser-cut with Y-Shaped motifs similarly to the methods of Section 2.2.

Mechanical testing Same methods as in Section 2.2.

Local strain analysis To analyze the change in local strain, black dots were initially printed on a PET sheet at the nodes of the tri-branched structures using a laser printer (Xerox Phaser 3600) before laser cutting the Y-shaped motifs. Pictures were taken at various elongations. The coordinates of the dots were then extracted using post-processing of the pictures (Adobe Photoshop CC 2017) and detection using ImageJ. A custom written MATLAB script (MATLAB R2017, Mathworks) was used to track the displacement of the dots to estimate the local strain. The procedure is summarized in Figure 2.48.
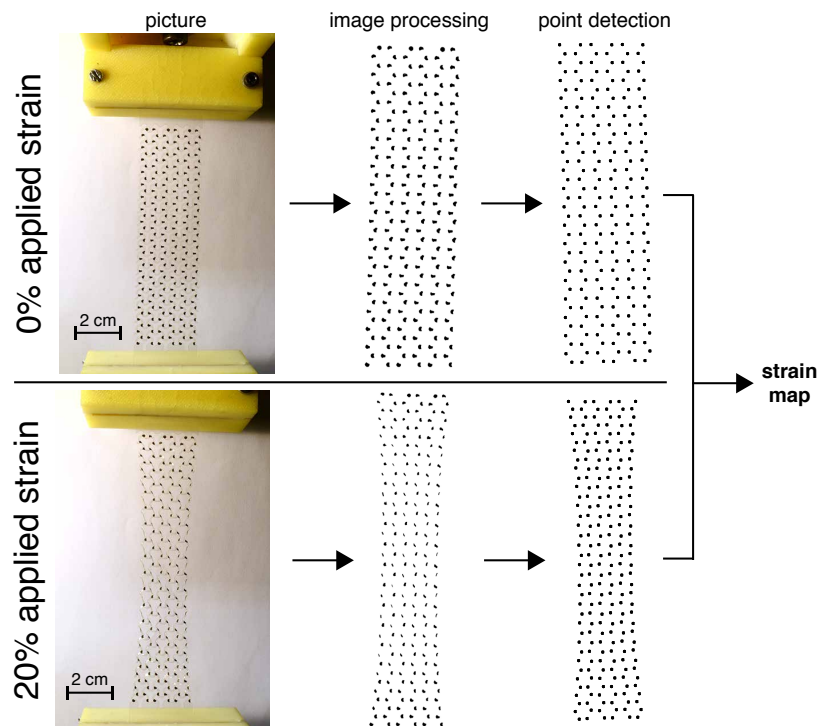
Figure 2.48 – **Methods to calculate gradient strain maps.** Pictures of samples at 0% and 20% strain (top and bottom) are first taken. Image post-processing allows to put in evidence the dots. The coordinates of the dots are then extracted using imaging software.

2.6.3 Results

Effect of geometry on elasticity First, the effect of the Y-shaped motif geometry on the mechanical properties of a patterned film was investigated. Sheets of 100 µm thick PET (polyethylene terephthalate) were cut in dogbone shapes (Appendix Fig. A.1) with smooth Y-shaped cuts of varying parameters a (as defined in Fig. 2.18). Each sample was stretched up to failure (Fig. 2.49A), and its spring constant was calculated by looking at the slope in the elastic regime. The effect of the parameter a on the spring constant k is shown in Figure 2.49B (with r kept constant at 917 µm). Results show that as a increases, the effective spring constant diminishes. Similarly to results observed in Section 2.2, this is due to the ligaments between the Y-shaped motifs becoming less wide. An exponential relationship was used to estimate the spring constant as a function of the length of the branches a (Equation 2.9, shown in black on Fig. 2.49B).

$$k = 8.04 \cdot exp(-0.273 \cdot a) \tag{2.9}$$

, where k is the spring constant.
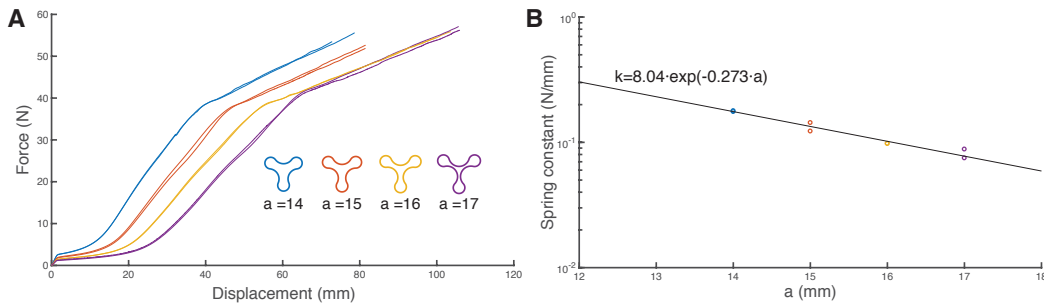
Figure 2.49 – **Effect of parameter a on the spring constant.** (**A**) Force displacement curves for PET sheets cut with Y-shaped motifs using various parameters a (2 samples per condition). (**B**) Effect of the parameter a on the spring constant of the structure (extracted from the linear region of plot A). The black line is an exponential fit.

Gradient implementation These observations were used to modify localy the spring constant of a patterned films in order to create a mechanical gradient. The gradient was implemented around the clamped location of a sheet by modifying the parameter a over 6 rows of Y shapes along the direction of the track (along the y-axis) and keeping the "softest" patterns in the center (Fig. 2.50A). Parameter a was changed such that the local strain changes linearly as a function of the row number. From Hooke's law (Equ. 2.10), this means that the inverse of the spring constant has to change linearly as a function of row number.

$$\Delta x = \frac{F}{k} \tag{2.10}$$

, where F is the applied force on a spring, and Δx is the displacement of the spring.

Figure 2.50B shows an example of implementation and details how the parameter a is changed along the sample (as a function of the row number). This should theoretically translate into a linear change of the local strain.
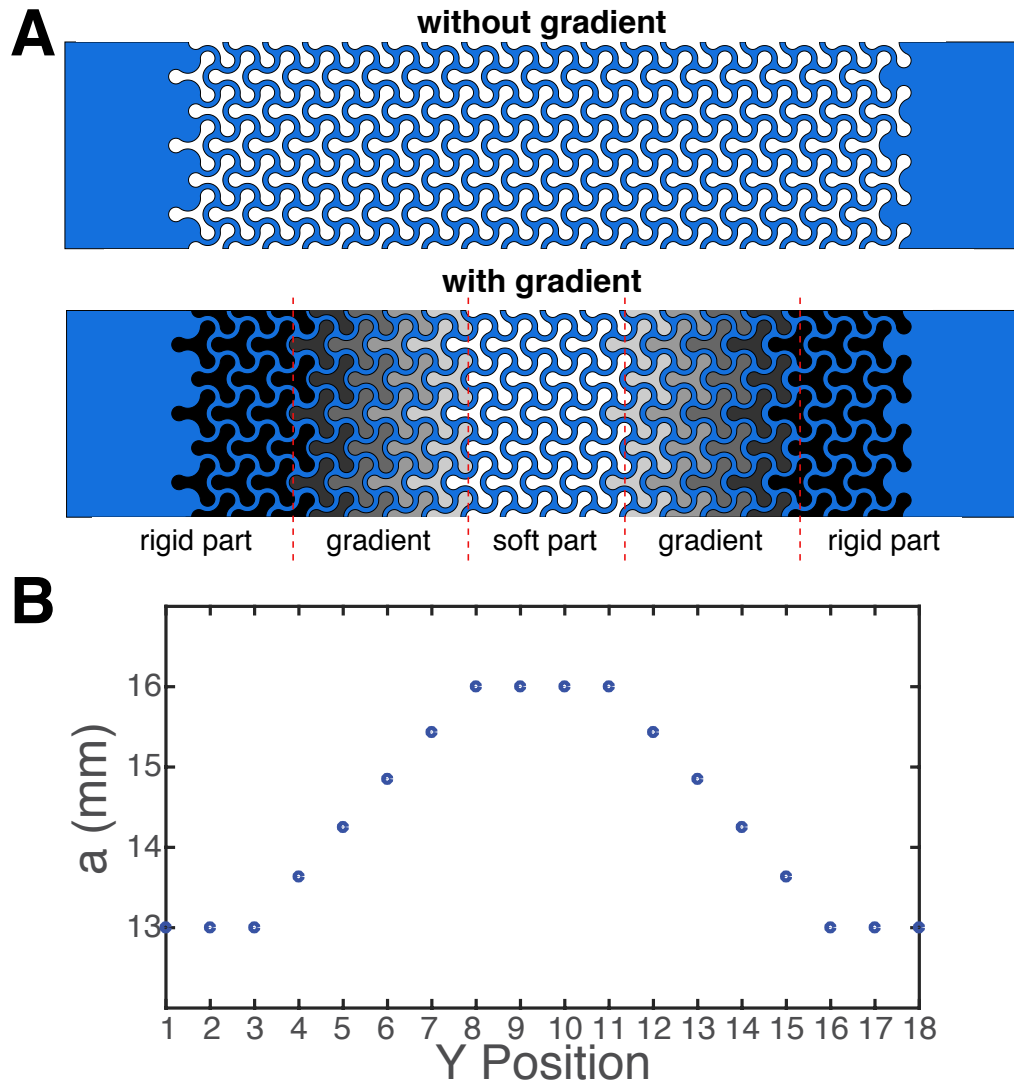
Figure 2.50 – **Concept of strain gradients with Y-shaped motifs.** (**A**) Illustration of a sheet patterned uniformly with Y-shapes compared to a sheet with a gradient of Y-shapes. The shades of grey inside the Y-shaped motifs correspond to changes in the geometrical parameter a. (**B**) Parameter a is changed according to the position of the Y-shaped motif along the sample length, for the sample with a gradient.

Local strain   These cuts were implemented into a PET sheet with printed black dots at each intersection of the tri-branched ligaments. The PET sheet was uni-axially stretched up to 20% and pictures were taken at 0% and 20% applied strain. The change in "local strain" was estimated by measuring the relative displacement of each black dot along the y-axis. The corresponding strain maps for a sample with and without a gradient structure are shown in Figures 2.51A and 2.51B respectively. The average strain at each row was calculated and compared for both conditions on Figure 2.51C. It can be observed, as expected, that structure with the gradient of Y-shaped motifs is much smoother than for the structure without any gradient. These results are in line with the the theoretical approach described above, as the branch length a was modified in order to obtain a linear gradient.
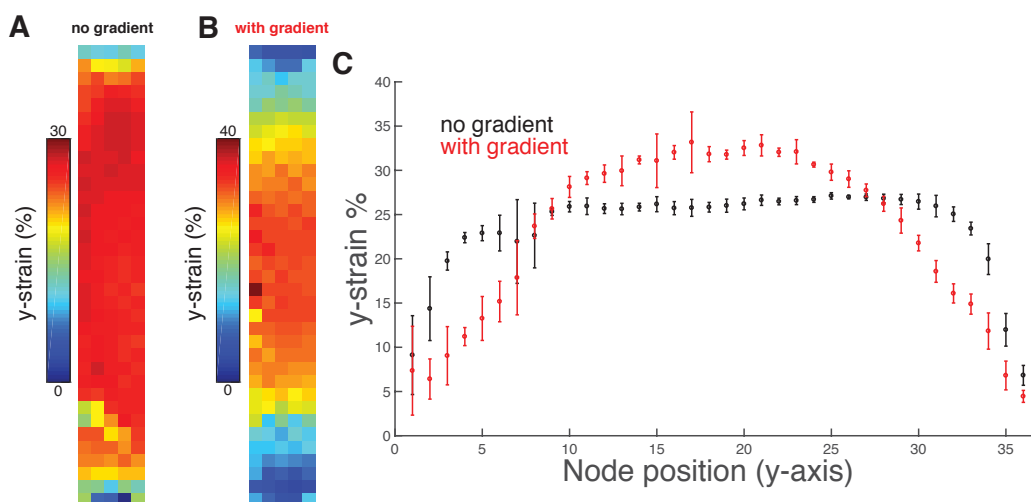
Figure 2.51 – **Strain maps comparison with and without gradients.** (**A**) Strain map (only y-component) for a structure without any gradient stretched with an applied strain of 20%.(**B**) Strain map (only y-component) for a structure without a gradient stretched with an applied strain of 20%. (**C**) Average "local" strain along the y-axis for each structure. The bars denote standard error of the mean.

It can be noticed that the "local" strain at the center of the structures are higher than the applied strains: for the gradient structure the plateau is around 33%, and for the "no gradient" structure the plateau is around 25% (Fig. 2.51C). This is because the test was performed under constant elongation. As the gradient structure is overall stiffer than the no gradient structure, the local strain at the center is higher. To avoid this issue in the future, the two samples should had been stretched at constant force. Moreover, the reason why the "local" strain at the center of the "no gradient" structure is larger than 20% is because the sample had locations without any Y-shaped motifs, meaning some parts were not stretching (see Fig. 2.48), thus the effective applied strain was higher.

2.6.4 Summary and discussion

Summary   This preliminary study shows the feasibility of using Y-shaped motifs with varying geometrical parameters to modify locally the mechanical properties of the overall structure. The study was performed macroscopically on structured PET sheets. The "local" strain was estimated discretely with dots at the nodes of the tri-branched structures. Results show that indeed it was possible to modify the "local" strain linearly along the structure by modifying accordingly parameter a of the Y-shapes along the direction of stretching.

Outlook   This study demonstrates the feasibility of integrating strain gradients, but various aspects still need to be studied and optimized more thoroughly. One of the variables that wasn't addressed for example is the length of the "gradient zone". Indeed, the longest this gradient zone, the smoother the transition, but the overall equivalent spring constant of the interconnect will be also higher, compared to a track patterned uniformly with the same Y-shaped motifs. Moreover, it is still unclear if implementing these gradients in encapsulated interconnects will actually impact the long-term reliability of devices using this technique, by reducing the strain peaks at the rigid-soft interface. A previous study used a similar concept by modifying the wavelength of a serpentine near the rigid components and showed that this improved the electromechanical reliability under long-term cycling [164].

Thus, future work for the approach presented here would be to implement these gradients zones near the connectors locations on micro-patterned interconnects encapsulated in silicone. The effect of the encapsulation on these strain gradients will also need to be investigated. Indeed, it is unclear if the mechanical properties of the encapsulation itself will dominate the mechanical properties of the interconnects micro-patterned with Y-shaped gradients. One way of testing these gradient structures on the micro-scale would be to fabricate samples of alternating tracks with and without gradients encapsulated in silicone, similarly to the ones in Section 2.5. These samples could then be stretched uni-axially for thousands of cycles while their electrical resistance is monitored. This will allow to observe if indeed these gradients improve the electromechanical reliability under fatigue. If this technique was proven to work, it could then highly benefit future neural implants, by opening up the possibility of integrating rigid components such as integrated circuits and improving their interface with the stretchable interconnect by using Y-shaped gradients.

2.7 Conclusion

This chapter described a technique to engineer reversible elasticity in interconnects made of multi-layers of metallic and plastic thin films (~2 μm thick) embedded in silicone (~100-150 μm thick). This was achieved by micro-patterning Y-shaped cuts into the multi-layered films. The patterning technique was inspired by stretchable micro-cracked gold films evaporated on silicone. Interestingly, the kirigami approach here was based on the optimization of the cuts shape, instead of the resulting interconnects. The design optimization of these Y-shaped cuts converged towards structures that resemble other well-known shapes in the field of stretchable electronics, such as serpentines and horse-shoe designs. As opposed to conventional meandres, the proposed micro-patterning technique yielded tracks with multi-axial stretchability, due to the radial symmetry of the pattern. Moreover, the scale of these structures were implemented on a smaller scale (one order of magnitude smaller) than the electrical layouts: the branches of the Y were ~15 μm, whereas typical tracks were around 150-200 μm wide. This allows for the design of electrical layouts independently of the strain-relief patterns.

An interesting aspect of this technique is that the electro-mechanical properties of these patterned interconnects can be easily modelled with electrical and mechanical FEA, as well as with large plastic films patterned with macroscopically sized Y-shaped motifs. This can allow for the rapid testing of various geometries without necessitating to go through complex and costly clean-room fabrication processes. Moreover, the wide variety of properties associated to each of these shapes can be used to locally tune the electro-mechanical properties of the interconnects. This was briefly shown in the context of implementing strain gradients near the rigid connectors attached to the interconnects.

Overall, this technology seems to successfully address most of the requirements that were described in the introduction of this thesis. Indeed, the development of stretchable interconnects is necessary for the development of future soft neural implants. From a dynamic perspective, these interconnects need to undergo mechanical strains during surgical implantation and once implanted in the body without electrical or mechanical failure. And from a static perspective, the mechanical properties of these devices need to be closer to the ones of the nervous system. One potential issue with this technology however is the equivalent "sheet" resistance, calculated to be around 15 Ω/sq, which might be a bit too large for certain devices that can only be addressed with implantable pulse generators with low (10-12 V) voltage compliance.

In the next chapters, this patterning technique will be used to fabricate stretchable interconnects encapsulated in silicone in the context of various neural implants for recording and stimulation. For all devices, the geometrical parameters of the Y-shaped motif that will be used are the ones that were found to be optimal in this chapter: a = 16 μm, r = 5.5 μm and L = 26 μm.

3 Application: Auditory Brainstem Implant

Outline This chapter presents an application for the micro-patterned stretchable interconnects in the context of a soft Auditory Brainstem Implant (ABI) to electrically stimulate the cochlear nucleus (CN). The chapter is organized in three sections:

- **Clinical background** Background information on ABIs in the clinic

- **Cadaveric study** Cadaveric study to demonstrate a proof of concept of a soft ABI

- **Mouse study** Functional chronic study of a soft miniaturized ABI in mice

Scientific contributions The contents of this chapter are in preparation for two manuscripts:

- **Nicolas Vachicouras**, Osama Tarabichi, Vivek V. Kanumuri, Christina M. Tringides, Yohann Thenaisie, Lorenz Epprecht, Jennifer Macron, Florian Fallegger, Valentina Paggi, Stephen McInturff, Ahad Qureshi, M. Christian Brown, Daniel J. Lee, Stéphanie P. Lacour, "Micro-patterned elastic film technology enables proof of concept of a soft auditory brainstem implant" (in preparation)

- Osama Tarabichi, Vivek V. Kanumuri, Julian Klug, **Nicolas Vachicouras**, Maria J. Duarte, Lorenz Epprecht, Elliott D. Kozin, Katherine Reinshagen, Stéphanie P. Lacour, M. Christian Brown, Daniel J. Lee. "Three-dimensional (3D) surface reconstruction of the human cochlear nucleus: Implications for auditory brainstem implant (ABI) design", (submitted)

3.1 Clinical background

3.1.1 Introduction

Data from the National Institutes of Deafness and Other Communication Disorder show that around 0.2-0.3 % of children in the United States are born deaf or hard-of-hearing. Current cochlear implants (CIs) provide auditory benefits to patients who suffer profound hearing loss, by electrically stimulating the cochlea. There is however a subset of deaf patients who cannot benefit from the CI. This can be due to a small or absent cochlea, a small or absent auditory nerve, tympanic ossification or injury, scarring of the inner ear, or damage to the auditory nerve due to meningitis, trauma, or tumors.

3.1.2 Contemporary ABI designs

To restore partial hearing and ideally speech perception in these patients, the Auditory Brainstem Implant was developed (ABI). The ABI is an electrical interface that bypasses the inner ear and the VIIIth nerve and stimulates the auditory brainstem on the surface of the coclear nucleus (Fig. 3.1).
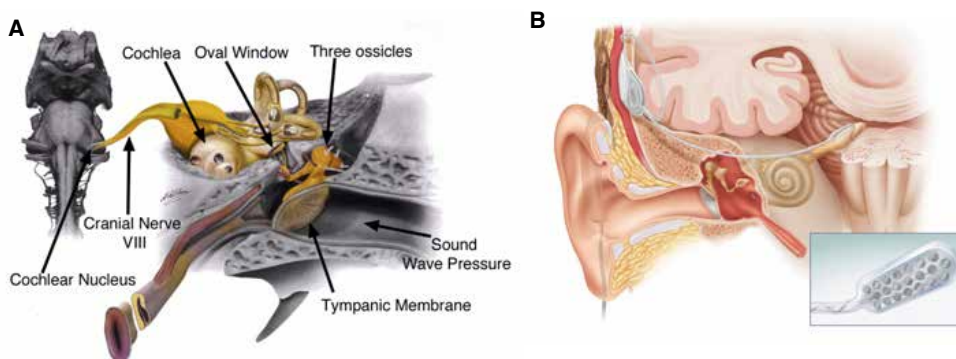
Figure 3.1 – **Anatomy of ABI location.** (**A**) Anatomical view of the hearing pathways highligthing the location of the cochlear nucleus (CN). (**B**) Cartoon showing the location of the ABI on the CN [165].

The first ABI was implanted in a human in 1979 at the House Ear Institute in California using a pair of ball electrodes [166]. The design of the ABI has evolved since then and currently all commercially available ABIs are shaped like a paddle with surface electrodes made of platinum disks (Fig. 3.2A). In the U.S, currently only the Nucleus 24 Auditory Brainstem Implant developed by Cochlear Ltd is FDA approved since 2000 for teenagers and adults suffering from Neurofibromatosis Type II (NF2) [167]. In Europe the MED'EL and Neurelec ABIs are also approved. The devices are quite similar to CIs in the sense that the microphone and processor (worn externally by the patient) as well as the internal receiver and stimulator are the same as for CI implants (Fig. 3.2B).
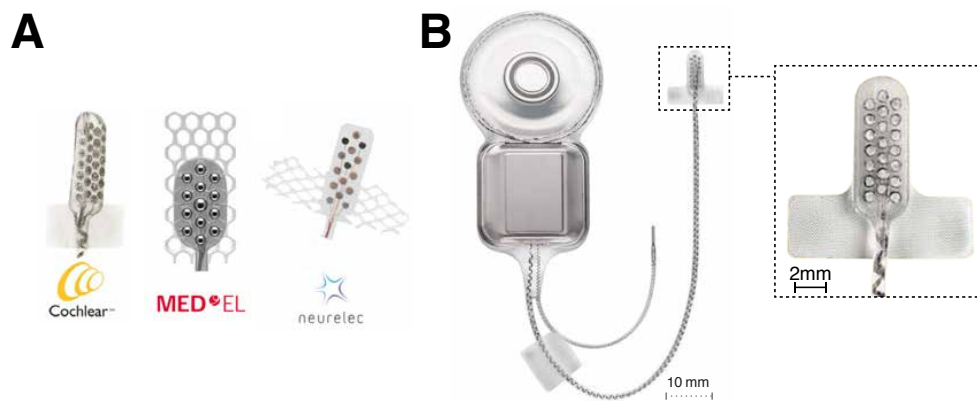
Figure 3.2 – **Commercially available ABIs.** (**A**) Commercially available ABI paddles worldwide: Cochlear Ltd., MED'EL and Neurelec (from left to right). Adapted from [168]. (**B**) Overview of a complete ABI system with the counter-electrode and receiver (from Cochlear Ltd) [24].

3.1.3 Neuroanatomy and neurophysiology

Cochlear nucleus anatomy   The target of the ABI is the cochlear nucleus (CN). The CN is situated on the dorso-lateral surface of the brainstem and is subdivided in three different anatomical structures: the Dorsal CN (DCN), the Posteroventral CN (PVCN) and the Anteroventral CN (AVCN). The CN is the first relay station for all ascending sound information coming from the cochlea through the auditory nerve fibers (AN fibers).

Interestingly, in all mammals with normal hearing, the terminations of the auditory nerve form an ordered spatial organisation [169]. Each auditory nerve encodes for a particular range of frequencies over the dynamic range. It is common to assign to each AN fiber a characteristic frequency (CF) which corresponds to the acoustic frequency which elicits a neural response at the lowest intensity. The spatial organization of the AN fibers and its relation to their CFs is called the tonotopy. This tonotopy is present in each part of the cochlear nucleus (DCN, PVCN and AVCN) and is a major neuroanatomical feature which is taken advantage of in ABIs (Fig. 3.3).

The DCN is of particular interest, because it is believed to be the primary target of the ABI. The DCN is composed of many different types of cells and it contains two kinds of output neurons: the fusiform cells (pyramidal cells) and the giant cells (which are larger in number). The primary target of these neurons is the contralateral inferior colliculus. The major issue with the DCN is that its cytoarchitecture is substantially different in humans compared to other animals. Moreover, the DCN has a substantial number of interneurons which don't project out, thus making it difficult to determine the precise role of the DCN in human hearing. In rodents, the DCN is also the most accessible subdivision for surface stimulation, thus making it an ideal anatomical target for electrical stimulation of the auditory brainstem. In humans, the DCN is quite large, compared to lower order mammals and it is believed that its primary role is the processing of acoustic information. Overall however, the function of the

DCN remains still unclear and it is partially due to its complex cytoarchitecture [170].
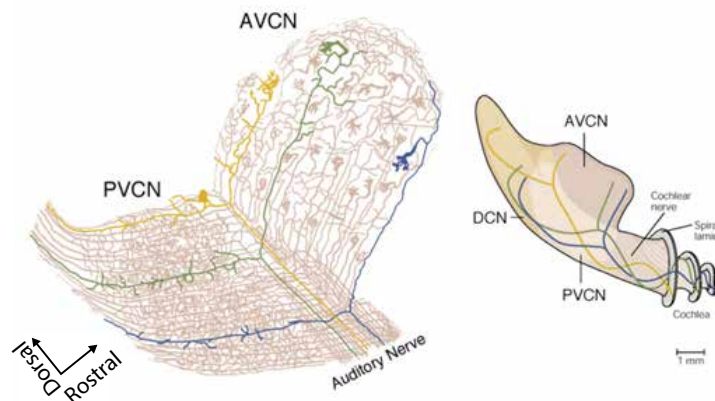
Figure 3.3 – **Cochlear nucleus anatomy.** Terminations of AN fibers in the CN and their tono-topic organization. Colors represent different characteristic frequencies. Adapted from [171].

The Inferior Colliculus   The CN has projections to different parts of the brainstem, including a large part within the Inferior Colliculus (IC). The IC is located in the midbrain and is composed of the central nucleus (ICCN) surrounded by a dorsal cortex and an external cortex located laterally. The ICCN also presents a tonotopy, where superficial neurons encode for lower acoustic frequencies and deeper neurons encode for higher acoustic frequencies.

Auditory Brainstem Responses   To observe the response of the auditory system to an external (electrical or acoustic) stimulus, a far field measurement of the evoked response is usually performed using surface electrodes placed on the ipsilateral ear and the vertex of the subject. These far field measurements arise when large groups of neurons simultaneously fire throughout the auditory pathway. The resulting recording is called the Auditory Brainstem Response (ABR). These ABRs are widely used clinically by audiologists, to verify that the peripheral auditory pathways are working properly in patients. In normal hearing mammals, the ABR presents five positive peaks as illustrated on Figure 3.4 which shows an acoustically evoked ABR (aABR) in a mouse. It has been established (in cat studies) that the first peak, PI, is generated by the auditory nerve (Spiral Ganglions), PII primarily by the VCN globular bushy cells, and PIII is generated by CN spherical cells and cells receiving inputs from globular cells [172–174]. PIV and PV are probably generated by higher level neural populations.

3.1.4   Indication

A large cohort of patients who cannot benefit from CIs suffer from a rare genetic disease called Type II Neurofibromatosis (NF2). Incidence of NF2 is approximately 1 in 40'000 [175]. These patients have tumors growing around their VIIIth nerve (benign vestibular schwannomas), which need to be removed during a surgical procedure. These tumors either cause damage to the nerve resulting in hearing loss, or deafness occurs after the invasive surgical procedure to remove this tumor, which often results in the destruction of the VIIIth nerve [175].
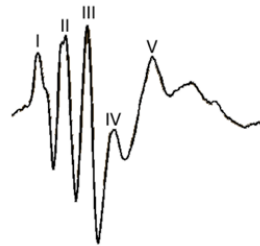
Figure 3.4 – **Auditory Brainstem Response.** Illustration of a typical five-peak ABR in a normal hearing mouse [172–174].

In 2005 in Italy, Dr. Colletti started implanting also pediatric patients as well as adults with other conditions than NF2, such as cochlear nerve aplasia, cochlear ossification, or congenitally deaf children [176–179]. Results in non-tumor patients showed significant auditory benefits compared to NF2 patients [176, 180–182]. It is believed that these differences might be due to the survival of some cell types in the CN [183]. However, in the U.S, for now only adult NF2 patients are allowed to be implanted with an ABI and the largest group of implanted patients (in 2007) is at the House Ear Institute and Clinic in Los Angeles, California [175]. Ongoing clinical trials in the U.S are assessing the use of ABIs for non-NF2 adult patients [184] as well as for pediatric patients [185].

3.1.5 Surgical approach

Usually the surgical procedure in NF2 patients is performed during the same procedure where the acoustic neuromas are removed. An incision is performed for translabyrinthine craniotomy and upon removal of the acoustic neuromas, the ABI is inserted into the lateral recess of the fourth ventricule overlying the surface of the CN (Fig. 3.5) [2]. The main issue with the surgery is that the CN itself is not directly accessible and the surgical procedure is performed blindly. Indeed, the human CN is approximately 3 mm wide along its dorsolateral and ventrolateral axis, and a large part of the VCN is located under the middle cerebellar peduncle which is inaccessible for implantation [175]. To validate the position of the ABI on the auditory brainstem, an audiologist stimulates the electrodes on the contour of the ABI in a bipolar configuration and records electrically evoked Auditory Brainstem Responses (eABRs) [186]. Side effects are also monitored during this step.

The implant is then turned on usually 2 to 4 weeks post implantation and an audiologist verifies which electrodes elicit non-auditory sensations such as dizziness, or tingling and turns them off. Moreover, the electrodes that evoke sound perception are ranked dependent on the relative sound pitch perceived by the patient. This pitch ranking information is then used in the internal programming of the ABI stimulator. These tests are performed repeatedly during the first months after implantation, as results might vary through time. Figure 3.6 summarizes the key steps in ABI patient management.
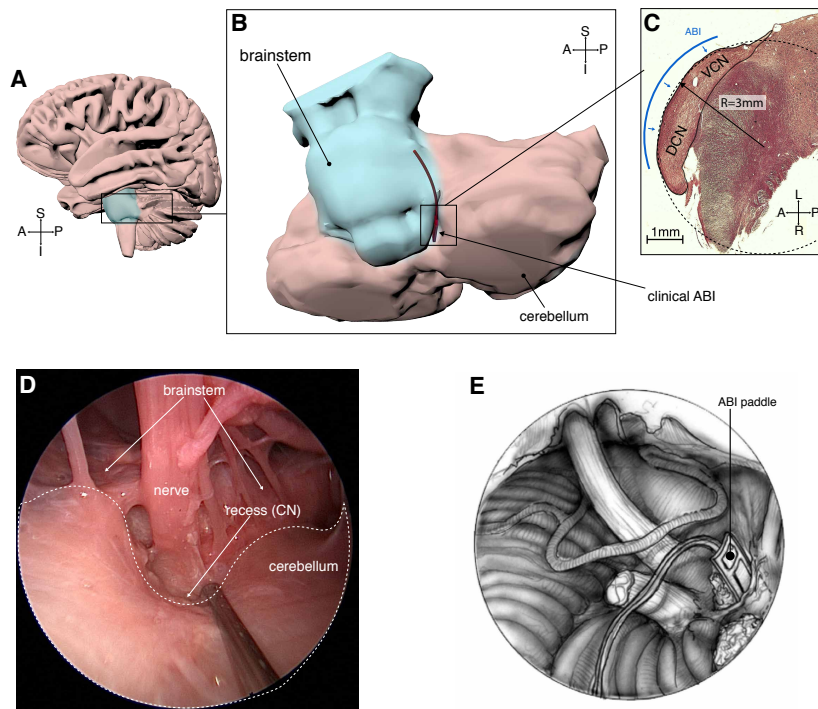
Figure 3.5 – **ABI surgical placement.** (**A**) 3D reconstruction of a human brain from a high-resolution MRI highligting in blue the brainstem [187]. (**B**) 3D reconstruction of the brainstem (blue) and the cerebellum (pink) showing the location of the clinical ABI paddle (red). (**C**) High resolution histological reconstruction of the human CN showing in blue the position of the ABI surface array. (**D**) Endoscopic view of the lateral recess of the fourth ventricle. (**E**) Cartoon showing the surgical placement of the ABI in the lateral recess of the fourth ventricle [2].
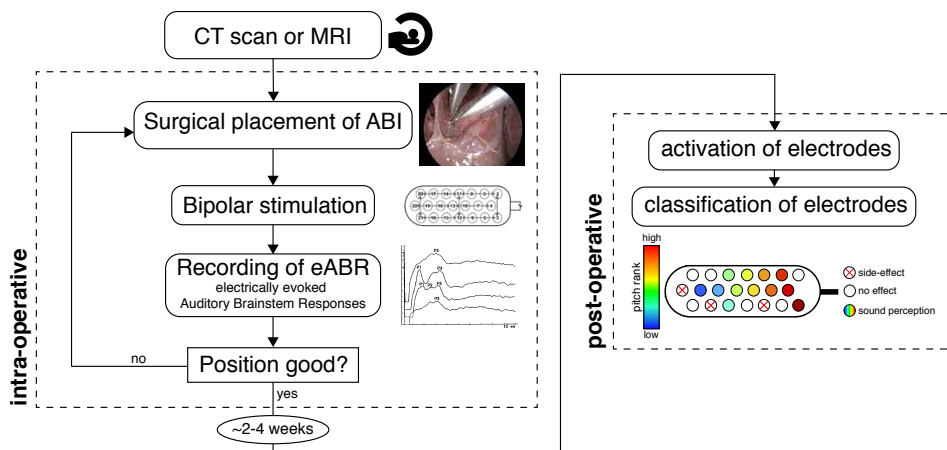
Figure 3.6 – **ABI patient management.** Summary of the key steps in ABI patient management. Insets adapted from [186].

3.1.6 Outcomes and issues

Since the first patient in 1979 [188], 1'500 patients have benefited from the ABI technology [175] and it was shown that the ABI procedure had little complications [183]. Unfortunately, very few ABI users achieve speech understanding without lip reading. The majority of patients only perceive general sound cues that complement lip reading [2, 168]. In contrast, most CI users have some degree of open set speech comprehension. Moreover, compared to CIs, it was shown that stimulation thresholds were in general higher with ABIs [189] and more importantly, there seems to be a very wide range of outcomes in ABI patients in terms of speech perception [2, 186] (Fig. 3.7A). Pediatric patients under the age of 2 seem to benefit the most from ABIs thanks to brain plasticity, whereas older children are unlikely to develop sufficient language skills. In general, pediatric users achieve sound detection, even though language development and auditory performance are often delayed or incomplete. More generally, most clinics report that outcomes of pediatric ABI patients are lower than children with CIs [190].

Moreover, many electrodes have to be turned off as they generate side-effects. Typically, these side effects were observed on the ipsilateral side of the implanted ear and comprised of transitory dizziness or tingling sensations in the leg, arm and throat of patients [180] (Fig. 3.7B). This is believed to be due to current spread or to electrodes positioned on non-auditory structures, thus stimulating other brain regions. In pediatric patients, electrode migration was also one of the main causes of complications necessitating revisions. Indeed, dislocation of the array out of the recess can typically be caused by the stiff electrode lead or torque of the electrode during growth [190].

Indeed, Barber et al. looked at CT (Computed Tomography) scans of ABI adult and pediatric patients and observed that the position of the ABI with respect to the CN was extremely variable and usually correlated with speech perception outcomes as well as with the ratio of electrodes eliciting side-effects and auditory sensations (Fig. 3.7C). This study also highlighted the existence of "sweet spots" on the array, that corresponds to neighbouring electrodes having lower activation thresholds than surrounding ones (shown with red circles on Fig. 3.7C) [191] . This observation supports the hypothesis that current clinical ABIs are in close contact with the CN only in a small area, due to their rigidity. It has also been argued that the anatomy of the CN in NF2 patients is also distorted because of the effect of the tumors, which could partly explain poor results [180].
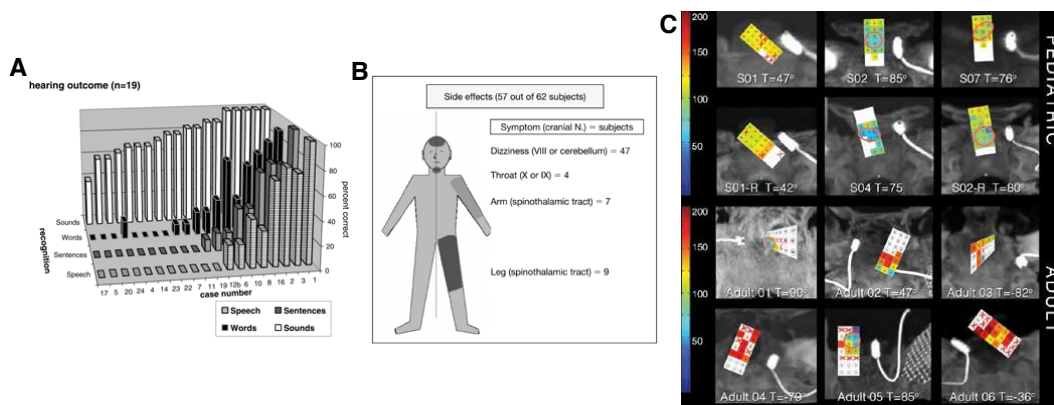
Figure 3.7 – **Issues with ABI patients.** (**A**) Audiologic outcomes of ABI patients [186]. The x-axis represents the number of the patient. The y-axis is the type of test used (sound, word, sentence and speech recognition). The z-axis shows the percentage of correct answers. (**B**) Location and incidence of non-auditory side effects after ABI activation [180]. (**C**) CT scan posterior views of pediatric (top) and adults (bottom) ABI patients. Perceptual thresholds are coded according to the left scale for electrodes that evoked sound sensations. Electrodes with a red cross elicited side-effects. Electrodes in white didn't have any effect. The red circles indicate the sweet spot (low threshold electrodes) [191].

There is therefore still room for improvement to restore better speech comprehension in deaf patients using ABIs. The findings described above highlight the importance of ABI position with respect to its anatomical target and how it influences outcomes (speech perception and side effects).

Moreover, it is still unclear which cells and auditory pathways are really stimulated. In particular the tonotopical gradient of the CN might not be present in persons without an auditory nerve [175]. This poses intrinsic difficulties in trying to understand how the ABI works. Thus it was suggested that more fundamental research of the CN should be conducted to better understand how the ABI works [192].

One proposed way of improving the ABI is by changing the hardware of the microelectrode array itself. The House group suggested making a penetrating ABI (PABI), which would better access the tonotopical gradient by stimulating at different depths. Also a penetrating ABI could allow to access the PVCN through the surface of the DCN. These PABIs were first tested in cats and were used in a FDA approved human clinical trial [170, 193]. Even though the PABI showed lower threshold, increased pitch range, and high selectivity, improvements in speech recognition were not observed [194]. This approach has since then been abandoned.

3.2 Cadaveric study of a soft ABI

3.2.1 Introduction

Outcomes of ABIs in the clinic discussed in the previous section showed that a proper positioning of the ABI on the CN is critical to get better outcomes in terms of speech perception. In particular, it would allow for a larger number of electrodes to elicit auditory sensations instead of eliciting side-effect or no effects at all, that are thought to be because of poor contact between the electrodes and the CN.

Here, it is proposed to fabricate an ABI that is much softer than the current stiff ABI paddle, and which can conform to the curvature of the CN and could possibly remain in place post-operatively thanks to its flexibility. Moreover, such a soft ABI could also improve the biomechanical matching of the implant to the tissue as described in Chapter 1. The proposed soft ABI is made using micro-patterned PI/Pt/PI interconnects with Y-shaped motifs, embedded into a soft silicone matrix. The coating of the electrode is made of the soft stretchable Pt/PDMS composite described in Chapter 2 (Fig. 3.8A).

Such a soft ABI could then better conform to the curvature of the CN and could potentially improve speech perception in humans. This is illustrated in Figure 3.8B which sows how a soft ABI conforms perfectly to the curvature of a model of the CN (made of an agarose gel molded using a high resolution MRI of a human brainstem) compared to a rigid ABI for which half of the electrodes are not in contact.

In this study, a soft ABI was designed using 3D reconstructions from histological and MRI data of human CN, and was tested for ease of surgical implantation on the CN in human cadaveric specimens. The electrochemical properties of the soft ABI were also compared to a clinical ABI in vitro and while implanted on the auditory brainstem of the cadaver. Finally, the compatibility of the soft ABIs with clinical imaging techniques was also assessed.
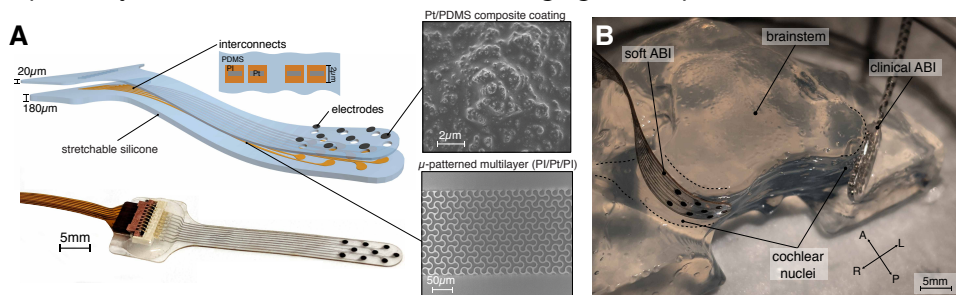
Figure 3.8 – **Soft ABI conforms better to the surface of the CN than a clinical ABI.** (**A**) Schematic representation and picture of the soft ABI: micro-patterned multilayers of polyimide and platinum (bottom inset) form the interconnects which are encapsulated between two layers of stretchable silicone. The electrodes sites are coated with a Pt-PDMS composite to decrease their impedance (top inset). (**B**) Picture showing the soft ABI conforming and the rigid clinical array not conforming to the curved surfaces of the right and left model DCNs, respectively. The agarose gel model is based on a 3D MRI reconstruction of the human brainstem. A: anterior, P: posterior, L: lateral, M: medial

3.2.2 Methods

Device manufacturing The device was manufactured using the methods presented in Chapter 2. The dimensions of the electrodes array were kept the same as the Cochlear clinical ABI (3.5x8 mm^2). The total length of the device (from the tip of the array to the connector) was 30 mm. In order to keep the same electrode diameter ($\varnothing = 700$ μm) for direct comparison, the soft ABI array had only 9 electrodes (vs. 21 for the clinical device). The connector was made of a surface mounted ZIF-connector (FH33-9S-0.5SH, Hirose Electric Co Ltd), which was connected to a custom made flex-PCB (Printed Circuit Board) break-out board.
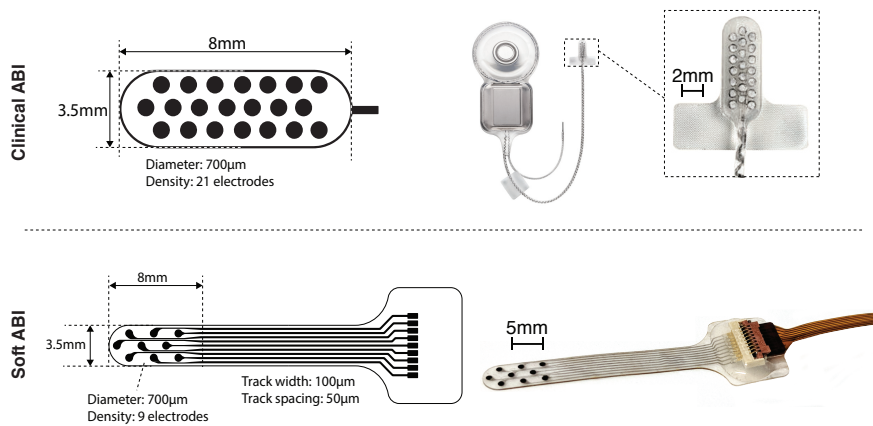
Figure 3.9 – **Comparison of soft ABI design with clinical ABI.** Dimensions of the clinical ABI (from Cochlear Ltd.) and the soft ABI are shown in the top and bottom of the figure, respectively.

Cadaveric surgical approach Fresh human cadaveric specimens (head only) were obtained from the Anatomy Gifts Registry (Maryland, USA) and thawed to room temperature (21° C) prior to experimentation. All surgical manipulation was performed at the Joseph Nadol Otolaryngology surgical training laboratory at the Massachusetts Eye and Ear Infirmary by trained otolaryngology surgical staff (including resident, fellow, and attending surgeons). First, a retro-auricular incision was made posterior to the right ear and the soft tissue was dissected to reveal the mastoid bone. Under binocular microscopy, a standard translabyrinthine craniotomy approach was then performed to enable identification of the ABI implantation site at the cerebellopontine angle of the brainstem, specifically in the lateral recess over the dorsal cochlear nucleus. All images and videos were recorded using standard HD cameras (Karl Storz, Germany) coupled to operative microscopes (Olympus, Japan) or Ear 0°/30°/70° endoscopes (Karl Storz, Germany).

Agarose models Agarose gel models (made of one part) used throughout the study were obtained by dissolving agar powder (3% w/w, Agar Agar Patissier) in boiling DI water for 1 min; the solution was then shaped in custom-made silicone molds and kept in the fridge for about an hour before demolding. Agarose models requiring the gluing of multiple parts (such as for the recess model) were made with a slightly different protocol detailed in Appendix A.5.

Voltage Transients   Voltage transients (VTs) were measured using an oscilloscope (Tektronix, MDO3014) connected to a titanium counter electrode and the working electrode. Measurements were performed in PBS 1X, while stimulating in parallel with an external current source (Isolated Pulse Stimulator Model 2100, AM Systems) with symmetrical biphasic pulses of 1 mA in amplitude, 300 µs in pulse width, at a frequency of 100 Hz. The double layer voltage was extracted from VTs by removing the resistive drop, as described in previous studies [195, 196].

Electrochemistry   In vitro electrochemical impedance spectroscopy (EIS) and cyclic voltammetry (CV) were measured using a 3-electrode setup in phosphate buffered saline (PBS 1X), with an Ag/AgCl reference electrode, and a platinum counter-electrode. EIS and CV tests were performed using a potentiostat (Gamry Instruments, REF 600). EIS was performed from 1 MHz to 1 Hz, with a voltage amplitude of 100 mV. CV was performed from -0.6 V to +0.8 V at a speed of 100 mV/s. In vivo EIS was performed on a two-electrode setup, using a subcutaneous wire as the counter electrode, with a potentiostat (PalmSens3, PalmSens BV) from 50 kHz to 1 Hz, with a voltage amplitude of 100mV.

Hydrosoluble guide   The hydrosoluble guide was made of poly(vinyl alcohol) (PVA) (KU-RARAY POVAL ®8-88). It was prepared by dissolution of 12 wt% of PVA in deionized water at 90°C under stirring for 2 hours. After complete dissolution of the powder, the solution was poured in a silicone mold on a hot plate, settled at 40°C for 24 hours in order to slowly evaporate the water and to obtain a homogeneous dry layer of PVA. This step was repeated once to reach the targeted guide thickness of 1 mm. The dry PVA layer was then cut with a razor blade to the final dimensions of the guide (l = 6 mm; w = 1 mm; h = 1 mm). To immobilize the rigid backing on the soft ABI, the procedure described in Wu et al. was used [197]. First the silicone surface was plasma activated. A droplet of the 12 wt% PVA solution was then put on the activated surface of the soft ABI and the rigid PVA spine was properly placed on the liquid film to ensure a complete wetting of the guide. The assembly was left to incubate for 5 minutes at room temperature before finalizing the immobilization process of the hydrosoluble guide at 110°C on a hot plate for 15 min.

MRI sequences of human brain   Ultrahigh resolution 7.0 Tesla MRI sequences were obtained from Lusebrink et al [187]. The resulting voxels with isotropic resolution of 250 µm were 64 times smaller than the standard clinical resolution of 1 mm and required 8 hours of scan time.

Histology of human CN   This study was approved by the institution's Human Studies Committee (# 1447618, exempt). Post-mortem human brainstem sections of the left CN from three healthy adult patients were used for histological reconstructions. Axial brainstem sections 10-20 µm in thickness were alternatively stained with protargol, cresyl violet Nissl stain or hematoxylin.

DCN curvature estimation from histological specimens   The CN was identified using light microscopy and its borders were manually traced in each relevant section. Laterality selection (left vs. right) was based on overall ease of CN identification and quality of preservation in sections. Sections were aligned using vessels, histologic artifacts, and other features that remained consistent between sections. The DCN trace was isolated and imported into MATLAB (Mathworks, MA, USA) for further curvature analysis. The trace of the DCN from histological reconstructions was fitted with a circle using a previously proposed method for circle fitting of a cloud of points in a 2D plane [198].

MRI of ABI   A T2 weighted scan was performed on a clinical MRI device with 3.0 Tesla field strength on the clinical and the soft ABI while implanted inside the cadaveric specimen. This sequence is regularly used in clinical evaluations. The following protocol were used: TE 80 ms, TR 3000 ms, FOV 26.5 x 16 cm^2, slice thickness/spacing: 2 mm.

Computed Tomography (CT) scans of ABI   Non-contrast computed tomography imaging was performed on Discovery CT 750HD (General Electric, USA) CT scanners. Images were obtained using 2 mm slices, 120 kVP, and 240 mA.

3.2.3 Results

CN curvature The ability of the soft ABI to conform to the curvature of the CN was first assessed. This was done by estimating the radius of curvature of the CN using histological reconstructions, in order to define the target thickness of the soft ABI. The CN was successfully extracted from human brain histological slices (three different specimens) as shown in Fig. 3.10A. The contours of the DCN surface were extracted manually for each histological slice of each brainstem specimen (about 10-20 slices for each specimen). Fig. 3.10B shows examples of DCN surfaces extracted from all histological slices of one specimen. The average radius of curvature of the DCN across the three specimens and across all histological slices was in average 2.85 ± 0.5 mm (Fig. 3.10C).
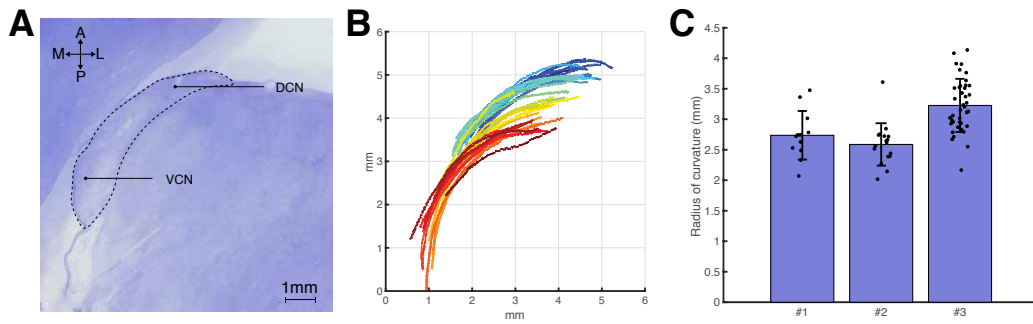
Figure 3.10 – **Curvature measurements of the DCN surface from histological specimens.** (**A**) Representative histological section of a human brainstem. (**B**) Traces of the dorsal cochlear nucleus (DCN) extracted from histological sections. (**C**) Radius of curvature for three different histological specimens and for various histological slices. Error bars denote standard deviation.

It is important to note that the average radius calculated here is probably underestimated, as histological slices tend to shrink the anatomical structures because the tissues are dry and don't contain any more CSF. The use of high resolution MRI reconstructions, such as the ones obtained by Lusebrink et al. [187], could allow a better estimate of the CN curvature.

Definition of the soft ABI thickness Based on the calculations of curvature above, the radius of curvature of the CN was defined at 2.85 mm, knowing that this was a very conservative value. Thus, the maximum thickness for a sheet of PDMS to conform by capilarity to a cylinder of 2.85 mm in radius was defined using the results from Section 2.5.2 (Fig. 2.47). Equation 3.1, from Py et al., was therefore applied to a cylinder of radius 2.85 mm, with the surface tension of CSF at 22°C ($\gamma = 61.55$ mJ/m^2, [199]) and to a substrate of PDMS (E = 1 MPa and $\nu = 0.49$) [64].

$$t_{max} = \sqrt[3]{\frac{R^2 \cdot 24 \left(1 - \nu^2\right) \gamma}{E}} \approx 210 \mu m \tag{3.1}$$

The calculated theoretical maximum thickness for the ABI can therefore be 210 μm. It was therefore decided to fabricate the soft ABI with an approximate total target thickness of 200 μm, knowing that in reality the radius of curvature of the DCN was larger, due to it being soaked in CSF. The soft ABI that was fabricated in this study comprised of 9 electrodes of similar size as the clinical ABI, for direct comparison.

To confirm the target thickness, an agarose model of the brainstem and cerebellum incorporating the IVth ventricule (reconstructed from human MRI data) was fabricated. The clinical ABI and the soft ABI were both inserted into the lateral recess of the left and right CN, respectively. The soft ABI conformed perfectly to the curvature, whereas the clinical ABI was too stiff and some of the electrodes were not in contact with the agarose model (Fig. 3.11).

It is important to note that the agarose model from Figure 3.11 is not a completely realistic model. Indeed, in reality the cerebellum is in much closer contact to the brainstem, and the tissues are quite soft and surrounded by CSF. However, this picture illustrates quite well the overall concept of a conformable ABI, even though it doesn't depict reality perfectly.
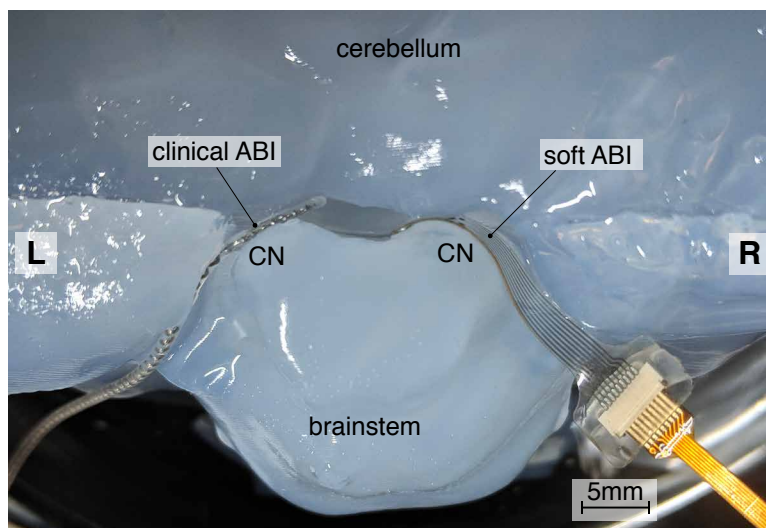
Figure 3.11 – **Clinical and soft ABI in an agarose model of the lateral recess of the IVth ventricule.** The clinical (left) and soft (right) ABIs are inserted into the left and right lateral recess on the surface of the CN.

In vitro electrochemical characterization   The electrochemical properties of the finalized soft ABI device were first chacaterized by EIS (Electrochemical Impedance Spectroscopy) in PBS (Phosphate buffered saline). The impedance at 1 kHz was in average 5.8 kΩ (Fig. 3.12A). Moreover, the electrodes were stimulated with symmetrical biphasic pulses at 1 mA while the voltage drop at the electrochemical interface and along the track was recorded. These voltage transients (VT) showed that the voltage at the interface was kept below 0.3 V, at a stimulation amplitude of 1 mA (Fig. 3.12B). The current range for the clinical ABI is typically between 0 to 1.75 mA [200].
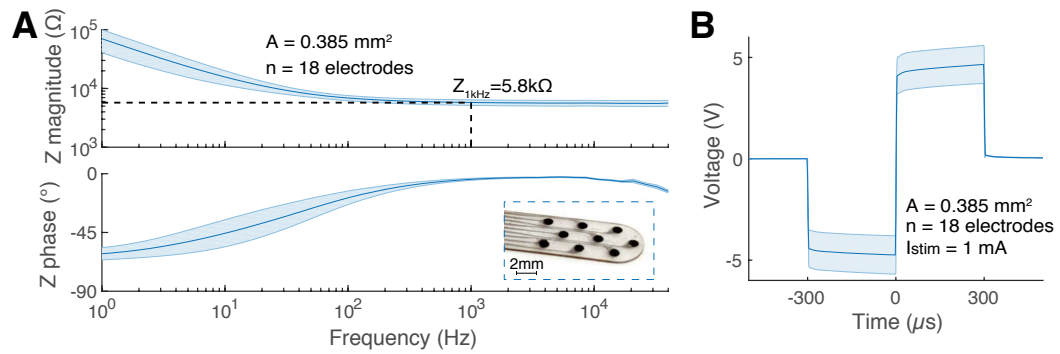
Figure 3.12 – **In vitro electrochemical characterization of the soft ABI.** (**A**) Electrical impedance magnitude (top) and phase (bottom) of the soft ABI electrodes measured in PBS as a function of frequency. (**B**) Voltage measured on the soft ABI upon stimulation in PBS with a 1 mA biphasic current pulse (300 µs in width) at 100 Hz. Shaded areas denote standard deviation. n = 2 samples, with 9 electrodes per device.

Based on the electromechanical characterization of the interconnects from Chapter 2, the DC resistance of the track alone was expected to be around 4 kΩ: indeed the sheet resistance of the micro-patterned interconnects is around R_s = 15-20 Ω/sq., and the aspect ratio of the tracks is in average L/w = 23 mm / 100 µm = 230. Thus the track resistance should be $R = R_s \frac{L}{w} \approx 4k\Omega$. The in vitro impedance measurement also takes into account the spreading resistance in the bulk of the PBS (resistivity of $\rho \approx 0.6\Omega m$). This series resistance can be approximated by $R_{bulk} = \frac{\rho}{4r} \approx 400\Omega$. Finally, the electrode-tissue interface impedance depends on the electrochemical properties of the coating. Thanks to its increased rough surface and thus large electrochemical surface, the composite coating impacts minimally the impedance at high frequency (the cut-off frequency in the EIS spectrum is around 100 Hz). Theoretically, the impedance at 1 kHz should be mostly resistive (as indicated by the impedance phase close to 0) and should account for only the resistive components described above (track resistance and bulk resistance) which should add up to 4.4 kΩ. The measured difference of 1.5 kΩ can be due to the fact that some tracks have a narrower width at some locations, as well as resistive components that arise from the interface between the composite coating and the electrode, as well as between the electrode pads and the connector. Moreover, the EIS data seem to indicate that the electrode-tissue interface impedance is very small, thanks to the high electrochemical surface area of the composite and the relatively large diameter of the electrode. These observations are consistent with the voltage transients that show that most of the voltage drop is resistive.

Surgical implantation in a cadaver   The ease of insertion of the soft ABI in the lateral recess of the IVth ventricule was then assessed in two cadaveric specimens. A retrosigmoid approach was peformed to expose the lateral recess. First, a clinical ABI was implanted into the recess and then the soft ABI was also successfully inserted into the recess. Figure 3.13 shows endoscopic views of both implants in the lateral recess.
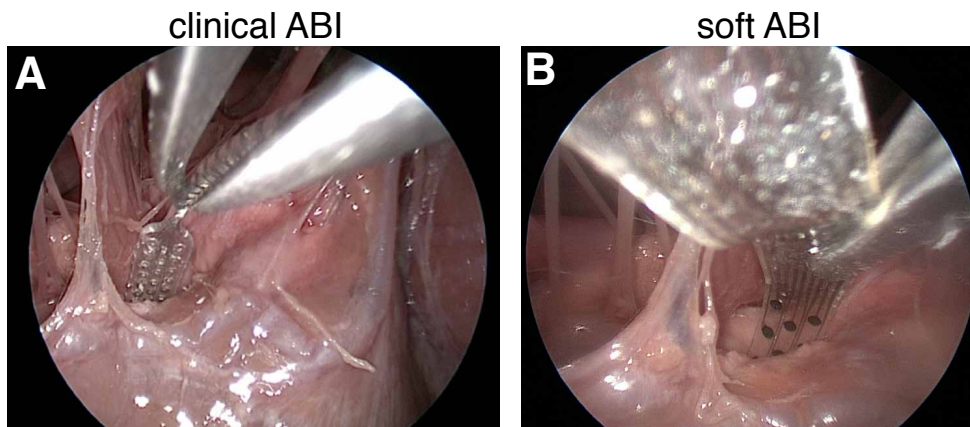
Figure 3.13 – **Endoscopic view of the implanted clinical and soft ABI.** Endoscopic view of a clinical ABI (**A**) and soft ABI (**B**) inserted in the lateral recess of the IVth ventricle in a human cadaver.

Clearly, the stiff clinical ABI was easier to handle and insert in the lateral recess. The soft ABI was a bit harder to push inside the recess with tweezers because of its softness, but eventually the surgeon was able to insert the device in the recess. These initial experiments highlighted the need to fabricate a guide for both devices, that can be used to manipulate the array more distally, instead of grabbing them from a more proximal location, to avoid pinching the electrode sites with the tweezers. These are very important aspects to consider for ABI surgery, as the anatomical target is in a blind spot and the surgical procedure requires multiple manipulations until appropriate positioning is reached. Also it is important to keep in mind that the anatomy of the cadaver doesn't mimic the actual environment in an alive patient. Indeed, the spaces between the neural structures are exaggeratedly larger in the cadaveric specimen, and a cadaveric model lacks the pulsation of tissues due to CSF, respiration and blood flow, which will complicate the insertion. Thus, a surgical approach in a cadaveric specimen is a good way to perform a preliminary assessment of the surgical procedure, but it is important to keep in mind the limitations and differences that will arise during a surgery in an alive patient.

Impedance spectroscopy   EIS was performed on both ABIs in vitro before surgical insertion. The in vitro impedance at 1 kHz was 5.78 ± 0.62 kΩ (n=18) for the soft ABI and 2.11 ± 0.07 kΩ (n=9) for the clinical ABI (Fig. 3.14(A-B)). This difference was expected, as the resistance of the electrical tracks in the soft ABI is much larger than the resistance of the wires used in the clinical ABI, due to the use of patterned thin films.

In vitro EIS was performed again after explantation of the arrays. The in vitro impedance of the soft explanted ABI was 6.21 ± 0.75 kΩ, and 2.07 ± 0.22 kΩ for the clinical ABI (Fig. 3.14A-B). These results indicate that there was minimal damage to the electrodes during surgical implantation for both arrays.

EIS was also performed inside the cadavers. An increase of the impedance at 1 kHz compared to in vitro was observed for both arrays once implanted in the cadaver (average change in resistance for the clinical ABI: $\Delta R = 4.71$ kΩ, and for the soft ABI: $\Delta R = 4.97$ kΩ). This change can be explained by a simplified electrical model of the brain-electrode interface (Fig. 3.14C), where R_{track} is the track resistance of the device, C_i and R_{ct} are the electrode capacitance and resistance modelling charge transfer mechanisms at the interface, and R_{bulk} is the bulk resistance to the current spreading through the medium [201]. Here, in a first approximation, the change in medium should mostly affect R_{bulk}, which depends only on the electrode shape and resistivity of the medium (ρ). For a circular electrode of radius r, $R_{bulk} = \frac{\rho}{4 \cdot r}$ [202].

Because the electrode radius is the same for both devices, this change in resistance is expected to be due only to the increase in resistivity between the in vitro medium (PBS 1X $\rho = 0.6$ Ω·m) and the cadaveric specimen (approximated with resistivity values extracted from explanted human gray matter $\rho = 7.84$ Ω·m). A theoretical calculation of R_{bulk} using the values above, predict a change in resistance of $\Delta R = 5.17$ kΩ for both arrays, which is consistent with the values observed.
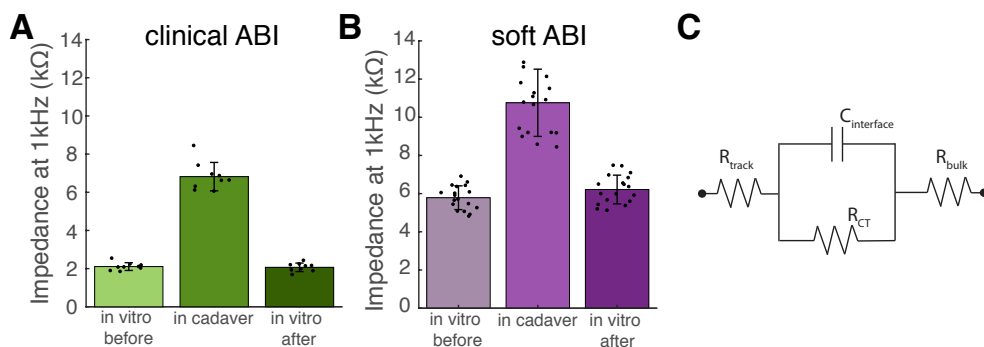
Figure 3.14 – **Impedance spectroscopy comparison of the clinical and soft ABIs.** (**A**) Electrochemical impedance spectroscopy of the clinical ABI in vitro before insertion, in the cadaver and in vitro after insertion (n=9). (**B**) Same for the soft ABI (n=18). (**C**) Simplified equivalent electrical circuit of the electrode-tissue interface. Bars denote standard deviation.

Voltage transients   As expected, the EIS measurements above highlighted that the main differences between the clinical and soft ABIs from an impedance perspective is the increase in track resistance for the soft ABI. However, these results provided little information on differences in the impedance at the electrode-tissue interface. Voltage Transients (VTs) were thus measured upon stimulation at 1 mA in vitro for each ABI. Each VT had a characteristic shape with an initial resistive drop followed by capacitive charging, corresponding to the double layer voltage (Figure 3.15A). In light of the impedance measurements, the resistive drop was expected to be larger for the soft ABI. However, extracting the double layer voltage from the VTs, revealed that it was 0.80 ± 0.22 V (n=18) for the clinical ABI and 0.32 ± 0.05 V (n=9) for the soft ABI (Figure 3.15B). The inset in Figure 3.15B shows representative examples of extracted double layer voltages for both ABIs. These data indicate that the electrodes of the soft ABI have a larger electrochemical area, even though the geometrical surface area of the electrodes in both arrays is the same. These outcomes are not surprising, as the composite coating used on the soft ABI electrodes has an extremely rough surface. Overall, these results indicate that the interfacial impedance of the soft ABI is lower than the clinical array, thanks to its coating, meaning that for a given stimulation current, the voltage at the electrode-tissue interface will be lower, resulting in lower risk of side-electrochemical reactions that might damage the electrodes or the tissue. Conversely, this also means that the soft ABI can stimulate with higher currents before reaching the water window limits, which are defined as the voltages below and above which water oxidation and reduction (water electrolysis) take place (usually around -0.6 and +0.8 V for platinum electrodes).
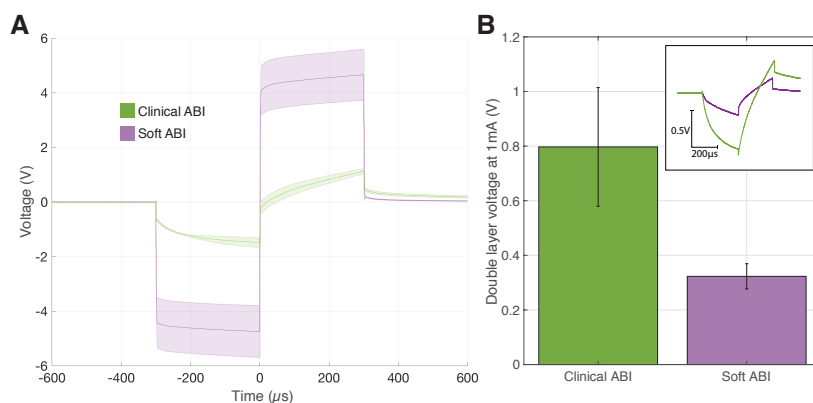
Figure 3.15 – **Voltage transients comparison of the clinical and soft ABIs.** (**A**) Voltage Transients (VT) measured at 1 mA. (**B**) Voltage at the double layer extract from the VTs (representative examples in the inset) for the soft (purple) and clinical (green) ABIs. Shaded areas and bars denote standard deviation (soft ABI n=18, clinical ABI n=9).

Cyclic voltammetry   Cyclic voltammetry (CV) was also performed on each array in vitro within the water window limits of -0.6 and +0.8 V (Fig. 3.16A). The Charge Storage Capacity (CSC) was extracted by integrating the cathodic area of the voltammogram. The average CSC of the soft ABI (21.23 ± 4.19 mC/cm^2, n = 5) was 13 times larger than that of the

clinical ABI (1.60 ± 0.37 mC/cm^2, n $= 5$) (Fig. 3.16B). These results confirm the previous observations of the VTs and show that the electrochemical surface area of the soft ABI electrodes are superior than the clinical ABI.
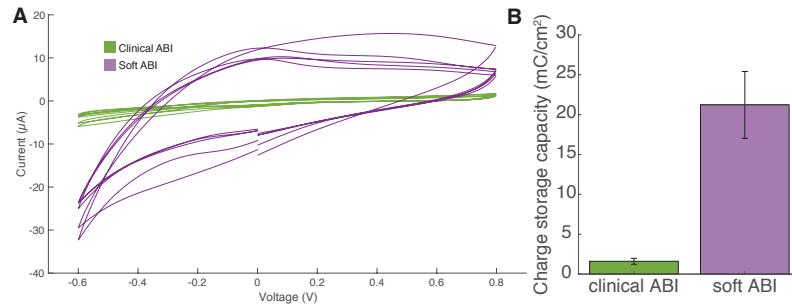
Figure 3.16 – **Cyclic voltammetry comparison of the clinical and soft ABIs.** (**A**) Cyclic voltammograms measured at 0.1 V/s for both ABIs. (**B**) Charge storage capacity for the soft and clinical ABIs. Error bars denote standard deviation (soft ABI n=5, clinical ABI n=5).

Compatibility with imaging techniques   Next, the compatibility of the clinical and soft ABIs with conventional clinical imaging techniques was assessed. First, Magnetic Resonance Imaging (MRI) at 3T was performed on the same cadaveric head specimen implanted once with the clinical ABI and once with the soft ABI. The MRI revealed an artefact in the brainstem around the clinical ABI (Fig. 3.17 left), while the soft ABI didn't create any artefact but was not visible on the scan (Fig. 3.17 right). Endoscopic visualization of the ABI post MRI confirmed that both arrays hadn't migrated during imaging (shown in the insets in Fig. 3.17).
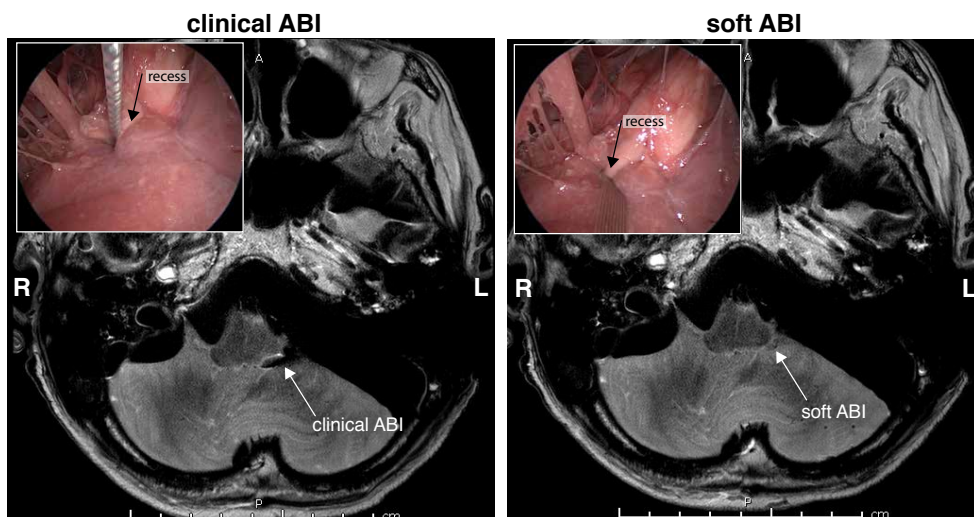
Figure 3.17 – **MRI comparison of the clinical and soft ABI.** MRI in a cadaveric specimen of a clinical (left) and a soft (right) ABI. The insets show post-MRI endoscopic views of the ABIs in the lateral recess to confirm that the devices didn't migrate during imaging.

These results are not surprising as the quantity of metal that a clinical ABI contains is much higher than the thin metal films used in the soft ABI. Even though the absence of MRI artefact is an advantage for the soft ABI technology, it was also pointed out that the soft ABI was not at all visible. Thus the development of soft ABIs would require some kind of marker to locate the ABI on MRI scans. Another potential issue to consider with soft ABIs is the connector. The metal content of the connector might be larger than the metal interconnects and more importantly the presence of ferromagnetic metals, such as Nickel alloys commonly used, might generate large artefacts too. However, it is possible to find alternative solutions by using connectors with non ferromagnetic metals and/or with less metal content.

Another important imaging technique is Computed Tomography (CT). CT scans were also performed on a cadaveric head specimen implanted with the soft ABI. The image didn't present any artefacts or distorsions in the surrounding brain, while the ABI was visible (Fig. 3.18B). For comparison, a CT scan from a pediatric patient implanted with a clinical ABI shows distorsions and artefacts around the clinical implant (Fig. 3.18A).
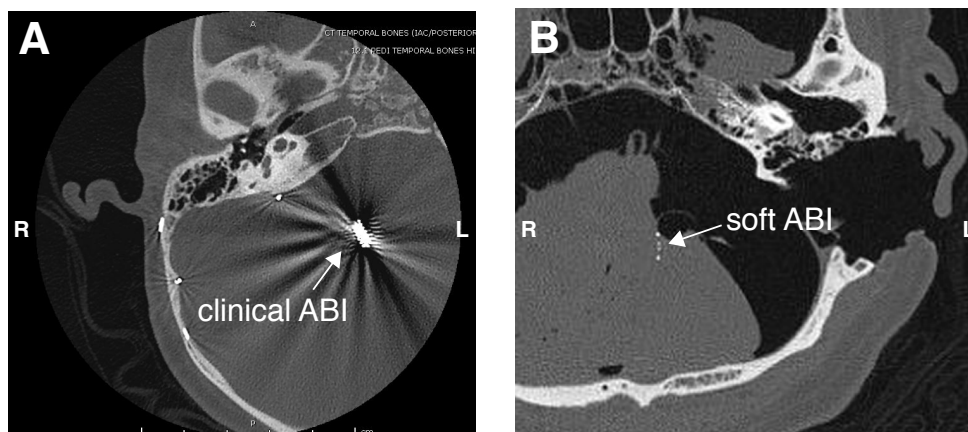
Figure 3.18 – **CT scan comparison of the clinical and soft ABI.** (**A**) CT scan of a paediatric patient with a clinical ABI. (**B**) CT scan of the cadaver implanted with a soft ABI.

The CT scan experiments highlighted differences that were more striking than the MRI tests: the artefact generated by the clinical ABI indeed distorted a large portion of the image, while the soft ABI didn't generate any distorsions. Interestingly, unlike the MRI scan, the electrodes of the soft ABI were visible on the CT scan. Thus a marker would technically not be required for CT scan compatibility.

Overall, these imaging tests suggest that the soft ABI, thanks to its thin film technology, would perform better than current clinical devices in terms of artefact generation during MRI and CT scans, which might provide better diagnostic information to medical doctors. However, artefact generation is only one aspect of MRI compatibility. Indeed, future tests will also need to assess if the magnetic field during MRI scans would induce currents in the devices that might generate heating or movement of the implant that could damage neural tissues.

Rigid guide   In order to facilitate the insertion of the ABI in the lateral recess, a temporary hydrosoluble guide (made of PVA, poly(vinyl alcohol)) was bonded to the back of the electrode array to facilitate handling with surgical tweezers and to temporarily rigidify the tip of the implant (Fig. 3.19A). Surgical insertion of the modified soft ABI was much easier and quicker (Fig. 3.19B). The hydrosoluble guide can then dissolve once in contact with the neural tissue and cerebro-spinal fluid (CSF), and allow the ABI to regain its initial softness and conform naturally to the CN.

In the clinic, it is important that the array remains stiff for at least 30 minutes in order to allow potential repositioning of the array. Thus, in order to estimate how long the hydrosoluble guide can remain stiff, dummy devices with the PVA guide were put in water and their mass was measured every five minutes and the ability to handle them was assessed manually. Figure 3.19C shows the change in mass of the dummy ABI with the guide, as a function of time (n = 5). The light grey zones shows the time range when the guide was too soft to be handled (n = 5), and the dark grey zone indicates the time when the guide delaminated from the array. The red dotted line corresponds to the mass of the array without the guide. Figure 3.19D shows swelling over time in PBS solution of a hydrosoluble PVA guide grafted on a dummy soft ABI. Initially the guide is completely dry and rigid (t=0 min) and is immersed in PBS solution at room temperature under gently shaking (100 rpm). Every 5 minutes, the sample is removed from the aqueous medium and wiped with a tissue to remove excess and non-absorbed water. The guide is both swelling and dissolving during its immersion. The edges of the guide become smoother after 10 minutes and the swelling causes bending of the assembly after 30 minutes, leading to the partial degrafting of the guide after 45 minutes, to release the stress at the interface between the silicone and the guide.

This experiment shows that in these aqueous conditions the soft ABI and the guide can be handled easily for most than 30 minutes. These conditions here are however much harsher in terms of PVA dissolution compared to in vivo conditions (the PVA guide was immersed in a completely aqueous solution combined with stirring, thus accelerating its degradation). Therefore, the hydrosoluble guide is expected to remain "functional" for a much longer amount of time during a real surgery in vivo.
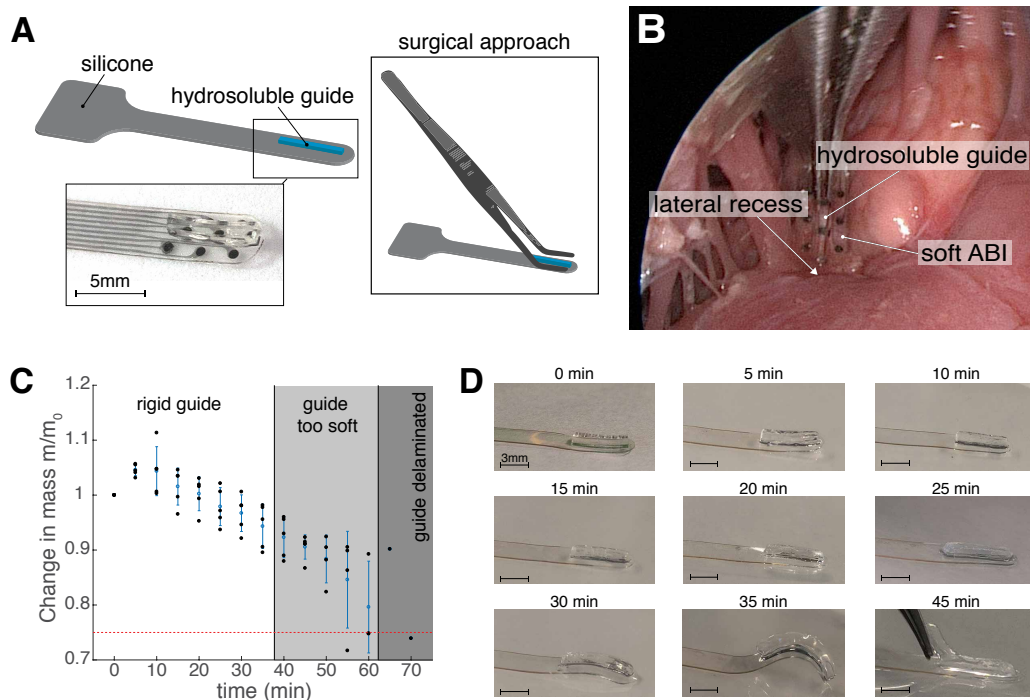
Figure 3.19 – **Hydrosoluble guide to temporarily rigidify the soft ABI during insertion.** (**A**) Schematic illustration of a soft ABI, temporally rigidified with a PVA hydrosoluble guide.The guide enables an easy handling of the assembly with tweezers during surgical procedures. The inset picture represents a soft ABI with a hydrosoluble guide grafted on its backside. (**B**) Insertion of a soft ABI grafted with a PVA guide in the lateral recess of a human cadaver. (**C**) Change in mass over time of a non-active soft ABI grafted with a hydrosoluble guide (n=5). The red dashed line represents the limit corresponding to the bare silicone without a grafted guide. (**D**) Swelling over time in PBS solution of a hydrosoluble PVA guide grafted on a dummy soft ABI.

These results indicate that the insertion of the ABI device can be greatly improved with the grafting of a hydrosoluble guide. This guide allows not only to rigidify the otherwise soft device, which facilitates its insertion in the lateral recess, but also creates an "anchoring" point which allows the surgeon to hold the implant at a more distal part of the array, without damaging the electrodes.

3.2.4 Conclusion

Summary This section showed that it is possible to fabricate a human-sized soft ABI device using micro-patterned stretchable interconnects. Histological analysis of the human brainstem provided design inputs for this device and indicated that using a silicone thickness of 200 μm was sufficient to make the device conform to the curvature of the DCN in an agarose model, compared to a stiff clinical ABI which couldn't conform. More importantly, this study demonstrated the possibility of implanting such a soft ABI using cadaveric specimens without damaging the device, and showed that using a dissolvable hydrogel guide grafted at the back of the electrode array could be used to temporarily rigidify the ABI and facilitate handling and insertion. The guide was shown to dissolve in about 40 to 60 minutes in water, suggesting longer dissolution times in vivo that are suitable for typical ABI implantations. The electrochemical characteristics of the soft ABI and its coating were also compared to the clinical ABI and showed that the soft ABI had an overall impedance larger than the clinical device (5.8 kΩ vs. 2.1 kΩ, respectively), which was expected due to the use of metallic thin films in the soft ABI, compared to metallic wires. However, VTs and CV characterization of the electrode-electrolyte interface showed that the soft ABI electrodes had a lower interfacial impedance, suggesting the possibility to use larger currents without damaging the electrodes or the tissue. Finally, MRI scans revealed that the soft ABI didn't generate any artefacts compared to the clinical device, but it was also not visible. However, CT scans showed that the clinical ABI generated large artefacts that distorted the overall image, whereas the soft ABI didn't generate any artefact, while being visible.

Limitations This preliminary study demonstrates the possibility of fabricating and implanting a soft ABI device, but didn't address some important technical issues, such as anchoring the connector to the bone while maintaining the ABI in place. Moreover, at this point it is unclear if the array would be mechanically more stable chronically, compared to a clinical ABI. Moreover, impedance measurements in vivo showed that the impedance of the soft ABI electrodes was almost twice as high as the clinical device electrodes. These conductivities might be insufficient to guarantee that the ABI stimulator can provide sufficient current to stimulate the CN (typically between 0 to 1.75 mA), as the stimulator might reach voltage compliance at lower currents. However, this issue might be overcome if the new soft ABI had smaller electrodes (which are feasible with the proposed technology), which may require smaller currents (for a constant density). Indeed, the coating used in the soft ABI has a electrochemical surface area high enough that seems to indicate that the only impedance increase in tissue would be mostly due to spreading resistance, which scales in $1/r$ (r being the radius of the electrodes), whereas charge density scales as $1/r^2$. Nevertheless, these are only speculations at the moment. Another alternative would be to diminish the interconnects resistance by increasing the thickness of platinum. This might however impact the electromechanical properties of the array.

Outlook Overall, this study is a preliminary technological and surgical proof of concept for the use of a soft ABI, but still doesn't address the main hypothesis that a soft ABI would perform better than a rigid device. A good animal model to test this hypothesize could be Non-Human Primates (NHPs), which have a similar anatomy as humans (Fig. 3.20) and thus can be implanted with an ABI with the same surgical approach, even though the paddle needs to be reduced in size [203]. Future work could thus use such an animal model in order to develop a clinically relevant chronically implanted soft ABI and to compare it to a rigid ABI. In these animal models, the pattern of activation thresholds could be measured, which could be an indication for good electrode conformability. Obtaining more uniform activation thresholds across the array will help towards the goal of having more usable electrodes that don't generate side-effects. This model could offer insights into whether a soft ABI would be mechanically more stable than a clinical rigid ABI and whether this translated to better overall performance in terms of speech perception for deaf patients. In fine, the only way to demonstrate the latter would be a human clinical trial.
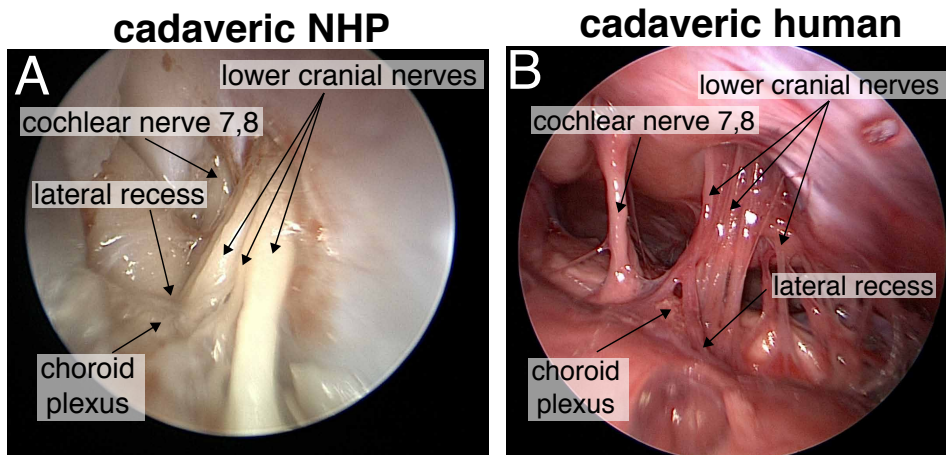
Figure 3.20 – **Anatomical comparison of NHP and human lateral recess.** Anatomical comparison of the lateral recess of the fourth ventricule in a cadaveric Non-Human Primate (**A**) and in a cadaveric human specimen (**B**).

3.3 Mouse ABI

3.3.1 Introduction

In the previous section it was shown that a soft ABI could potentially be used to replace current devices in the clinic, by improving conformability of the device to the surface of the Dorsal Cochlear Nucleus (DCN) as well as the electrochemical properties of the electrodes interface. Although cadaveric specimens are very useful to assess the feasibility of a surgical procedure using this new technology, it is not a suitable model to demonstrate functionality of a chronic neural implant for electrical stimulation of the DCN.

Here, it is proposed to use a non-deafened mouse model to assess the functionality of this technology with a smaller scale ABI implanted for four weeks on the DCN. The auditory pathways of this mouse model have been extensively studied in the past and thus make up for a good animal model for hearing research [204–206].

The main disadvantage of this model is that the mouse CN is very small: the DCN surface spans about 500x500µm^2, thus reducing the potential number of electrodes that can be used to stimulate it. Moreover, accessing the DCN surface from the lateral recess like in humans is extremely difficult. An alternative surgical approach to access the DCN has been proposed in rodents, by removing the cerebellum and exposing the DCN surface [207]. This approach poses some challenges in terms of animal survivability, but it has shown promising results in previous acute studies in rats [196, 208]. The development of a chronic ABI could thus provide insights on the mechanisms of DCN stimulation, which could in turn guide the design of better stimulation protocols for clinical ABIs.

The main objectives of this study is to design a soft ABI and surgical approach appropriate for the mouse anatomy. Moreover, the goal is to demonstrate the 4-week functionality of the implanted soft ABI to successfully activate the auditory pathways through electrical stimulation of the DCN.

3.3.2 Methods

Implant fabrication   The mouse ABI was manufactured using the methods presented in Chapter 2. It was constituted of an array of 3 electrodes ($\oslash = 150\mu m$). The connector was made of a surface mounted 4-pin header. The fourth channel was used as a control for stimulation artefacts during concurrent neuronal recordings. Figure 3.21 shows a picture of the mouse ABI, and its geometrical and electrical layouts.
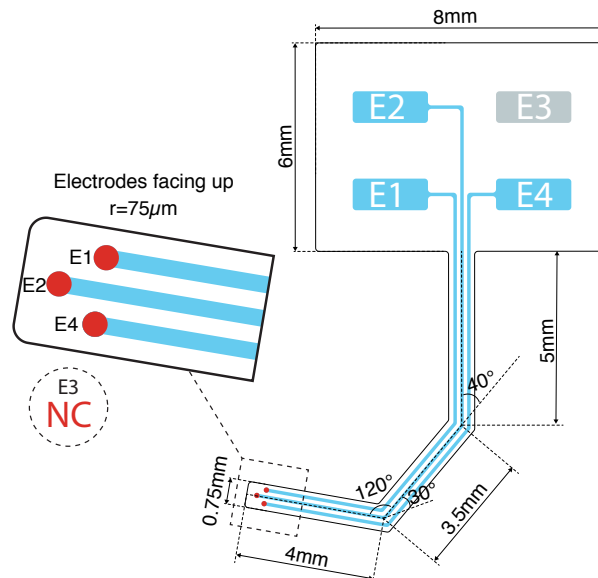
Figure 3.21 – **Mouse ABI device dimensions and electrical layouts.** The mouse ABI was made of 3 electrodes and a forth control channel (not connected to any electrode).

Animals   Ten CBA/CaJ mice (3 females, 7 males) were used in this study. Mice age ranged from 5 to 18 weeks and weights between 20 and 40 g. All experimental procedures were performed in accordance with the National Institute of Health guidelines for the care and use of laboratory animals as well as approved animal care and use protocols at the Massachusetts Eye & Ear Infirmary (Boston, MA).

Surgical procedure   An intraperitoneal systemic injection of Ketamine [20%] (diluted in saline, injection of 0.5mL/g) and Xylazine [10%] (diluted in saline, injection of 0.5mL/g) was administered to the mouse. During the surgical procedure supplementary doses of Ketamine (70% of the initial Ketamine dose) were injected when the mouse was waking up (determined on the base of paw pinch reflexes).

After the initial anesthesia, the mouse was shaved and positioned in a stereotaxic instrument. The temperature of the mouse was kept at 37°C with a heating pad. The heating pad was disconnected during recordings to avoid noise from the power network. The whole surgery was performed in a non-sterilized environment inside an acoustically isolated chamber.

A midline incision of the skin was created and the skin was removed to expose the caudal part of the skull, and the back muscles were removed to expose the left occipital bone. A double occipital craniotomy was performed and the cerebellum was suctioned in order to expose the CN (Fig. 3.22A-B). A rectangular craniotomy was then performed on the contra-lateral side of the CN (right side) rostrally from the right lambdoid suture, using a surgical blade (Fig. 3.22D).
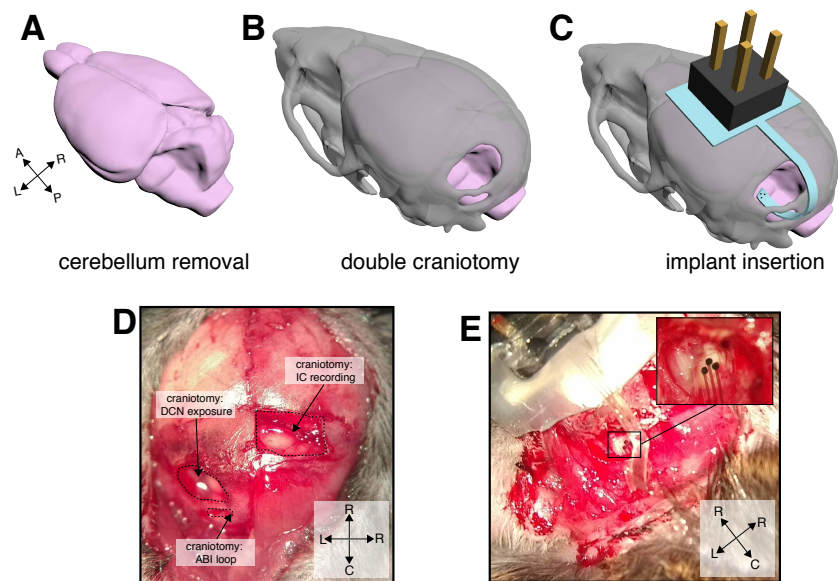
Figure 3.22 – **Surgical procedure of ABI implantation in the mouse.** (**A**) 3D image illustrating the cerebellum being succtioned to expose the Dorsal Cochlear Nucleus (DCN). (**B**) 3D image showing the locations of both craniotomies. The large craniotomy is where the DCN was exposed. (**C**) 3D illustration showing how the ABI was fixated on the skull and how it loops through both craniotomies, in order for the electrodes to be in contact with the DCN. (**D**) Picture showing both ABI craniotomies (left) and the craniotomy for the Inferior Colliculus (IC) probe (right). (**E**) Picture showing the ABI looping through both craniotomies.

Auditory Brainstem Responses   Auditory Brainstem Responses (ABR) were recorded using three subcutaneous needles inserted below the ipsilateral ear pinna and on the vertex of the mouse head. A differential measurement was performed between these two electrodes using a third common reference electrode inserted on the back of the mouse at the level of its tail. The three electrodes were connected to a preamplifier (DL Instruments, Model 1201 Low Noise Voltage Preamplifier) with a gain of 10'000 and a band-pass filter (300 Hz - 3 kHz, 5 poles). The preamplifier was situated inside the chamber and was connected to a computer situated outside the chamber. Data were acquired at a sampling frequency of 20 kHz and are averaged across 512 trials for a duration of 15 ms.

To record acoustically evoked ABRs (aABRs), a custom-made microphone was inserted in the left ear of the mouse. A click sound (broadband noise) was then generated at various

intensities from 0 to 80 dB in steps of 20 dB and aABRs were recorded to confirm that the mouse had normal hearing (Fig. 3.23). All recorded aABRs at weeks 0 and week 4 across all mice can be seen in Appendix A.6.
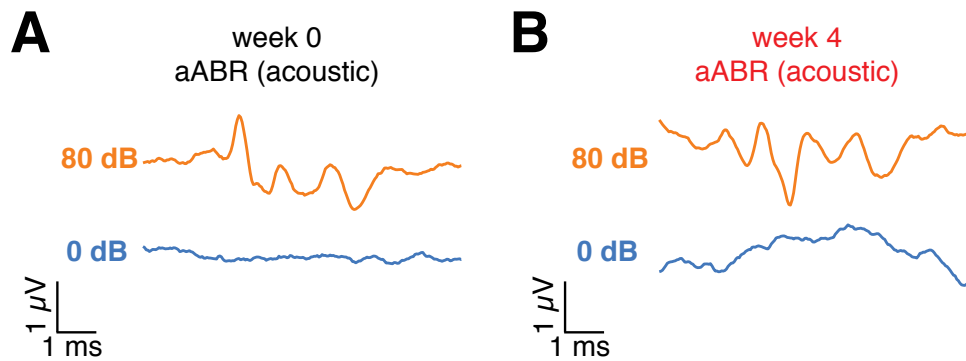
Figure 3.23 – **Representative examples of aABR recordings.** (**A**) Representative Acoustically evoked Auditory Brainstem Response (aABR) at 0 and 80 dB recorded in a mouse on week 0. (**B**) aABR for the same mouse recorded on week 4.

Electrically evoked ABRs (eABRs) were recorded in the same way, upon electrical stimulation of the cochlear nucleus (CN) with the ABI. These eABR recordings were performed during week 0 (intra-operative) and week 4 (last time point) simultaneously to IC recordings (see below). During weeks 1 to 3, eABR recordings were performed alone upon electrical stimulation of the CN.

IC recordings Neural recordings of the inferior colliculus (IC) were performed with a 16-channel ($\varnothing = 50$ µm) linear penetrating electrode array (NeuroNexus Technologies A1x16-3mm-50-177-A16). The probe was held by a stereotaxic aligner and inserted on the dorso-ventral direction in the cerebellum, such as it accessed the tonotopic organization of the central nucleus of the IC. The 16-channel IC probe was connected to a preamplifier (Plexon PBX3/16spr-G1000) with a gain of 1'000 and a band-pass filter (150 Hz -1 pole and 8 kHz - 3 poles). Data acquired at a sampling frequency of fs = 25kHz from all 16-channels were transferred to a computer located outside the anechoic chamber. The recordings lasted 30 ms upon stimulation and were averaged (20 averages) for each channel. A global reference was used for all electrodes with a subcutaneous wire inserted near the mouse neck.

To confirm the location of the IC probe, acoustic tones were generated at various frequencies (8 to 45.25 kHz, in steps of 1/2 octaves) and at various intensities (from 0 to 80 dB in 20 dB steps) in the left ear of the mouse while the IC activity (root-mean-square of the IC recording) was recorded using custom-made software on each of the 16 channels. The IC electrode placement was confirmed by observing a tonotopic shift along the IC probe as the frequency of the acoustic stimuli increased (Fig. 3.24). All acoustic IC maps recorded from all mice are shown in Appendix Fig. A.7.
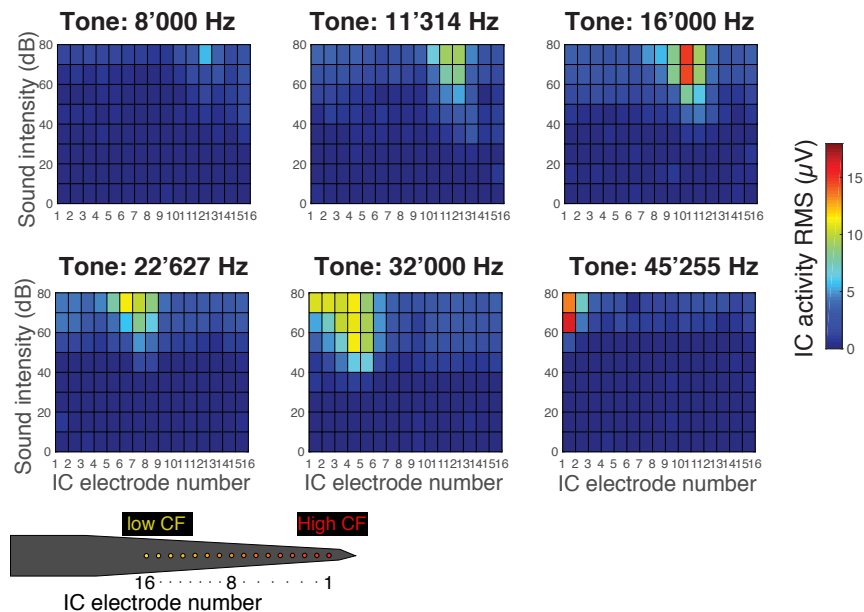
Figure 3.24 – **Calibration of IC probe using acoustic stimulation.** Example of recordings from the Inferior Colliculus (IC) generated by acoustic stimulation at various tones (one map for each tone). The x-axis of each map represents the IC electrode number, and the y-axis represents the sound intensity. As the tones increase in frequency, the IC activity (measured by root mean square) shifts from high electrode numbers to low electrode numbers

IC recordings were then performed upon electrical stimulation of the CN using the ABI at various intensities and using different electrodes configurations.

After the initial recordings at week 0 (intra-operatively), the IC probe was removed, and the IC craniotomy was covered with quick-seal. The IC craniotomy was opened up again 4 weeks later to perform a final recordings session, by implanting again the IC probe, following the same procedure as described above.

ABI implantation   The mouse ABI was inserted such that the electrode tracks form a loop and the electrodes were in contact with the mouse cochlear nucleus (Fig. 3.22C,E). A muscle plug was used to keep the ABI in place in the craniotomy with the DCN exposed.

At week 0 (intra-operative), the CN was stimulated using the ABI. After the stimulation/recording session, the ABI was fixated with dental cement on the skull.

Electrical stimulation   Monopolar electrical stimulation with the mouse ABI was performed using a custom-made stimulator. The same ground as the IC recording probe was used.

Trains of bi-phasic symmetrical pulses (the polarity of each pulse was alternated) were used

to stimulate the CN at a frequency of 23 Hz. Each phase lasted 200 μs and the current amplitude ranged from 0 to 150 μA with steps of 25 μA. Each pulse train lasted 0.5 s and was followed by an off period of 0.5 s, for a comparison to baseline (i.e. 14 pulses per train). Each of these pulse trains were repeated in total 30 times for each current amplitude (i.e 420 (14x30) stimulation pulses per current amplitude). The amplitude order of each pulse train was chosen randomly by a computer. During stimulation, eABRs and IC recordings were performed simultaneously, for a period of 15 ms after the end of the stimulation pulse.

Impedance Spectroscopy   In vitro electrochemical impedance spectroscopy (EIS) was measured with a potentiostat (PalmSens3, PalmSens BV) using a 2-electrode setup in phosphate buffered saline (PBS 1X), with a Ti wire reference and counter electrode. EIS was performed from 1 MHz to 1 Hz, with a voltage amplitude of 200 mV.

In vivo EIS was performed with the same potentiostat and parameters and a two-electrode setup using a subcutaneous wire as the counter and reference electrode. EIS in vivo were performed weekly, each time at the end of the stimulation procedure.

Data processing   Acoustically evoked ABR (aABR) recordings were averaged across 512 trials and were reported without any additional post-processing.

Electrically evoked ABR (eABR) recordings were averaged across 430 trials and were filtered with a low-pass Butterworth filter (order 5, $f_c = 3$ kHz).

IC recordings were first filtered with a Butterworth high-pass filter (order 5, $f_c = 500$ Hz) and a low-pass filter (order 5, $f_c = 3000$ Hz). Spike detection was then performed using a threshold of 3 times the standard deviation of the filtered baseline signal (recordings without any stimulation). The IC spike rate was calculated on a 0.1 ms sliding window. IC spike rate during baseline (spontaneous activity) was subtracted from the IC spike rate during electrical stimulation. Post Stimulus Time Histograms (PSTHs) were then generated to show the evolution of the spike rate as a function of time. The spike rates during the first 1.2 ms were ignored, due to stimulation artefacts. IC activity a_{IC} was defined as the integral of IC spike rate during the first 10 ms (Equation 3.2), for a given stimulation amplitude.

$$a_{IC} = \int_0^{10ms} PSTH(t)dt \tag{3.2}$$

The IC activity was normalized for each mouse by dividing it by the highest IC activity observed in a mouse across all stimulation electrodes and recording sessions (weeks 0 and 4).

3.3.3 Results

Animals In total ten mice were implanted with an ABI, but only 5 of them survived for 4 weeks. A sixth mouse was discarded from the experiment, because the connector failed and the electrodes were non functional after 4 weeks. In the end, only 4 mice were considered for the data analysis (Fig. 3.25).

		Impedances						Electrophysiology	
		In vitro	Implantation	Week 1	Week 2	Week 3	Week 4	Intra-op	Week 4
	ABI-98	3/3	NO DATA	2/3	DEAD	DEAD	DEAD	3/3	DEAD
	ABI-99	3/3	3/3	3/3	3/3	3/3	3/3	3/3	3/3
Sep. 2018	ABI-91	3/3	3/3	DEAD	DEAD	DEAD	DEAD	3/3	DEAD
	ABI-88	3/3	3/3	3/3	3/3	2/3	DEAD	3/3	DEAD
	ABI-96	3/3	3/3	2/3	2/3	DEAD	DEAD	3/3	DEAD
March. 2018	ABI-68	2/3	2/3	3/3	NO DATA	0/3	3/3	3/3	3/3
	ABI-27	3/3	3/3	3/3	3/3	3/3	3/3	3/3	3/3
Sep. 2017	ABI-25	3/3	3/3	3/3	3/3	3/3	3/3	3/3	3/3
	ABI-24	3/3	3/3	1/3	1/3	NO DATA	2/3	3/3	0/3
	ABI-5	3/3	2/3	3/3	3/3	2/3	DEAD	3/3	DEAD

Figure 3.25 – **Table summarizing the mice used in the experiment.** Each cell reports on the number of electrodes which were functional (out of three).

Electrophysiological setup Activation of the auditory pathways using ABI stimulation was confirmed by recording electrically evoked auditory brainstem responses (eABRs) using subcutaneous electrodes, as well as recording spiking activity in the contra-lateral Inferior Colliculus (IC) using a penetrating probe through a third craniotomy in the midbrain. eABRs were monitored weekly, whereas IC recordings were first performed intra-operatively (on week 0) and again on week 4 to confirm that the array was still functional and stimulating the auditory pathways. Unlike the ABI, the IC probe was not implanted chronically, but it was removed at the end of the stimulation/recording session on week 0 and was reinserted in the IC on week 4. The location of the IC probe was confirmed by acoustic calibration, as explained in the methods section. The entire stimulation and recording setup in summarized in Figure 3.26.
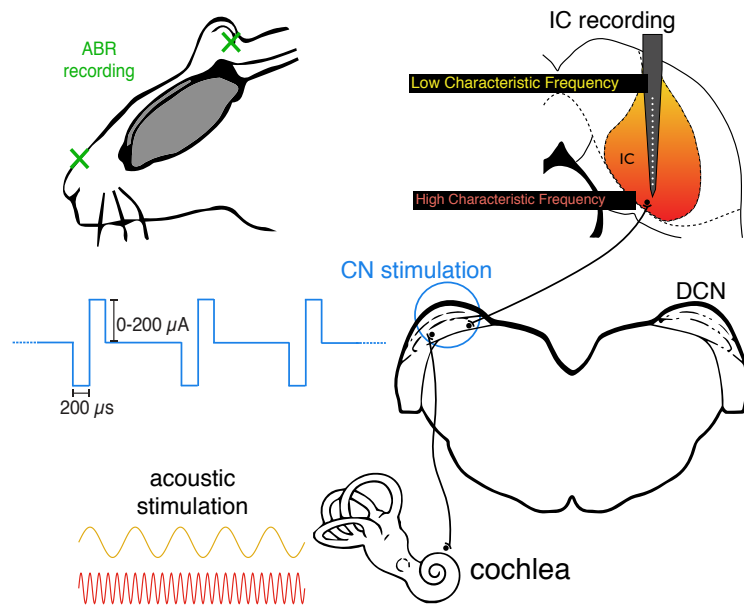
Figure 3.26 – **Electrophysiological setup of the mouse ABI stimulation and recording.** Auditory Brainstem Responses (ABRs) were recorded using surface electrodes on the vertex and left ear (top left). Acoustic tones were used to calibrate the position of the 16-channels penetrating probe in the Inferior Colliculus (IC). Stimulation of the CN was performed using the soft ABI with biphasic pulses (shown in blue). The black diagram on the right shows the projections of the CN to the contra-lateral IC.

Timeline   The timeline of the experiment was the following: the ABI was first tested in vitro. Then after ABI implantation (week 0), eABR and IC recordings were performed upon monopolar electrical stimulation of each of the three electrodes. At the end of the session, impedances of all three electrodes were measured. Then mice were anaesthetized weekly for 3 weeks, eABRs were recorded upon stimulation of each electrodes, and the impedances of all three electrodes were also monitored. Finally, on week 4, an IC probe was implanted again and a last session of monopolar stimulation was performed while both eABRs and IC activity were recorded. The electrodes were measured one last time on week 4. The experimental timeline is shown in Figure 3.27.
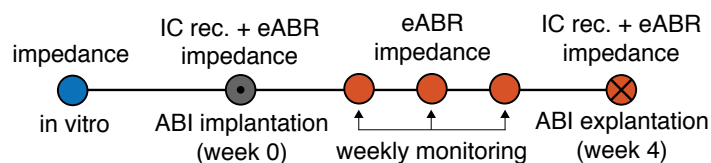
Figure 3.27 – **Timeline of chronic mouse ABI experiment.** Impedance measurements and eABR recordings are performed weekly. The IC recording probe is inserted only temporarily and then removed at the end of the surgery on week 0. It is re-inserted on week 4 for the last IC recordings.

ABI implantation Soft ABIs were successfully fabricated using micro-patterned interconnects (Fig. 3.28A). The surgical procedure described in the Methods section was also successful and allowed placement of the electrode array on the surface of the DCN (Fig. 3.28B).
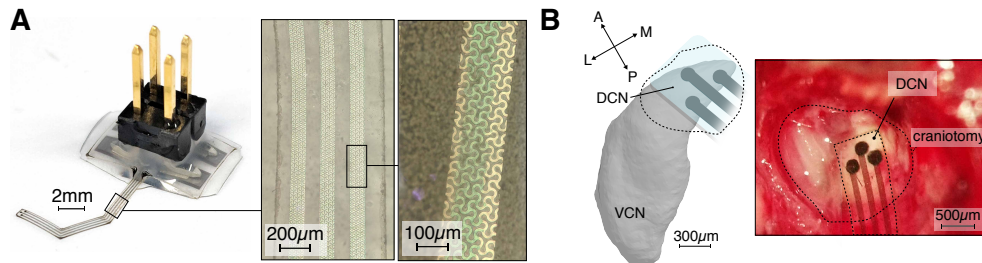
Figure 3.28 – **Microfabrication of the mouse ABI and its interface with the DCN.** (**A**) Picture of the mouse ABI and the micro-patterned electrical tracks. (**B**) Surgical image of the ABI on the surface of the DCN and illustration of the electrode array on a 3D reconstructed mouse CN (courtesy of Muniak *et al.* [204]).

Impedance evolution Electrochemical impedance spectroscopy (EIS) of the electrode array (3 electrodes per array) was performed in vitro before implantation, and weekly after each stimulation session. The EIS spectra of the electrodes in vitro, in vivo on week 0, and in vivo on week 4, are shown in Figure 3.29A. The impedance of interest here was set to 10 kHz (instead of the typical 1 kHz), because the impedance at this frequency is much closer to the resistance of the system (the double layer capacitance being short-circuited at higher frequency) and thus more representative to estimate how much current can be injected before reaching the voltage compliance of the stimulator (12 V). The average in vitro impedance at 10 kHz of all electrodes was 7.7 $\pm$ 4.9 kΩ, and the average in vivo impedance remained stable around 45 to 75 kΩ. Measurements were sometimes inconsistent, due to subcutaneous counter electrode positioning in the mouse. Thus some data points were discarded on some days. Overall, most electrodes remained under 80 kΩ, which is the theoretical impedance limit for stimulation at 150 µA with a voltage compliance of 12 V.
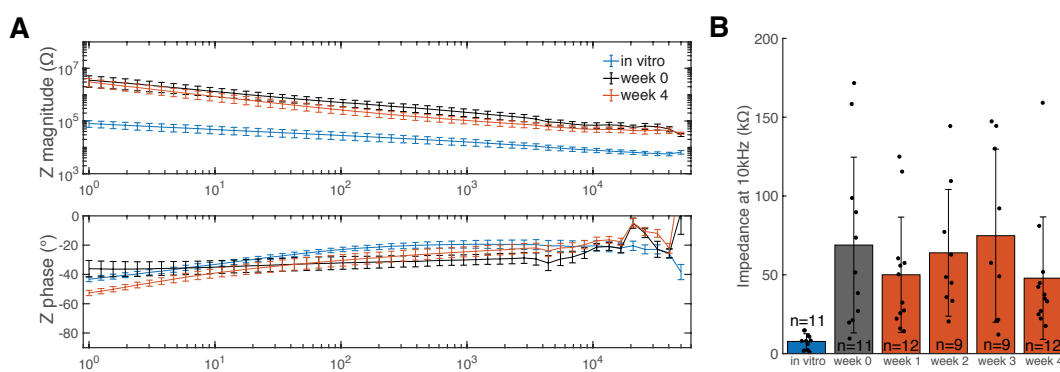
Figure 3.29 – **Impedance evolution of ABI electrodes.** (**A**) Electrochemical impedance spectroscopy in vitro (in blue, n=11), on week 0 (in black, n=11) and on week 4 (in red, n=12). Error bars denote standard error of the mean. (**B**) Impedance at 10 kHz at various timepoints for all electrodes. Error bars denote standard deviation. Data from 4 mice (3 electrodes each).

eABR   Electrically evoked ABRs by monopolar stimulation were recorded weekly with all three ABI electrodes in each mouse. The number of eABR peaks varied widely across mice and time point (between one and three peaks, Appendix A.8). These variations are possibly due to changes in the position of the subcutaneous recording electrodes. Nevertheless eABRs were generated consistently with ABI stimulation, indicating activation of the auditory pathways, as shown on the examples of Figure 3.30.
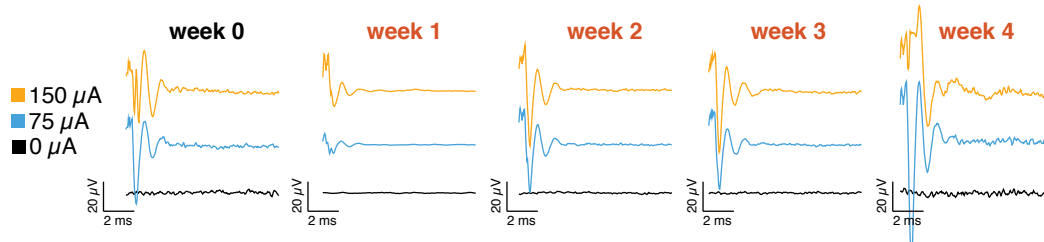
Figure 3.30 – **Example of weekly eABRs evoked by monopolar stimulation.**

IC recordings   In order to confirm stimulation of the auditory pathways, recordings in the IC were also performed at weeks 0 and 4 using a penetrating linear probe. The elicited spiking activity was averaged across all trials and all recording electrodes to generate Post-Stimulus Time Histograms (PSTH) for each stimulation electrode. Neural activity was consistently observed during the first 15 ms after the stimulation pulse (Appendix A.9). Differences in the stimulation patterns were observed on weeks 0 and 4. These variations can be explained by slight differences in the IC probe location, or by tissue scaring in the IC from the initial penetration on week 0. Examples of PSTHs at weeks 0 and 4 on the same mouse are shown in Fig. 3.31(A-B). Level curves of normalized IC activity (defined as the integral of the PSTH and normalized by the highest activity observed in a given mouse across all electrodes) were plotted for weeks 0 and 4 across all mice and all stimulation electrodes (Fig. 3.31C). These level curves show a general decrease in IC activity on week 4, which might have been influenced by scarring of the IC on week 0 or by weakened mice after 4 weeks of repeated sessions under anaesthesia. However, these data confirm that the ABI remained on the DCN surface and successfully stimulated the auditory pathways after 4 weeks of implantation.
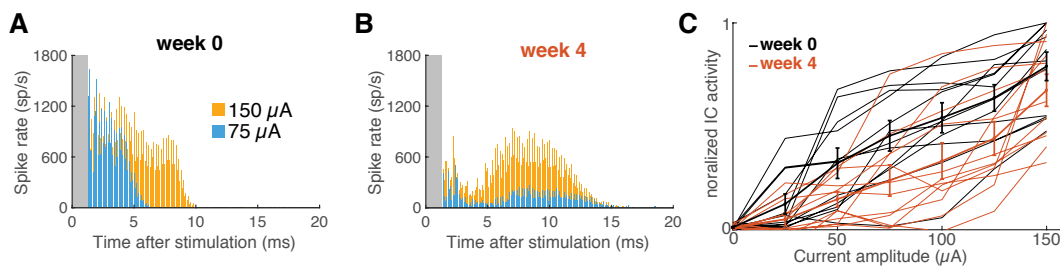
Figure 3.31 – **Activation of the IC by monopolar stimulation.** (**A**) Example of a Post-Stimulus Time Histogram (PSTH) elicited by monopolar stimulation on week 0. (**B**) PSTH of the same mouse and same stimulation electrode on week 4. (**C**) Level curves of IC activity for all stimulation electrodes across all mice. The bold curves show the average for weeks 0 (in black) and 4 (in red). n = 3x4 = 12. Bars denote standard error of the mean.

Controls   In order to control that the stimulation artefacts didn't generate false spikes in IC recordings or false peaks in eABR recordings, recordings were also performed by stimulating with the control pin of the ABI connector which wasn't connected to any electrode of the ABI array. Figures 3.32 A and B show examples of eABRs upon electrical stimulation of a functional electrode compared to the control. Similarly, Figures 3.32 C and D show PSTHs evoked by electrical stimulation of a functional electrode and a control electrode, respectively. The data show that no eABR peaks or spiking activity in the IC are generated by the stimulation artefact using the control electrode.
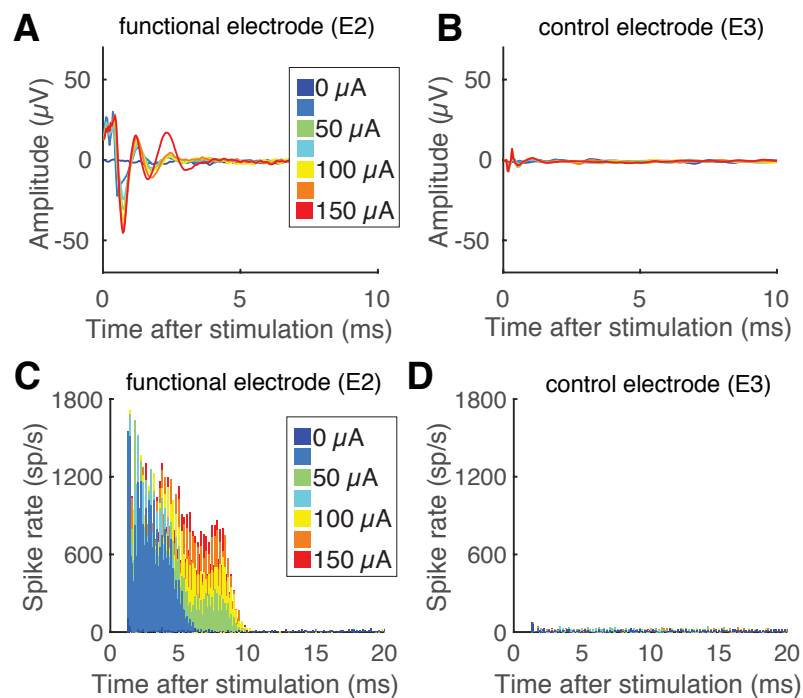
Figure 3.32 – **Comparison of neurological recordings with a control electrode for stimulation artefact rejection.** (**A**) Electrically evoked ABRs with a functional electrode compared to a (**B**) control electrode. (**C**) PSTH using a functional electrode compared to a (**D**) control electrode. This data shows that the stimulation artefact doesn't generate fake neural activity (eABR peaks or spikes in the IC recordings).

3.3.4 Conclusion

Summary   This study showed it was possible to use the micro-patterned tracks technology to fabricate miniaturized implants in the context of a soft ABI for mice. A new surgical procedure was presented to implant that ABI chronically on the mouse DCN surface that was tested for a period of four weeks. Weekly in vivo impedance measurements of the electrodes in four mice revealed that they remained stable over time, even though a few outliers appeared from time to time probably due to a setup mistake. Functionality of all electrodes was confirmed by recording eABRs through subcutaneous electrodes, and spiking activity in the IC using a micro-electrode penetrating probe. The recorded eABRs waveforms were generally inconsistent throughout timepoints and mice, with waveforms presenting different numbers of peaks (one to three peaks were generally observed). For that reason, IC recordings were also performed on weeks 0 and 4, to confirm that the ABI was still functional and that it was still stimulating the auditory pathways. The PSTHs at weeks 0 and 4 recorded with the IC probe were quite different across mice and timepoints, and it was observed that in average the IC activity on week 4 was lower compared to week 0. At this stage the main hypothesis was that the measurements on week 4 were affected by scaring of the IC due to the initial penetration of the array on week 0. Nevertheless, the experiment showed that the ABI remained functional and stimulated the auditory pathways for an implantation period of four weeks.

Limitations   One of the limitations of this study was the selected animal model. Indeed, the surface of the mouse DCN is quite small ($\sim$500x500 μm^2) and only three electrodes could fit on the array. It was therefore not possible to assess the capability of addressing the tonotopy of the DCN with ABI stimulation. Moreover, because of the anatomy of the mouse brain, it was impossible to insert the ABI in the lateral recess, like it is done in humans. Thus this animal model could not be used to assess important clinical aspects, such as the implant-brain interface stability over time. The surgical procedure that was selected here involved removal of the cerebellum to access the surface of the DCN, which caused a relatively high mortality rate in the animals in the chronic stage (40% of animal died within the four weeks). As of now however no better alternative was found. Finally, the analysis of the recorded eABRs and IC recordings remained very superficial, but in-depth analysis could reveal valuable information. Here, the objective of the analysis was to mainly confirm functionality of the device and activation of the auditory pathways.

Outlook   Future work could benefit from the extensive analysis of the recordings performed in this study, which might provide clues onto how the ABI implantation and stimulation impacts the neurophysiology of the CN and auditory pathways over time. Moreover, as discussed in the previous section, the use of larger animal models, such as NHPs, could be more relevant for the translation of this technology to the clinic. In the end, the development of this chronic ABI model is a very valuable tool for more fundamental research and could therefore be used to provide important information on the mechanisms of electrical stimulation of the CN that could be extremely helpful for the optimization of stimulation protocols in clinical devices.

4 Application: ECoG

Outline This chapter demonstrates the use of a soft neural implant using micro-patterned stretchable interconnects for recording electrocorticograms (ECoGs) in an acute setting in a minipig. It is organized in four sections:

- **Introduction** Short background on ECoGs

- **Methods** Description of the methodologies used during the experiment

- **Results** Presentation of the results

- **Conclusion** Summary of the experiments and outlook for future work

Scientific Contributions The contents of this chapter are currently being prepared to be submitted to a journal.

4.1 Introduction

Electrocorticography consists in the monitoring of the cortex neural activity using a surface electrode array that is placed under the dura, on the surface of the brain [209]. In the clinic, electrocorticograms (ECoGs) of Local Field Potentials (LFPs) are typically recorded over a few weeks in drug-resistant epileptic patients during ambulatory care to localize the foca of the epileptic activity in order to guide their surgical resection [210]. ECoGs are also used intra-operatively as a neuronavigation tool to help neurosurgeons localize and avoid cutting critical cortical areas (eloquent cortex) that are responsible for motor and language function during brain resections, usually in epileptic patients or patients with brain tumours [211].

Current clinical devices have relatively large electrode sizes (> 1 mm in diameter, ~10 mm pitch) embedded in a thick (a few mm) silicone paddle, that make the device quite stiff compared to neural tissue, thus not conforming optimally to the curvature of the brain surface. In consequence, these devices do not allow optimal localization of neural activity because they average the neural activity over a larger area, and the electrodes lack optimal contact to the brain.

Thanks to current developments in soft bioelectronics and micro-electronics, flexible thin (<10 µm) microelectrodes have been proposed to replace the stiff and large electrodes commonly used in the clinic [212]. Recently µECoG grids made from polyimide or parylene C have been used to record LFPs with a much higher spatial resolution in smal animal models such as rats [142, 213], as well as in larger animal models such as non-human primates [138] and minipigs [214], and even up to humans [215, 216]. These promising technologies have shown that smaller electrodes can increase spatial resolution [26], but the materials used are still relatively rigid (E~ GPa) compared to the soft neural tissues (E~ 100 kPa) and increase the overall biomechanical mismatch between the implant and the tissue (cf. Chapter 1).

The use of softer µECoGs has been previously demonstrated in a small animal model (mouse) [143], but studies of electrode size are limited in such models. Thus, the use of a larger animal model could be beneficial. Minipigs have been proposed as a suitable animal model for acute studies [217]. Indeed a large region of minipig somatosensory cortex encodes for the receptive fields of the pig's snout (Fig. 4.1, [218]). Even though chronic studies in such animal models are hard to perform, because of the large sinuses [217], this model makes it easy to assess the functionality and recording capabilities of new technologies for µECoGs in acute settings.

MRI safety and compatibility are other important considerations for ECoGs used in the clinic. Contemporary implants are not MRI compatible and generate large artefacts which hide parts of the brain, because of the large quantity of metal used in their manufacturing. This makes it very difficult to confirm placement of the implant and even to make sure it did not move during the implantation period. This is particularly relevant in the case of ECoG arrays used to monitor epileptic activity in the brain. Assessing the MRI compatibility and safety of new ECoG array technologies is therefore critical [82] and only recently has there been thorough studies on the compatibility of microfabricated devices with MRI [83–85].
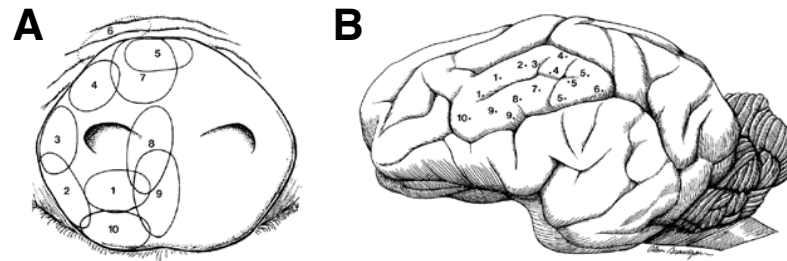
Figure 4.1 – **Somatotopic representation of the pig snout.** Receptive fields on the snout of the pig (**A**) and their corresponding somatotopic representation in the brain (**B**) [218].

In this chapter, a µECoG grid was fabricated using micro-patterned platinum tracks with a stretchable composite coating. The objective of the experiment was to show that such an array was capable of recording LFPs in a large animal model (a mini-pig) and was compared to a typical ECoG used in the clinic. These neurophysiological experiments were complemented with a preliminary MRI study, where the effects of temperature increase and artefact generation of a 3T-MRI were assessed in a phantom.

4.2 Methods

Implant fabrication   The µECoG electrode array was fabricated with the method presented in Chapter 2. Briefly, a stack of PI/Pt/PI (1µm/100nm/1µm) was patterned with Y-shaped cuts (Fig. 4.2(B-C)) and 16 electrical interconnects, and transferred between two layers of PDMS (substrate of 140 µm and encapsulation of 20 µm with openings on the electrode and connector sites), as shown on Figure 4.2A. The electrode diameter was 300 µm. A ZIF connector (Hirose Electric Co., LTD, FH12-16S-1SH) was mounted on the connector pads using a conductive silver paste (EPOXY Technology Inc.,H27D Part A) and encapsulated with a silicone adhesive (Dow Corning, DC 734 RTV clear). The electrode sites were coated with a Pt/PDMS composite, made of Pt micro-particles (avg. size 0.27-0.47 µm, 99.9% purity, STREM Chemicals, ref:93-7833) and PDMS (Dow Corning, Sylgard 184) in a 30% w/w. The final device is shown on Figure 4.2E.

The µECoG was compared to a clinical array (AD-TECH, subdural electrode 2x4 array, electrode diameter 2.3 mm, pitch of 10 mm) shown on Figure 4.2D.
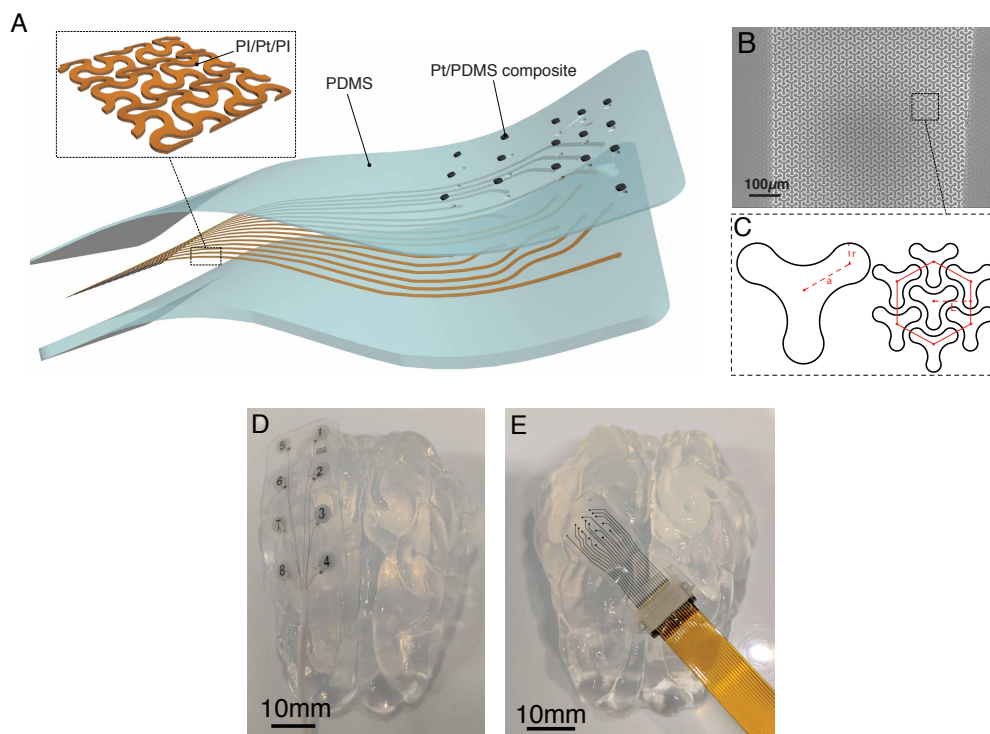
Figure 4.2 – **Fabrication of an ECoG grid using micro-patterned interconnects.** (**A**) Exploded view of the fabrication process of the µECoG, showing the main PDMS, polyimide and platinum layers. (**B**) SEM image of a conductive track patterned with an hexagonal matrix of Y-shaped patterns. (**C**) Design definition of the Y-shaped pattern. (**D**) Clinical ECoG array (AD-TECH) on an agarose brain of a minipig. (**E**) Finished µECoG with its ZIF connector and Flex-PCB on an agarose brain of a minipig.

Surgical procedure   The experimental protocol was approved by the cantonal and federal veterinary authorities (Canton de Vaud in Switzerland, license authorisation number VD3117). One farm pig (15 kg, female) was used in this experiment. Anaesthesia was induced with isoflurane and maintained with intravenous propofol. Oxygen supply was provided with a tube positioned around the snout. Once the animal was fully anaesthetized, aN intravenous lead was placed on its ear and the animal was then taken off the face mask and intubated with active respiration. Heart rate, body temperature and blood oxygenation were constantly monitored. The animal was placed on the surgery table over a heating blanket and was covered with sterile draps with the top of its head exposed. A large frontal to posterior incision over the skull was performed. The skin and underlying muscle were separated from the skull and pulled aside with forceps to maximize the exposed skull area. Four burr holes were drilled with a 5 mm diameter drill at the corners of the exposed skull. With a Kerison, the skull between the holes was cut to open a square bone flap, which was removed to expose the dura. The dura mater was cut open with a scalpel blade and flapped over, except over 2 mm laterally along the midline to avoid the large blood vessel over the midline. The brain was continuously kept wet with saline solution.

Snout stimulation   Wires with needles (neurology needle electrodes, Ambu) were inserted in pairs at various locations on the snout to form a 2x3 grid on the upper and middle part of the snout (Fig. 4.3(A-B)). Each location of the snout was then stimulated by sending 3, 5 and 8 mA biphasic current pulse trains (300 µs per phase) on each pair of electrodes at a frequency of 1.1 Hz. Each stimulation session lasted about 1 minute, while neural activity was recorded from the brain.
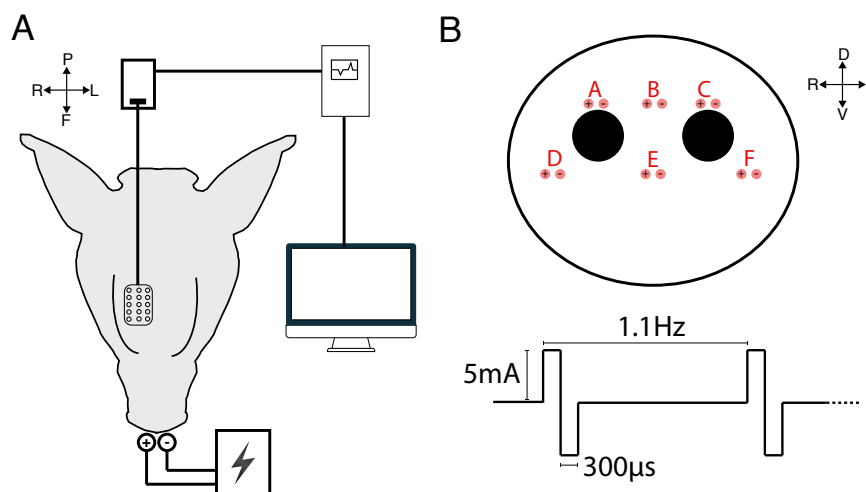
Figure 4.3 – **Electrical setup for snout stimulation and brain recording on a minipig.** (**A**) Electrical setup of the experiment, with snout stimulation, and pre-amplifier and recording system connected to the array on the minipig's brain. (**B**) Position of the bipolar stimulation needles on the minipig's snout (top) and stimulation pulse used for the snout stimulation (bottom).

Electrocorticography   In order to locate the somatosensory cortex of the snout, a clinical array was first positioned to cover most of the posterior right hemisphere. After locating which electrodes gave the most signal upon stimulation of the snout, the µECoG was positioned around the same location. The location of each array is shown with red dots on Figure 4.4A.

The clinical array was manually wired to a commercial connector (Omnetics Connector Corp.), which was connected to a pre-amplifier (Tucker-Davis Technologies, PZ5 NeuroDigitizer) and then to a processor (Tucker-Davis Technologies, RZ2 BioAmp Processor) linked to a computer (Fig. 4.3A). The µECoG was similarly connected to an Omnetics connector through a flex-PCB via a breakout board.

The sampling frequency of the data acquisition was 24441 Hz. Recordings were acquired with a bandpass filter (0.5 Hz - 5 kHz) and a notch filter at 60 Hz. No subsampling was performed. The recordings were triggered upon stimulation for a period of 50 ms, starting 10 ms before the stimulation and ending 40 ms after the stimulation.

A teflon-coated wire stripped at its end (Cooner wire) was inserted under the skin near the craniotomy and served as the ground. The reference electrode was made of a gold track encapsulated between two layer of PDMS with a circular opening at the electrode site (diameter 5 mm). The reference electrode was inserted subdurally on the left hemisphere.
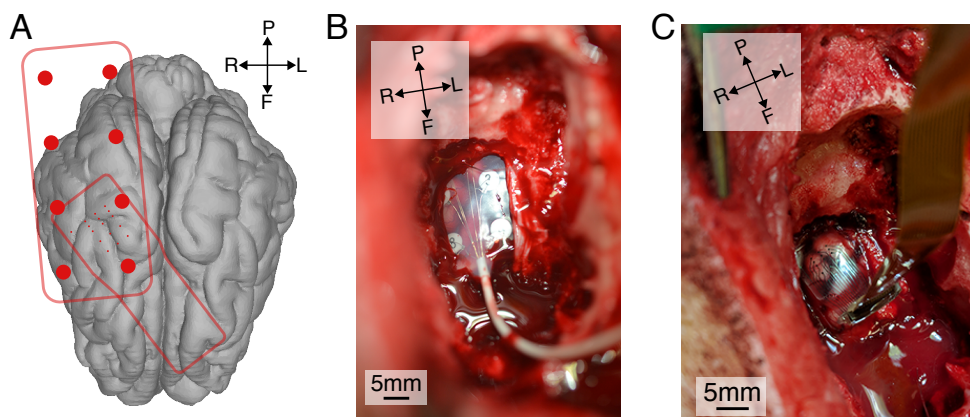
Figure 4.4 – **Location of the ECoG grids on the minipig cortex.** (**A**) Schematic representation showing with red dots the location of the clinical device array and µECoG on the right hemisphere of the pig brain. (**B**) Picture of the clinical grid on the right hemisphere. (**C**) Picture of the µECoG grid on the right hemisphere.

In vitro electrochemical impedance spectroscopy   Electrochemical impedance spectroscopy (EIS) of the electrodes was measured in vitro right before and after the surgical procedure, using a 3-electrode setup in phosphate buffered saline (PBS 1X), with an Ag/AgCl reference electrode, and a platinum counter-electrode (CE). EIS was performed using a potentiostat (Gamry Instruments, REF 600) from 1MHz to 1Hz, with a voltage amplitude of 100 mV. All electrodes were always stimulated for a few second with biphasic pulses (0.5 mA, 300 µs) to activate the electrodes before impedance measurement.

In vivo electrochemical impedance spectroscopy   EIS was also performed in vivo, using a 2-electrode setup, at the end of the recording sessions. A teflon-coated wire stripped at its end was inserted under the skin near the craniotomy and served as a CE.

Long-term ageing   Prior to testing, two µECoGs were sterilized with ethylene oxide (EtO) at 55°C. EIS was performed before and after sterilization. Then the devices were immersed in PBS for 35 days at 37°C in a hermetically sealed glass vial. EIS was performed on all 16 electrodes at various time intervals during the testing periods. The resistance between each neighbouring track was also measure at the end of the test by removing the devices from the PBS and drying them, in order to check for short-circuits. The resistance was measured by applying a DC voltage of 1 V using a multimeter (Model 2000 Multimeter, Keithley) .

Magnetic resonance imaging   Magnetic Resonance Imaging (MRI) was performed on a 3.0 Tesla MRI scanner (SIEMENS MAGNETOM Prisma). T1 and T2 sequences were used for the artefact analysis (sequence parameters in Appendices A.10 and A.11 respectively). A different T1-weighted sequence that lasted 2:55 min was repeated 5 consecutive times for the heat analysis (sequence parameters in Appendix A.12).

For artefact analysis, the arrays were positioned into a circular beaker between two 15 mm thick disks of agarose (agar powder mixed in deionized water, 3% w/w, Agar Agar Patissier). Another clinical intraoperative strip with 4 electrodes (Medtronic) was used for comparison.

For heat analysis, the µECoG grid was placed to the surface of a Siemens plastic bottle (1900ml 8624186 K228) and a temperature sensor (TSD202A, Biopac Systems Inc.) was positioned on top of it (4.5). The test was performed three times, with the µECoG grid positioned along all three axes of the MRI.
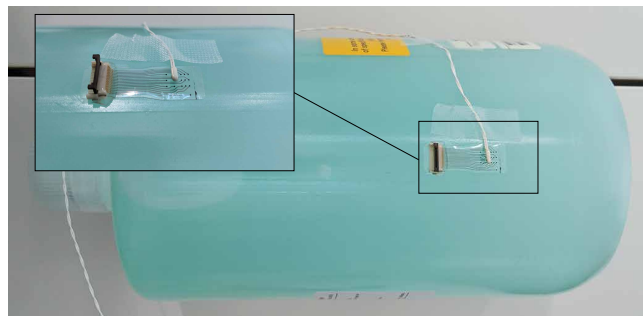
Figure 4.5 – **Setup to assess the effect of MRI on heating of the ECoG.** The µECoG is placed on a Siemens plastic bottle and the temperature probe is positioned on top of it. The picture shows the setup for the array positioned along the z-axis of the MRI.

ECoG post-processing   The neural recordings were processed using MATLAB 2017 (The MathWorks Inc.). No additional filtering was applied to the recorded data.

Statistical tests   1-way ANOVA and multi-comparison tests were performed to show statistical significance. Statistically significant effects were reported for $p<0.05$, and were corrected using a Bonferroni correction for multi-comparison tests.

4.3 Results

4.3.1 ECOG recordings

Clinical array   First, the clinical grid was placed on the right hemisphere of the pig brain. The snout was stimulated at 8 mA with electrode pairs C and F (upper and lower left snout). Consistent evoked responses were successfully recorded with the clinical grid on the contra-lateral hemisphere of the cortex. Figure 4.6A shows in blue representative Local Field Potentials (LFP) recorded on a frontal electrode of the grid upon stimulation of the snout (location C). Average LFP responses recorded across all 8 electrodes of the clinical grid upon stimulation of pair C are shown in Figure 4.6B. Heat maps were generated by calculating at each electrode site the integral of the rectified signal. They indicate a larger neural activity for lateral frontal electrodes when using stimulation pairs at the snout location C (Fig. 4.6C). That location was thus chosen for the placement of the μECoG.
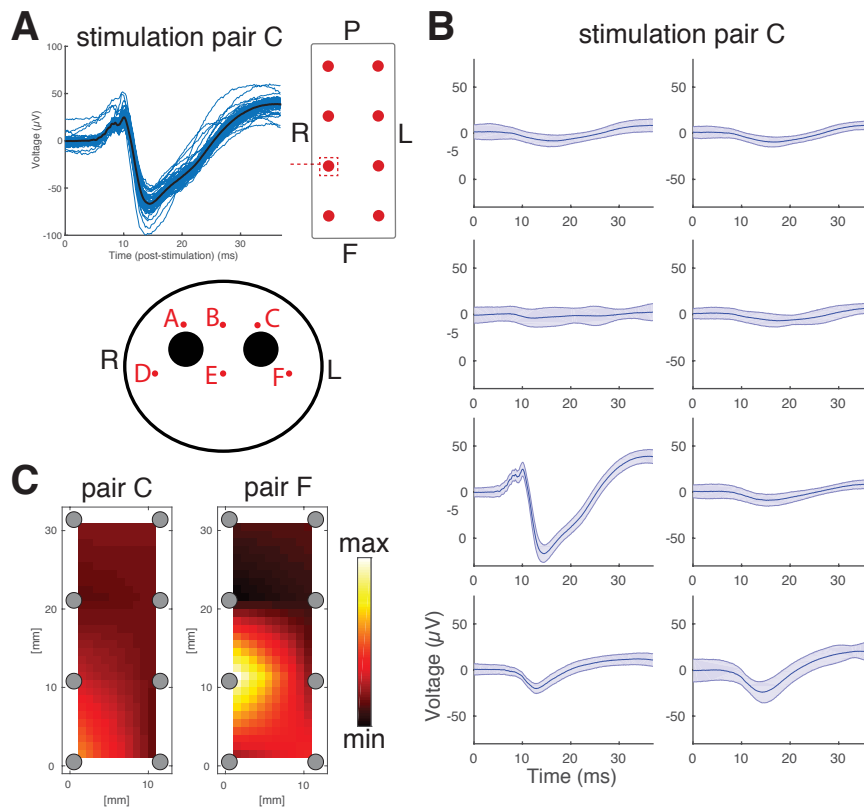
Figure 4.6 – **ECoG recordings with the clinical array.** (**A**) LFPs recorded on an electrode site of the clinical array upon stimulation (8 mA) of the snout at location C (blue curves show single trials and the black curve is the average). The snout schematic is a reminder of the stimulation pairs location on the snout. L: left, R: right, P: posterior, F: frontal. (**B**) LFPs recorded on all electrode sites of the clinical array upon stimulation (8 mA) of the snout at location C. Shaded regions represent standard deviation. (**C**) Heat maps of the activation over the entire grid for different stimulation pairs of the snout (each color map is normalized to the highest recorded activation for a given stimulation pair).

µECoG array The soft µECoG was fabricated using micro-patterned interconnects encapsulated in silicone. The Y-shape motif that was used had parameters: a = 16 µm, r = 5.5 µm and L = 26 µm, which corresponds to the optimized design from Section 2.3. After removing the clinical array from the cortex, the µECoG was positioned on the frontal part of the right hemisphere. The ideal target would had been to position it at the same location as the lateral electrode that yielded the highest evoked responses of the clinical grid (on Fig. 4.6).

Unfortunately, the µECoG position was not lateral enough, due to the size of the craniotomy that was not large enough (Fig. 4.4A). Nevertheless, evoked LFPs were also successfully recorded using the µECoG grid (Fig. 4.7A). Using the stimulation pair on the snout at location C (left snout), the microelectrodes recorded LFPs of varying intensity across the grid (Fig. 4.7B). Heatmaps for all 6 stimulations pairs of the snout show a larger activity when stimulating the left contra-lateral side of the snout. This is expected as the somatosensory representations of the snout are mostly located on the contra-lateral brain hemisphere. The locations with the highest neural activity on these heatmaps, show that the array was indeed too medial. One can observe that the electrodes at the edge are recording higher intensity signals, for stimulation pairs B, E and F on the snout. The neural activity seems to be location-dependent, as it moves from the electrodes on the right of the array (with pairs B and E) to the frontal electrodes of the array with pair F, which is consistent with the location of the stimulation pairs on the snout. Conversely, there seems to be almost none or very little activity for the ipsilateral stimulation pairs A and D.

Even though the micro-electrodes were not positioned exactly at the location of the larger clinical electrodes, results seem to indicate, as expected and as previously described in other studies, that more information can be extracted from smaller electrodes.

It was also observed that higher stimulation amplitude on the snout evoked larger LFP responses. This in accordance with previous similar studies [26]. Figure 4.8A shows how typical LFPs (averaged across trials) change as a function of stimulation amplitude. Statistical significance was observed for the effect of current amplitude on the peak-to-peak LFP amplitude (Fig. 4.8B, $p < 10^{-6}$ for all combinations).
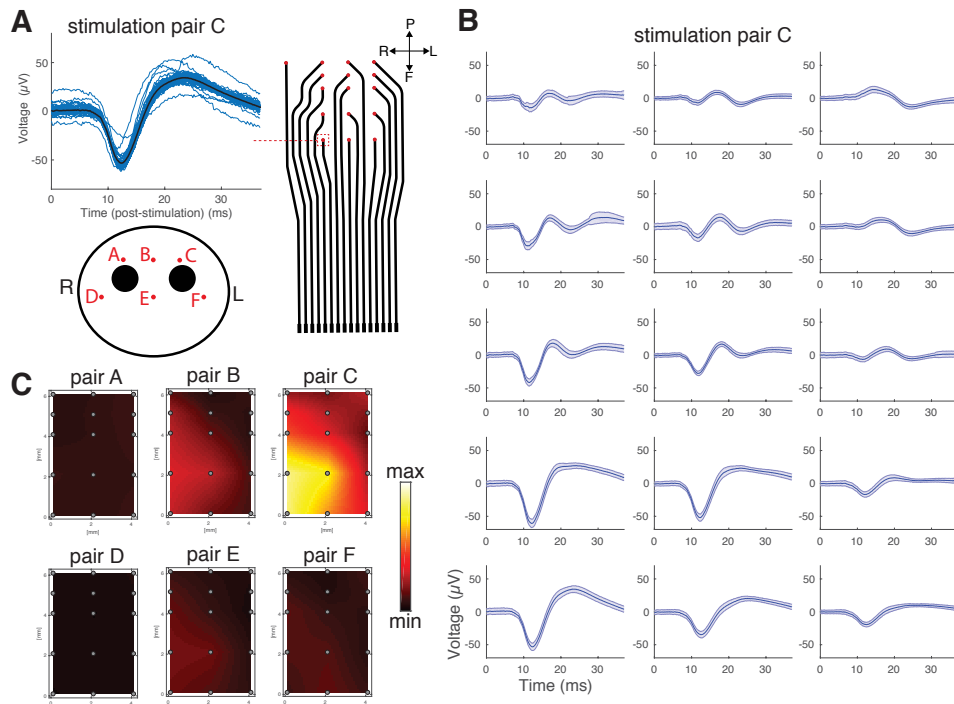
Figure 4.7 – **ECoG recordings with the µECoG array.** (**A**) Example of LFPs recorded with the µECoG grid upon stimulation at 8 mA at the snout location C (blue curves are single trials and the black curve is the average). The snout schematic is a reminder of the stimulation pairs location on the snout. L: left, R: right, P: posterior, F: frontal. (**B**) LFPs recorded on all electrode sites of the clinical array upon stimulation (8 mA) of the snout at location C. Shaded regions represent standard deviation. (**C**) Heat maps of the activation over the entire grid for different stimulation pairs of the snout (each color map is normalized to the highest recorded activation for a given stimulation pair).
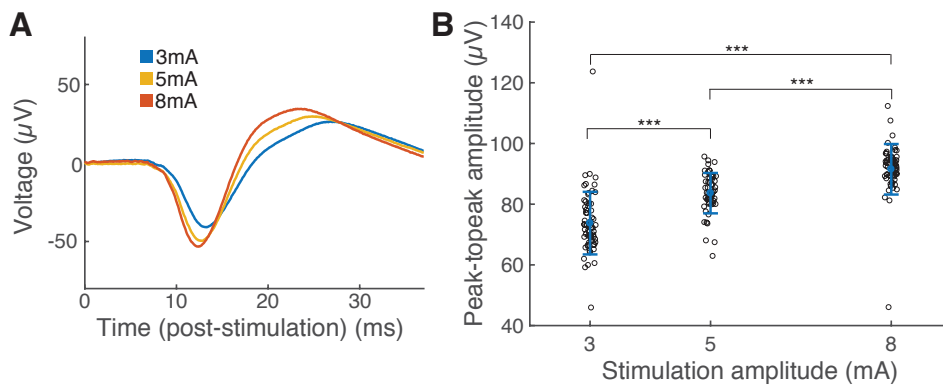
Figure 4.8 – **Effect of stimulation amplitude on LFP peak-to-peak.** (**A**) Examples of average evoked LFPs at various stimulation amplitudes. (**B**) Peak-to-peak amplitude of the LFP recorded across all trials on one channel as a function of stimulation amplitude. *** denote statistical signifiance with p<0.001. Error bars denote standard deviation.

4.3.2 Electrochemical impedance spectroscopy

A simplified electrical model of the electrode-electrolyte is shown in Figure 4.9C, where two series resistances R_{track} and R_{bulk} model the resistance of the micro-patterned interconnects and the spreading resistance of the electrode into the medium (tissue or PBS), respectively. The electrode-electrolyte interface is modelled by an interfacial capacitance C_i in parallel of a charge transfer resistance R_{ct}, which represent the main two charge injection mechanisms (capacitive and faradaic) from a metalic electrode to an electrolyte [201].

Electrochemical impedance spectroscopy (EIS) was first performed on all electrodes of the µECoG in vitro (in Phosphate Buffered Saline, PBS) before recordings, then in vivo while the implant was on the brain, and then again in vitro after the recordings. The measured EIS spectra are shown in Fig. 4.9A. The impedances at 1 kHz extracted from all electrodes show an increase of the in vitro impedance from 3.2 ± 0.6 kΩ to 5.3 ± 2 kΩ in vitro, before and after the experiment. The average in vivo impedance at 1 kHz was 15.7 ± 6.0 kΩ (Fig. 4.9B).

In order to isolate the effect of the coating at the interface from the actual micro-patterned interconnects, the impedance at 100 kHz was also extracted (the interfacial capacitor is shorted at high frequency). The 100 kHz in vitro impedance changed from 2.2 ± 0.2 kΩ before the experiment to 2.3 ± 0.3 kΩ after the experiment. The in vivo impedance was measured at 6.9 ± 2.4 kΩ (Fig. 4.9B).
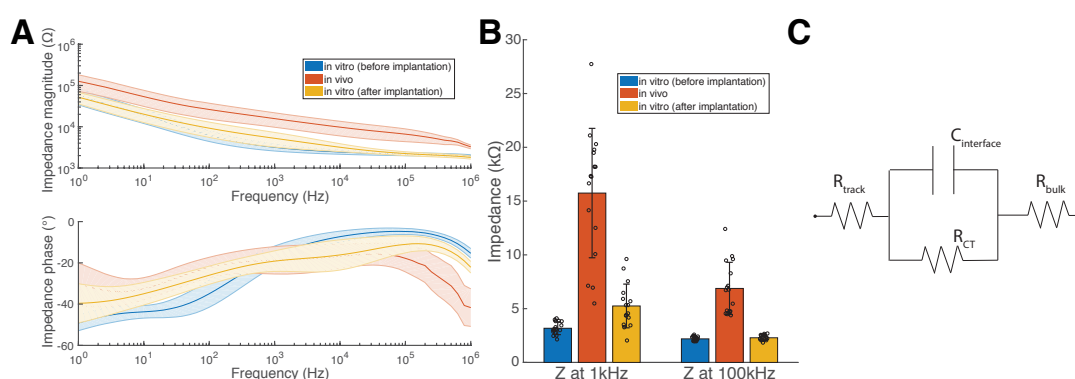
Figure 4.9 – **Impedance spectroscopy of the µECoG.** (**A**) Impedance spectra on all 16 electrodes of the µECoG grid, in vitro before (blue) and after the experiment (orange), and in vivo (red). Shaded areas denote standard deviation. (**B**) Impedance at 1kHz and 10kHz on all 16 electrodes. Same color code as A. Bars denote standard deviation. (**C**) Equivalent simplified electrical circuit of the electrode-electrolyte interface, where R_{track} is the track resistance, R_{bulk} is the spreading resistance in the medium, R_{ct} is the charge transfer resistance, and C_i is the interfacial capacitance.

Using the simplified model of Figure 4.9C, the impedance measurements can be better interpreted. Impedance measurements at higher frequency (~100 kHz), bypass the electrode interface and represent a better measurement of the interconnect resistance (in vitro, the spreading resistance is negligible for that size of electrodes). Thus, the impedance data from

Figure 4.9B indicate that there is little change of the interconnect resistance before and after the experiment, suggesting little damage to the interconnects upon surgical manipulation. However, it looks like there is a larger impedance change at lower frequency (1 kHz) indicating a probable change at the electrode coating.

Moreover, the change in impedance from in vitro to in vivo is consistent with a simple model of the spreading resistance R_{bulk} (Equation 4.1 [202]), which depends only on the resistivity of the medium (ρ) and the electrode radius r (150 µm here).

$$R_{bulk} = \frac{\rho}{4r} \qquad (4.1)$$

The resistivities of PBS and of minipig cortex can be found in the litterature [34]: $\rho_{PBS}=$ 0.6 Ω m and $\rho_{cortex}=$3 Ω m. With these values, Equation 4.1 predicts an increase in the spreading resistance of $\Delta R_{bulk}=$ 4 kΩ. The impedance results from Figure 4.9 indicate an average change of $\Delta R_{bulk}=$ 4.7 kΩ, which is consistent with the simplistic proposed model.

4.3.3 Sterilization and long-term ageing

Sterilization The impedance at 1kHz of two µECoGs (total of 30 functional electrodes) was first measured in vitro (2.9 ± 0.4 kΩ). Then the two grids were sterilized in ethylene oxide (EtO) at 55°C. Three months after sterilization, the devices were taken out of their packaging and the in vitro impedance at 1 kHz was measured at 3.5 ± 0.8 kΩ (Fig. 4.10A). An average increase of ~ 20% was observed (p$<10^{-3}$). However, it is unclear if this was due to the fact that the array was sterilized or if an oxide layer formed on the electrode coating during these three months, leading to an increase of impedance. A better test would be to perform the measurements immediately before and after sterilization. Moreover, this sterilization test only addressed changes in electrical properties due to EtO. Mechanical characterization should also be performed in order to evaluate the effect of EtO sterilization om the mechanical properties of the implants. Finally, no test was performed to evaluate if the sterilization was really effective. Measurements of bio-activity before and after sterilization need to be performed in a standardized manner to assess the efficacy of sterilization [219].

Ageing In order to assess the longevity of the µECoG technology in the context of epilepsy monitoring, a real-time ageing test was performed after sterilization, for 35 days (ECoG grids for epilepsy are usually implanted for less than three weeks). The µECoG was kept in PBS at 37°C in passive conditions (no stimulation). The impedance was monitored at various time points. At the end of the test, shorts between tracks in a dry environment were measured across all neighbouring electrode pairs (applied voltage: 1 V).

Electrical shorts between neighbouring electrode were all above an acceptability threshold of 40 kΩ, which was defined as one order of magnitude larger than the electrode impedance [73] (Fig. 4.10B). The impedance spectra of all electrodes during the entire period of ageing (35

days) is shown in Figure 4.10C. These spectra indicate the electrodes impedance remained stable, as confirmed by the impedance at 1 kHz which remained in the range of 3-4 kΩ during the entire duration of the test (Fig. 4.10D).

These preliminary results indicate that the µEcOG might be suitable for short term implantation under passive conditions (only recording), from a purely electrical perspective. However, testing in PBS has been thought to not be harsh enough to mimic the in vivo environment. Reactive accelerated ageing using hydrogen peroxide has been suggested as a better alternative [220].
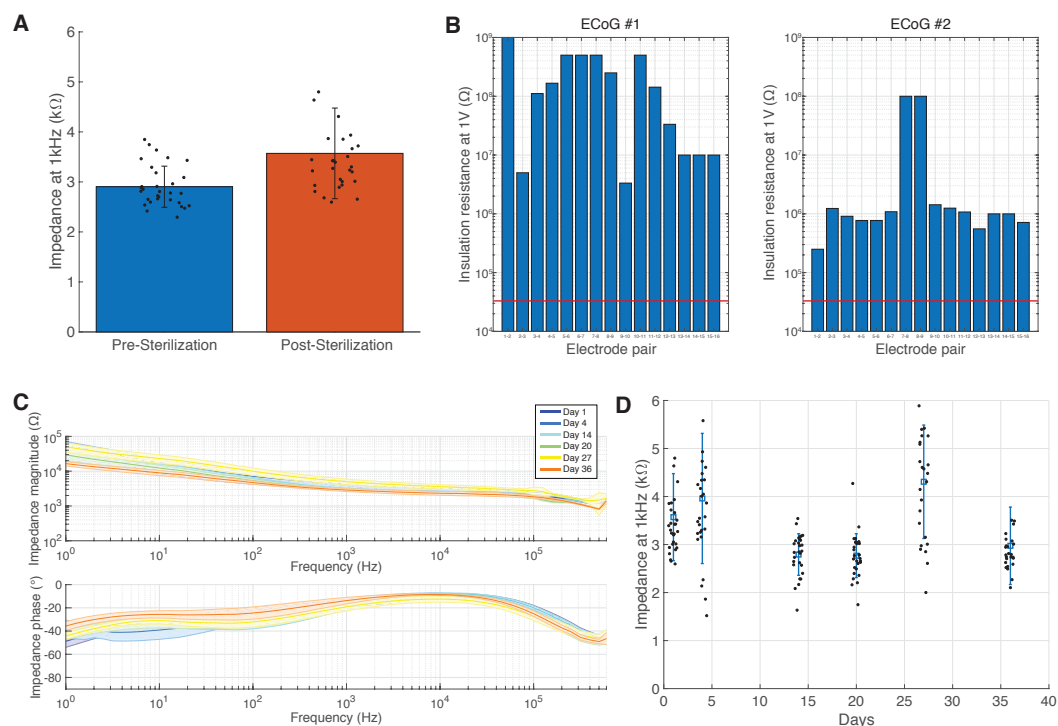
Figure 4.10 – **Sterilization and long-term ageing of µECoG in passive conditions.** (**A**) Impedance at 1 kHz before and after EtO sterilization (2 µECoGs, each with 15 functional electrodes, n=30). (**B**) Short circuits after 35 days of ageing measured on neighbouring electrodes on two grids. The red lines indicate an acceptable threshold (one order of magnitude higher than the electrode impedance). (**C**) Electrochemical impedance spectroscopy on all 30 electrodes at various time points during real-time ageing. The shaded error bars indicate standard deviation. (**D**) Impedance at 1 kHz of all 30 electrodes at various time points during real-time ageing. The error bars denote standard deviation.

4.3.4 Magnetic resonance imaging

Artefact generation Preliminary tests were performed to assess the MRI (Magnetic Resonance Imaging) compatibility and safety of the μECoG technology, in particular the micropatterned interconnects encapsulated in silicone. First, the μECoG was assessed for artefact generation in a 3T-MRI. The test was performed in a phantom brain made of agarose for a T1-weighted sequence as well as a T2-weighted sequence. A clinical electrode strip was also imaged for comparison. Figure 4.11A shows the axes definition of the MRI. Figures 4.11B and C show the clinical electrode strip and μECoG grid in the phantom brain, respectively.

Images taken from both sequences on different planes (Fig. 4.11(D-K)), show the generation of large artefacts for the entire clinical strip at the connector site, as well as at the electrodes sites. For the T1-weighted sequence, the height of the artefact is about 12.6 mm, and for the T2-weighted sequence it is 10.5 mm, on the Y-Z plane. Interestingly, the μECoG grid doesn't generate any artefacts at the electrode sites, indicating that the metal in the interconnects is thin enough to avoid any artefact generation. The electrode array contour can be clearly seen on Figure 4.11I. However, the connector (highlighted with a dotted line on Figures 4.11 E, G, I and K) generated a large artefact. This indicates that an alternative connector using non-ferromagnetic materials or with lower metal content need to be found to guarantee that the array will not interfere with diagnostic information during brain imaging.
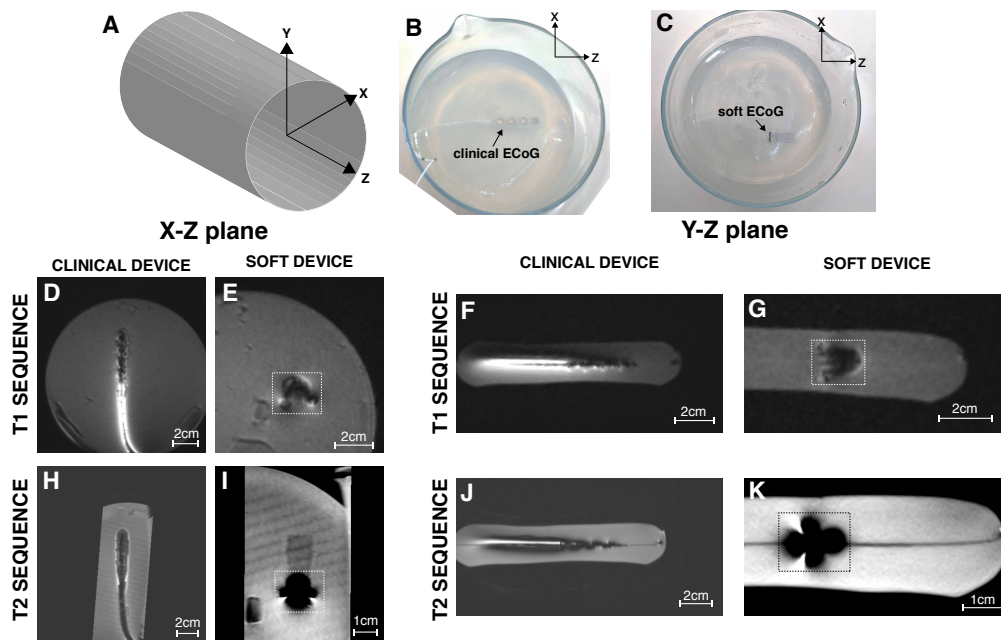
Figure 4.11 – **Artefact generation by 3T-MRI for a clinical and μECoG grid.** (**A**) Axes definition of the MRI machine. (**B**,) Clinical strip in a phantom brain made of two agarose sheets. (**C**) μECoG in the same phantom brain. (**D-G**) Images of T1-weighted sequences from the clinical array (D and F) and the μECoG grid (E and G). (**H-K**) Images of T1-weighted sequences from the clinical array (H and J) and the μECoG grid (I and K). The rectangular dottes lines show the location of the μECoG connector.

Temperature increase   Finally, a test was performed to observe if MRI induced a temperature increase at the surface of the electrode array. Indeed, as per ISO 14708:2014, the acceptable level of temperature increase for an implantable device is at maximum 2°C [221]. The test was performed by positioning the µECoG on a phantom bottle at three different orientations, as shown on the inset of Figure 4.12. Five consecutive T1-weighted sequences were then performed and a temperature probe at the surface of the grid measured the increase in temperature. Results show that for all orientations, the maximum increase in temperature after 15 minutes was less than 1°C. The increase in temperature was lower for the array oriented along the Y-axis (shown in red). This might be due to the fact, that in this configuration, the array was not positioned in the center of the MRI, compared to the two other orientations (cf. inset of 4.12). Moreover, a control was performed without any array, using only the temperature probe. An increase up to 0.6°C was also observed for the probe alone. This can be explained by the fact that probably currents are also induced in the sensor itself, thus increasing its temperature. Overall in this configuration, the increase of temperature of the array itself was well bellow the tolerable limit. It is important to note however that an MRI induced temperature increase comes from resonance phenomena induced by the MRI Radio-frequency (RF) pulses. Thus modifying the electrical path length, including adding a connector, could modify the observed behaviour.
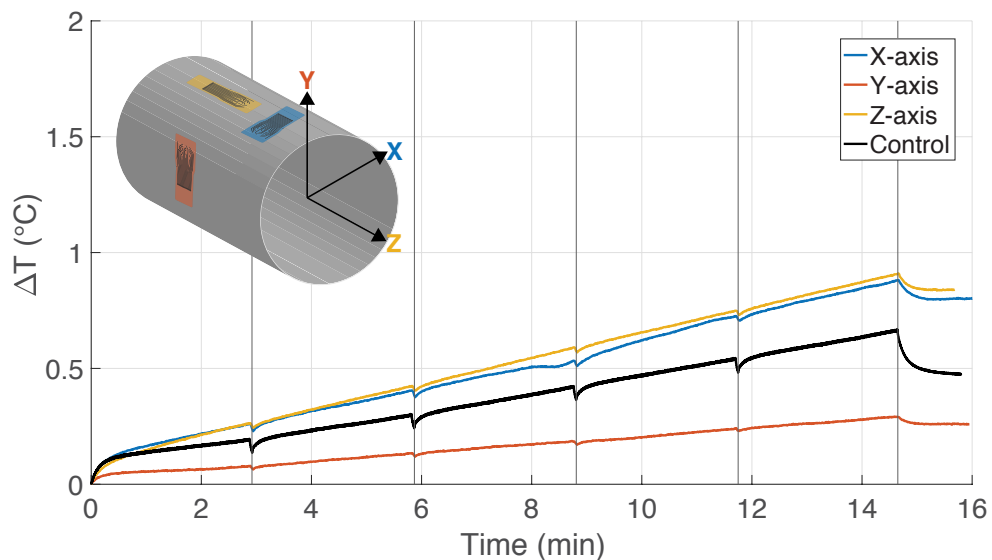
Figure 4.12 – **Temperature increase of the µECoG due to MRI.** Temperature increase as a function of time during 3T MRI T1-weighted sequences (five sequences of about 3 minutes each). Each color represents a different orientation of the array on the phantom brain in the MRI machine (inset). The five dark lines indicate the end of each MRI sequence.

4.4 Conclusion

Summary and discussion   This study showed how Y-shaped micro-patterned stretchable interconnects could be used to develop a soft µECoG electrode grid. Results showed the capability of the µECoG grid to record LFPs, evoked by electrical stimulation of the snout, at the surface of the minipig somatosensory cortex in an acute setting. As demonstrated in previous study, the use of smaller electrode sites (300 µm diameter) compared to clinically sized electrodes (2.3 mm diameter), allows to resolve LFPs in a smaller location. Unfortunately, in this study, analysis of the recorded signals showed that the array was positioned too medially, and thus could not cover the entire contra-lateral cortex somatosensory map of the snout. Moreover, only one animal was tested in this study, which is good enough for a proof-of-concept, but not enough to assess fully the recording capabilities of the device and how these differ from clinical devices.

Impedance measurements at high frequency (>10 kHz) in vitro and in vivo also indicated that the interconnects were not damaged during manipulation of the soft µECoG, showing how robust the technology is. Indeed, the surgical implantation of such grids is probably the most critical aspect from a mechanical stress perspective. However, impedance measurements at lower frequencies (<1 kHz) seemed to indicate that the coating could potentially have been damaged, or that blood residues had remained at the surface.

EtO sterilization tests showed that the technology was compatible with sterilization from a purely electrical point of view, but there still needs to be a thorough assessment of the sterilization efficiency in terms of removing any bioactivity as well as assessing its impact on the mechanical properties of the silicone encapsulation.

Long-term ageing also demonstrated electrical functionality of the device for a duration of 35 days in PBS. That duration is sufficient for the use of ECoG grids in the context of ambulatory epilepsy monitoring, but might be too short for other uses of µECoGs that might need to be permanently implanted in the body. Moreover, it is unclear if PBS is a good enough model to mimic the in vivo environment, and other alternatives might need to be tested, such as reactive accelerated ageing using hydrogen peroxide.

Finally, preliminary results showed that the micro-patterned interconnects embedded in silicone didn't generate any artefacts during MRI, compared to clinical devices. However, the connector generated a large artefact. This is thought to be due to their large metal content as well as the use of ferromagnetic materials, typically Nickel alloys. Alternatives need thus to be found. Nevertheless, the absence of artefacts at the electrode location is already positive, as that is the critical location where the brain is located (the connector is usually attached further away on the bone). Moreover, preliminary results showed that this technology didn't cause an increase in temperature due to MRI, even though tests with the device's final length and its connector will need to be performed to make sure the RF pulses don't induce any temperature increase. Overall further thorough testing using appropriate norms and better phantom models are necessary [86–89].

Comparison with other technologies   This preliminary study shows promising results for the use of soft microelectrodes for brain surface recordings. Previous studies have reported similar results using micro-electrodes encapsulated in flexible, but not stretchable, substrates, such as polyimide or parylene. The main difference here is that these materials have elastic moduli in the range of GPa, versus MPa for silicones. This means that to achieve similar levels of conformability (i.e. similar bending stiffness), in order to obtain a good electrode-tissue contact and thus more specific recordings, it is necessary to use very thin (< 10 μm) films. This might be adequate for small arrays in controlled situations in animal, but for larger human-sized grids, thin substrates might be too difficult to handle for a surgeon. Moreover, the use of polyimide-like substrates can easily crease and thus plastically deform during manipulation, which might then limit the conformability of these devices to the brain surface.

Outlook   Overall, the use of micro-electrodes, such as the ones presented in this study, could potentially have positive implications for the future use of such arrays in epileptic patients, that could allow the surgeons to more precisely localize epileptic foci. To that respect, one needs to also keep in mind the precision of the surgical brain ressection itself, that might in any way be much worse than the ECoG resolution. However, that increase in resolution might be more valuable for other applications such as brain machine interfaces (BMI) for tetraplegic or paraplegic patients. Indeed, recording of the motor cortex with microelectrodes might allow a finer control of a robotic arm. Promising work has been carried out in non human primates (NHP), where researchers were able to stably decode 3D arm positions for one year in a NHP [222]. And other groups proposed the use of a 128-channel device that could be used for BMI. [223]. For now, only electrode strips with four electrodes have been used to record ECoGs in a patient with locked-in syndrom for 28 weeks, that allowed her to control a computer typing program [224].

In the end this work paves the way to a long-term study, that will be necessary to asses the long-term recording capabilities of these arrays when chronically implanted. Indeed, the softness of the technology and its elecromechanical stability under mechanical stress could prove to be critical and very valuable for its long-term performance. Unfortunately, a mini-pig might not be a suitable model for such an experiment because of the formation of large sinuses [217]. Future chronic work could benefit however from the use of other models such as NHPs.

5 Application: Spinal Cord Stimulation

Outline Here, the chronic functionality of the technology was assessed in a mechanically challenging environment, in the context of spinal cord stimulation in non human primates. The chapter is subdivided in four sections:

- **Introduction** Short background on spinal cord stimulation

- **Methods** Description of the methodologies used for the experiment

- **Results** Presentation of the results

- **Conclusion** Discussion of the results and outlook for future work

Scientific Contributions A manuscript with the contents of this chapter is currently in preparation for submission to a peer-reviewed journal.

5.1 Introduction

Epidural Electrical Stimulation (EES) of the spinal cord has been widely used in the clinic to relieve pain from patients suffering from neuropathic chronic pain [225, 226]. More recently, EES has been proposed as a therapy to restore locomation after spinal cord injury (SCI) by stimulating the dorsal part of the spinal cord caudal of the lesion. The idea was first tested in rodent models, where EES helped improve rehabilitation after partial SCI by providing voluntary control of locomotion [227]. The exact mechanisms of EES in the context of locomotion are still under investigation, but putative models have been proposed. EES is thought to activate spinal reflex circuits, which in turn activate motorneurons, resulting in elicited movements [228]. EES was recently used by independent groups to improve locomotor performance and enabling voluntary control of walking during rehabilitation in individuals who had sustained a spinal cord injury (SCI) [229–231]. In these cases, EES was used in conjonction to intense rehabilitation to improve stepping. More sophisticated approaches were also proposed in Non-Human Primates (NHP) with complete SCI, by using combined neural recordings in the cortex and EES to bypass the injury location in the spinal cord [232]. In that study, EES was triggered based on the decoding of cortical activity, using a closed-loop cerebral motor cortex recordings and electrical stimulation of the spinal cord. The approaches presented above have focused mostly on stimulation of the lumbar portion of the spinal cord, but EES has also been used for rehabilitation of upper limbs in NHPs, by stimulation of the cervical location of the spinal cord [233].

One of the challenges associated with EES is the requirement for compliant electrodes, that can sustain the static and dynamic mechanical stresses due to spinal cord anatomy and movements. This has motivated the use of softer electrode arrays. Soft spinal implants built with micro-cracked gold technology have for example been used in rats [143] as well as in pigs [234]. A more relevant animal model to mimic human-like spinal cord anatomy are NHPs. Moreover, EES in the context of rehabilitation after SCI requires the specific targeting of various leg muscles (extensors, flexors, left and right). Thus, the ability to tailor-make the electrical layout of the array to fit to the anatomical dimensions of the target spinal cord is an important feature to optimize outcomes. In this study, two NHPs were chronically implanted with personalized spinal arrays and their stimulation capability and impedances were assessed up to 43 days. The main objective was to evaluate the functionality of stretchable interconnects in a mechanically challenging environment in the context of spinal cord stimulation.

5.2 Methods

Implants fabrication The spinal cord implants were fabricated with the methods presented in Chapter 2. Briefly, a stack of PI/Pt/PI (1μm/100nm/1μm) was patterned with Y-shaped cuts and transferred between two layers of PDMS (substrate of 200 μm and encapsulation of 250 μm, with openings on the electrode and connector sites). Implants were fabricated with two different designs tailored for implantation at the L4-L5 and L6-L7 spinal segments. Both implants comprised eight electrode sites (2x0.7 mm^2). The devices were wired to standard

8-polar leads with ring connectors. The wires were put in contact with the electrode pads using a conductive silver paste (EPOXY Technology Inc.,H27D Part A) and encapsulated with a silicone adhesive (Dow Corning, DC 734 RTV clear). The electrode sites were coated with a Pt/PDMS composite, made of Pt micro-particles (avg. size 0.27-0.47 µm, 99.9% purity, STREM Chemicals, ref:93-7833) and PDMS (Dow Corning, Sylgard 184) in a 30% w/w.

Animal husbandry   Experiments were approved by the Institutional Animal Care and Use Committee of Bordeaux (CE50, France) under the license number 50120102-A and performed in accordance with the European Union directive of 22 September 2010 (2010/63/EU) on the protection of animals used for scientific purposes in an AAALAC-accredited facility (Chinese Academy of Science, Beijing, China). Two healthy adult male fascicularis monkeys (Macaca fascicularis, China) weighing around 5 kg each were used for the experiment.

Surgical procedure   All the surgical procedures were performed under full anaesthesia induced with atropine (0.04 mg kg^{-1}) and ketamine (10 mg kg^{-1}, intramuscular injection) and maintained under 1%-3% isoflurane after intubation. A certified functional neurosurgeon supervised all the surgical procedures. The spinal implants were inserted into the epidural space of the lumbar spinal cord according to previously described methods [235]. Monkey HH01 was implanted with an implant on the caudal segments of the lumbar spinal cord, as well with another implant from a different technology (not mentioned in this study) implanted on the rostral segments. Conversely, monkey HH08 was implanted with an implant at the rostral location of the spinal cord (and another device was positioned caudally for another study). The caudal implant was inserted at the L6–L7 vertebrae and pulled until it reached the L4-L5 vertebrae. The rostral implant was inserted at the L4–L5 vertebrae and pulled until it reached the L2-L3 vertebrae.

The tip of the lead was protected with a female cap. The entire lead was implanted under the skin. A skin incision at days 15 and 43 post-surgery was performed to access the lead connector and perform stimulation and impedance measurements.

Impedance spectroscopy   In vitro electrochemical impedance spectroscopy (EIS) was performed with a 3-electrode setup in phosphate buffered saline (PBS 1X), with an Ag/AgCl reference electrode, and a platinum counter-electrode. EIS was performed using a potentiostat (Gamry Instruments, REF 600) from 1 MHz to 1 Hz, with a voltage amplitude of 100 mV.

In vivo EIS was performed with a 3-electrode setup using two subcutaneous needles as counter and reference electrodes. The same potentiostat and parameters as in vitro were used.

Epidural stimulation   Stimulation was performed on each electrode site using charge-balanced symmetric biphasic pulses (300 µs pulse width, 1 Hz pulse rate). A subcutaneous needle was used as a counter electrode. Each electrode was stimulated sequentially and the

current amplitude was increased until reaching activation threshold and tonic contraction (current amplitude range of 0 – 10 mA). Muscle activation thresholds and tonic contraction were assessed visually by a veterinary. Voltage transients (VTs) were recorded during stimulation at the threshold and tonic contraction amplitudes, using an oscilloscope connected between the stimulation electrode and a subcutaneous needle used as reference.

5.3 Results

5.3.1 Array fabrication

Both spinal implants were successfully manufactured using the micro-patterned polyimide-platinum construct encapsulated in silicone (Fig. 5.1A), each with a different layout to optimize specific stimulation locations of the spinal cord. The caudal array had five functional electrodes out of the eight (Fig. 5.1B), and the rostral array had all eight electrodes functional (Fig. 5.1C). Functionality was assessed by impedance spectroscopy with an impedance limit of 100 kΩ at 1kHz. The full implant-lead system with the female connector cap is shown in Figure 5.1D.
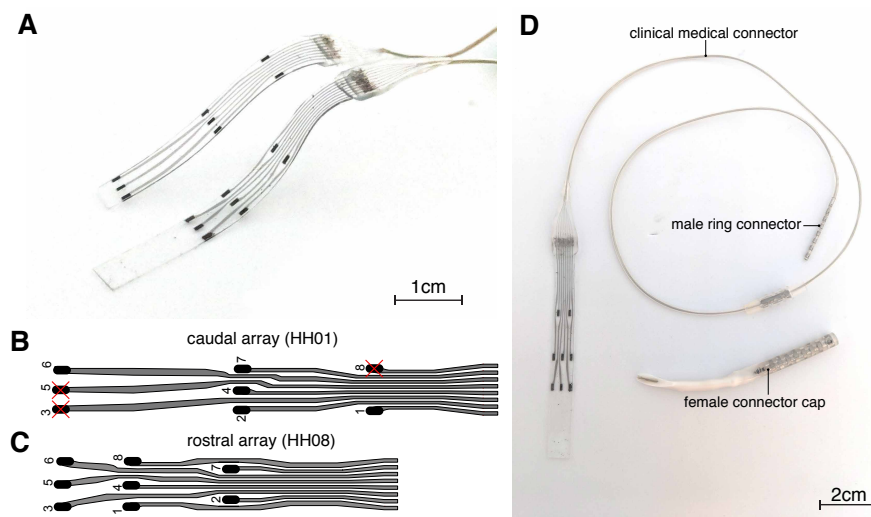
Figure 5.1 – **Implants for spinal cord stimulation.** (**A**) Picture of the finalised implants for stimulation of the monkey spinal cord. (**B**) Layout of the caudal array. Red crosses indicate non-functional electrodes. (**C**) Layout for the rostral array. (**D**) The electrodes were connected using a commercial ring connector with the mating connector acting as a protection cap when implanted.

5.3.2 Array implantation

The location of both implants on the spinal cord is schematically shown in Figure 5.2A. The caudal array was implanted in HH01 and the rostral array was implanted in HH08 (Fig. 5.2B). The surgical implantation was performed successfully on both monkeys and the device survived mechanically the implantation procedure. Figure 5.2C shows the array located on the rostral lumbar segments of HH08. The other implant on the picture located on the caudal lumbar segments of HH08 was made with another technology for another study, which is not discussed here. X-Ray imaging on days 15 and 43 showed that the device remained in place for the entire implantation period (Fig. 5.2(D-E)). A steep S-shaped bend can be observed at the connector location, illustrating the static mechanical environment of the device. Unfortunately, the devices had to be explanted after 43 days of implantation, due to an infection on the skin near the connector. This was thought to be due to the repeated skin incisions to expose the connector. Interestingly, the explantation of the device was very smooth, and no tissue encapsulation around the implant due to foreign body reaction was observed, indicating good bio-integration of the device.
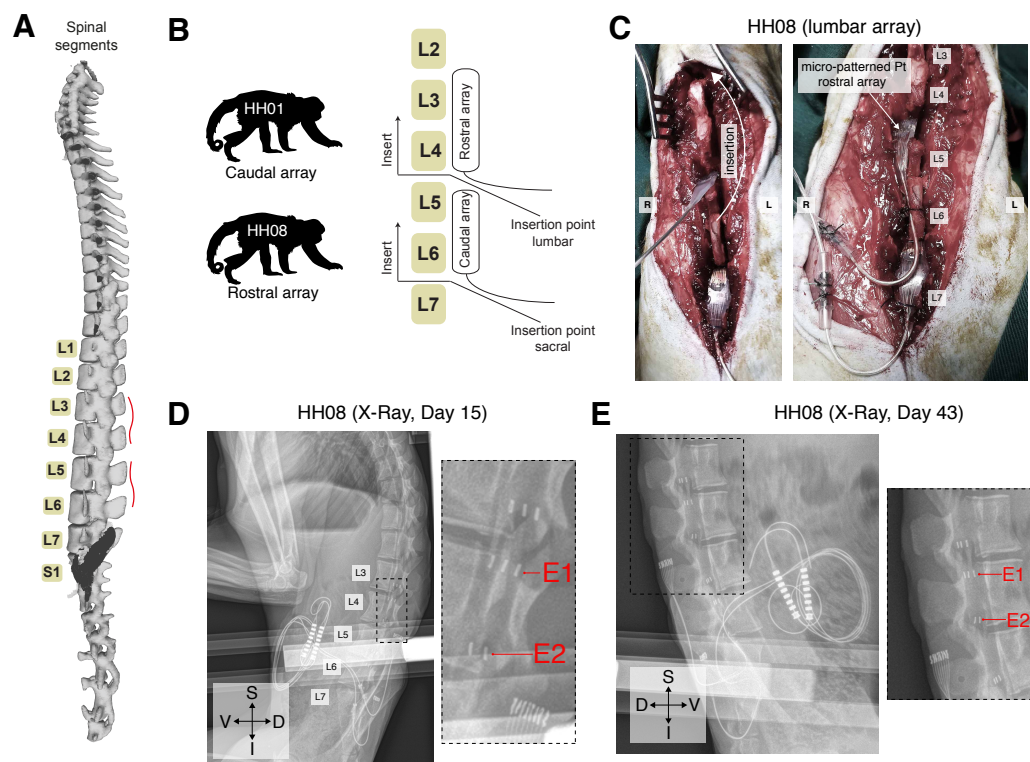
Figure 5.2 – **Surgical implantation of the spinal implants.** (**A**) Schematic representation of the spinal cord and the location of both implants shown in red. (**B**) Schematic summarizing the insertion points of both caudal and rostral implants and in which animals each device was implanted. (**C**) Pictures of the rostral array intra-operatively on the spinal cord of HH08. (**D**) X-ray image of HH08 on day 15. (**E**) X-Ray image of HH08 on day 43. V: ventral, D: dorsal, S: superior, I: inferior

5.3.3 Epidural electrical stimulation

Electrical stimulation Epidural electrical stimulation (EES) was performed with all electrodes, on the day of the surgery, and at days 15 and 43 post-implantation. For each electrode, the current was increased slowly until reaching muscle activation threshold (visual observation) and until reaching tonic contraction (muscle saturation, that was also visually observed). The voltage was monitored and recorded for these two currents. The current amplitudes at which threshold and tonic contraction were observed are shown on Figure 5.3A.

Thresholds The average activation thresholds on days 0, 15 and 43 were 0.78 ± 0.52 mA, 0.71 ± 0.38 mA and 1.03 ± 0.36 mA, respectively. Paired t-tests failed to show a statistically significant difference in thresholds between days 0 and 15, and days 0 and 43. However a statistically significant difference was observed between day 15 and 43 (p=0.017), suggesting an increase in muscle activation threshold. Such an increase of threshold could be caused by scarring of tissue between the implant and the spine, thus pushing the electrodes away from the tissue.

Tonic contraction The average tonic contraction amplitudes on days 0, 15 and 43 were 1.16 ± 0.48 mA, 1.5 ± 0.32 mA and 1.9 ± 0.44 mA, respectively. The data suggest a larger correlation of implantation time and increasing current amplitudes for maximum contraction. This could also be explained by foreign body reaction pushing the array away from the spine. The corresponding charge densities at threshold and at maximum tonic contraction are also shown on the right axis of Figure 5.3A. The dynamic range for all electrodes at all time points was below 60 $\mu C/cm^2$.

Voltages Figure 5.3B shows the minimum voltage (reported in absolute value) observed during stimulation at threshold and tonic contraction. Implantable pulse generators (IPG) usually have a voltage compliance around 10.5 to 12 V. Given the results, it seems like the impedance of the electrodes would had been too high to stimulate within voltage compliance with an IPG. This could be due to poor contact of electrodes to the tissue, or an intrinsic limitation of the interconnects sheet resistance that might be too high. Figures 5.3 C and D, show the voltage transients raw data at threshold and maximum contraction, respectively.
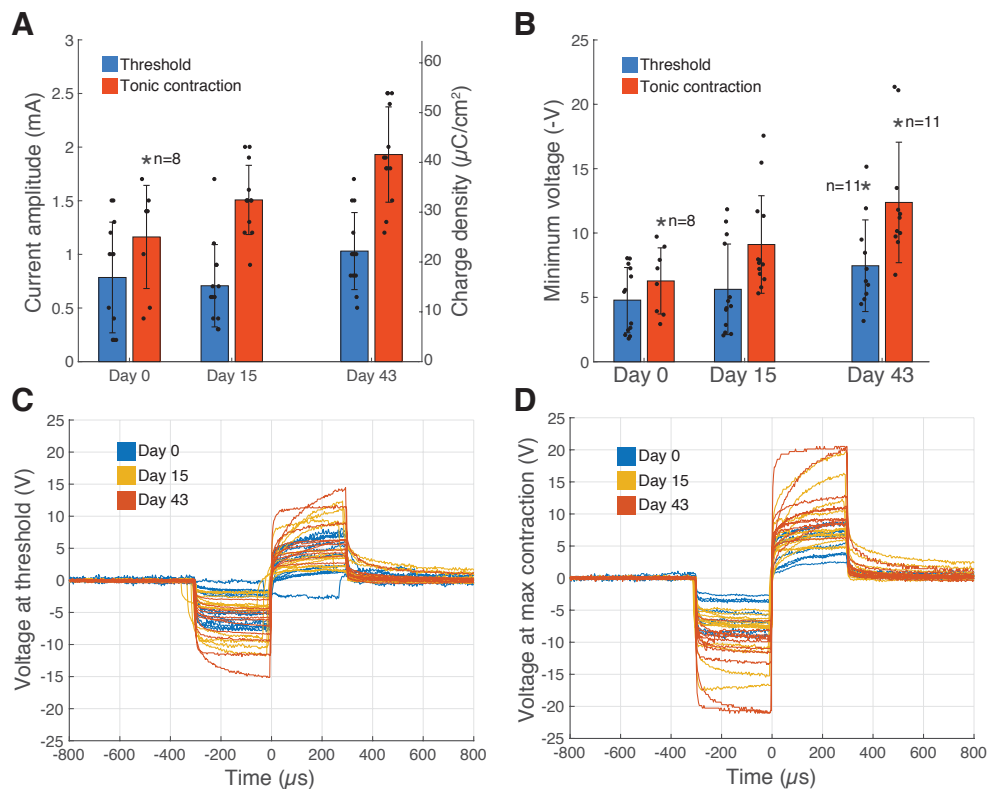
Figure 5.3 – **Epidural electrical stimulation with spinal implants.** (**A**) Current stimulation thresholds (in blue) and currents of maximum muscle contraction (in red) at various implantation days. The left y-axis shows the current amplitude and the right y-axis indicates the corresponding charge density. (**B**) Corresponding minimum voltage measured during stimulation at threshold (in blue) and at maximum tonic contraction (in red). (**C**) Voltage transients at threshold stimulation amplitude at various time points for all electrodes. (**D**) Voltage transients at maximum contraction stimulation amplitude. Total of n = 15 samples in all figures, unless otherwise stated. Error bars denote standard deviation.

5.3.4 Impedance evolution

Impedance spectroscopy Electrochemical impedance spectroscopy (EIS) was performed on all electrodes in vitro before and after implantation. EIS was also performed in vivo on the day of implantation and on days 15 and 43 post-implantation. The impedance spectra of all electrodes at different time points are shown in Figure 5.4A.

In vivo impedances The impedance at 1 kHz was extracted and plotted in Figure 5.4B. A large range of impedances was observed in vivo, between 4 and 24 kΩ with large variations across time points, even though the average impedance remained relative stable at 10.8 ± 4.1 kΩ, 7.3 ± 4.2 kΩ and 10.3 ± 6.2 kΩ on days 0, 15 and 43, respectively.

In vitro impedances In vitro impedances before implantation were in average 3.0 ± 1.3 kΩ, and 3.7 ± 0.9 kΩ after implantation. Two electrodes were discarded from the measurements after implantation, as they broke between days 15 and 43. These results show that the in vitro impedance of the electrodes remained quite stable and suggest that the electrodes survived quite well when implanted. This strengthen the hypothesis that the wide range of impedances observed in vivo combined to the wide range of stimulation thresholds are probably due to poor electrode-tissue interface. rather than electrode degradation.
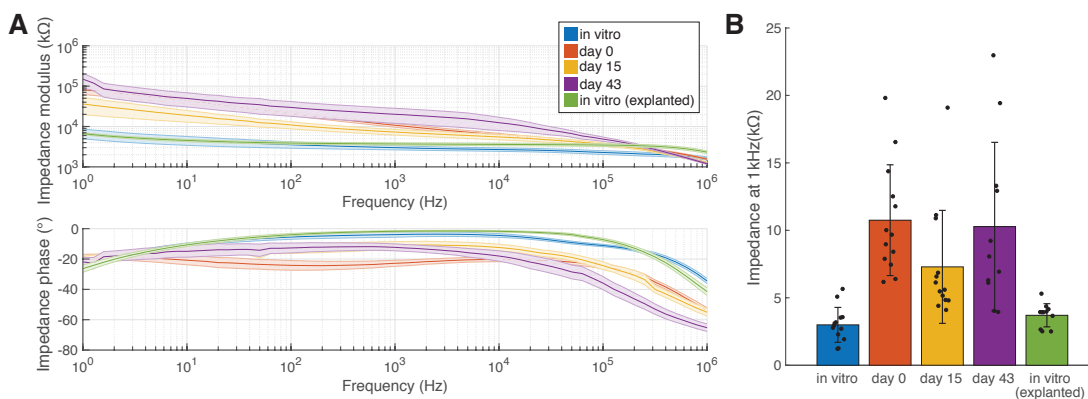
Figure 5.4 – **In vivo impedances of spinal array.** (**A**) Impedance spectra of all electrodes at different time points. (**B**) Impedance at 1 kHz for all electrodes at different time points. Shaded error bars represent standard error of the mean. Error bars represent standard deviation. The number of sample was n = 13 up to day 15, and n = 11 afterwards.

Failure analysis Visual inspection revealed that the failure of two electrodes was due to the thin-film delamination at the connector contact. This was due to the fact that the electrode contact was not well adhered to the silicone superstrate. This issue can be easily solved by increasing the contact pad surface such that a larger part remains bonded to the superstrate.

5.4 Conclusion

Summary   In this experiment, micro-patterned stretchable thin films embedded in silicone were used to tailor-make spinal implants for EES in NHPs. Two devices were fabricated, with a total of 13 functional electrodes and were implanted in two NHPs, in the sacral and lumbar portions of the spinal cord. Electrical stimulation was performed at three time points during the 43 days of implantation and was successful in eliciting movement of the hind-limbs. Impedance measurements revealed that two electrodes were broken during implantation, and visual inspection after explantation showed that this was caused by delamination of the thin films near the connector site. Interestingly, impedance measurements showed a wide range of values for the implanted arrays, while the in vitro impedances before implantation and after explanation showed that all functional electrodes had more or less the same impedance values. This raises the question why such a large range of impedances was observed in vivo. These results seem to indicate that large variations of impedance in vivo were due to the electrode-tissue interface. This is corroborated by the large variance of thresholds and maximum contraction stimulation amplitudes observed during implantation.

Limitations   The main limitation of this study is that the implantation period was too short (43 days) to clearly assess any trends in impedances and stimulation thresholds. The premature explantation of the array was due to infections believed to be caused by repeated skin incisions to expose the connector. It is thus hard to make any claims whether thresholds increased as a function of implantation time. The number of electrode was also too small (n = 13) to get any statistically significant data. Finally, more frequent stimulation during the implantation period could have allowed to better assess the long-term in vivo stimulation capability of the array. In particular, corrosion of the platinum micro-particles in the coating might be a concern.

Outlook   This study highlighted how the technology is versatile and allows the fabrication of neural implants at a larger scale, while facilitating the incorporation of personalized electrical layouts. Future studies should aim at implanting arrays for a longer duration (3 to 6 months). Achieving such long term studies would require alternative methods to access the connector. The use of a pedestal/connector system on the skull of the NHP could be a solution. Moreover, failure modes revealed the importance of designing appropriately the thin-films around the connector to avoid failures. Indeed, X-Rays imaging showed a steep S-shaped bend near the connector at the location where the array enters the epidural space between the vertebra and the spinal cord. Implementation of gradient structures such as the ones described in Chapter 2 could contribute to more robust devices. Moreover, implementation of frequent EES in the experimental protocol to assess long-term stimulation capability of the arrays, could be performed in the context of spinal cord injury research. Finally, these results indicate that the sheet resistance of the technology might be too high for this particular application and increasing the thickness of the metal layers might be necessary. However, this might lead to reduced stretchability and thus requires careful optimization.

6 Discussion and Perspectives

6.1 Discussion

6.1.1 New technology for stretchable bioelectronics

Requirements   The introduction of the thesis highlighted the importance of developing softer bioelectronic interfaces to replace current neural prosthesis that have a large biomechanical mismatch with neural tissues, because of their intrinsic stiffness. In particular, an emphasis was put on the electro-mechanical requirements of future stretchable interconnects to be used in the context of neural implants. Moreover, it was highlighted that the manufacturing techniques of new technologies should ideally be compatible with microfabrication and large-scale wafer processing to allow for the versatile fabrication of electrode arrays with a large range of dimensions and designs. These technologies should also be compatible with a wide use of materials, in order to facilitate their translation to medical grade materials.

Electro-mechanical characteristics   Here, these points were successfully addressed. Micro-patterning of Y-shaped motifs allowed to engineer reversible elasticity in multi-layers of plastic and metallic thin films (150 nm of platinum sandwiched between 2 µm of polyimide) encapsulated in an intrinsically stretchable silicone. It was demonstrated that these interconnects could reversible stretch up to 1 million cycles at an applied strain of 10%, while their resistance had only increased by 8-45%. It was also shown that these micro-patterned interconnects could stretch up to 80% before electrical and mechanical failure, whereas non-patterned tracks would electro-mechanically fail at strains below 5%. It was also shown that the integration of such interconnects in silicone minimally impacted the silicone elastic modulus as well as its capability to conform by capillarity to cylindrical surfaces with radii of curvature above 2 mm. Finally, it was possible to use this technology to pattern interconnects down to 20 µm in width, and electrodes with diameters as small as 100 µm.

This technology also allows the use of a large range of materials. For example, it should be possible to replace polyimide with parylene, whose use in the clinic is more widespread.

Context with other technologies   Technologies for stretchable bioelectronics are usually classified into two categories: (1) intrinsically stretchable materials, that use relative motion of micro-nano structures such as metallic nanowires, microcracked films or micro-particles to relieve strain while maintaining a percolating pathways. These techniques thus relay on the micro and nano-structures formed by stochastic processes. The other category (2) consists in more conventional materials that are designed into deterministic shapes to allow strain relief mechanisms, such as meanders, serpentines, fractal designs or horse-shoe geometries that can deform in-plane or out-of-plane to relieve strain. Interestingly, the micro-patterning of Y-shaped motifs presented here can be considered as a technology that tries to get the best of the two worlds. Indeed, the Y shapes are deterministic, and it was shown how it is possible to use relatively simple models to control and tune the electro-mechanical properties of patterned interconnects. However, unlike conventional techniques using tortuous designs, this patterning technique is isotropic and is engineered on a smaller scale than the electrical layout itself (micro-patterns ∼ 10 μm for interconnect layouts ∼ 100 μm in width and up to 5-8 cm in length). Thus, the micro-patterning can be made independently of the electrical layout, which facilitates greatly the design of stretchable electronic circuits.

6.1.2   Demonstration of functionality

This technology was also used, in conjunction with a previously described stretchable composite coating, to manufacture neural electrodes to interface with the central nervous system of various animal models. These devices were shown to successfully stimulate the auditory pathways in 4 mice over a period of 4 weeks, as well as the spinal cord of 2 monkeys over 6 weeks. Neural recordings were also shown to be possible with an ECoG grid used on the somatosensory cortex of a minipig, in an acute setting. These experiments demonstrated how versatile this technology can be, and how it can be used to fabricate various sizes of electrode grids, with electrode areas ranging from 0.008 mm^2 to 1.4 mm^2 and with the total number of electrodes ranging from 3 to 32.

6.1.3   Handling

One of the challenges associated with soft neural implants is their surgical handling to allow insertion into different regions of the body. These points were addressed successfully in this work, in the context of ABIs, for which their insertion into the laterall recess of the fourth ventricule can be challenging when using softer materials. A solution was proposed by using a hydrosoluble guide grafted at the back of the electrode array. This guide was used to temporarily rigidify the device during surgical insertion, as well as to facilitate handling with surgical tools (such as tweezers).

6.1.4 Imaging techniques

Compatibility with clinical imaging techniques is also an important factor to consider when developing neural implants. This is critical firstly as a post-operative procedure to make sure the device is correctly in place and to control for potential adverse events, for example subdural hematomas that might arise from ECoG implantation on the brain surface. Compatibility with imaging techniques is also important in order to offer the possibility to patients to go through imaging for other potential diseases or traumas that might arise throughout their lifetime. In this work, it was shown that even though these devices had no artefacts with MRI, they were also not visible at all, in the context of ABIs in a cadaveric head. MRI in phantom brain also showed no artefacts at the electrode levels, but the connector generated a large artefact. These observations suggest the necessity of using MRI markers to localize the device, as well as the use of appropriate connectors with non-ferromagnetic materials. CT scans on the other hand showed that in human cadaveric specimens, the ABI was visible but presented no artefact, compared to a clinical ABI that generated a large artefact. Finally, it was also shown that the electrode sites of a spinal implant were perfectly visible on X-Ray images.
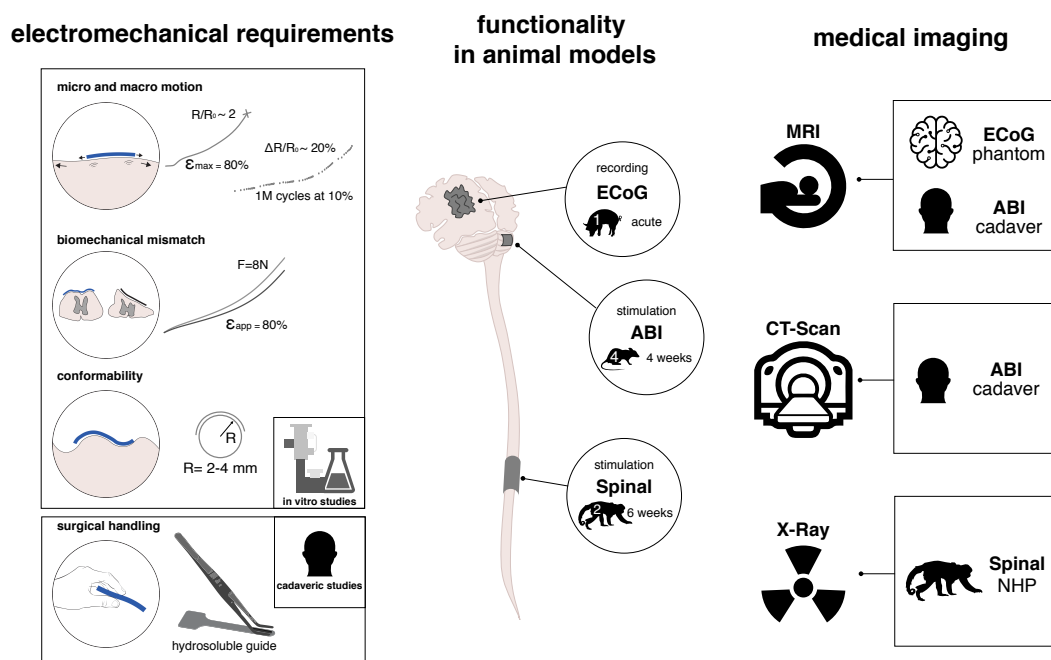
Figure 6.1 – **Summary and main achievement of thesis.** The images on the left show how the technology addresses the important mechanical challenges identifies in the introduction. The schematic in the center summarizes the three devices that were fabricated and specifies the animal models and target anatomical locations. The diagram on the right summarizes various imaging techniques that were tested with these devices.

6.2 Perspectives

6.2.1 Technology roadmap

Even though the technology was successfully tested in various animal models for implantation periods up to 6 weeks, major developments still need to be undertaken to push this technology to the clinic. The most critical issue is to guarantee long-term (> 10 years) adhesion of all the layers to avoid ingress of ionic fluids that will corrode the metal tracks. Even though the combination of polyimide with PDMS should guarantee proper functionality of the devices for a few months in vivo, defects and voids between the PDMS, polyimide and platinum layers might lead to water vapor condensation eventually leading to bubbles and delamination of the various layers, thus exposing the platinum to ionic fluids [75]. One possible solution is the use of non-organic ceramics, such as SiC (silicon carbide) that could be used around the platinum tracks. The challenge with such a material is that it is brittle and might be more sensitive to small local strains. Thus, optimization of the Y-shaped geometry might still be necessary. Accelerated ageing in wet environment, during stimulation, as well as under mechanical stress should then be performed to estimate the functionality of the device for a prolonged implantation time. The use of reactive accelerated ageing in oxygen peroxide should also be considered as an alternative method to mimic the in vivo environment.

The development of various types of neural interfaces in this work also revealed that in some contexts the sheet resistance of these micro-patterned interconnect (calculated to be around 15-20 Ω/sq.) might limit stimulation capabilities, with respect to compliance voltage limitations from implantable pulse generators (typically around 10-15 V). This was the case specifically for the spinal arrays. An obvious way of circumventing this issue is by increasing the thickness of platinum. However, similarly to adding SiC, these modifications might impact the mechanical performance of the device and proper mechanical analysis and optimization of the Y-shaped motifs might be necessary. Future work should also be carried out to implement strain gradients, that might provide better long-term reliability at the connector-interconnect interface.

Finally, the use of such a technology in the clinic will be greatly facilitated by the use of medical grade materials. A silicone replacement has already been suggested in the appendix, but process optimizations might still be necessary to replace the polyimide layers by a more suitable medical grade material such as parylene. Overall, the advantage of this technology is that it can be implemented on a large range of materials and the geometrical parameters of the Y shapes can be tuned to obtain a large range of electro-mechanical characteristics which might be more suitable for certain materials and/or applications.

6.2.2 Auditory brainstem implants

The ABI was one of the main focus as an application for this technology. The main hypotheses were that a better contact of the electrodes to the CN as well as a mechanically more stable interface compared to current rigid clinical devices, would ameliorate ABI outcomes in patients, in terms of speech perception. One of the challenges to test these hypotheses is the requirements to fabricate and surgically implant a soft ABI in the lateral recess of the fourth ventricle, to access the CN surface. These challenges were addressed successfully thanks to this technology. The analysis of human MRI reconstructions and brainstem histological sections motivated the use of a soft array that could conform to the curvature of the CN. These measurements were used to demonstrate a proof-of-concept for using a soft ABI to replace the conventional rigid arrays currently used in the clinic, by showing the capability of surgically handling and implanting such an array in cadaveric specimens. Moreover, it was shown that implantation of the soft ABI was feasible in cadaveric specimen, and that the grafting of a hydro-soluble mechanical guide to temporary stiffen the array allowed an even greater ease of insertion of the implant in the recess. In addition, the use of a stretchable coating with high electrochemical area increased the electro-mechanical performance of the electrodes at the electrode-tissue interface, compared to the conventional platinum electrodes currently used in ABIs.

The same technology was also used to manufacture miniaturized mouse ABIs that could activate the auditory pathways through electrical stimulation of the CN surface for up to four weeks. In vivo impedance spectroscopy also confirmed that the electrode remained functional for the entire duration of the implantation. Unfortunately, the proposed surgical procedure for the mouse ABI was quite different than the approach in humans, and didn't allow a fair comparison with clinical devices, such as evaluating the fixation of the ABI connector and cable to the bone or to evaluate the mechanical stability of the ABI over time. Moreover functional comparison of a soft and a rigid array is impossible in a mouse model due to the reduced size of the CN. A more appropriate model would be Non-Human Primates (NHPs), which have a similar anatomy as humans and thus could be implanted with an ABI with the same surgical approach, even though the paddle would need to be slightly reduced in size. Moreover, the chronic electrophysiological data in mice was not analyzed in depth, as it could provide some interesting insights onto the chronic effects of CN stimulation on the auditory pathways. Nevertheless, the ABI developed here was shown to be a good tool to pursue more fundamental research on mice to better understand the mechanisms of CN electrical stimulation, even though the mouse mortality rate of the surgery was quite high, due to brainstem suctioning.

The surgical approach in cadavers provided valuable insights and showed how using a temporary guide could improve surgical insertion of the device. However, the surgery was performed on cadaveric specimens, in which the anatomy can be quite different than in alive humans, making the surgery more difficult. Another current co-morbidity of an ABI surgery are schwanommas that can deform the anatomy and make the surgery much more difficult. Moreover, the

work presented here does not directly answer the question if a soft ABI would perform better than a rigid device in terms of speech perception in humans. Future work should therefore first address this question by using larger animals, such as NHPs, to compare chronically the differences between a soft and rigid device. Ultimately, a clinical trial will be the only way to assess with certainty if a soft ABI can provide better open-set speech perception in deaf patients.

6.2.3 New materials and applications

Transparent electrodes   The advantage of this micro-patterning technique is that a priori it could be used to pattern any kind of materials. For example this worked showed on the macro-scale that this technique could be used with ITO, an electrically conductive, brittle and transparent material. Thus, replacing the polyimide with for example parylene, and using ITO instead of platinum, could potentially allow the fabrication of transparent stretchable electrodes. The main challenges with such developments would be process optimization to etch ITO, as well as making sure the mechanics of these Y-shaped motifs have low enough local strains under elongation as to not fracture the ITO, which is a brittle material, compared to platinum which is more ductile.

Softer encapsulations   In the discussions in Chapter 2, it was also shown that the use of softer encapsulation materials could theoretically increase the stretchability of these interconnects. Future developments could thus envision the use of softer silicones (E ~ 100-500 kPa), or even the use of hydrogels (E < 100 kPa) to allow for even softer interfaces [236], while increasing their electro-mechanical performance under mechanical stress.

Integration of active components   In light of these proposed material modifications, one could envision new applications for this technology using active components. The use of polyimide as a carrier material with this technology can facilitate the wiring of active components such as LEDs (Light Emitting Diodes), multiplexers or other ASICs (Application-Specific Integrated Circuit) using different methods such as wire bonding or flip-chip [237–242]. In contrast, these techniques are not available for alternative technologies such as micro-cracked gold films on silicone, as the gold film is too thin (<50 nm) for wire-bonding, and the silicone might also thermally degrade during the process. Thus, these new possibilities open up the potential for other applications, such as the use of stretchable transparent electrodes in ITO combined with LEDs to fabricate opto-electronic devices. With the increased usage of optogenetics in neuroscience research [243–245], such a tool could be very interesting to study and compare the effects of electrical and optical stimulation on the nervous system [246].

Mechanically challenging environments   In the end, the developments showed in this work could also benefit other types of interfaces, that require softer materials, stretchable interconnects, and temporary rigidification strategies for surgical insertion. Anatomical locations with mechanically challenging environments, such as the heart [247–250] or bladder, are good examples of organs that experience large changes in volume, where such technologies could bring a great benefit compared to conventional stiff devices. Similarly, the handling techniques presented here using a hydro-soluble guide could allow the development of new devices to access other types of cavities, such as intrasulcular electrodes [72], or ECoGs that could be slid through small craniotomies between the brain and the skull using temporary guides.

A Appendix

A.1 Dogbone dimensions for macroscopic study
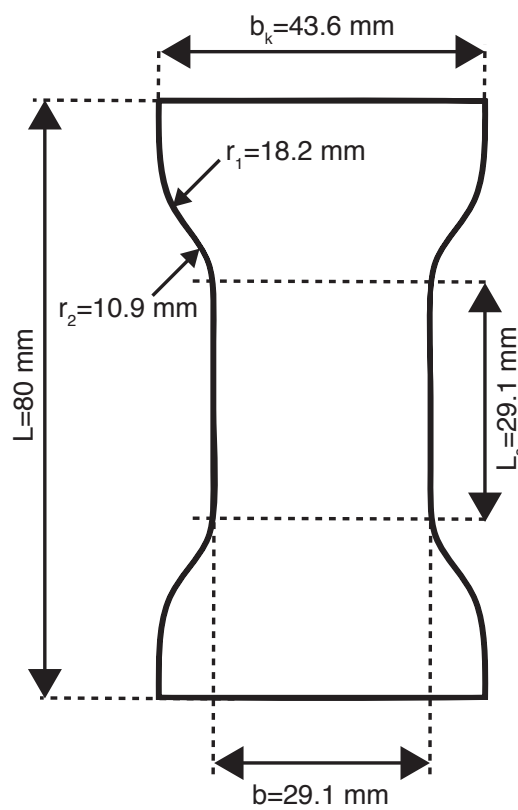
Figure A.1 – **Dogbone dimensions for macroscopic study.**

A.2 Mechanical characterization of medical grade silicone

Objective Important properties of Sylgard 184 and a medically approved alternative silicone, Nusil MED-6215 are characterized here: (1) the spin-coating properties, (2) their plasma-bonding capability and (3) their elastic modulus.

Spin-coating curve Both silicones were spin-coated at various target speeds (X, as defined in Fig. A.2A) on a $4''$ silicon wafer and cured at $80°C$. Their thickness was measured with an optical microscope. The resulting spin-coating curve (relationship between spin-coating speed and resulting thickness) shows similar results for both silicones (Fig. A.2B). This was expected as the viscosities of the sylgard 184 and the medical grade silicone are similar (respectivelly $5100cP$ and $5500cP$).
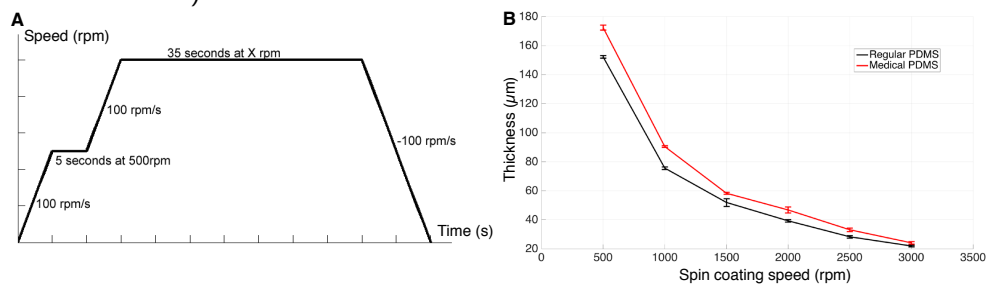
Figure A.2 – **Spin coating curve of silicones.** (**A**) Spin-coating protocol for a target speed X. (**B**) Silicone thickness as a function of spin-coating speed target X, for Sylgard 184 (black) and a medical grade silicone (red)

Plasma-bonding Two strips of the medical-grade silicone were partially bonded together after an oxygen plasma (on Fig. A.3). Both strips were then pulled away from each-other. Mechanical failure occurred first in the silicone, before the bonded region indicating a strong (or strong enough) bonding energy between the two layers.
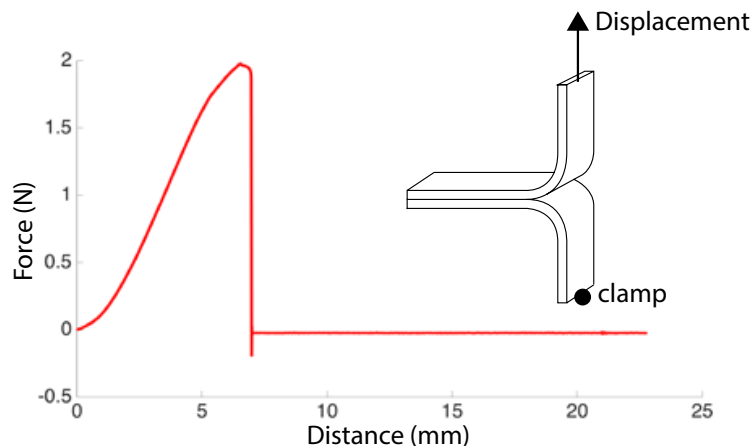
Figure A.3 – **Force displacement curve for plasma bonding test.** Two strips of medical grade silicone were plasma-bonded to each-other (inset) and pulled from eachother until mechanical failure. The plot shows the corresponding force-displacement curve

Elastic modulus   Each silicone was spin-coated to a target thickness of $200 \mu m$ and cut in a dogbone shape following DIN 53504:2009-10 [251]. The samples were then stretched until failure (Fig.A.4A inset). The corresponding stress-strain curves for both silicones are shown in Fig.A.4A (n=8 for each silicone). The elastic modulus was extracted for each silicone, resulting into very close values for both silicones ($E = 1.5MPa$ and $E = 2.2MPa$, for the regular and medical grade silicone respectively, Fig. A.4B).
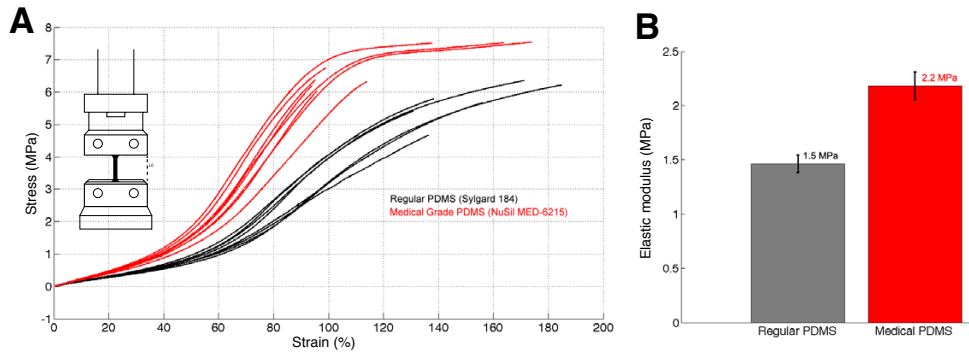
Figure A.4 – **Mechanical properties of regular and medical grade silicone.** (**A**) Stress-strain curves of dogbone cut films of regular (black) and medical grade silicones (red). (**B**) Average and standard deviation of the elastic modulus for each silicone (n=8).

Conclusion   These tests show that the medical grade silicone has similar properties as the Sylgard 184, suggesting that both silicones can be used interchangeabily and should not affect the mechanical properties and processing of the devices presented in this thesis.

A.3   Smooth Y-Shaped optimization: values

Table A.1 shows the actual values obtained from the FEA optimization.

Table A.1 – **Summary of results for the optimization study.** The first two columns give the value of parameters a and r that were tested. The 3rd column gives the corresponding maximum local strain calculated by ABAQUS on the structure for an applied strain of 20%. The 4th column gives the relative change in resistance calculated by COMSOL relative to a track made of non-patterned (bare) Pt.

a (mm)	r (mm)	Max local strain (%)	Relative resistance R/R_{Pt}
13	4	68.41	3.58
14	4	57.71	3.96
15	4	38.59	4.29
16	4	26.12	4.56
11	5	67.06	3.72
12	5	53.27	4.3
13	5	41.08	4.92
14	5	27.47	5.53
15	5	15.38	6.04
16	5	8.2	6.41
9	6	63.55	3.63
10	6	53.27	4.37
11	6	40.75	5.29
12	6	30.17	6.42
13	6	19	7.69
14	6	9.9	8.94
15	6	5	9.92
16	6	3	10.41
8	7	53.7	4.13
9	7	42.57	5.21
10	7	34.21	6.77
11	7	22.83	9.09
12	7	12.3	12.56
13	7	5.96	17.47
14	7	3.53	23.29
15	7	2.48	27.51
16	7	1.96	27.48
10	8	21.63	15.39
13.75	5.25	22.44	5.95
16	5.5	4.7	7.94

A.4   Mechanical properties of materials used in mechanical studies

Table A.2 summarizes the mechanical properties (elastic modulus and Poisson's ratios) of the materials used in the mechanical studies [133, 252].

Table A.2 – **Mechanical properties of various materials used in the mechanical studies.**

Material	Elastic modulus	Poisson's ratio
Sylgard 184	1 MPa	0.49
Polyimide (PI)	2.5 GPa	0.34
Titanium (Ti)	110 GPa	0.32
Platinum (Pt)	171 GPa	0.39
Silicon oxide (SiO_2)	66.3 GPa	0.15

A.5 Fabrication of brain structures in agarose

The brain structures were reconstructed from a high-resolution MRI (voxel size of $250\mu m$) and exported to a STL (Standard Triangle Language) file (Fig. A.5A). The STL files were then printed by stereolithography with a Formlabs Standard Resin ($100\mu m$ resolution) to generate the positive molds (Fig. A.5B).

The positive molds were then casted with a 2-parts silicone (Ecoflex) inside a plastic recipient, degassed for 15 minutes to remove any large bubbles, and cured at $80°C$ for 3 hours. The silicone (negative mold) was then removed manually from the positive form (Fig. A.5C).

Agarose (Agarose DNA Grade (100 bp - 23 kb), Electran for electrophoresis) was finally diluted into deionized water ($1.5\% w/w$) by heating up the solution in a micro-wave until the solution was clear. The agarose solution was then poured into the two parts of the negative mold and kept at $3°C$ for at least 60 minutes. An additional solution of agarose ($50mL$) was made at $3\% w/w$ and was used to glue the two parts of the mold together (Fig. A.5D).
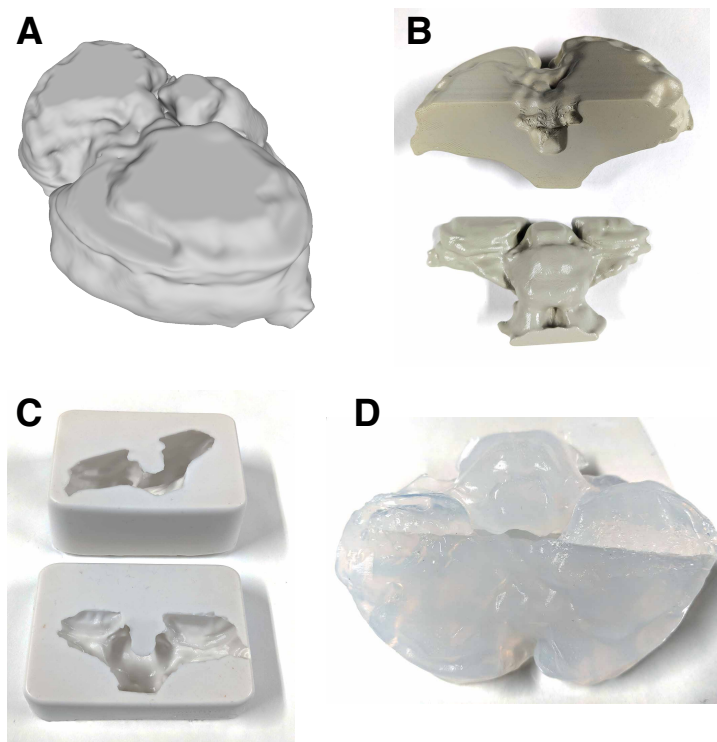
Figure A.5 – **Fabrication process of brain structures in agarose.** (**A**) 3D file of the brain structure reconstructed from an MRI. (**B**) 3D printed two-parts positive molds using stereolithography. (**C**) Negative molds in silicone. (**D**) Final agarose brain structures glued together.

A.6 Acoustically evoked ABRs
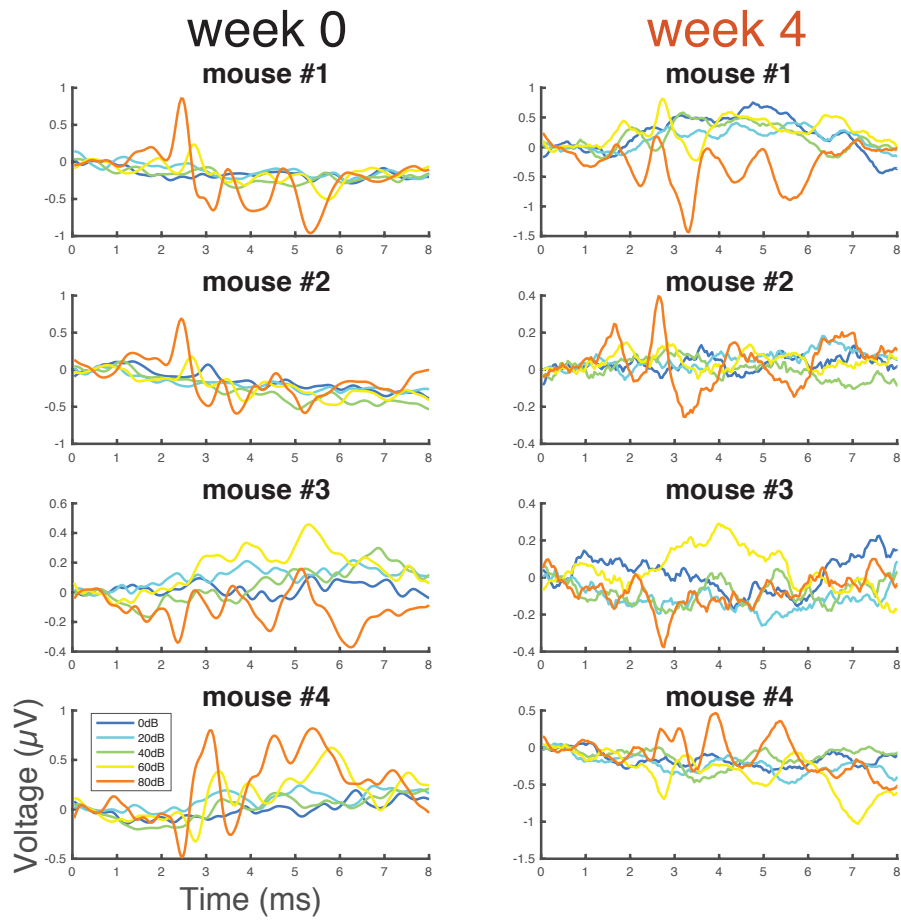
Figure A.6 – **Acoustically evoked ABRs for all 4 mice.** Acoustically evoked Auditory Brainstem Responses (aABRs) using broad-band noise. Each row is a different mouse, and the two columns show data for weeks 0 and 4. Each aABR color represents a different sound intensity.

A.7   IC acoustic Calibration
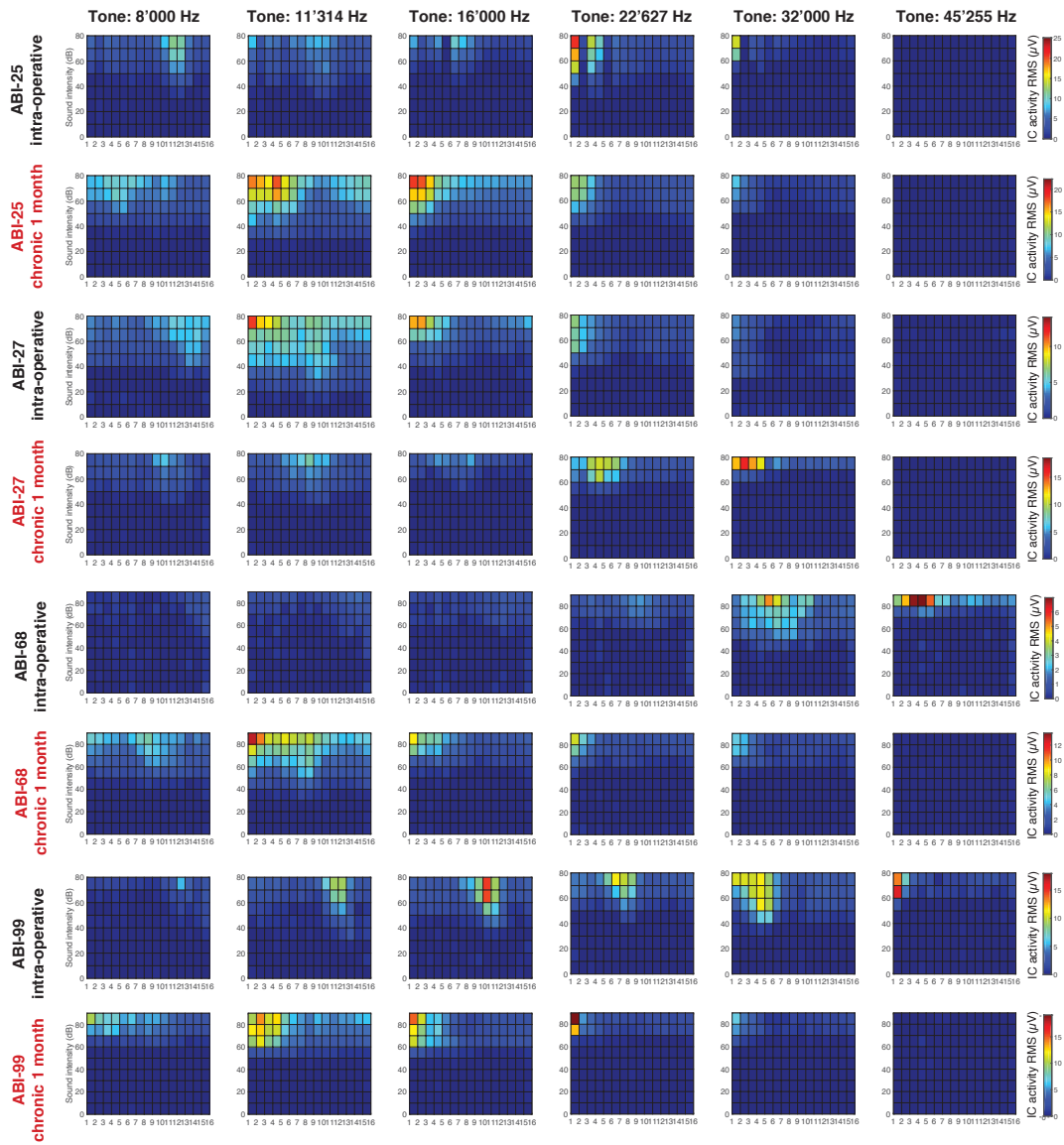
Figure A.7 – **Acoustic calibration of IC probe in all 4 mice.** Each map shows the IC activity RMS as a function of IC electrode number (x-axis) and of sound intensity (y-axis). Each pair of rows shows data for weeks 0 and 4 for a given mouse. Each column is a different acoustic tone frequency.

A.8 Monopolar eABRs
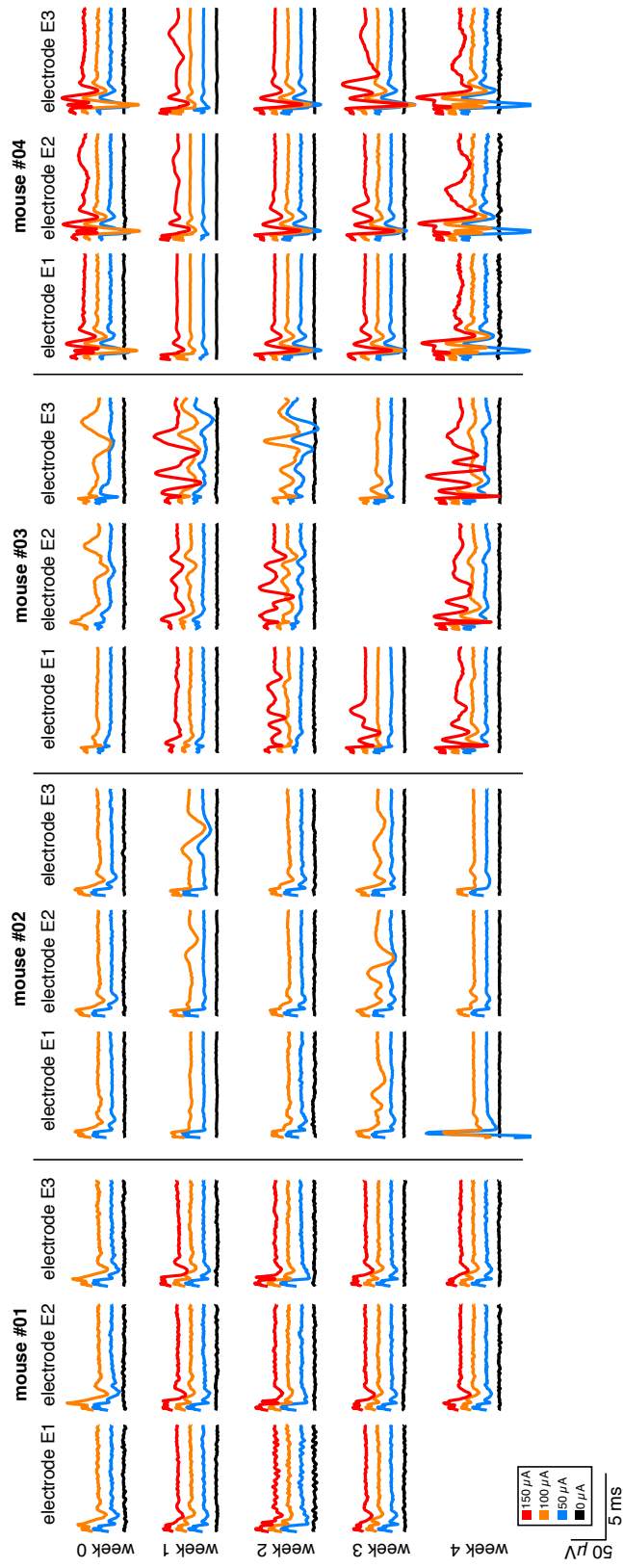
Figure A.8 – **Monopolar eABRs across all mice.** Data shown at different time points.

A.9 Monopolar IC activity
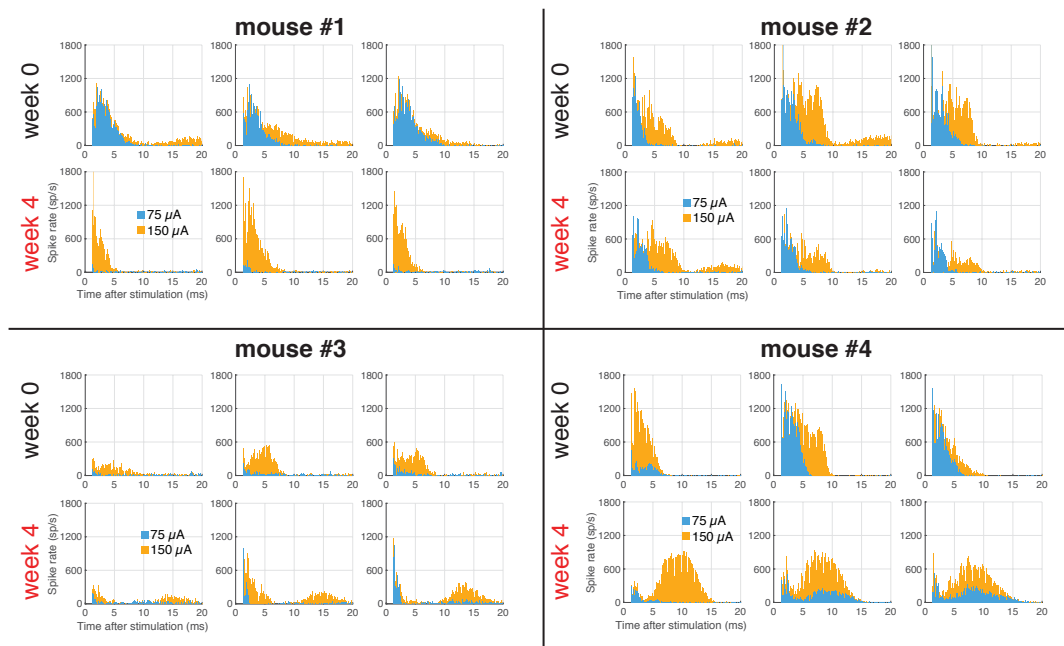
Figure A.9 – **PSTHs of IC activity upon monopolar eABRs across all mice.** Post-Stimulus Time Histograms at weeks 0 and 4.

A.10   MRI parameters for artefact testing - T1 Sequence

SIEMENS MAGNETOM Prisma

TA: 4:44 PM: FIX Voxel size: 1.0×1.0×1.0 mmPAT: 2 Rel. SNR: 1.00 : tfl

Properties

Prio recon	Off
Load images to viewer	On
Inline movie	Off
Auto store images	On
Load images to stamp segments	Off
Load images to graphic segments	Off
Auto open inline display	Off
Auto close inline display	Off
Start measurement without further preparation	Off
Wait for user to start	On
Start measurements	Single measurement

Routine

Slab group	1
Slabs	1
Dist. factor	50 %
Position	R1.8 A13.5 F30.5 mm
Orientation	Sagittal
Phase enc. dir.	A >> P
AutoAlign	Head > Brain
Phase oversampling	0 %
Slice oversampling	15.4 %
Slices per slab	208
FoV read	256 mm
FoV phase	100.0 %
Slice thickness	1.00 mm
TR	2300.0 ms
TE	2.25 ms
Averages	1
Concatenations	1
Filter	Prescan Normalize
Coil elements	HC1-7;NC1,2

Contrast - Common

TR	2300.0 ms
TE	2.25 ms
Magn. preparation	Non-sel. IR
TI	900 ms
Flip angle	8 deg
Fat suppr.	None
Water suppr.	None

Contrast - Dynamic

Averages	1
Averaging mode	Long term
Reconstruction	Magnitude
Measurements	1
Multiple series	Each measurement

Resolution - Common

FoV read	256 mm
FoV phase	100.0 %
Slice thickness	1.00 mm
Base resolution	256
Phase resolution	100 %
Slice resolution	100 %
Phase partial Fourier	7/8
Slice partial Fourier	7/8
Interpolation	Off

Resolution - iPAT

PAT mode	GRAPPA
Accel. factor PE	2
Ref. lines PE	24
Accel. factor 3D	1
Reference scan mode	Integrated

Resolution - Filter Image

Image Filter	Off
Distortion Corr.	Off
Prescan Normalize	On
Unfiltered images	Off
Normalize	Off
B1 filter	Off

Resolution - Filter Rawdata

Raw filter	Off
Elliptical filter	Off

Geometry - Common

Slab group	1
Slabs	1
Dist. factor	50 %
Position	R1.8 A13.5 F30.5 mm
Orientation	Sagittal
Phase enc. dir.	A >> P
Slice oversampling	15.4 %
Slices per slab	208
FoV read	256 mm
FoV phase	100.0 %
Slice thickness	1.00 mm
TR	2300.0 ms
Multi-slice mode	Single shot
Series	Ascending
Concatenations	1

Geometry - AutoAlign

Slab group	1
Position	R1.8 A13.5 F30.5 mm
Orientation	Sagittal
Phase enc. dir.	A >> P
AutoAlign	Head > Brain
Initial Position	R1.8 A13.5 F30.5
R	1.8 mm
A	13.5 mm
F	30.5 mm
Initial Rotation	-9.53 deg
Initial Orientation	Sagittal

Geometry - Navigator

System - Miscellaneous

Positioning mode	FIX
Table position	H
Table position	0 mm
MSMA	S - C - T
Sagittal	R >> L
Coronal	A >> P
Transversal	F >> H
Coil Combine Mode	Adaptive Combine
Save uncombined	Off

Figure A.10 – **MRI T1 sequence parameters for artefact testing (part 1).**

SIEMENS MAGNETOM Prisma

System - Miscellaneous

Matrix Optimization	Off
AutoAlign	Head > Brain
Coil Select Mode	Off - AutoCoilSelect

System - Adjustments

B0 Shim mode	Tune up
B1 Shim mode	TrueForm
Adjust with body coil	Off
Confirm freq. adjustment	Off
Assume Dominant Fat	Off
Assume Silicone	Off
Adjustment Tolerance	Auto

System - Adjust Volume

Position	Isocenter
Orientation	Transversal
Rotation	0.00 deg
A >> P	263 mm
R >> L	350 mm
F >> H	350 mm
Reset	Off

System - pTx Volumes

B1 Shim mode	TrueForm
Excitation	Non-sel.

System - Tx/Rx

Frequency 1H	123.257291 MHz
Correction factor	1
Gain	Low
Img. Scale Cor.	1.000
Reset	Off
? Ref. amplitude 1H	0.000 V

Physio - Signal1

1st Signal/Mode	None
TR	2300.0 ms
Concatenations	1

Physio - Cardiac

Magn. preparation	Non-sel. IR
TI	900 ms
Fat suppr.	None
Dark blood	Off
FoV read	256 mm
FoV phase	100.0 %
Phase resolution	100 %

Physio - PACE

Resp. control	Off
Concatenations	1

Inline - Common

Subtract	Off
Measurements	1
StdDev	Off
Save original images	On

Inline - MIP

MIP-Sag	Off
MIP-Cor	Off
MIP-Tra	Off
MIP-Time	Off

Inline - MIP

Save original images	On

Inline - Composing

Distortion Corr.	Off

Sequence - Part 1

Introduction	On
Dimension	3D
Elliptical scanning	Off
Reordering	Linear
Asymmetric echo	Allowed
Flow comp.	No
Multi-slice mode	Single shot
Echo spacing	6.8 ms
Bandwidth	200 Hz/Px

Sequence - Part 2

RF pulse type	Normal
Gradient mode	Normal
Excitation	Non-sel.
RF spoiling	On
Incr. Gradient spoiling	Off
Turbo factor	210

Sequence - Assistant

Mode	Off

Figure A.11 – **MRI T1 sequence parameters for artefact testing (part 2).**

A.11 MRI parameters for artefact testing - T2 Sequence

SIEMENS MAGNETOM Prisma

TA: 6:56 PM: FIX Voxel size: 0.5×0.5×0.5 mmPAT: Off Rel. SNR: 1.00 : spcR

Properties

Prio recon	Off
Load images to viewer	On
Inline movie	Off
Auto store images	On
Load images to stamp segments	Off
Load images to graphic segments	Off
Auto open inline display	Off
Auto close inline display	Off
Start measurement without further preparation	Off
Wait for user to start	Off
Start measurements	Single measurement

Routine

Slab group	1
Slabs	1
Position	R12.7 A28.1 F0.9 mm
Orientation	S > C-29.2 > T-16.8
Phase enc. dir.	A >> P
AutoAlign	---
Phase oversampling	10 %
Slice oversampling	16.7 %
Slices per slab	96
FoV read	153 mm
FoV phase	100.0 %
Slice thickness	0.50 mm
TR	1400 ms
TE	98 ms
Averages	1.7
Concatenations	1
Filter	Raw filter, Prescan Normalize
Coil elements	HC1-7;NC1,2

Contrast - Common

TR	1400 ms
TE	98 ms
MTC	Off
Magn. preparation	None
Flip angle	120 deg
Fat suppr.	None
Blood suppr.	Off
Restore magn.	On

Contrast - Dynamic

Averages	1.7
Reconstruction	Magnitude
Measurements	1
Multiple series	Each measurement

Resolution - Common

FoV read	153 mm
FoV phase	100.0 %
Slice thickness	0.50 mm
Base resolution	320
Phase resolution	100 %
Slice resolution	50 %
Phase partial Fourier	Allowed
Slice partial Fourier	7/8
Interpolation	Off

Resolution - iPAT

PAT mode	None

Resolution - Filter Image

Image Filter	Off
Distortion Corr.	Off
Prescan Normalize	On
Unfiltered images	Off
Normalize	Off
B1 filter	Off

Resolution - Filter Rawdata

Raw filter	On
Elliptical filter	Off

Geometry - Common

Slab group	1
Slabs	1
Position	R12.7 A28.1 F0.9 mm
Orientation	S > C-29.2 > T-16.8
Phase enc. dir.	A >> P
Slice oversampling	16.7 %
Slices per slab	96
FoV read	153 mm
FoV phase	100.0 %
Slice thickness	0.50 mm
TR	1400 ms
Series	Ascending
Concatenations	1

Geometry - AutoAlign

Slab group	1
Position	R12.7 A28.1 F0.9 mm
Orientation	S > C-29.2 > T-16.8
Phase enc. dir.	A >> P
AutoAlign	---
Initial Position	R12.7 A28.1 F0.9
R	12.7 mm
A	28.1 mm
F	0.9 mm
Initial Rotation	0.00 deg
Initial Orientation	S > C
S > C	-29.2
> T	-16.8

Geometry - Saturation

Fat suppr.	None
Restore magn.	On
Special sat.	None

Geometry - Navigator

System - Miscellaneous

Positioning mode	FIX
Table position	H
Table position	0 mm
MSMA	S - C - T
Sagittal	R >> L
Coronal	A >> P
Transversal	F >> H
Coil Combine Mode	Adaptive Combine

Figure A.12 – **MRI T2 sequence parameters for artefact testing (part 1).**

SIEMENS MAGNETOM Prisma

System - Miscellaneous

Save uncombined	Off
Matrix Optimization	Performance
AutoAlign	---
Coil Select Mode	Off - AutoCoilSelect

System - Adjustments

B0 Shim mode	Tune up
B1 Shim mode	Volume-selective
Adjust with body coil	Off
Confirm freq. adjustment	Off
Assume Dominant Fat	Off
Assume Silicone	Off
Adjustment Tolerance	Auto

System - Adjust Volume

Position	Isocenter
Orientation	Transversal
Rotation	0.00 deg
A >> P	263 mm
R >> L	350 mm
F >> H	350 mm
Reset	Off

System - pTx Volumes

B1 Shim mode	Volume-selective
Excitation	Slab-sel.
pTx Volume	1
Vol. Property	B1 Shim Vol.
Position	R24.5 A4.0 F3.5 mm
Orientation	C > S33.5 > T-2.6
Rotation	-70.69 deg
F >> H	68 mm
R >> L	55 mm
A >> P	51 mm
Vol. Visibility	On

System - Tx/Rx

Frequency 1H	123.257291 MHz
Correction factor	1
Gain	High
Img. Scale Cor.	1.000
Reset	Off
? Ref. amplitude 1H	0.000 V

Physio - Signal1

1st Signal/Mode	None
Trigger delay	0 ms
TR	1400 ms
Concatenations	1

Physio - Cardiac

Magn. preparation	None
Fat suppr.	None
Dark blood	Off
FoV read	153 mm
FoV phase	100.0 %
Phase resolution	100 %

Physio - PACE

Resp. control	Off
Concatenations	1

Inline - Common

Subtract	Off
Measurements	1
StdDev	Off
Save original images	On

Inline - MIP

MIP-Sag	Off
MIP-Cor	Off
MIP-Tra	Off
MIP-Time	Off
Save original images	On

Inline - Composing

Distortion Corr.	Off

Sequence - Part 1

Introduction	On
Dimension	3D
Elliptical scanning	Off
Reordering	Linear
Flow comp.	No
Echo spacing	6.7 ms
Adiabatic-mode	Off
Bandwidth	289 Hz/Px

Sequence - Part 2

Echo train duration	422 ms
RF pulse type	Normal
Gradient mode	Fast
Excitation	Slab-sel.
Flip angle mode	Constant
Turbo factor	98

Sequence - Assistant

Allowed delay	30 s

Figure A.13 – **MRI T2 sequence parameters for artefact testing (part 2).**

A.12 MRI parameters for temperature testing

SIEMENS MAGNETOM Prisma

TA: 2:55 PM: REF Voxel size: 0.4×0.4×2.0 mmPAT: 2 Rel. SNR: 1.00 : tse

Properties

Prio recon	Off
Load images to viewer	On
Inline movie	Off
Auto store images	On
Load images to stamp segments	Off
Load images to graphic segments	Off
Auto open inline display	Off
Auto close inline display	Off
Start measurement without further preparation	Off
Wait for user to start	On
Start measurements	Single measurement

Routine

Slice group	1
Slices	24
Dist. factor	20 %
Position	R1.7 P1.4 F14.6 mm
Orientation	Sagittal
Phase enc. dir.	A >> P
AutoAlign	---
Phase oversampling	40 %
FoV read	180 mm
FoV phase	100.0 %
Slice thickness	2.0 mm
TR	1190.0 ms
TE	6.7 ms
Averages	3
Concatenations	2
Filter	Prescan Normalize, Elliptical filter
Coil elements	HC1-7;NC1,2

Contrast - Common

TR	1190.0 ms
TE	6.7 ms
TD	0.0 ms
MTC	Off
Magn. preparation	None
Flip angle	150 deg
Fat suppr.	None
Water suppr.	None
Restore magn.	Off

Contrast - Dynamic

Averages	3
Averaging mode	Long term
Reconstruction	Magnitude
Measurements	1
Multiple series	Each measurement

Resolution - Common

FoV read	180 mm
FoV phase	100.0 %
Slice thickness	2.0 mm
Base resolution	256
Phase resolution	80 %
Phase partial Fourier	Off
Trajectory	Cartesian
Interpolation	On

Resolution - iPAT

PAT mode	GRAPPA
Accel. factor PE	2
Ref. lines PE	32
Reference scan mode	Self-calibration

Resolution - Filter Image

Image Filter	Off
Distortion Corr.	Off
Prescan Normalize	On
Unfiltered images	Off
Normalize	Off
B1 filter	Off

Resolution - Filter Rawdata

Raw filter	Off
Elliptical filter	On

Geometry - Common

Slice group	1
Slices	24
Dist. factor	20 %
Position	R1.7 P1.4 F14.6 mm
Orientation	Sagittal
Phase enc. dir.	A >> P
FoV read	180 mm
FoV phase	100.0 %
Slice thickness	2.0 mm
TR	1190.0 ms
Multi-slice mode	Interleaved
Series	Interleaved
Concatenations	2

Geometry - AutoAlign

Slice group	1
Position	R1.7 P1.4 F14.6 mm
Orientation	Sagittal
Phase enc. dir.	A >> P
AutoAlign	---
Initial Position	R1.7 P1.4 F14.6
R	1.7 mm
P	1.4 mm
F	14.6 mm
Initial Rotation	0.00 deg
Initial Orientation	Sagittal

Geometry - Saturation

Sat. region	1
Thickness	80 mm
Position	L1.1 A111.9 F15.4 mm
Orientation	C > T-7.8 > S0.5
Shape	Standard
Water suppr.	None
Restore magn.	Off
Special sat.	None

Geometry - Navigator

System - Miscellaneous

Positioning mode	REF
Table position	H

Figure A.14 – **MRI parameters for temperature testing (part 1).**

System - Miscellaneous

Table position	0 mm
MSMA	S - C - T
Sagittal	R >> L
Coronal	A >> P
Transversal	F >> H
Coil Combine Mode	Adaptive Combine
Save uncombined	Off
Matrix Optimization	Off
AutoAlign	---
Coil Select Mode	Off - AutoCoilSelect

System - Adjustments

B0 Shim mode	Tune up
B1 Shim mode	TrueForm
Adjust with body coil	Off
Confirm freq. adjustment	Off
Assume Dominant Fat	Off
Assume Silicone	Off
Adjustment Tolerance	Auto

System - Adjust Volume

Position	Isocenter
Orientation	Transversal
Rotation	0.00 deg
A >> P	263 mm
R >> L	350 mm
F >> H	350 mm
Reset	Off

System - pTx Volumes

B1 Shim mode	TrueForm

System - Tx/Rx

Frequency 1H	123.257291 MHz
Correction factor	1
Gain	High
Img. Scale Cor.	1.000
Reset	Off
? Ref. amplitude 1H	0.000 V

Physio - Signal1

1st Signal/Mode	None
TR	1190.0 ms
Concatenations	2

Physio - Cardiac

Magn. preparation	None
Fat suppr.	None
Dark blood	Off
FoV read	180 mm
FoV phase	100.0 %
Phase resolution	80 %
Trajectory	Cartesian

Physio - PACE

Resp. control	Off
Concatenations	2

Inline - Common

Subtract	Off
Measurements	1
StdDev	Off
Save original images	On

Inline - MIP

MIP-Sag	Off
MIP-Cor	Off
MIP-Tra	Off
MIP-Time	Off
Save original images	On

Inline - Composing

Distortion Corr.	Off

Sequence - Part 1

Introduction	On
Dimension	2D
Compensate T2 decay	Off
Reduce Motion Sens.	On
Contrasts	1
Flow comp.	No
Multi-slice mode	Interleaved
Free echo spacing	Off
Echo spacing	6.65 ms
Bandwidth	399 Hz/Px

Sequence - Part 2

Define	Turbo factor
Echo trains per slice	24
Phase correction	Automatic
Acoustic noise reduction	None
RF pulse type	Fast
Gradient mode	Fast
Hyperecho	Off
WARP	Off
Red. EC sensitivity	Off
Turbo factor	6

Sequence - Assistant

Mode	Min flip angle
Min flip angle	130 deg
Allowed delay	60 s

Figure A.15 – **MRI parameters for temperature testing (part 2).**

Bibliography

[1] NIDCD, "Cochlear Implants." [Accessed 08.11.2018]. Available from: http://www.nidcd.nih.gov/health/hearing/pages/coch.aspx, 2013.

[2] M. S. Schwartz, S. R. Otto, R. V. Shannon, W. E. Hitselberger, and D. E. Brackmann, "Auditory brainstem implants.," *Neurotherapeutics : the journal of the American Society for Experimental NeuroTherapeutics*, vol. 5, pp. 128–36, jan 2008.

[3] J. S. Perlmutter and J. W. Mink, "Deep Brain Stimulation," *Annual Review of Neuroscience*, vol. 29, no. 1, pp. 229–257, 2006.

[4] R. B. North, D. H. Kidd, M. Zahurak, C. S. James, and D. M. Long, "Spinal Cord Stimulation for Chronic, Intractable Pain," *Neurosurgery*, vol. 32, pp. 384–395, mar 1993.

[5] FDA, "Argus II Retinal Prosthesis System - H110002," *FDA Report*, 2013.

[6] T. Yang, S. Hakimian, and T. H. Schwartz, "Intraoperative Eclctrocorticography(ECog): indications , techniques , and utility in epilepsy surgery," *Epileptic Disorder*, vol. 16, no. 3, pp. 271–279, 2014.

[7] L. R. Hochberg, D. Bacher, B. Jarosiewicz, N. Y. Masse, J. D. Simeral, J. Vogel, S. Haddadin, J. Liu, S. S. Cash, P. van der Smagt, and J. P. Donoghue, "Reach and grasp by people with tetraplegia using a neurally controlled robotic arm," *Nature*, vol. 485, no. 7398, pp. 372–375, 2012.

[8] P. Sisterson, Nathaniel D. (University of Pittsburgh School of Medicine Pittsburgh and P. Richardson, R. Mark (University of Pittsburgh School of Medicine Pittsburgh, "Long-Term Results of Responsive Neurostimulation in Different Seizure Onset Locations," *Neurosurgery*, vol. 70, no. 4, pp. 23–24, 2012.

[9] M. Capogrosso, T. Milekovic, D. Borton, F. Wagner, M. Moraud, J.-b. Mignardot, N. Buse, J. Gandar, D. Xing, E. Rey, S. Duis, Y. Jianzhong, W. K. D. Ko, P. Detemple, T. Denison, S. Micera, and E. Bezard, "Europe PMC Funders Group Europe PMC Funders Author Manuscripts A Brain – Spinal Interface Alleviating Gait Deficits after Spinal Cord Injury in Primates," *Nature*, vol. 539, no. 7628, pp. 284–288, 2017.

Bibliography

[10] A. Handforth, C. M. DeGiorgio, S. C. Schachter, B. M. Uthman, D. K. Naritoku, E. S. Tecoma, T. R. Henry, S. D. Collins, B. V. Vaughn, R. C. Gilmartin, D. R. Labar, G. L. Morris, M. C. Salinsky, I. Osorio, R. K. Ristanovic, D. M. Labiner, J. C. Jones, J. V. Murphy, G. C. Ney, and J. W. Wheless, "Vagus nerve stimulation therapy for partial-onset seizures: A randomized active-control trial," *Neurology*, vol. 51, no. 1, pp. 48–55, 1998.

[11] S. I. Ryu and K. V. Shenoy, "Human cortical prostheses: lost in translation?," *Neurosurgical Focus*, vol. 27, no. 1, p. E5, 2009.

[12] R. R. Harrison, P. T. Watkins, R. J. Kier, R. O. Lovejoy, D. J. Black, B. Greger, and F. Solzbacher, "A Low-Power Integrated Circuit for a Wireless 100-Electrode Neural Recording System," *IEEE Journal of Solid-State Circuits*, vol. 42, pp. 123–133, jan 2007.

[13] P. Gutruf and J. A. Rogers, "Implantable, wireless device platforms for neuroscience research," *Current Opinion in Neurobiology*, vol. 50, pp. 42–49, 2018.

[14] D. Reynolds, G. Z. Duray, R. Omar, K. Soejima, P. Neuzil, S. Zhang, C. Narasimhan, C. Steinwender, J. Brugada, M. Lloyd, P. R. Roberts, V. Sagi, J. Hummel, M. G. Bongiorni, R. E. Knops, C. R. Ellis, C. C. Gornick, M. A. Bernabei, V. Laager, K. Stromberg, E. R. Williams, J. H. Hudnall, and P. Ritter, "A Leadless Intracardiac Transcatheter Pacing System," *New England Journal of Medicine*, vol. 374, no. 6, pp. 533–541, 2016.

[15] S. F. Cogan, "Neural Stimulation and Recording Electrodes," *Annual Review of Biomedical Engineering*, vol. 10, no. 1, pp. 275–309, 2008.

[16] S. F. Cogan, K. A. Ludwig, C. G. Welle, and P. Takmakov, "Tissue damage thresholds during therapeutic electrical stimulation," *Journal of Neural Engineering*, vol. 13, p. 021001, apr 2016.

[17] C. Hassler, T. Boretius, and T. Stieglitz, "Polymers for neural implants," *Journal of Polymer Science Part B: Polymer Physics*, vol. 49, no. 1, pp. 18–33, 2011.

[18] R. Cowan, "New Approaches to Preserve Residual Hearing and Improve Performance for Cochlear Implant Recipients." [Accessed on: 20.11.2018]. Available from: https://www.audiology.org.nz/Userfiles/file/NZAS%202014_Cowan%20et%20al_Preserving%20Residual%20Hearing_July%202014.p   2014.

[19] J. Badia, S. Raspopovic, J. Carpaneto, S. Micera, and X. Navarro, "Spatial and functional selectivity of peripheral nerve signal recording with the transversal intrafascicular multichannel electrode (TIME)," *IEEE Transactions on Neural Systems and Rehabilitation Engineering*, vol. 24, no. 1, pp. 20–27, 2016.

[20] Frost and Sullivan, "Analysis of the U.S. Neurostimulation Market: Rapid Technology Advancements Paves New Opportunites and Boost the Market," tech. rep., Frost & Sullivan, 2013.

[21] M. Jorfi, J. L. Skousen, C. Weder, and J. R. Capadona, "Progress towards biocompatible intracortical microelectrodes for neural interfacing applications," *Journal of Neural Engineering*, vol. 12, p. 011001, feb 2015.

[22] Medtronic, "Specify™ 5-6-5 Implant Manual." [Accessed on 20.11.2018]. Available from: http://kategorizacia.mzsr.sk/Pomocky/Download/RequestAttachment/8526, 2009.

[23] Ad-Tech, "AdTech Product Catalogue." [Accessed on 20.11.2018]. Available from: https://www.severnhealthcare.com/images/documents/ad-tech/AD-TECHCatalogue-2015.pdf, 2014.

[24] Cochlear Ltd, "Cochlear Nucleus Profile Auditory Brainstem Implant (ABI541)." [Accessed on: 29.11.2018]. Available from: https://www.cochlear.com/uk/for-professionals/sound-connection/cochlear-widens-its-range-of-implantable-hearing-solutions, 2010.

[25] Cortec Gmbh, "Little Girl Overcomes Big Disease – Thanks to Latest Technology." [Accessed on 29.11.2018]. Available from: https://www.brainlinks-braintools.uni-freiburg.de/news/id/599/, 2017.

[26] X. Wang, C. A. Gkogkidis, O. Iljina, L. D. J. Fiederer, C. Henle, I. Mader, J. Kaminsky, T. Stieglitz, M. Gierthmuehlen, and T. Ball, "Mapping the fine structure of cortical activity with different micro-ECoG electrode array geometries," *Journal of Neural Engineering*, vol. 14, p. 056004, oct 2017.

[27] S. P. Lacour, G. Courtine, and J. Guck, "Materials and technologies for soft implantable neuroprostheses," *Nature Reviews Materials*, vol. 1, p. 16063, oct 2016.

[28] J.-W. Jeong, G. Shin, S. I. Park, K. J. Yu, L. Xu, and J. A. Rogers, "Soft Materials in Neuroengineering for Hard Problems in Neuroscience," *Neuron*, vol. 86, no. 1, pp. 175–186, 2015.

[29] D. Prodanov and J. Delbeke, "Mechanical and Biological Interactions of Implants with the Brain and Their Impact on Implant Design," *Frontiers in Neuroscience*, vol. 10, p. 11, feb 2016.

[30] a. K. Ommaya, "Mechanical properties of tissues of the nervous system.," *Journal of biomechanics*, vol. 1, no. 2, pp. 127–138, 1968.

[31] G. Fallenstein, V. Hulce, and J. Melvin, "Dynamic mechanical properties of human brain tissue," *Journal of Biomechanics*, vol. 2, no. 3, pp. 217–226, 1969.

[32] S. Cheng, E. C. Clarke, and L. E. Bilston, "Rheological properties of the tissues of the central nervous system: A review," *Medical Engineering and Physics*, vol. 30, no. 10, pp. 1318–1337, 2008.

[33] A. Goriely, M. G. Geers, G. A. Holzapfel, J. Jayamohan, A. Jérusalem, S. Sivalo-ganathan, W. Squier, J. A. van Dommelen, S. Waters, and E. Kuhl, "Mechanics of the brain: perspectives, challenges, and opportunities," *Biomechanics and Modeling in Mechanobiology*, vol. 14, no. 5, pp. 931–965, 2015.

[34] D. E. Harrison, R. Cailliet, D. D. Harrison, S. J. Troyanovich, and S. O. Harrison, "A review of biomechanics of the central nervous systempart III: Spinal cord stresses from postural loads and their neurologic effects," *Journal of Manipulative and Physiological Therapeutics*, vol. 22, no. 6, pp. 399–410, 1999.

[35] D. E. Koser, E. Moeendarbary, J. Hanne, S. Kuerten, and K. Franze, "CNS cell distribution and axon orientation determine local spinal cord mechanical properties," *Biophysical Journal*, vol. 108, no. 9, pp. 2137–2147, 2015.

[36] A. F. Christ, K. Franze, H. Gautier, P. Moshayedi, J. Fawcett, R. J. Franklin, R. T. Karadottir, and J. Guck, "Mechanical difference between white and gray matter in the rat cerebellum measured by scanning force microscopy," *Journal of Biomechanics*, vol. 43, no. 15, pp. 2986–2992, 2010.

[37] S. Budday, R. Nay, R. de Rooij, P. Steinmann, T. Wyrobek, T. C. Ovaert, and E. Kuhl, "Mechanical properties of gray and white matter brain tissue by indentation," *Journal of the Mechanical Behavior of Biomedical Materials*, vol. 46, pp. 318–330, 2015.

[38] L. E. White, T. J. Andrews, C. Hulette, A. Richards, M. Groelle, J. Paydarfar, and D. Purves, "Structure of the human sensorimotor system. I: Morphology and cytoarchitecture of the central sulcus," *Cerebral Cortex*, vol. 7, no. 1, pp. 18–30, 1997.

[39] J. Bradbury, "Molecular Insights into Human Brain Evolution," *PLoS Biology*, vol. 3, no. 3, p. e50, 2005.

[40] H. C. Elliott, "Cross-sectional diameters and areas of the human spinal cord," *The Anatomical Record*, vol. 93, pp. 287–293, nov 1945.

[41] M. E. Wagshul, P. K. Eide, and J. R. Madsen, "The pulsating brain: A review of experimental and clinical studies of intracranial pulsatility," *Fluids and Barriers of the CNS*, vol. 8, no. 1, p. 5, 2011.

[42] S. Hirsch, D. Klatt, F. Freimann, M. Scheel, J. Braun, and I. Sack, "In vivo measurement of volumetric strain in the human brain induced by arterial pulsation and harmonic waves.," *Proc. Int. Soc. Mag. Res. Med.*, vol. 21, p. 2444, 2012.

[43] G. Franceschini, *the Mechanics of Human Brain Tissue*. PhD thesis, University of Trento, 2006.

[44] S. K. Rosahl and S. Rosahl, "No easy target: anatomic constraints of electrodes interfacing the human cochlear nucleus," *Operative Neurosurgery*, vol. 72, pp. ons 58–ons 65, mar 2013.

[45] M. a. Hopcroft, W. D. Nix, and T. W. Kenny, "What is the Young's modulus of silicon?," *Journal of Microelectromechanical Systems*, vol. 19, no. 2, pp. 229–238, 2010.

[46] V. S. Polikov, P. a. Tresco, and W. M. Reichert, "Response of brain tissue to chronically implanted neural electrodes," *Journal of Neuroscience Methods*, vol. 148, pp. 1–18, 2005.

[47] M. P. Ward, P. Rajdev, C. Ellison, and P. P. Irazoqui, "Toward a comparison of microelectrodes for acute and chronic recordings," *Brain Research*, vol. 1282, pp. 183–200, 2009.

[48] S. R. Goldstein and M. Salcman, "Mechanical Factors in the Design of Chronic Recording Intracortical Microelectrodes," *IEEE Transactions on Biomedical Engineering*, vol. BME-20, no. 4, pp. 260–269, 1973.

[49] H. Lee, R. V. Bellamkonda, W. Sun, and M. E. Levenston, "Biomechanical analysis of silicon microelectrode-induced strain in the brain," *Journal of Neural Engineering*, vol. 2, pp. 81–89, dec 2005.

[50] A. A. Sharp, A. M. Ortega, D. Restrepo, D. Curran-Everett, and K. Gall, "In vivo penetration mechanics and mechanical properties of mouse brain tissue at micrometer scales," *IEEE Transactions on Biomedical Engineering*, vol. 56, no. 1, pp. 45–53, 2009.

[51] A. Ersen, S. Elkabes, D. S. Freedman, and M. Sahin, "Chronic tissue response to untethered microelectrode implants in the rat brain and spinal cord.," *Journal of Neural Engineering*, vol. 12, no. 1, p. 016019, 2015.

[52] J. C. Barrese, J. Aceros, and J. P. Donoghue, "Scanning electron microscopy of chronically implanted intracortical microelectrode arrays in non-human primates," *Journal of Neural Engineering*, vol. 13, p. 026003, apr 2016.

[53] D. J. Chew, L. Zhu, E. Delivopoulos, I. R. Minev, K. M. Musick, C. A. Mosse, M. Craggs, N. Donaldson, S. P. Lacour, S. B. McMahon, and J. W. Fawcett, "A Microchannel Neuroprosthesis for Bladder Control After Spinal Cord Injury in Rat," *Science Translational Medicine*, vol. 5, pp. 210ra155–210ra155, nov 2013.

[54] J. H. Lee, H. Kim, J. H. Kim, and S.-H. Lee, "Soft implantable microelectrodes for future medicine: prosthetics, neural signal recording and neuromodulation," *Lab on a Chip*, vol. 16, no. 6, pp. 959–976, 2016.

[55] S. P. Lacour, S. Benmerah, E. Tarte, J. FitzGerald, J. Serra, S. McMahon, J. Fawcett, O. Graudejus, Z. Yu, and B. Morrison, "Flexible and stretchable micro-electrodes for in vitro and in vivo neural interfaces," *Medical & Biological Engineering & Computing*, vol. 48, no. 10, pp. 945–954, 2010.

[56] J. K. Nguyen, D. J. Park, J. L. Skousen, A. E. Hess-Dunning, D. J. Tyler, S. J. Rowan, C. Weder, and J. R. Capadona, "Mechanically-compliant intracortical implants reduce

the neuroinflammatory response," *Journal of Neural Engineering*, vol. 11, no. 5, pp. 1–27, 2014.

[57] I. R. Minev, N. Wenger, G. Courtine, and S. P. Lacour, "Research Update: Platinum-elastomer mesocomposite as neural electrode coating," *APL Materials*, vol. 3, p. 014701, jan 2015.

[58] A. Garcia-Sandoval, A. Pal, A. M. Mishra, S. Sherman, A. R. Parikh, A. Joshi-Imre, D. Arreaga-Salas, G. Gutierrez-Heredia, A. C. Duran-Martinez, J. Nathan, S. M. Hosseini, J. B. Carmel, and W. Voit, "Chronic softening spinal cord stimulation arrays," *Journal of Neural Engineering*, vol. 15, no. 4, 2018.

[59] V. R. Feig, H. Tran, M. Lee, and Z. Bao, "Mechanically tunable conductive interpene-trating network hydrogels that mimic the elastic moduli of biological tissue," *Nature Communications*, vol. 9, no. 1, pp. 1–9, 2018.

[60] W. C. Huang, X. C. Ong, I. S. Kwon, C. Gopinath, L. E. Fisher, H. Wu, G. K. Fedder, R. A. Gaunt, and C. J. Bettinger, "Ultracompliant Hydrogel-Based Neural Interfaces Fabricated by Aqueous-Phase Microtransfer Printing," *Advanced Functional Materials*, vol. 28, no. 29, pp. 1–10, 2018.

[61] H. C. Lee, F. Ejserholm, J. Gaire, S. Currlin, J. Schouenborg, L. Wallman, M. Bengtsson, K. Park, and K. J. Otto, "Histological evaluation of flexible neural implants; flexibility limit for reducing the tissue response?," *Journal of Neural Engineering*, vol. 14, p. 036026, jun 2017.

[62] X. Chen, "Making Electrodes Stretchable," *Small Methods*, vol. 1, no. 4, p. 1600029, 2017.

[63] Z. Suo, E. Y. Ma, H. Gleskova, and S. Wagner, "Mechanics of rollable and foldable film-on-foil electronics," *Applied Physics Letters*, vol. 74, no. 8, pp. 1177–1179, 1999.

[64] C. Py, P. Reverdy, L. Doppler, J. Bico, B. Roman, and C. N. Baroud, "Capillarity induced folding of elastic sheets," *The European Physical Journal Special Topics*, vol. 166, pp. 67–71, feb 2009.

[65] J. A. Rogers, *Stretchable Bioelectronics for Medical Devices and Systems*. Microsystems and Nanosystems, Cham: Springer International Publishing, 2016.

[66] J. A. Rogers, T. Someya, and Y. Huang, "Materials and Mechanics for Stretchable Electronics," *Science*, vol. 327, pp. 1603–1607, mar 2010.

[67] A. J. Shoffstall, S. Srinivasan, M. Willis, A. M. Stiller, M. Ecker, W. E. Voit, J. J. Pancrazio, and J. R. Capadona, "A Mosquito Inspired Strategy to Implant Microprobes into the Brain," *Scientific Reports*, vol. 8, no. 1, pp. 1–10, 2018.

[68] Z. J. Du, C. L. Kolarcik, T. D. Kozai, S. D. Luebben, S. A. Sapp, X. S. Zheng, J. A. Nabity, and X. T. Cui, "Ultrasoft microwire neural electrodes improve chronic tissue integration," *Acta Biomaterialia*, vol. 53, pp. 46–58, 2017.

[69] M.-c. Lo, S. Wang, S. Singh, V. B. Damodaran, H. M. Kaplan, J. Kohn, D. I. Shreiber, and J. D. Zahn, "Coating flexible probes with an ultra fast degrading polymer to aid in tissue insertion," *Biomedical Microdevices*, vol. 17, p. 34, apr 2015.

[70] D.-H. Kim, J. Viventi, J. J. Amsden, J. Xiao, L. Vigeland, Y.-S. Kim, J. A. Blanco, B. Panilaitis, E. S. Frechette, D. Contreras, D. L. Kaplan, F. G. Omenetto, Y. Huang, K.-C. Hwang, M. R. Zakin, B. Litt, and J. A. Rogers, "Dissolvable films of silk fibroin for ultrathin conformal bio-integrated electronics," *Nature Materials*, vol. 9, no. 6, pp. 511–517, 2010.

[71] C. Xie, J. Liu, T. M. Fu, X. Dai, W. Zhou, and C. M. Lieber, "Three-dimensional macroporous nanoelectronic networks as minimally invasive brain probes," *Nature Materials*, vol. 14, no. 12, pp. 1286–1292, 2015.

[72] T. Matsuo, K. Kawasaki, T. Osada, H. Sawahata, T. Suzuki, M. Shibata, N. Miyakawa, K. Nakahara, A. Iijima, N. Sato, K. Kawai, N. Saito, and I. Hasegawa, "Intrasulcal electrocorticography in macaque monkeys with minimally invasive neurosurgical protocols.," *Frontiers in systems neuroscience*, vol. 5, no. May, p. 34, 2011.

[73] R. K. Shepherd, J. Villalobos, O. Burns, and D. A. X. Nayagam, "The development of neural stimulators: a review of preclinical safety and efficacy studies," *Journal of Neural Engineering*, vol. 15, no. 4, p. 041004, 2018.

[74] Toxikon, "Medical Device Testing Guide." [Accessed on 02.06.2018]. Available from: http://toxikon.com/resources/medical-device-testing-guide/, 2013.

[75] a. Vanhoestenberghe and N. Donaldson, "Corrosion of silicon integrated circuits and lifetime predictions in implantable electronic devices.," *Journal of neural engineering*, vol. 10, no. 3, p. 031002, 2013.

[76] S. Zeitler, E. Wendler-Kalsch, W. Preidel, and V. Tegeder, "Corrosion of platinum electrodes in phosphate buffered saline solution," *Materials and Corrosion/Werkstoffe und Korrosion*, vol. 48, pp. 303–310, may 1997.

[77] M. Matsumoto, T. Miyazaki, and H. Imai, "Oxygen-enhanced dissolution of platinum in acidic electrochemical environments," *Journal of Physical Chemistry C*, vol. 115, pp. 11163–11169, 2011.

[78] A. K. Ahuja, J. D. Dorn, A. Caspi, M. J. McMahon, G. Dagnelie, L. DaCruz, P. Stanga, M. S. Humayun, and R. J. Greenberg, "Blind subjects implanted with the Argus II retinal prosthesis are able to improve performance in a spatial-motor task," *British Journal of Ophthalmology*, vol. 95, no. 4, pp. 539–543, 2011.

[79] D. W. L. Hukins, a. Mahomed, and S. N. Kukureka, "Accelerated aging for testing polymeric biomaterials and medical devices," *Medical Engineering and Physics*, vol. 30, no. 10, pp. 1270–1274, 2008.

[80] ASTM F1980 A, "Standard Guide for Accelerated Aging of Sterile Barrier Systems for Medical Devices," *ASTM International, West Conshohoken, PA*, 2016.

[81] P. Takmakov, K. Ruda, K. Scott Phillips, I. S. Isayeva, V. Krauthamer, and C. G. Welle, "Rapid evaluation of the durability of cortical neural implants using accelerated aging with reactive oxygen species," *Journal of Neural Engineering*, vol. 12, p. 026003, apr 2015.

[82] J. B. Erhardt, E. Fuhrer, O. G. Gruschke, J. Leupold, M. C. Wapler, J. Hennig, T. Stieglitz, and J. G. Korvink, "Should patients with brain implants undergo MRI?," *Journal of Neural Engineering*, vol. 15, p. 041002, aug 2018.

[83] F. Santiesteban, S. Swanson, D. Noll, and D. Anderson, "Magnetic Resonance Compatibility of Multichannel Silicon Microelectrode Systems for Neural Recording and Stimulation: Design Criteria, Tests, and Recommendations," *IEEE Transactions on Biomedical Engineering*, vol. 53, pp. 547–558, mar 2006.

[84] S. Zhao, X. Liu, Z. Xu, H. Ren, B. Deng, M. Tang, L. Lu, X. Fu, H. Peng, Z. Liu, and X. Duan, "Graphene Encapsulated Copper Microwires as Highly MRI Compatible Neural Electrodes," *Nano Letters*, p. acs.nanolett.6b03829, 2016.

[85] P. Serano, L. M. Angelone, H. Katnani, E. Eskandar, and G. Bonmassar, "A novel brain stimulation technology provides compatibility with MRI," *Scientific Reports*, vol. 5, pp. 1–10, 2015.

[86] ASTM F2052, "Standard Test Method for Measurement of Magnetically Induced Displacement Force," *ASTM International, West Conshohoken, PA*, 2015.

[87] ASTM F2182, "Standard test method for measurement of radio frequency induced heating near passive implants during magnetic resonance imaging," *ASTM International, West Conshohoken, PA*, 2011.

[88] ASTM F2213, "Standard Test Method for Measurement of Magnetically Induced Torque on Medical Devices in the Magnetic Resonance Environment," *ASTM International, West Conshohoken, PA*, 2017.

[89] ASTM F2119, "Standard Test Method for Evaluation of MR Image Artifacts from Passive Implants," *ASTM International, West Conshohoken, PA*, 2013.

[90] ASTM F2503, "Standard Practice for Marking Medical Devices and Other Items for Safety in the Magnetic Resonance Environment 1," *ASTM International, West Conshohoken, PA*, 2013.

[91] Nicolas Vachicouras, C. M. Tringides, and S. P. Lacour, "Engineering reversible elasticity in ductile or brittle thin films and products resulting from said engineering." PCT/EP2017/080876, 2016.

[92] S. Wagner and S. Bauer, "Materials for stretchable electronics," *MRS Bulletin*, vol. 37, no. 3, pp. 207–213, 2012.

[93] D. H. Kim and J. a. Rogers, "Stretchable electronics: Materials strategies and devices," *Advanced Materials*, vol. 20, no. 24, pp. 4887–4892, 2008.

[94] T. Sekitani, Y. Noguchi, K. Hata, T. Fukushima, T. Aida, and T. Someya, "A Rubberlike Stretchable Active Matrix Using Elastic Conductors," *Science*, vol. 321, pp. 1468–1472, sep 2008.

[95] Z. Chen, W. Ren, L. Gao, B. Liu, S. Pei, and H.-M. Cheng, "Three-dimensional flexible and conductive interconnected graphene networks grown by chemical vapour deposition.," *Nature materials*, vol. 10, no. 6, pp. 424–428, 2011.

[96] K. S. Kim, Y. Zhao, H. Jang, S. Y. Lee, J. M. Kim, K. S. Kim, J.-H. Ahn, P. Kim, J.-Y. Choi, and B. H. Hong, "Large-scale pattern growth of graphene films for stretchable transparent electrodes," *Nature*, vol. 457, no. 7230, pp. 706–710, 2009.

[97] C. F. Guo, Q. Liu, G. Wang, Y. Wang, Z. Shi, Z. Suo, C.-w. Chu, and Z. Ren, "Fatigue-free, superstretchable, transparent, and biocompatible metal electrodes," *Proceedings of the National Academy of Sciences*, vol. 112, pp. 12332–12337, oct 2015.

[98] M. Park, J. Park, and U. Jeong, "Design of conductive composite elastomers for stretchable electronics," *Nano Today*, vol. 9, no. 2, pp. 244–260, 2014.

[99] S. Rosset, M. Niklaus, P. Dubois, and H. R. Shea, "Metal ion implantation for the fabrication of stretchable electrodes on elastomers," *Advanced Functional Materials*, vol. 19, no. 3, pp. 470–478, 2009.

[100] A. Larmagnac, S. Eggenberger, H. Janossy, and J. Vörös, "Stretchable electronics based on Ag-PDMS composites," *Scientific Reports*, vol. 4, pp. 1–7, 2014.

[101] F. Xu and Y. Zhu, "Highly conductive and stretchable silver nanowire conductors," *Advanced Materials*, vol. 24, no. 37, pp. 5117–5122, 2012.

[102] T. S. Hansen, K. West, O. Hassager, and N. B. Larsen, "Highly stretchable and conductive polymer material made from poly(3,4-ethylenedioxythiophene) and polyurethane elastomers," *Advanced Functional Materials*, vol. 17, no. 16, pp. 3069–3073, 2007.

[103] O. Graudejus, P. Görrn, and S. Wagner, "Controlling the morphology of gold films on poly(dimethylsiloxane)," *ACS Applied Materials and Interfaces*, vol. 2, no. 7, pp. 1927–1933, 2010.

[104] I. M. Graz, D. P. J. Cotton, and S. P. Lacour, "Extended cyclic uniaxial loading of stretchable gold thin-films on elastomeric substrates," *Applied Physics Letters*, vol. 94, no. 7, p. 071902, 2009.

[105] S. P. Lacour, S. Wagner, Z. Huang, and Z. Suo, "Stretchable gold conductors on elastomeric substrates," *Applied Physics Letters*, vol. 82, no. 15, p. 2404, 2003.

[106] Z. Yu, O. Graudejus, C. Tsay, S. P. Lacour, S. Wagner, and B. Morrison, "Monitoring hippocampus electrical activity in vitro on an elastically deformable microelectrode array.," *Journal of neurotrauma*, vol. 26, no. 7, pp. 1135–1145, 2009.

[107] Y. Cao, T. G. Morrissey, E. Acome, S. I. Allec, B. M. Wong, C. Keplinger, and C. Wang, "A Transparent, Self-Healing, Highly Stretchable Ionic Conductor," *Advanced Materials*, vol. 29, no. 10, pp. 1–9, 2017.

[108] C. Keplinger, J. Y. Sun, C. C. Foo, P. Rothemund, G. M. Whitesides, and Z. Suo, "Stretchable, transparent, ionic conductors," *Science*, vol. 341, no. 6149, pp. 984–987, 2013.

[109] J. B. Chossat, Y. L. Park, R. J. Wood, and V. Duchaine, "A soft strain sensor based on ionic and metal liquids," *IEEE Sensors Journal*, vol. 13, no. 9, pp. 3405–3414, 2013.

[110] J. H. So, J. Thelen, A. Qusba, G. J. Hayes, G. Lazzi, and M. D. Dickey, "Reversibly deformable and mechanically tunable fluidic antennas," *Advanced Functional Materials*, vol. 19, no. 22, pp. 3632–3637, 2009.

[111] M. D. Dickey, "Stretchable and Soft Electronics using Liquid Metals," *Advanced Materials*, vol. 29, no. 27, pp. 1–19, 2017.

[112] A. Hirsch, H. O. Michaud, A. P. Gerratt, S. de Mulatier, and S. P. Lacour, "Intrinsically Stretchable Biphasic (Solid-Liquid) Thin Metal Films," *Advanced Materials*, pp. 1–6, 2016.

[113] W. Dang, V. Vinciguerra, L. Lorenzelli, and R. Dahiya, "Printable stretchable interconnects," *Flexible and Printed Electronics*, vol. 2, no. 1, 2017.

[114] S. Nagels and W. Deferme, "Fabrication approaches to interconnect based devices for stretchable electronics: A review," *Materials*, vol. 11, no. 3, 2018.

[115] H. Jiang, D.-Y. Khang, J. Song, Y. Sun, Y. Huang, and J. a. Rogers, "Finite deformation mechanics in buckled thin films on compliant supports.," *Proceedings of the National Academy of Sciences of the United States of America*, vol. 104, no. 40, pp. 15607–15612, 2007.

[116] N. Bowden, S. Brittain, and A. Evans, "Spontaneous formation of ordered structures in thin films of metals supported on an elastomeric polymer," *Nature*, vol. 393, no. May, pp. 146–149, 1998.

[117] S. P. Lacour, J. Jones, Z. Suo, and S. Wagner, "Design and performance of thin metal film interconnects for skin-like electronic circuits," *IEEE Electron Device Letters*, vol. 25, no. 4, pp. 179–181, 2004.

[118] M. Drack, I. Graz, T. Sekitani, T. Someya, M. Kaltenbrunner, and S. Bauer, "An Imperceptible Plastic Electronic Wrap," *Advanced Materials*, vol. 27, no. 1, pp. 34–40, 2015.

[119] D.-Y. Khang, H. Jiang, Y. Huang, and J. A. Rogers, "A Stretchable Form of Single-Crystal," *Science*, vol. 311, no. January, pp. 208–212, 2006.

[120] W. M. Choi, J. Song, D. Y. Khang, H. Jiang, Y. Y. Huang, and J. a. Rogers, "Biaxially stretchable "wavy" silicon nanomembranes," *Nano Letters*, vol. 7, no. 6, pp. 1655–1663, 2007.

[121] S. Xu, Z. Yan, K.-I. Jang, W. Huang, H. Fu, J. Kim, Z. Wei, M. Flavin, J. McCracken, R. Wang, A. Badea, Y. Liu, D. Xiao, G. Zhou, J. Lee, H. U. Chung, H. Cheng, W. Ren, A. Banks, X. Li, U. Paik, R. G. Nuzzo, Y. Huang, Y. Zhang, and J. A. Rogers, "Assembly of micro/nanomaterials into complex, three-dimensional architectures by compressive buckling," *Science*, vol. 347, no. 6218, pp. 154–159, 2015.

[122] D.-H. Kim, J. Song, W. M. Choi, H.-S. Kim, R.-H. Kim, Z. Liu, Y. Y. Huang, K.-C. Hwang, Y.-w. Zhang, and J. a. Rogers, "Materials and noncoplanar mesh designs for integrated circuits with linear elastic responses to extreme mechanical deformations.," *Proceedings of the National Academy of Sciences of the United States of America*, vol. 105, no. 48, pp. 18675–18680, 2008.

[123] D. Gray, J. Tien, and C. Chen, "High-Conductivity Elastomeric Electronics," *Advanced Materials*, vol. 16, no. 5, pp. 393–397, 2004.

[124] M. Gonzalez, F. Axisa, M. Vanden Bulcke, D. Brosteaux, B. Vandevelde, and J. Vanfleteren, "Design of Metal Interconnects for Stretchable Electronic Circuits using Finite Element Analysis," in *2007 International Conference on Thermal, Mechanical and Multi-Physics Simulation Experiments in Microelectronics and Micro-Systems. EuroSime 2007*, pp. 1–6, IEEE, 2007.

[125] F. Axisa, F. Bossuyt, T. Vervust, and J. Vanfleteren, "Laser based fast prototyping methodology of producing stretchable and conformable electronic systems," *Proceedings - 2008 2nd Electronics Systemintegration Technology Conference, ESTC*, pp. 1387–1390, 2008.

[126] R. Carta, P. Jourand, B. Hermans, J. Thoné, D. Brosteaux, T. Vervust, F. Bossuyt, F. Axisa, J. Vanfleteren, and R. Puers, "Design and implementation of advanced systems in a flexible-stretchable technology for biomedical applications," *Sensors and Actuators A: Physical*, vol. 156, no. 1, pp. 79–87, 2009.

[127] J. A. Fan, W.-H. Yeo, Y. Su, Y. Hattori, W. Lee, S.-Y. Jung, Y. Zhang, Z. Liu, H. Cheng, L. Falgout, M. Bajema, T. Coleman, D. Gregoire, R. J. Larsen, Y. Huang, and J. A. Rogers, "Fractal design concepts for stretchable electronics," *Nature Communications*, vol. 5, pp. 1–8, 2014.

[128] Q. Ma and Y. Zhang, "Mechanics of Fractal-Inspired Horseshoe Microstructures for Applications in Stretchable Electronics," *Journal of Applied Mechanics*, vol. 83, no. 11, p. 111008, 2016.

[129] X. Ning, X. Wang, Y. Zhang, X. Yu, D. Choi, N. Zheng, D. S. Kim, Y. Huang, Y. Zhang, and J. A. Rogers, "Assembly of Advanced Materials into 3D Functional Structures by Methods Inspired by Origami and Kirigami: A Review," *Advanced Materials Interfaces*, vol. 5, p. 1800284, jul 2018.

[130] L. Xu, T. C. Shyu, and N. A. Kotov, "Origami and Kirigami Nanocomposites," *ACS Nano*, vol. 11, no. 8, pp. 7587–7599, 2017.

[131] T. C. Shyu, P. F. Damasceno, P. M. Dodd, A. Lamoureux, L. Xu, M. Shlian, M. Shtein, S. C. Glotzer, and N. a. Kotov, "A kirigami approach to engineering elasticity in nanocomposites through patterned defects," *Nature Materials*, vol. 14, no. 8, pp. 785–789, 2015.

[132] J. Wu, Z. J. Liu, J. Song, Y. Huang, K. C. Hwang, Y. W. Zhang, and J. A. Rogers, "Stretchability of encapsulated electronics," *Applied Physics Letters*, vol. 99, p. 061911, aug 2011.

[133] T. Pan, M. Pharr, Y. Ma, R. Ning, Z. Yan, R. Xu, X. Feng, Y. Huang, and J. A. Rogers, "Experimental and Theoretical Studies of Serpentine Interconnects on Ultrathin Elastomers for Stretchable Electronics," *Advanced Functional Materials*, vol. 27, no. 37, pp. 1–8, 2017.

[134] S. Xu, Y. Zhang, L. Jia, K. E. Mathewson, K.-i. Jang, J. Kim, H. Fu, X. Huang, P. Chava, R. Wang, S. Bhole, L. Wang, Y. J. Na, Y. Guan, M. Flavin, Z. Han, Y. Huang, and J. A. Rogers, "Soft Microfluidic Assemblies of for the Skin," *Science*, vol. 344, no. April, pp. 70–74, 2014.

[135] F. Bossuyt, T. Vervust, and J. Vanfleteren, "Stretchable electronics technology for large area applications: Fabrication and mechanical characterization," *IEEE Transactions on Components, Packaging and Manufacturing Technology*, vol. 3, no. 2, pp. 229–235, 2013.

[136] Y. Zhang, S. Wang, X. Li, J. A. Fan, S. Xu, Y. M. Song, K. J. Choi, W. H. Yeo, W. Lee, S. N. Nazaar, B. Lu, L. Yin, K. C. Hwang, J. A. Rogers, and Y. Huang, "Experimental and theoretical studies of serpentine microstructures bonded to prestrained elastomers for stretchable electronics," *Advanced Functional Materials*, vol. 24, no. 14, pp. 2028–2037, 2014.

[137] Q. Ma and Y. Zhang, "Mechanics of Fractal-Inspired Horseshoe Microstructures for Applications in Stretchable Electronics," *Journal of Applied Mechanics*, vol. 83, no. 11, p. 111008, 2016.

[138] B. Rubehn, C. Bosman, R. Oostenveld, P. Fries, and T. Stieglitz, "A MEMS-based flexible multichannel ECoG-electrode array," *Journal of Neural Engineering*, vol. 6, no. 3, p. 036003, 2009.

[139] H. Toda, T. Suzuki, H. Sawahata, K. Majima, Y. Kamitani, and I. Hasegawa, "Simultaneous recording of ECoG and intracortical neuronal activity using a flexible multichannel electrode-mesh in visual cortex," *NeuroImage*, vol. 54, no. 1, pp. 203–212, 2011.

[140] J. Viventi, D.-H. Kim, L. Vigeland, E. S. Frechette, J. A. Blanco, Y.-S. Kim, A. E. Avrin, V. R. Tiruvadi, S.-W. Hwang, A. C. Vanleer, D. F. Wulsin, K. Davis, C. E. Gelber, L. Palmer, J. Van der Spiegel, J. Wu, J. Xiao, Y. Huang, D. Contreras, J. A. Rogers, and B. Litt, "Flexible, foldable, actively multiplexed, high-density electrode array for mapping brain activity in vivo," *Nature Neuroscience*, vol. 14, no. 12, pp. 1599–1605, 2011.

[141] D. Khodagholy, T. Doublet, M. Gurfinkel, P. Quilichini, E. Ismailova, P. Leleux, T. Herve, S. Sanaur, C. Bernard, and G. G. Malliaras, "Highly conformable conducting polymer electrodes for in vivo recordings," *Advanced Materials*, vol. 23, no. 36, pp. 268–272, 2011.

[142] K. Tybrandt, D. Khodagholy, B. Dielacher, F. Stauffer, A. F. Renz, G. Buzsáki, and J. Vörös, "High-Density Stretchable Electrode Grids for Chronic Neural Recording," *Advanced Materials*, vol. 30, p. 1706520, apr 2018.

[143] I. R. Minev, P. Musienko, A. Hirsch, Q. Barraud, N. Wenger, E. M. Moraud, J. Gandar, M. Capogrosso, T. Milekovic, L. Asboth, R. F. Torres, N. Vachicouras, Q. Liu, N. Pavlova, S. Duis, A. Larmagnac, J. Vörös, S. Micera, Z. Suo, G. Courtine, and S. P. Lacour, "Electronic dura mater for long-term multimodal neural interfaces," *Science*, vol. 347, no. 6218, pp. 159–163, 2015.

[144] M. Schuettler, D. Pfau, J. S. Ordonez, C. Henle, P. Woias, and T. Stieglitz, "Stretchable tracks for laser-machined neural electrode arrays," *Proceedings of the 31st Annual International Conference of the IEEE Engineering in Medicine and Biology Society: Engineering the Future of Biomedicine, EMBC 2009*, pp. 1612–1615, 2009.

[145] Y. Morikawa, S. Yamagiwa, H. Sawahata, R. Numano, K. Koida, M. Ishida, and T. Kawano, "Ultrastretchable Kirigami Bioprobes," *Advanced Healthcare Materials*, vol. 7, no. 3, pp. 1–10, 2018.

[146] K. W. Meacham, R. J. Giuly, L. Guo, S. Hochman, and S. P. DeWeerth, "A lithographically-patterned, elastic multi-electrode array for surface stimulation of the spinal cord," *Biomedical Microdevices*, vol. 10, no. 2, pp. 259–269, 2008.

[147] M. Schuettler, S. Stiess, B. V. King, and G. J. Suaning, "Fabrication of implantable microelectrode arrays by laser cutting of silicone rubber and platinum foil," *Journal of Neural Engineering*, vol. 2, no. 1, 2005.

[148] C. Henle, M. Schuettler, and T. Stieglitz, "Towards Electrocorticographic Electrodes for Chronic Use in BCI Applications," in *Towards Practical Brain-Computer Interfaces* (B. Z. Allison, S. Dunne, R. Leeb, J. Del R. Millán, and A. Nijholt, eds.), Biological and Medical Physics, Biomedical Engineering, ch. 5, pp. 85–90, Berlin, Heidelberg: Springer Berlin Heidelberg, 2013.

[149] S. P. Lacour, D. Chan, S. Wagner, T. Li, and Z. Suo, "Mechanisms of reversible stretchability of thin metal films on elastomeric substrates," *Applied Physics Letters*, vol. 88, no. 20, p. 204103, 2006.

[150] DIN 53504, "Testing of rubber - Determination of tensile strength at break, tensile stress at yield, elongation at break and stress values in a tensile test," 2009.

[151] S. E. Schausberger, R. Kaltseis, M. Drack, U. D. Cakmak, Z. Major, and S. Bauer, "Cost-Efficient Open Source Desktop Size Radial Stretching System With Force Sensor," *IEEE Access*, vol. 3, pp. 556–561, 2015.

[152] T. Li, Z. Suo, S. P. Lacour, and S. Wagner, "Compliant thin film patterns of stiff materials as platforms for stretchable electronics," *Journal of Materials Research*, vol. 20, pp. 3274–3277, dec 2005.

[153] M. Ying, A. P. Bonifas, N. Lu, Y. Su, R. Li, H. Cheng, A. Ameen, Y. Huang, and J. A. Rogers, "Silicon nanomembranes for fingertip electronics," *Nanotechnology*, vol. 23, no. 34, 2012.

[154] B. Rubehn and T. Stieglitz, "In vitro evaluation of the long-term stability of polyimide as a material for neural implants," *Biomaterials*, vol. 31, no. 13, pp. 3449–3458, 2010.

[155] X. Lei, S. Kane, S. Cogan, H. Lorach, L. Galambos, P. Huie, K. Mathieson, T. Kamins, J. Harris, and D. Palanker, "SiC protective coating for photovoltaic retinal prosthesis," *Journal of Neural Engineering*, vol. 13, no. 4, 2016.

[156] E. Bernardin, C. Frewin, R. Everly, J. Ul Hassan, S. Saddow, E. K. Bernardin, C. L. Frewin, R. Everly, J. Ul Hassan, and S. E. Saddow, "Demonstration of a Robust All-Silicon-Carbide Intracortical Neural Interface," *Micromachines*, vol. 9, no. 8, p. 412, 2018.

[157] J. S. Ordonez, C. Boehler, M. Schuettler, and T. Stieglitz, "Silicone rubber and thin-film polyimide for hybrid neural interfaces - A MEMS-based adhesion promotion technique," *International IEEE/EMBS Conference on Neural Engineering, NER*, vol. 49, no. 0, pp. 872–875, 2013.

[158] T. L. Edwards, C. L. Cottriall, K. Xue, M. P. Simunovic, J. D. Ramsden, E. Zrenner, and R. E. MacLaren, "Assessment of the Electronic Retinal Implant Alpha AMS in Restoring Vision to Blind Patients with End-Stage Retinitis Pigmentosa," *Ophthalmology*, vol. 125, no. 3, pp. 432–443, 2018.

[159] J. Ortigoza-Diaz, K. Scholten, C. Larson, A. Cobo, T. Hudson, J. Yoo, A. Baldwin, A. Weltman Hirschberg, and E. Meng, "Techniques and Considerations in the Microfabrication of Parylene C Microelectromechanical Systems," *Micromachines*, vol. 9, no. 9, p. 422, 2018.

[160] Y. Su, X. Ping, K. J. Yu, J. W. Lee, J. A. Fan, B. Wang, M. Li, R. Li, D. V. Harburg, Y. A. Huang, C. Yu, S. Mao, J. Shim, Q. Yang, P. Y. Lee, A. Armonas, K. J. Choi, Y. Yang, U. Paik, T. Chang, T. J. Dawidczyk, Y. Huang, S. Wang, and J. A. Rogers, "In-Plane Deformation Mechanics for Highly Stretchable Electronics," *Advanced Materials*, vol. 29, no. 8, pp. 1–12, 2017.

[161] N. Naserifar, P. R. LeDuc, and G. K. Fedder, "Material Gradients in Stretchable Substrates toward Integrated Electronic Functionality," *Advanced Materials*, vol. 28, no. 18, pp. 3584–3591, 2016.

[162] Z. Wu, S. Zhang, A. Vorobyev, K. Gamstedt, K. Wu, C. Guo, and S. H. Jeong, "Seamless modulus gradient structures for highly resilient, stretchable system integration," *Materials Today Physics*, vol. 4, pp. 28–35, 2018.

[163] A. Romeo, Q. Liu, Z. Suo, and S. P. Lacour, "Elastomeric substrates with embedded stiff platforms for stretchable electronics," *Applied Physics Letters*, vol. 102, no. 13, 2013.

[164] M. Jablonski, F. Bossuyt, J. Vanfleteren, T. Vervust, and H. De Vries, "Reliability of a stretchable interconnect utilizing terminated, in-plane meandered copper conductor," *Microelectronics Reliability*, vol. 53, no. 7, pp. 956–963, 2013.

[165] I. House Clinic, "FDA Approves Clinical Trial of Auditory Brainstem Implant Procedure for Children in the U.S.." [Accessed 04.09.2018]. Available from: https://www.houseclinic.com/about/research/pediatricabi/press-02, 2013.

[166] B. J. Edgerton, W. F. House, and W. Hitselberger, "Hearing by cochlear nucleus stimulation in humans.," *The Annals of otology, rhinology & laryngology. Supplement*, vol. 91, no. 2 Pt 3, pp. 117–24, 1982.

[167] U.S. Food and Drug Administration, "Nucleus 24 Auditory Brainstem Implant System." [Accessed 06.09.2018]. Available from: https://www.accessdata.fda.gov/scrIpts/cdrh/cfdocs/cfpma/pma.cfm?id=P000015, 2000.

[168] C. Vincent, "Auditory Brainstem Implants: How Do They Work?," *The Anatomical Record: Advances in Integrative Anatomy and Evolutionary Biology*, vol. 295, pp. 1981–1986, nov 2012.

[169] B. Clopton, J. Winfield, and F. Flammino, "Tonotopic Organization: Review and Analysis," *Brain research*, vol. 76, pp. 1–20, 1974.

[170] D. B. McCreery, R. V. Shannon, J. K. Moore, and M. Chatterjee, "Accessing the tonotopic organization of the ventral cochlear nucleus by intranuclear microstimulation.," *IEEE transactions on rehabilitation engineering : a publication of the IEEE Engineering in Medicine and Biology Society*, vol. 6, pp. 391–9, dec 1998.

[171] M. Eric R. Kandel, P. James H. Schwartz, MD, P. Thomas M. Jessell, P. Steven A. Siegelbaum, and P. A. J. Hudspeth, "Summary for Policymakers," in *Climate Change 2013 - The Physical Science Basis* (Intergovernmental Panel on Climate Change, ed.), pp. 1–30, Cambridge: Cambridge University Press, 2013.

[172] J. R. Melcher, I. M. Knudson, B. C. Fullerton, J. J. Guinan, B. E. Norris, and N. Y. Kiang, "Generators of the brainstem auditory evoked potential in cat. I. An experimental approach to their identification.," *Hearing research*, vol. 93, pp. 1–27, apr 1996.

[173] J. Melcher and N. Kiang, "Generators of the brainstem auditory evoked potential in cat III: identified cell populations," *Hearing research*, vol. 93, pp. 52–71, 1996.

[174] J. Melcher, J. G. Jr, I. Knudson, and N. Kiang, "Generators of the brainstem auditory evoked potential in cat. II. Correlating lesion sites with waveform changes," *Hearing research*, vol. 93, pp. 28–51, 1996.

[175] D. McCreery, "Cochlear nucleus auditory prostheses," *Hearing research*, vol. 242, pp. 64–73, 2008.

[176] V. Colletti, M. Carner, V. Miorelli, M. Guida, L. Colletti, and F. Fiorino, "Auditory brainstem implant (ABI): new frontiers in adults and children.," *Otolaryngology–head and neck surgery : official journal of American Academy of Otolaryngology-Head and Neck Surgery*, vol. 133, pp. 126–38, jul 2005.

[177] J. Y. Choi, M. H. Song, J. H. Jeon, W.-S. Lee, and J. W. Chang, "Early surgical results of auditory brainstem implantation in nontumor patients.," *The Laryngoscope*, vol. 121, pp. 2610–8, dec 2011.

[178] L. Sennaroglu, I. Ziyal, A. Atas, G. Sennaroglu, E. Yucel, S. Sevinc, M. C. Ekin, S. Sarac, G. Atay, B. Ozgen, O. E. Ozcan, E. Belgin, V. Colletti, and E. Turan, "Preliminary results of auditory brainstem implantation in prelingually deaf children with inner ear malformations including severe stenosis of the cochlear aperture and aplasia of the cochlear nerve.," *Otology & neurotology : official publication of the American Otological Society, American Neurotology Society [and] European Academy of Otology and Neurotology*, vol. 30, pp. 708–15, sep 2009.

[179] K. S. Noij, E. D. Kozin, R. Sethi, P. V. Shah, A. B. Kaplan, B. Herrmann, A. Remen-schneider, and D. J. Lee, "Systematic Review of Nontumor Pediatric Auditory Brainstem Implant Outcomes," *Otolaryngology-Head and Neck Surgery*, vol. 153, pp. 739–750, nov 2015.

[180] V. Colletti, "Auditory outcomes in tumor vs. nontumor patients fitted with auditory brainstem implants.," *Advances in oto-rhino-laryngology*, vol. 64, pp. 167–85, jan 2006.

[181] V. Colletti and R. V. Shannon, "Open set speech perception with auditory brainstem implant?," *The Laryngoscope*, vol. 115, pp. 1974–8, nov 2005.

[182] V. Colletti, R. Shannon, M. Carner, S. Veronese, and L. Colletti, "Outcomes in nontumor adults fitted with the auditory brainstem implant: 10 years' experience.," *Otology & neurotology : official publication of the American Otological Society, American Neurotology Society [and] European Academy of Otology and Neurotology*, vol. 30, pp. 614–8, aug 2009.

[183] V. Colletti, R. V. Shannon, M. Carner, S. Veronese, and L. Colletti, "Complications in auditory brainstem implant surgery in adults and children.," *Otology & neurotology : official publication of the American Otological Society, American Neurotology Society [and] European Academy of Otology and Neurotology*, vol. 31, pp. 558–64, jun 2010.

[184] ClinicalTrials.gov, "Auditory Brainstem Implant (ABI) in Adult Non-Neurofibromatosis Type 2 Subjects." [Accessed 06.09.2018]. Available from: https://clinicaltrials.gov/ct2/show/NCT01736267, 2012.

[185] ClinicalTrial.gov, "A Safety Study of the Auditory Brainstem Implant for Pediatric Profoundly Deaf Patients." [Accessed 06.09.2018]. Available from: https://clinicaltrials.gov/ct2/show/NCT02102256, 2014.

[186] M. Sanna, F. Di Lella, M. Guida, and P. Merkus, "Auditory brainstem implants in NF2 patients: results and review of the literature.," *Otology & neurotology : official publication of the American Otological Society, American Neurotology Society [and] European Academy of Otology and Neurotology*, vol. 33, no. 2, pp. 154–64, 2012.

[187] F. Lüsebrink, A. Sciarra, H. Mattern, R. Yakupov, and O. Speck, "T1-weighted in vivo human whole brain MRI dataset with an ultrahigh isotropic resolution of 250 μm," *Scientific Data*, vol. 4, p. 170032, 2017.

[188] W. F. House and W. E. Hitselberger, "Twenty-year report of the first auditory brain stem nucleus implant," *Annals of Otology, Rhinology and Laryngology*, vol. 110, no. 2, pp. 103–104, 2001.

[189] R. Shannon and S. Otto, "Psychophysical measures from electrical stimulation of the human cochlear nucleus," *Hearing research*, vol. 47, pp. 159–168, 1990.

Bibliography

[190] L. Sennaroğlu, V. Colletti, T. Lenarz, M. Manrique, R. Laszig, H. Rask-andersen, N. Göksu, E. Offeciers, R. Behr, Y. Bayazıt, J. Casselman, S. Freeman, D. J. Lee, R. V. Shannon, M. Kameswaran, A. Zarowski, M. S. Schwartz, B. Bilginer, A. Kishore, G. Sennaroğlu, E. Yücel, S. Saraç, A. Ataş, L. Colletti, O. Driscoll, I. S. Moon, L. Gärtner, A. Huarte, G. Nyberg, Ö. Mocan, G. Atay, M. D. Bajin, B. Ç. Çınar, Ö. Batuk, M. Yaralı, F. E. Aydınlı, F. Aslan, M. Cigdem, H. B. Özkan, J. M. Hans, J. Kosaner, M. Polak, L. Sennaroğlu, V. Colletti, T. Lenarz, M. Manrique, R. Laszig, H. Rask-andersen, N. Göksu, E. Offeciers, S. Saeed, Y. Bayazıt, J. Casselman, S. Freeman, P. Kileny, D. J. Lee, V. Robert, M. Kameswaran, A. Hagr, A. Zarowski, M. S. Schwartz, B. Bilginer, A. Kishore, G. Sennaroğlu, E. Yücel, S. Saraç, and A. Ataş, "Consensus statement : Long-term results of ABI in children with complex inner ear malformations and decision making between CI and ABI Consensus statement : Long-term results of ABI in children with complex inner ear malformations and decision making betw," *Cochlear Implants International*, vol. 17, no. 4, pp. 163–171, 2016.

[191] S. R. Barber, E. D. Kozin, A. K. Remenschneider, S. V. Puram, M. Smith, B. S. Herrmann, M. E. Cunnane, M. C. Brown, and D. J. Lee, "Auditory brainstem implant array position varies widely among adult and pediatric patients and is associated with perception," *Ear and Hearing*, vol. 38, no. 6, pp. e343–e351, 2017.

[192] D. R. Moore and R. V. Shannon, "Beyond cochlear implants: awakening the deafened brain.," *Nature neuroscience*, vol. 12, pp. 686–91, jun 2009.

[193] D. McCreery, T. Yuen, and L. Bullara, "Chronic microstimulation in the feline ventral cochlear nucleus: physiologic and histologic effects," *Hearing research*, vol. 149, pp. 223–238, 2000.

[194] S. R. Otto, R. V. Shannon, E. P. Wilkinson, W. E. Hitselberger, D. B. McCreery, J. K. Moore, and D. E. Brackmann, "Audiologic Outcomes With the Penetrating Electrode Auditory Brainstem Implant," *Otology & Neurotology*, vol. 29, pp. 1147–1154, dec 2008.

[195] S. Cogan, T. Plante, and J. Ehrlich, "Sputtered iridium oxide films (SIROFs) for low-impedance neural stimulation and recording electrodes," *The 26th Annual International Conference of the IEEE Engineering in Medicine and Biology Society*, vol. 4, pp. 4153–4156, 2004.

[196] A. A. Guex, N. Vachicouras, A. E. Hight, M. C. Brown, D. J. Lee, and S. P. Lacour, "Conducting polymer electrodes for auditory brainstem implants," *Journal of Materials Chemistry B*, vol. 3, no. 25, pp. 5021–5027, 2015.

[197] D. Wu, Y. Luo, X. Zhou, Z. Dai, and B. Lin, "Multilayer poly(vinyl alcohol)-adsorbed coating on poly(dimethylsiloxane) microfluidic chips for biopolymer separation," *ELECTROPHORESIS*, vol. 26, pp. 211–218, jan 2005.

[198] I. Bucher, "Circle fit." [Accessed 17.11.2018]. Available from: https://www.mathworks.com/matlabcentral/fileexchange/5557-circle-fit?focused=5059278&tab=function, 1991.

[199] A. Kratochvíl and E. Hrnčíř, "Correlations between the cerebrospinal fluid surface tension value and 1. Concentration of total proteins 2. Number of cell elements," *General Physiology and Biophysics*, vol. 21, no. 1, pp. 47–53, 2002.

[200] Cochlear Ltd, "Nucleus ABI541 auditory brainstem implant Physician's Guide." [Accessed on: 29.11.2018]. Available from: https://www.cochlear.com/uk/for-professionals/sound-connection/cochlear-widens-its-range-of-implantable-hearing-solutions, 2017.

[201] A. Mercanzini, P. Colin, J.-C. Bensadoun, A. Bertsch, and P. Renaud, "In vivo electrical impedance spectroscopy of tissue reaction to microelectrode arrays.," *IEEE transactions on bio-medical engineering*, vol. 56, pp. 1909–18, jul 2009.

[202] J. Newman, "Resistance for Flow of Current to a Disk," *Journal of The Electrochemical Society*, vol. 113, no. 5, p. 501, 1966.

[203] Z. M. Wang, Z. J. Yang, F. Zhao, B. Wang, X. C. Wang, P. R. Qu, and P. N. Liu, "Auditory rehabilitation in rhesus macaque monkeys (Macaca mulatta) with auditory brainstem implants," *Chinese Medical Journal*, vol. 128, no. 10, pp. 1363–1369, 2015.

[204] M. a. Muniak, A. Rivas, K. L. Montey, B. J. May, H. W. Francis, and D. K. Ryugo, "3D model of frequency representation in the cochlear nucleus of the CBA/J mouse.," *The Journal of comparative neurology*, vol. 521, pp. 1510–32, may 2013.

[205] M. A. Muniak and D. K. Ryugo, "Tonotopic organization of vertical cells in the dorsal cochlear nucleus of the CBA/J mouse," *Journal of Comparative Neurology*, vol. 522, no. 4, pp. 937–949, 2014.

[206] G. Milinkeviciute, M. A. Muniak, and D. K. Ryugo, "Descending projections from the inferior colliculus to the dorsal cochlear nucleus are excitatory," *Journal of Comparative Neurology*, vol. 525, no. 4, pp. 773–793, 2017.

[207] E. D. Kozin, K. N. Darrow, A. E. Hight, A. E. Lehmann, A. B. Kaplan, M. C. Brown, and D. J. Lee, "Direct Visualization of the Murine Dorsal Cochlear Nucleus for Optogenetic Stimulation of the Auditory Pathway," *Journal of Visualized Experiments*, vol. 95, p. 52426, jan 2015.

[208] R. U. Verma, A. a. Guex, K. E. Hancock, N. Durakovic, C. M. McKay, M. C. C. Slama, M. C. Brown, and D. J. Lee, "Auditory responses to electric and infrared neural stimulation of the rat cochlear nucleus.," *Hearing research*, vol. 310, pp. 69–75, apr 2014.

[209] J. Parvizi and S. Kastner, "Promises and limitations of human intracranial electroencephalography," *Nature Neuroscience*, vol. 21, no. 4, pp. 474–483, 2018.

[210] P. Kwan, S. C. Schachter, and M. J. Brodie, "Drug-resistant epilepsy.," *The New England journal of medicine*, vol. 365, pp. 919–26, sep 2011.

[211] S. S. Kim, I. E. McCutcheon, D. Suki, J. S. Weinberg, R. Sawaya, F. F. Lang, D. Ferson, A. B. Heimberger, F. Demonte, and S. S. Prabhu, "Awake craniotomy for brain tumors near eloquent cortex: Correlation of intraoperative cortical mapping with neurological outcomes in 309 consecutive patients," *Neurosurgery*, vol. 64, no. 5, pp. 836–845, 2009.

[212] J. P. Seymour, F. Wu, K. D. Wise, and E. Yoon, "State-of-the-art MEMS and microsystem tools for brain research," *Microsystems & Nanoengineering*, vol. 3, no. February 2018, p. 16066, 2017.

[213] H. Takahashi, T. Ejiri, M. Nakao, N. Nakamura, K. Kaga, and T. Hervé, "Microelectrode array on folding polyimide ribbon for epidural mapping of functional evoked potentials," *IEEE Transactions on Biomedical Engineering*, vol. 50, no. 4, pp. 510–516, 2003.

[214] M. Gierthmuehlen, X. Wang, A. Gkogkidis, C. Henle, J. Fischer, T. Fehrenbacher, F. Kohler, M. Raab, I. Mader, C. Kuehn, K. Foerster, J. Haberstroh, T. M. Freiman, T. Stieglitz, J. Rickert, M. Schuettler, and T. Ball, "Mapping of sheep sensory cortex with a novel microelectrocorticography grid," *Journal of Comparative Neurology*, vol. 522, no. 16, pp. 3590–3608, 2014.

[215] D. Khodagholy, J. N. Gelinas, T. Thesen, W. Doyle, O. Devinsky, G. G. Malliaras, and G. Buzsáki, "NeuroGrid: recording action potentials from the surface of the brain," *Nature Neuroscience*, vol. 18, pp. 310–315, feb 2015.

[216] M. Ganji, E. Kaestner, J. Hermiz, N. Rogers, A. Tanaka, D. Cleary, S. H. Lee, J. Snider, M. Halgren, G. R. Cosgrove, B. S. Carter, D. Barba, I. Uguz, G. G. Malliaras, S. S. Cash, V. Gilja, E. Halgren, and S. A. Dayeh, "Development and Translation of PEDOT:PSS Microelectrodes for Intraoperative Monitoring," *Advanced Functional Materials*, vol. 28, no. 12, pp. 1–11, 2018.

[217] M. Gierthmuehlen, T. Ball, C. Henle, X. Wang, J. Rickert, M. Raab, T. Freiman, T. Stieglitz, and J. Kaminsky, "Evaluation of μECoG electrode arrays in the minipig: Experimental procedure and neurosurgical approach," *Journal of Neuroscience Methods*, vol. 202, no. 1, pp. 77–86, 2011.

[218] S. L. Craner and R. H. Ray, "Somatosensory cortex of the neonatal pig: I. Topographic organization of the primary somatosensory cortex (SI)," *Journal of Comparative Neurology*, vol. 306, no. 1, pp. 24–38, 1991.

[219] F. A. Zuleta, P. Velasquez, and P. N. De Aza, "Effect of various sterilization methods on the bioactivity of laser ablation pseudowollastonite coating," *Journal of Biomedical Materials Research - Part B Applied Biomaterials*, vol. 94, no. 2, pp. 399–405, 2010.

[220] M. G. Street, C. G. Welle, and P. A. Takmakov, "Automated reactive accelerated aging for rapid in vitro evaluation of neural implant performance," *Review of Scientific Instruments*, vol. 89, p. 094301, sep 2018.

[221] "ISO 14708-1:2014 Implants for surgery - Active implantable medical devices - Part 1: General requirements for safety, marking and for information to be provided by the manufacturer," 2014.

[222] Z. C. Chao, Y. Nagasaka, and N. Fujii, "Long-term asynchronous decoding of arm motion using electrocorticographic signals in monkeys.," *Frontiers in neuroengineering*, vol. 3, p. 3, nov 2010.

[223] K. Matsushita, M. Hirata, T. Suzuki, H. Ando, T. Yoshida, Y. Ota, F. Sato, S. Morris, H. Sugata, T. Goto, T. Yanagisawa, and T. Yoshimine, "A Fully Implantable Wireless ECoG 128-Channel Recording Device for Human Brain–Machine Interfaces: W-HERBS," *Frontiers in Neuroscience*, vol. 12, no. July, pp. 1–11, 2018.

[224] M. J. Vansteensel, E. G. Pels, M. G. Bleichner, M. P. Branco, T. Denison, Z. V. Freudenburg, P. Gosselaar, S. Leinders, T. H. Ottens, M. A. Van Den Boom, P. C. Van Rijen, E. J. Aarnoutse, and N. F. Ramsey, "Fully Implanted Brain–Computer Interface in a Locked-In Patient with ALS," *New England Journal of Medicine*, vol. 375, no. 21, pp. 2060–2066, 2016.

[225] A. K. Compton, B. Shah, and S. M. Hayek, "Spinal cord stimulation: A review," *Current Pain and Headache Reports*, vol. 16, no. 1, pp. 35–42, 2012.

[226] K. Kumar, R. S. Taylor, L. Jacques, S. Eldabe, M. Meglio, J. Molet, S. Thomson, J. O'Callaghan, E. Eisenberg, G. Milbouw, E. Buchser, G. Fortini, J. Richardson, and R. B. North, "Spinal cord stimulation versus conventional medical management for neuropathic pain: A multicentre randomised controlled trial in patients with failed back surgery syndrome," *Pain*, vol. 132, no. 1-2, pp. 179–188, 2007.

[227] R. Van Den Brand, J. Heutschi, Q. Barraud, J. Digiovanna, K. Bartholdi, M. Huerlimann, L. Friedli, I. Vollenweider, E. M. Moraud, S. Duis, N. Dominici, S. Micera, P. Musienko, and G. Courtine, "Supplementary Materials for Restoring Voluntary Control of Locomotion after Paralyzing Spinal Cord Injury Supporting Online Material Multi-system neuroprosthetic training," *Published Science*, vol. 336, no. June, pp. 1182–1186, 2012.

[228] M. Capogrosso, N. Wenger, S. Raspopovic, P. Musienko, J. Beauparlant, L. Bassi Luciani, G. Courtine, and S. Micera, "A Computational Model for Epidural Electrical Stimulation of Spinal Sensorimotor Circuits," *Journal of Neuroscience*, vol. 33, no. 49, pp. 19326–19340, 2013.

[229] F. B. Wagner, J.-B. Mignardot, C. G. Le Goff-Mignardot, R. Demesmaeker, S. Komi, M. Capogrosso, A. Rowald, I. Seáñez, M. Caban, E. Pirondini, M. Vat, L. A. McCracken, R. Heimgartner, I. Fodor, A. Watrin, P. Seguin, E. Paoles, K. Van Den Keybus, G. Eberle,

B. Schurch, E. Pralong, F. Becce, J. Prior, N. Buse, R. Buschman, E. Neufeld, N. Kuster, S. Carda, J. von Zitzewitz, V. Delattre, T. Denison, H. Lambert, K. Minassian, J. Bloch, and G. Courtine, "Targeted neurotechnology restores walking in humans with spinal cord injury," *Nature*, vol. 563, no. 7729, pp. 65–71, 2018.

[230] M. L. Gill, P. J. Grahn, J. S. Calvert, M. B. Linde, I. A. Lavrov, J. A. Strommen, L. A. Beck, D. G. Sayenko, M. G. Van Straaten, D. I. Drubach, D. D. Veith, A. R. Thoreson, C. Lopez, Y. P. Gerasimenko, V. R. Edgerton, K. H. Lee, and K. D. Zhao, "Neuromodulation of lumbosacral spinal networks enables independent stepping after complete paraplegia," *Nature Medicine*, vol. 24, pp. 1677–1682, nov 2018.

[231] C. A. Angeli, M. Boakye, R. A. Morton, J. Vogt, K. Benton, Y. Chen, C. K. Ferreira, and S. J. Harkema, "Recovery of Over-Ground Walking after Chronic Motor Complete Spinal Cord Injury," *New England Journal of Medicine*, p. NEJMoa1803588, 2018.

[232] M. Capogrosso, T. Milekovic, D. Borton, F. Wagner, E. M. Moraud, J. B. Mignardot, N. Buse, J. Gandar, Q. Barraud, D. Xing, E. Rey, S. Duis, Y. Jianzhong, W. K. D. Ko, Q. Li, P. Detemple, T. Denison, S. Micera, E. Bezard, J. Bloch, and G. Courtine, "A brain-spine interface alleviating gait deficits after spinal cord injury in primates," *Nature*, vol. 539, no. 7628, pp. 284–288, 2016.

[233] B. Barra, C. Roux, M. Kaeser, G. Schiavone, S. P. Lacour, G. Courtine, E. M. Rouiller, E. Schmidlin, and M. Capogrosso, "Selective Recruitment of Arm Motoneurons in Nonhuman Primates Using Epidural Electrical Stimulation of the Cervical Spinal Cord," *40th Annual International Conference of the IEEE Engineering in Medicine and Biology Society*, pp. 1424 – 1427, 2018.

[234] G. Schiavone, F. Wagner, F. Fallegger, X. Kang, N. Vachicouras, B. Barra, M. Capogrosso, J. Bloch, G. Courtine, and S. P. Lacour, "Long-term functionality of a soft electrode array for epidural spinal cord stimulation in a minipig model," in *2018 40th Annual International Conference of the IEEE Engineering in Medicine and Biology Society (EMBC)*, (Honolulu, HI), pp. 1432–1435, IEEE, jul 2018.

[235] M. Capogrosso, F. B. Wagner, J. Gandar, E. M. Moraud, N. Wenger, T. Milekovic, P. Shkorbatova, N. Pavlova, P. Musienko, E. Bezard, J. Bloch, and G. Courtine, "Configuration of electrical spinal cord stimulation through real-time processing of gait kinematics," *Nature Protocols*, vol. 13, no. 9, pp. 2031–2061, 2018.

[236] H. Yuk, B. Lu, and X. Zhao, "Hydrogel bioelectronics," *Chemical Society Reviews*, 2019.

[237] M. Bakula, F. Ceyssens, and R. Puers, "Polymer-CMOS Hybrid Neural Probes for Large-Scale Neuro-Electronic Interfacing," *Proceedings*, vol. 2, p. 1066, dec 2018.

[238] G. A. DeMichele, S. F. Cogan, P. R. Troyk, Hongnan Chen, and Zhe Hu, "Multichannel wireless ECoG array ASIC devices," in *2014 36th Annual International Conference of the IEEE Engineering in Medicine and Biology Society*, pp. 3969–3972, IEEE, aug 2014.

[239] B. Ji, Z. Guo, M. Wang, B. Yang, X. Wang, W. Li, and J. Liu, "Flexible polyimide-based hybrid opto-electric neural interface with 16 channels of micro-LEDs and electrodes," *Microsystems & Nanoengineering*, vol. 4, p. 27, dec 2018.

[240] M. Komatsu, E. Sugano, H. Tomita, and N. Fujii, "A Chronically Implantable Bidirectional Neural Interface for Non-human Primates," *Frontiers in Neuroscience*, vol. 11, pp. 1–9, sep 2017.

[241] T. Stieglitz, M. Schuetter, and K. Koch, "Implantable biomedical microsystems for neural prostheses," *IEEE Engineering in Medicine and Biology Magazine*, vol. 24, pp. 58–65, sep 2005.

[242] D. Wildes, W. Lee, B. Haider, S. Cogan, K. Sundaresan, D. M. Mills, C. Yetter, P. H. Hart, C. R. Haun, M. Concepcion, J. Kirkhorn, and M. Bitoun, "4-D ICE: A 2-D Array Transducer With Integrated ASIC in a 10-Fr Catheter for Real-Time 3-D Intracardiac Echocardiography," *IEEE Transactions on Ultrasonics, Ferroelectrics, and Frequency Control*, vol. 63, pp. 2159–2173, dec 2016.

[243] O. Yizhar, L. E. Fenno, T. J. Davidson, M. Mogri, and K. Deisseroth, "Optogenetics in Neural Systems," *Neuron*, vol. 71, pp. 9–34, jul 2011.

[244] R. Pashaie, P. Anikeeva, Jin Hyung Lee, R. Prakash, O. Yizhar, M. Prigge, D. Chander, T. J. Richner, and J. Williams, "Optogenetic Brain Interfaces," *IEEE Reviews in Biomedical Engineering*, vol. 7, pp. 3–30, 2014.

[245] K. Deisseroth, "Optogenetics: 10 years of microbial opsins in neuroscience," *Nature Neuroscience*, vol. 18, pp. 1213–1225, sep 2015.

[246] C. Wrobel, A. Dieter, A. Huet, D. Keppeler, C. J. Duque-Afonso, C. Vogl, G. Hoch, M. Jeschke, and T. Moser, "Optogenetic stimulation of cochlear neurons activates the auditory pathway and restores auditory-driven behavior in deaf adult gerbils," *Science Translational Medicine*, vol. 10, p. eaao0540, jul 2018.

[247] J. Viventi, D.-H. Kim, J. D. Moss, Y.-S. Kim, J. a. Blanco, N. Annetta, A. Hicks, J. Xiao, Y. Huang, D. J. Callans, J. a. Rogers, and B. Litt, "A Conformal, Bio-Interfaced Class of Silicon Electronics for Mapping Cardiac Electrophysiology," *Science Translational Medicine*, vol. 2, pp. 24ra22–24ra22, mar 2010.

[248] Q.-Z. Chen, A. Bismarck, U. Hansen, S. Junaid, M. Q. Tran, S. E. Harding, N. N. Ali, and A. R. Boccaccini, "Characterisation of a soft elastomer poly(glycerol sebacate) designed to match the mechanical properties of myocardial tissue," *Biomaterials*, vol. 29, pp. 47–57, jan 2008.

[249] D.-H. Kim, N. Lu, R. Ghaffari, Y.-S. Kim, S. P. Lee, L. Xu, J. Wu, R.-H. Kim, J. Song, Z. Liu, J. Viventi, B. de Graff, B. Elolampi, M. Mansour, M. J. Slepian, S. Hwang, J. D. Moss, S.-M. Won, Y. Huang, B. Litt, and J. A. Rogers, "Materials for multifunctional

balloon catheters with capabilities in cardiac electrophysiological mapping and ablation therapy," *Nature Materials*, vol. 10, pp. 316–323, apr 2011.

[250] L. Xu, S. R. Gutbrod, Y. Ma, A. Petrossians, Y. Liu, R. C. Webb, J. A. Fan, Z. Yang, R. Xu, J. J. Whalen, J. D. Weiland, Y. Huang, I. R. Efimov, and J. A. Rogers, "Materials and Fractal Designs for 3D Multifunctional Integumentary Membranes with Capabilities in Cardiac Electrotherapy," *Advanced Materials*, vol. 27, pp. 1731–1737, mar 2015.

[251] Deutsches Institut für Normung, "DIN 53504 (2009-10) : Testing of rubber - Determination of tensile strength at break, tensile stress at yield, elongation at break and stress values in a tensile test," 2010.

[252] Materials AZO, "Platinum (Pt) - Properties, Applications." [Accessed 14.09.2018]. Available from: https://www.azom.com/article.aspx?ArticleID=9235, 2013.

Nicolas Vachicouras

Geneva, Switzerland, +41 78 876 14 69, n.vachicouras@gmail.com

EDUCATION

Ecole Polytechnique Fédérale de Lausanne (EPFL), Switzerland

PhD in Microsystems and Microelectronics	2015 – Jan 2019 (exp.)
M.Sc. Microengineering (Micro-Nano Systems) & Minor Biomedical Engineering	2012 - 2014
B.Sc. Microengineering	2009 - 2012

EXPERIENCE

Laboratory for Soft Bioelectronic Interfaces (Prof. S. Lacour), Campus Biotech, EPFL Jan 2015 – Present

- PhD Thesis: Development of stretchable bioelectronic soft neural interfaces. Conception, fabrication, in vitro characterization and animal testing
- Collaborations with: Prof. Courtine (EPFL), Prof. Bloch (CHUV) and Profs. Daniel J. Lee and M. Christian Brown (Harvard Medical School)

Aleva Neurotherapeutics, Lausanne July 2013 – Present

- R&D intern and consultant: Design verification, electrochemical testing, technical documentation and development of software interfaces for automatized testing of microelectrode arrays in R&D department. Worked in ISO-13485 environment.

Eaton-Peabody Laboratories (Massachusetts Eye & Ear Infirmary), Department of Otology and Laryngology, Harvard Medical School, Boston Feb 2014 – Aug 2014

- Conducted my Master Thesis on the *in vivo* functional characterization of a microelectrode array for electrical stimulation of the auditory brainstem in rodent.
- Performed animal surgeries, retrieved and analyzed neural data, and developed a computational model of the electrical stimulation of the cochlear nucleus in mice.

Institute for Value-Based Enterprise, Lausanne Oct 2011 - March 2012

- Participated in the "What a Young Entrepreneur Needs to Know" workshop series and wrote a business plan awarded a *Magna Cum Laude* certificate.

SCHOLARSHIPS AND AWARDS

2014 Poster Contest organized by the IEEE Student Branch at EPFL: 2nd Prize

Scholarship from the Zdenek and Michaela Bakala Foundation (2013-2014) for Master Thesis

START Lausanne 2012: Finalist in elevator pitch and business plan writing team contest

2011 International Contest of Applications in Nano-Micro Technology, Beijing: Swiss selections and "Best Contribution Award" in Beijing finals (team contest)

SKILLS

Computer Languages	C/C++, ASM, PHP, XHTML/CSS, Python
Engineering Software	LaTeX, MATLAB, Pro-Engineering CAD, Autodesk AUTOCAD, Eagle PCB Design, COMSOL Multiphysics
Microfabrication	Polymers processing, metal evaporation, wet and dry etching, photolithography, scanning electron microscopy
Electrochemistry	Electrochemical characterization of electrode arrays in vitro and in vivo
In vivo Experimentation	Resal module 1. Hands-on experience in handling of rodents, neuro-surgery on mice. Experimentation for electrical stimulation and recording of neural tissue in mice, rats, non-human primates, mini-pigs and human cadaveric specimens.

LANGUAGES
French (native), English (fluent), Greek (fluent, B-Level Certificate), German (elementary)

PATENTS
Engineering reversible elasticity in ductile or brittle thin films, PCT/EP2017/080876

PUBLICATIONS, PEER REVIEWED
Schiavone G, Wagner F W, Fallegger F, Kang X, Vachicouras N, Barra B, Capogrosso M, Block J, Courtine G., and Lacour SP. Long-term functionality of a soft electrode array for epidural spinal cord stimulation in a minipig model. In *2018 40th Annual International Conference of the IEEE Engineering in Medicine and Biology Society (EMBC)*, pp. 1432-1435. IEEE, (2018).

Vachicouras N, Tringides CM, Campiche PB, and Lacour SP. Engineering reversible elasticity in ductile and brittle thin films supported by a plastic foil. *Extreme Mechanics Letters*, *15*, 63-69, (2017).

Salomon R, Fernandez NB, van Elk M, Vachicouras N, Sabatier F, Tychinskaya A, Llobera J and Blanke O. *Changing motor perception by sensorimotor conflicts and body ownership*. Scientific reports, 6, (2016).

Guex AA, Vachicouras N, Hight AE, Brown MC, Lee DJ and Lacour SP. *Conducting polymer electrodes for auditory brainstem implants*. Journal of Materials Chemistry B, (2015).

Minev IR, Musienko P, Hirsch A, Barraud Q, Wenger N, Moraud EM, ... and Lacour SP. *Electronic dura mater for long-term multimodal neural interfaces*. Science, 347(6218), 159-163, (2015).

Cyganowski A, Minev IR, Vachicouras N, Musick K and Lacour SP, *Stretchable electrodes for neuroprosthetic interfaces*. Sensors*, 2012 IEEE* (pp. 1-4). IEEE (2012)

ABSTRACTS, CONFERENCES
Vachicouras N, Tarabichi O, Kanumuri VV, Brown MC, Lee DJ, and Lacour SP. *Conformable electrode arrays for chronic stimulation of the auditory brainstem in mice*. Presented a poster at Gordon Research Conferences – Neuroelectronic Interfaces, Galveston, USA (2018).

Vachicouras N, Tringides C, Campiche P and Lacour SP. *Reversible elasticity in ductile or brittle thin films supported by a plastic foil*. Presented a talk at Fall Materials Research Society Meeting, Boston, USA (2016).

Vachicouras N, Tringides C, Campiche P, Gupta S and Lacour SP. *Engineering Stretchable Platinum for Soft Neuroprosthesis*. Presented a talk at Spring Materials Research Society Meeting, Phoenix, USA (2016)